Monitoring Cancer Response to Treatment with Hyperpolarized 13C MRS

Eldirdiri, Abubakr

Publication date:
2017

Document Version
Publisher's PDF, also known as Version of record

PhD Thesis

Monitoring Cancer Response to Treatment with Hyperpolarized ^{13}C MRS

Author: Abubakr Eldirdiri
Supervisors: Jan Henrik Ardenkjær-Larsen, Ph.D., Andreas Kjær, Ph.D., Lars G. Hanson, Ph.D.

Technical University of Denmark
Kgs. Lyngby, Denmark

This project was funded by the Danish Research Council (Grant Number 1331-00259A) and the Danish National Research Foundation (Grant Number DNRF124).

A thesis submitted in fulfillment of the requirements for PhD degree

March 2017

Abstract

Monitoring the cancer response to treatment, non-invasively, by medical imaging is a key element in the management of cancer. For patients undergoing treatment, it is crucial to determine responders from non-responders in order to guide treatment decisions. Currently, PET is the most widely used technique for imaging tumor function by measuring the uptake of the glucose analogue FDG. FDG-PET can visualize changes in metabolic activity and indicate if a patient will respond to a particular therapy, sometimes within hours of the first treatment. However, PET is not effective in all tumor types, and the patient is exposed to ionizing radiation. The introduction of hyperpolarized ^{13}C MRS has opened completely new possibilities to study the biochemical changes in disease processes. Numerous ^{13}C-labeled compounds were proposed to interrogate various aspects of cancer cell metabolism.

The aim of this study is to investigate the relevance of [1-^{13}C]pyruvate and [1,4-$^{13}C_2$]fumarate in monitoring the changes in cellular metabolism and necrosis that may occur as a result of cancer therapy. This project also aims to improve existing ^{13}C MRSI methods to efficiently utilize the signal from hyperpolarized ^{13}C substrates.

Firstly, we investigate the effectiveness of hyperpolarized [1-^{13}C]pyruvate in detecting the treatment response in two types of NSCLC xenografted in mice, in comparison with FDG- and FLT-PET. We show here a significant reduction in tumor lactate levels, obtained by MRS, in HCC-827 tumors, as well as lower FLT- and FDG-PET uptake with erlotinib treatment. These findings were validated *ex vivo*, where LDH activity level and Ki-67 IHC staining was significantly lower in treated HCC-827 tumors. Furthermore, the reduction in LDH activity levels correlated with the lactate levels found using ^{13}C MRS. These findings indicate the hyperpolarized [1-^{13}C]pyruvate can be an alternative to FDG-PET.

In the second study, a polarization scheme for [1,4-$^{13}C_2$]fumarate in the SPINlab polarizer is presented. The feasibility of using [1,4-$^{13}C_2$]fumarate as marker for monitoring induced necrosis is demonstrated *in vivo* in two rat models; ischemia/reperfusion induced necrosis in kidneys and turpentine induced necrosis in muscle. High polarization was achieved for [1,4-$^{13}C_2$]fumarate in the SPIN-

lab and high [1,4-$^{13}C_2$]malate signal was observed from the necrotic tissue in both models. The elevated malate signal observed in the ischemia/reperfusion induced injury in kidney showed high correlation with well-known blood and urine bio-markers used to characterize acute kidney injuries. Moreover, simultaneous assessment of metabolism and necrosis was achieved using dual polarization of [1,4-$^{13}C_2$]fumarate and [1-^{13}C]pyruvate.

Finally, a symmetric echo planar spectroscopic imaging sequence for hyperpolarized ^{13}C spectroscopic acquisition in clinical scanners is presented with a reconstruction algorithm that separately reconstruct the data from odd and even echoes in order to reduce artifacts from gradient imbalances. The reconstruction algorithm employs re-gridding in the spatio-temporal frequency space to compensate for the chemical shift displacements. The sequence is compared with conventional phase-encoded chemical shift imaging on a clinical PET/MRI system in phantoms and a large animal model. The SNR per unit time of EPSI for ^{13}C at thermal equilibrium was comparable to CSI. The reconstruction pipeline improved the localization compared to direct FFT, which resulted in spatial blurring. The encoding speed of EPSI allowed dynamic imaging of tumor metabolism with high spatial and temporal resolutions and reduced blurring due to T_1 decay.

Acknowledgments

My sincere thanks to my supervisor Jan Henrik Ardenkjær-Larsen for giving me this wonderful opportunity to work with him, and also for his support, encouragement and inspiration. I also want to thank Andreas Kjær for his guidance and for providing valuable insights into biology. I want to express my thanks also to Lars G. Hanson for his tremendous aid.

Special thanks also go to Stefan Posse and his group at University of New Mexico for mentoring me and for creating an excellent research atmosphere during my stay with them.

I also want to thank Adam E. Hansen and the PET/MR team at Rigshospitalet; Marianne, Karin and Jacob for their great support during the experiments. I also want to thank Sacsha Gude for her help with the studies that took place at Hvidovre Hospital.

Thanks to my colleagues, especially Olexandr, Irina, Juan, Sean, Cihan, Mursal, Bannay, Kasper, Rie, Mette and Andreas for exchanging thoughts and ideas, challenging me and making every working day a great pleasure. Also a big thanks go to Signe for her support, patience and compassion.

I also want to express my gratitude to my family and friends for their continuous encouragement.

Abbreviations

CT	Computed tomography
MR	Magnetic resonance
PET	Positron emission tomography
MRS	Magnetic resonance spectroscopy
FDG	2-Deoxy-2-[^{18}F]fluoro-D-glucose
FLT	3'-[^{18}F]Fluoro-3'-deoxythymidine
DNP	Dynamic nuclear polarization
dDNP	Dissolution dynamic nuclear polarization
NSCLC	Non-small-cell lung cancer
IR	Ischemia/reperfusion
EPSI	Echo planar spectroscopic imaging
EGFR	Epidermal growth factor receptor
ATP	Adenosine triphosphatey
TKI	Tyrosine kinase inhibitor
TCA	Tricarboxylic acid
LDH	Lactate dehydrogenase
TMP, TDP, and TTP	thymidine mono-, di-, and tri-phosphate
CSI	Chemical shift imaging
MRSI	Magnetic resonance spectroscopic imaging
TR	Repetition time
TE	Echo time
FOV	Field of view
DCE	Dynamic contrast enhancement
AKI	Acute kidney injury
CrCl	Creatinine clearance
BUN	Blood urea nitrogen
KIM-1	Kidney injury molecule 1
NGAL	Neutrophil gelatinase-associated lipocalin
FA	[1,4-$^{13}C_2$]Fumaric acid
PA	[1-^{13}C]Pyruvic acid
LN_2	Liquid nitrogen
EDTA	Ethylenediaminetetraacetic acid disodium salt dehydrate
Tris	2-Amino-2-(hydroxymethyl)-1,3-propanediol

ADC	Analog-to-digital
SNR	Signal-to-noise ratio
BW	Bandwidth
SW	Spectral bandwidth
ETL	Echo train length
GLM	General linear model

Contents

Abstract **ii**

Acknowledgments **iii**

Abbreviations **vi**

Contents **vii**

List of figures **x**

List of tables **xvii**

1 Motivation and Outline **3**

2 Cancer Pathophysiology **7**

2.1 Proliferation in Cancer 7

2.2 Cancer Metabolism 10

2.3 Monitoring Cancer Response to Treatment with PET 11

2.3.1 FDG 12

2.3.2 FLT 12

3 Imaging Cancer with Hyperpolarized ^{13}C MRS **15**

3.1 NMR 15

3.2 DNP 17

3.3 Characterization of Cancer with Hyperpolarized ^{13}C Substrates . 19

3.3.1 Monitoring Cancer Metabolism with Hyperpolarized Pyruvate 20

3.3.2 [1,4-$^{13}C_2$]Fumarate as a Marker for Necrosis 20

3.4 Magnetic Resonance Spectroscopic Imaging 21

3.4.1 k-t Sampling Schemes for Hyperpolarized ^{13}C 25

3.4.2 Echo Planar Spectroscopic Imaging 26

4 Treatment Response in Non-Small-Cell Lung Cancer with Hyperpolarized [1-^{13}C]Pyruvate, FLT- and FDG-PET **29**

4.1 Objective 29

4.2 Animal Population 29

4.3 Hyperpolarization and MR Experiment . . . 30
4.4 FLT- and FDG-PET Experiment . . . 33
4.5 LDH and Ki-67 Signatures . . . 34
4.6 Discussion . . . 34
4.7 Conclusion . . . 36

5 Necrosis Monitoring with hyperpolarized [1,4-$^{13}C_2$]fumarate 37
5.1 Objectives . . . 37
5.2 Formulation of [1,4-$^{13}C_2$]Fumarate and [1-^{13}C]Pyruvate . . . 38
5.3 Single [1,4-$^{13}C_2$]Fumarate Polarization . . . 38
5.4 Dual [1,4-$^{13}C_2$]Fumarate and [1-^{13}C]Pyruvate Polarization . . . 41
5.5 Phantom MR Experiments for polarization and T_1 measurements 41
5.6 Necrosis Imaging in Rat Muscles . . . 43
5.6.1 Animal Model . . . 43
5.6.2 Combined PET/MR Experiments . . . 44
5.7 Ischemia/Reperfusion Induced Necrosis in Rat Kidneys . . . 46
5.7.1 Animal Model . . . 46
5.7.2 AKI Biomarkers . . . 46
5.7.3 MR Experiment . . . 48
5.8 Discussion . . . 50
5.9 Conclusion . . . 52

6 Implementation of ^{13}C Echo Planar Spectroscopic Imaging Sequence in a Clinical System 53
6.1 Objective . . . 53
6.2 Design of ^{13}C EPSI . . . 53
6.2.1 Echo Planar Readout Gradient . . . 54
6.2.2 Phase Encoding Gradient . . . 55
6.2.3 RF Pulses . . . 56
6.3 SNR Efficiency . . . 57
6.4 Reconstruction and Postprocessing . . . 57
6.5 SNR Phantom Experiment . . . 58
6.5.1 MR Acquisition Method . . . 58
6.5.2 Results of SNR Comparison . . . 60
6.5.3 Localization Assessment . . . 63
6.6 Phantom Experiment with Hyperpolarized [1-^{13}C]Pyruvate . . . 64
6.6.1 Hyperpolarized Phantom Preparation . . . 64

6.7 Animal experiment 66
6.7.1 Animal Model 66
6.7.2 Hyperpolarzed Media Preparation 66
6.7.3 PET/MR Acquisition 66
6.7.4 Results from Canine Cancer Patient 67
6.8 Discussion 69
6.9 Conclusion 71

7 Perspectives and Future Work **73**

Bibliography **74**

Appendices **95**

A Treatment response in non-small-cell lung cancer estimated with hyperpolarized ^{13}C pyruvate, FLT- and FDG-PET **97**

B Simultaneous imaging of hyperpolarized [1,4-$^{13}C_2$]fumarate, [1-^{13}C]pyruvate and 18F-FDG in rat model of necrosis in a clinical PET/MR **121**

C Fumarase activity: an in vivo and in vitro biomarker for acute kidney injury **151**

D Echo Planar Spectroscopic Imaging of Hyperpolarized ^{13}C in a Clinical PET/MRI scanner: Studies in Phantoms and Canine Cancer Patient **163**

List of Figures

2.1 Proliferation controlling receptors in the cell membrane and signal transduction in the cytoplasm. This figure is a simplification of the cell signaling pathways diagram by Hanahan and Weinberg [25]. Growth factors and inhibitors (e.g. TGFβ) are received by transmembrane receptors and these in turn deliver it to intracellular circuits. Apoptosis is controlled by a sensory mechanism that senses the extracellular and intracellular environments [32–34]. Extracellular sensors include survival and death signal receptors. Intracellular sensors monitor the cell condition, i.g. DNA damage, survival factor insufficiency, or hypoxia. The most important regulator here is the p53 tumor suppressor protein [35]. The protein p53, in response to DNA damage, signals to initiate DNA repair or apoptosis if the damage is irreparable. 8

2.2 Encoding gene of epidermal growth factor receptor in Non Small Cell Lung Cancer including extracellular binding domain, the trans-membrane domain and intracellular tyrosine kinase domain. HCC-827 cancer cells are activated by delE746-A750 deletion mutation in exon 19, were as NCI-H1975 is activated by L858R substitution in exon 21. Additionally, NCI-H1975 has a substitution mutation T790M in exon 20, which gives this cell line resistance to treatment by TKI. 9

2.3 Metabolism in normal cell (A) and cancer metabolic phenotype (B) with high glycolytic flux and increased lactate production. . 10

2.4 DNA synthesis from *de novo* and *salvage pathways*. 13

3.1 Randomly oriented spins in the absence of an external magnetic field. The resultant magnetization from superposition of the magnetic dipole moments of the spins in the ensemble is zero. The figure was reproduced with permission from [78]. 16

3.2 Spins orientation with the application of a magnetic field $\vec{B}_0$. The resultant magnetization from the spins' magnetic dipole moments points in the direction of the magnetic field. The figure was reproduced with permission from [78]. 16

3.3 Polarization values of proton and electron spins at 14 T magnet. In the high temperature approximation, the polarization of electron spins is 658 times greater than proton spins. At low temperature, $<$ 10 K, electron spins has already achieved full polarization. 18

3.4 Different k-t space acquisition schemes. CSI (a) has the highest spectral bandwidth, but require more excitations. EPSI (b) achieves a good compromise between the encoding efficiency and robustness by filling the data in on line in k-space at each excitation. Spiral spectroscopic imaging (c) can fill the k-t space in one excitation, but the resultant spectral bandwidth is very narrow, which dictates the use of interleave acquisitions. In centric ring acquisition (d), circles in the k-space are covered at the successive excitations using sinusoidal oscillating gradients. 27

4.1 Representative ^{13}C metabolic maps of pyruvate and lactate for both treated and untreated HCC-827 and H-1975 xenografted tumors. The metabolic maps are overlaid on proton images acquired at the same position as the CSI, with white arrows indicating the tumor position. 30

4.2 Quantitative evaluation of pyruvate, lactate and their ratio in HCC-827 (A) and H-1975 (B) tumors. A significant reduction in lactate level ($p < 0.005$) was observed for treated HCC-827 tumors compared to untreated. No significant change in metabolite levels was seen for H-1975 tumors. (C) Levels of LDH enzyme normalized to total protein content in HCC-827 tumor samples. A significant reduction was found in the treated tumors compared to untreated tumors ($p < 0.05$). (D) Correlation between levels of LDH enzyme normalized to the total protein content and lactate level evaluated by ^{13}C MRSI ($p < 0.01$). 31

4.3 Quantification of perfusion imaging, showing inflow (A) and outflow (B) coefficients for treated and untreated HCC-827 and H-1975 tumors. No significant difference in coefficients was found between cell lines and treatment. (C) shows a representative temporal development in signal enhancement, as well as the fitted, gamma-variate curves. Corresponding representative images are shown for three time points in (D), with arrows indicating the tumors. 32

4.4 (A) and (B) quantitative comparison between FDG and FLT uptake for treated and untreated HCC-827 and H-1975 tumors in units of % ID / g. Significant reduction in uptake was seen for both FDG and FLT (both $p < 0.002$) in treated HCC-827 tumors compared to untreated. No significant change in uptake was observed for H-1975 tumors. (C) Quantitative evaluation of Ki-67 staining showed a significantly reduced number of stained cells in treated HCC-827 tumors compared to the untreated ones ($p < 0.05$). 35

5.1 (A) The fluid path that goes into the SPINlab. The path consists of a syringe that contains the dissolution media and sample vial that contains the ^{13}C substrate to be polarized. The two are connected by two concentric tubes. During the dissolution, the dissolution medium is transferred through the inner tube to the sample vial where it dissolves the hyperpolarized substrate. The dissolved material flows back through the outer tube lumen toward the syringe and out of the SPINlab via the exit tube. (B) shows schematic draw of the sample vial. The vial is prepared, in the dual polarization scheme, by first adding the PA and then freezing it in LN_2 and then adding the FA. The vial is then kept in LN_2 during the rest of preparation of the fluid path to attain two separate layers in the vial. (C) shows the path of the vial once it is inserted in the SPINlab. The vial is initially placed in the airlock for 20 min to allow the sample to melt. Then, it is lowered in multiple steps, back and forth, along the path until it settles at the He sample pot to avoid excessive increase in temperature at the He pot. 39

5.2 The anatomical axial image of the first rat (A) acquired at the location of the necrotic tissue. The image was acquired with turbo spin echo (TR= 5.7 s, TE= 84 ms, echo train length of 18, number of phase encoding steps 234, Number of averages of 5, final matrix size of 256x256 covering a FOV of 100 mm x 100 mm with slice thickness of 2 mm). (B) shows the spectrum at the necrotic tissue with the fumarate peak the malate doublet. Clear malate signal can be observed in the spectrum. The small peak at the right of the spectrum at 164 ppm is due to fold over of the ^{13}C-urea phantom. (C) and (D) show the metabolic maps of fumarate and malate, respectively. Notice that the malate production is confined to the necrotic region. 43

5.3 The anatomical axial image of the second rat (A) acquired at the location of the necrotic tissue. The proton image was acquired similar to Figure 5.2A. A coronal maximum intensity projection image, which shows the FDG uptake by the different organs is illustrated in (B). (C) shows an axial slice (thickness of 12 mm, sum of 6 frames) with the FDG uptake in a plane containing the necrotic tissue. (D) and (E) show the phased real part spectra at the necrotic tissue, the blue box in (A), acquired for single injection of FA and dual injection of FA and PA, respectively. The malate signal can be seen in both spectra. In the dual FA and PA experiment, additional peaks are observed for lactate, alanine, pyruvate-hydrate and bicarbonate. The metabolic map of pyruvate, lactate, fumarate and malate, obtained from the dually polarization of FA and PA, are shown in (F, G , H and I). High lactate and malate signals are observed at the necrotic tissue. 44

5.4 Comparison between plasma creatinine, CrCl and BUN biomarkers before and after surgery. 46

5.5 Representative histological sections are shown in (A) for a CL kidney showing normal intact tubular cells and glomeruli, and (B) for a post-ischemic kidney showing a cellular cast in the tubular lumina (green arrow), complete sloughing of tubular epithelium (red arrow), interstitial edema (black arrow), and glomerular

edema (yellow arrow). The relative expression of injury markers, in (C) and (D), indicated significant upregulation of NGAL (p = 0.0145, n = 6) and KIM-1 (p = 0.0256, n = 6) respectively A paired two-sided Student's t-test was used to compare the CL and IR injured kidneys. 47

5.6 Anatomical ^{1}H kidney sections overlaid with (A) ^{13}C-labelled fumarate images and (B) ^{13}C-labelled malate images. Red arrow indicates the post-ischemic kidney and green arrow indicate contralateral kidney. (C) A malate/fumarate ratio is calculated from each kidney, giving rise to an elevated ratio in the post-ischemic kidney. 48

5.7 Correlation between renal injury and malate/fumarate ratio. A significant correlation was found between (A) NGAL and malate/-fumarate ratios, (B) KIM-1 and malate/fumarate ratio. 49

5.8 Correlation between urine and plasma fumarase activity. A significant correlation was found between (A) Urine fumarase activity and (B) Plasma fumarase activity. 50

6.1 Design of even and odd lobes of the readout gradient with the ADC readout events. 55

6.2 Pulse sequence diagram of the EPSI-FID with ETL = 128. . . . 56

6.3 The pipeline used for the reconstruction of the raw data and the correction of the broadening due to chemical shifts in opposite directions in the odd and even data. 59

6.4 A comparison of chemical shift displacement with (A) direct FFT reconstruction and (B and C) with reconstruction after spectral-spatial regridding. The images from odd (green) and even (magenta) echoes are overlaid. The locations of overlap appear in white and the non-overlap locations appear colored. In (B) spectral-spatial regridding removes the chemical shift displacement of bicarbonate and urea, which are within the spectral bandwidth, but increases the chemical shift displacement of acetate that is

aliased. In (C) the chemical shift displacement of the acetate peak is additionally corrected using its non-aliased frequency location in the reconstruction. 61

6.5 The [1- ^{13}C]acetate, ^{13}C-bicarbonate and ^{13}C-urea maps acquired by CSI and EPSI. Only the central part of the phantom is shown. The signal level in the maps is normalized with respect to the bicarbonate signal acquired with CSI. The spectrum from a single voxel at the center of each substrate is also shown for both CSI and EPSI. The line width (full width at half height) obtained with CSI was 12.2 Hz, 9.2 Hz and 10.6 Hz for [1-^{13}C]acetate, ^{13}C-bicarbonate and ^{13}C-urea respectively, whereas the line width obtained with EPSI was 11.7 Hz, 8.7 Hz and 9.8 Hz. 62

6.6 The center of each substrate as obtained from the proton image (blue dot) and the position of the substrate obtained from the CSI and EPSI acquisitions (green dot). 63

6.7 Dynamic images acquired for hyperpolarized [1-^{13}C]pyruvate in a 4.5 L phantom with EPSI and CSI. 65

6.8 (A) The the coil profile first dynamic image acquired for hyperpolarized [1-^{13}C]pyruvate as obtained with EPSI (A). (B) shows the decay of the signal from hyperpolarized pyruvate obtained by both EPSI and CSI. An exponential function was fitted to EPSI signal giving a time constant of 52 s. 65

6.9 The anatomical images (transversal, coronal and sagittal) acquired with TSE and used to position the spectroscopic grids for both CSI and EPSI (A, B and C). The green box is at the location of the tumor. 67

6.10 The acanthomatous ameloblastoma in the left mandible of the canine cancer patient (A). The PET-FDG image (slice thickness 2 mm) with high uptake in the tumor and brain regions is shown in (D). (B and E) show the pyruvate and lactate signals, obtained from the CSI acquisition using GLM, at the slice containing the tumor. Increased lactate production can be observed at the tumor and muscle sites. (C and F) show pyruvate and lactate im-

ages calculated from the dynamic EPSI by integrating over the frames in Figure 6.11. 68

6.11 Pyruvate and lactate build-up and decay across the slice containing the tumor. The figure also shows the spectrum with GLM fitting at the tumor site in the EPSI frame acquired 27 s after the end of injection. 69

6.12 (A) The build-up of pyruvate and its conversion to lactate obtained with dynamic FID acquisition over a 4 cm axial slab that includes the tumor region. (B and C) show the time curves for lactate and pyruvate obtained from the EPSI series (Figure 6.11) by integrating the pyruvate and lactate signals in each frame at the whole image and at the tumor region, respectively. 70

List of Tables

5.1 Solid state DNP build-up data for three different samples with two different loading profiles. 41

5.2 Liquid state polarization and T_1 measurements for the sample with FA (3.6 M) with 8 mM of AH111501 radical. 42

1

Motivation and Outline

Much of the early classical methods used to characterize cancer and monitor its progression or response to treatment, which are widely still in use [1], have been based on anatomical imaging. In those methods, changes in tumor size and texture, as it appears in x-ray computed tomography (CT) or magnetic resonance (MR) images, were used in the assessment. However, it can take up to several months before these methods can indicate whether the tumor is in remission state or still progressing with treatment. Therefore, considerable efforts are made to develop imaging modalities that can detect the cancer response to treatment as early as possible to ensure that the patient is receiving the right treatment without wasting valuable time.

These efforts led to advancements in fields like positron emission tomography (PET) [2–5] and magnetic resonance spectroscopy (MRS) [6–8]. These modalities can probe the tumor function, which is usually directly affected by treatment. The most widely used method in the clinic is PET that utilizes various radioactive tracers, with the most commonly used one being 2-deoxy-2-[^{18}F]fluoro-D-glucose (FDG). FDG-PET can show the high rates of glucose uptake and utilization by most cancer types. Additionally, FDG uptake in some types of cancers is reduced as early as 24 h after treatment [9,10], whereas it can take weeks or months before the tumors shrink. FDG-PET, however, cannot detect the presence and aggressiveness of some types of cancer because of their relatively low uptake or because the signal from the surrounding tissues or organ is high, making it difficult to distinguish the tumor. In addition, PET imaging involves exposure to ionizing radiation, which makes multiple close examination with this modality undesirable especially if the patient is young.

Proton (^{1}H) MRS has been successfully applied to assess the physiology of some cancer types like brain [11] and prostate cancers [8, 12, 13] because of their distinguishable metabolic profiles from normal cells. MRS also has the advantage that, unlike PET, it can give more complete picture of the metabolic pathways, since several metabolites can be quantified from the spectrum. However, a major obstacle with MRS is the inherently low sensitivity, which results in images with poor spatial resolution and long acquisition times. The low sensitivity also makes MRS with nuclei other than ^{1}H unfeasible.

MRS has been combined with hyperpolarization techniques to enhance the signal by several orders of magnitude [14]. Hyperpolarization has since been applied in *in vivo* imaging of ^{13}C labeled organic substrates that lie at crossroads of major metabolic pathways. The most notable example is [1-^{13}C]pyruvate, which has been widely used to observe the increased [1-^{13}C]lactate production in cancer due to the increased aerobic glycolysis [15–20]. Another promising substrate is [1,4-$^{13}C_2$]fumarate that allows monitoring cellular necrosis *in vivo* [21–24].

The purpose of this study is to investigate the non-invasive imaging of hyperpolarized ^{13}C substrates, namely [1-^{13}C]pyruvate and [1,4-$^{13}C_2$]fumarate, and their relevance in monitoring tumor response to treatment. In chapter 2 of the thesis, a background is given about some of the hallmarks of cancer related to proliferation and metabolism. A short background is also given on the use of PET to monitor cancer response to treatment with focus on two traces, FDG and 3'-[^{18}F]Fluoro-3'-deoxythymidine (FLT), which were used in the first study conducted in this PhD. Chapter 3 gives an introduction to nuclear magnetic resonance and hyperpolarization using the dissolution Dynamic Nuclear Polarization (dDNP) method. This chapter also highlights some of the promising ^{13}C substrates and their role in assessing cancer physiology with focus on [1-^{13}C]pyruvate and [1,4-$^{13}C_2$]fumarate. Finally, an introduction to ^{13}C MRS is given. In chapter 4 a study is presented in which the ^{13}C MRS of hyperpolarized [1-^{13}C]pyruvate was compared with FDG- and FLT-PET in monitoring the response of cancer to treatment. This comparison study was performed in two cell lines of non-small-cell lung cancer (NSCLC). Chapter 5 details the optimization of the chemical formulation of [1,4-$^{13}C_2$]fumarate and its polarization in the clinical SPINlab polarizer, since unlike [1-^{13}C]pyruvate, [1,4-$^{13}C_2$]fumarate has not been widely used in SPINlab. Then, the use of hyperpolarized [1,4-

$^{13}C_2$]fumarate to monitor necrosis is demonstrated in two models. The first one is turpentine induced necrosis in rat muscles and the second is ischemia/reperfusion (IR) induced necrosis in rat kidneys. Chapter 6 provides a detailed implementation of echo planar spectroscopic imaging (EPSI) sequence with robust reconstruction in a clinical MR system. Chapter 7 draws some perspectives and future work.

2

Cancer Pathophysiology

Cancer is believed to be a result of genetic alterations that manifest itself in a number of physiological characteristics [25, 26]. These characteristics or phenotypes drive the progressive transformation of normal human cells into highly malignant tumor[1]. The most prominent of them is the high proliferation rate achieved through self-sufficiency in growth signals, insensitivity to anti-growth signals, ability to evade programmed cell death and limitless replicative potential. Another important characteristics of cancer is the alteration in the energy metabolism to cope with the high rate of proliferation.

2.1 Proliferation in Cancer

Normal cells require growth signals or factors, typically produced by other cells and conveyed via certain types of proteins, before they can move from a dormant quiescent state into an active proliferative state [27–29]. These signals are transmitted into the cell by transmembrane receptors. Once the signal is received, it triggers a series of cascaded biological reactions within the cell that ends with DNA synthesis and cell multiplication, see Figure 2.1.

To maintain increased proliferation rates, cancer cells need to achieve self-sufficiency in growth stimulation and can acquire this in a number of ways [30, 31]. For instance, genetic modifications can result in structural alteration in the growth receptors on the cellular membranes making them fire continuously.

[1] We cover here some of the cancer phenotypes relevant to the studies presented in the following chapters. For more comprehensive review on cancer hallmarks refer to [25, 26].

In some cancer types, receptor overexpression may enable the cancer cells to become responsive to the normal levels of growth factor that normally will not cause proliferation. Moreover, cancer cells may acquire the ability to synthesize their own growth factors to which they are sensitive, unlike the case with normal cells where growth factors are synthesized externally by other types of cells. Another mechanism is to alter the components of the downstream reactions in the cytoplasm to induce proliferation without signal from upstream.

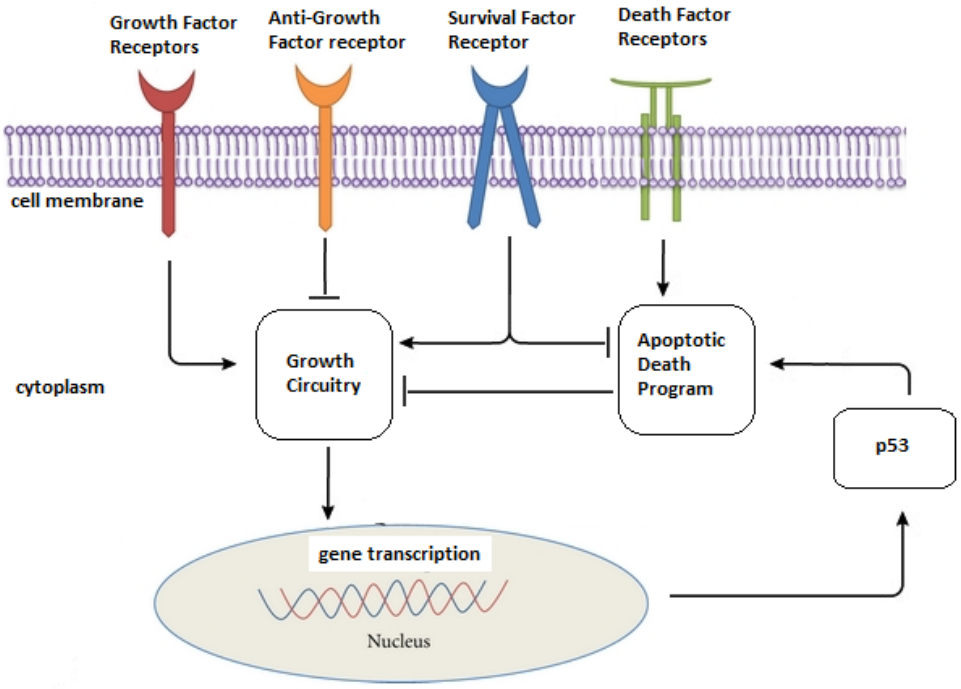

Figure 2.1: Proliferation controlling receptors in the cell membrane and signal transduction in the cytoplasm. This figure is a simplification of the cell signaling pathways diagram by Hanahan and Weinberg [25]. Growth factors and inhibitors (e.g. TGFβ) are received by transmembrane receptors and these in turn deliver it to intracellular circuits. Apoptosis is controlled by a sensory mechanism that senses the extracellular and intracellular environments [32–34]. Extracellular sensors include survival and death signal receptors. Intracellular sensors monitor the cell condition, i.g. DNA damage, survival factor insufficiency, or hypoxia. The most important regulator here is the p53 tumor suppressor protein [35]. The protein p53, in response to DNA damage, signals to initiate DNA repair or apoptosis if the damage is irreparable.

Cellular proliferation does not depend only on growth stimulatory signals but also is governed by growth inhibition, which works in a similar manner to stop proliferation [36, 37]. Moreover, Programmed cell death like apoptosis is an important mechanism that control the size of the cell population and guard against abnormalities [38, 39]. The cells must also evade these two mechanisms for the cancer to grow vigorously [40, 41].

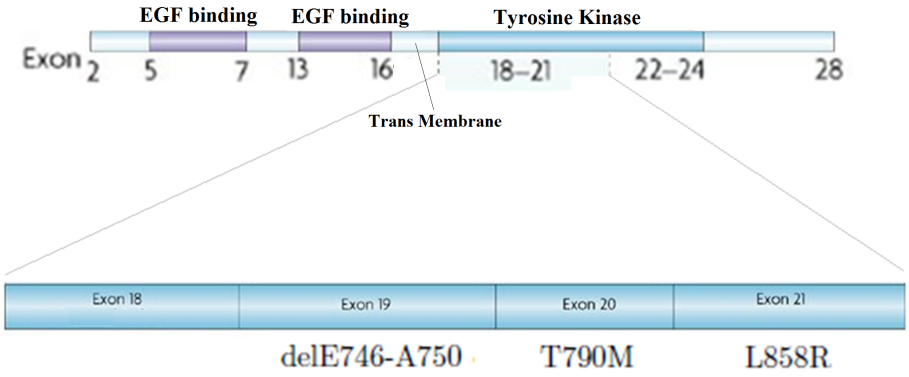

Figure 2.2: Encoding gene of epidermal growth factor receptor in Non Small Cell Lung Cancer including extracellular binding domain, the trans-membrane domain and intracellular tyrosine kinase domain. HCC-827 cancer cells are activated by delE746-A750 deletion mutation in exon 19, were as NCI-H1975 is activated by L858R substitution in exon 21. Additionally, NCI-H1975 has a substitution mutation T790M in exon 20, which gives this cell line resistance to treatment by TKI.

The overexpression in the epidermal growth factor receptors (EGFR) is an example of up-regulation in growth factor receptor that can be seen many cancer types, namely NSCLC, due to mutations in the four exons 18-21, which are in the encoding domain of the tyrosine kinase activity of the EGFR, see Figure 2.2. The most common of these mutations are delE746-A750 deletions in exon 19 as in HCC827 cells and L858R substitution in exon 21 as in NCI-H1975 cell [42–44], see chapter 4. EGFR has an intrinsic tyrosine kinase function. When activated, it transfers a phosphate group from adenosine triphosphate (ATP) and attached it to the amino acid tyrosine, which is a key step that initiates a cascaded signal that ends with DNA synthesis. The function of EGFR can effectively be inhibited by tyrosine kinase inhibitors (TKIs) like elrotinib that out-competes EGFR for ATP. Therefore, many types of NSCLC like HCC827 typically have

good response to therapy with TKIs [42, 45, 46]. However some types of NSCLC like NCI-H1975 has acquired resistance to TKIs due to T790M atypical mutation in exon 20 [47–50]. T790M increases the affinity of EGFR for ATP, therefore restoring its enzymatic function.

2.2 Cancer Metabolism

The alterations that cancer cells exhibit include modification in the energy metabolism that fuels cell growth and division. In normal cell, when oxygen is abundant, glucose is processed in the cytosol via glycolysis into pyruvate, producing 2 ATP units per glucose molecule. Pyruvate is then dispatched to the mitochondria where it enters the tricarboxylic acid (TCA) cycle that consumes oxygen and produce 18 ATP units per 1 pyruvate molecule. Under anaerobic conditions, glycolytic flux is increased to produce more ATP and most of the pyruvate is converted into lactate, Figure 2.3. This is catalyzed by lactate dehydrogenase (LDH). However, even in the presence of oxygen, most cancer cells limit their energy metabolism largely to glycolysis rather than the oxidative phosphorylation of pyruvate in the mitochondria [52]. This is done by upregulating the glucose transporters in the cell membranes to increase the glucose transfer to the cytoplasm.

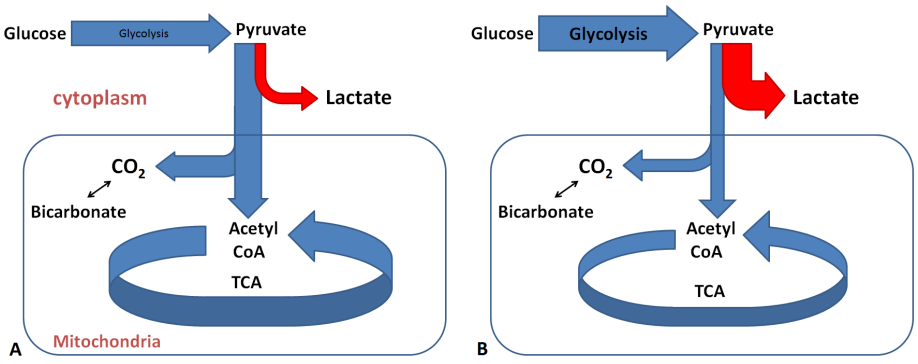

Figure 2.3: Metabolism in normal cell (A) and cancer metabolic phenotype (B) with high glycolytic flux and increased lactate production.

When noticing this metabolic phenotype Warburg hypothesized that cancer cells may have defective mitochondria incapable of maintaining oxidative

respiration. Most cancer cells, however, do not necessarily have compromised mitochondria [53]. The reason behind favoring the poor efficiency of ATP production by glycolysis over the oxidative phosphorylation is that the former is more capable of supporting the proliferation process [54, 55]. Glycolysis provides the intermediates needed for the biosynthesis like ribose for nucleotides and glycerol for lipids and cell membranes. Moreover, the rate of ATP production in glycolysis can be increased high enough to produce an amount of ATP that exceed that produced from oxidative phosphorylation [56, 57]. It has also been established that signaling pathways that affect proliferation also affect metabolism [58]. Perhaps the rationale behind the conversion of private into lactate and not oxidizing it to enhance the production of ATP is that, pyruvate oxidation cannot cope with the high glycolysis flux. Therefore, overexpression of lactate dehydrogenase A (LDH-A) in many cancer types is used as a mechanism to avoid accumulation of pyruvate [59].

2.3 Monitoring Cancer Response to Treatment with PET

PET is a functional imaging modality in which tracers, analogous to biological compounds, are labeled with isotopes that emit positrons. A positron from these isotopes travels a short distance, typically less than 1 mm, before it is annihilated when it interacts with an electron of a nearby atom. The annihilation results in a pair of gamma rays emitted in opposite directions, which can be detected using a gamma camera. After intravenous injection, these tracers can be entrapped in certain tissues or cells and then tomographic images of their distribution within the body can be obtained.

Examples of PET tracers are ^{11}C-thymidine [61, 62] and FLT [63] that are used to characterize proliferation, since thymidine can be taken up into the DNA during synthesis. [^{18}F]fluorotyrosine, L-[^{11}C]tyrosine and ^{11}C-methionine are examples of amino acids analogues that have been studied in oncology [64, 65], since the increased proliferation in cancer requires active protein synthesis, and therefore increased amino acid uptake by overexpression of amino acid transporters. Beside protein synthesis, lipids synthesis from choline as constituent of cellular membranes is also important during cell division and multiplication.

Therefore, choline ^{11}C and ^{18}F isotopes [66–68] has been used as markers for tumor malignancy. The major drawback with ^{11}C labeled tracers is their very short half-life. For this reason, ^{18}F labeled agents are commonly used. Here, more focus will be given to FDG and FLT tracers used in the first study of this PhD project, 4.

2.3.1 FDG

The most commonly used PET tracer in oncology is the glucose analogue, FDG. After injection, FDG leaks from the vasculature to the extracellular space. From there, glucose transporters, which are overexpressed in cancer, transport it into the cells. FDG is not fully processed via glycolysis. Unlike glucose, FDG lacks a hydroxyl group in position 2, which is required in the second step of the glycolysis. Therefore, FDG is trapped within the cells. Typically the uptake of FDG within tumor tissue is higher than for normal tissue, because of the overexpression in glucose transporters and the increased glycolysis.

A problem with FDG is its susceptibility to false-positive from normal body functions. For example, large muscle groups require more glucose when they are overexerted, which increases their FDG uptake. It is also well known that inflammation, e.g. resulting from cancer treatment via radiofrequency ablation or surgery, can lead to false positive, even if the treatment is working. Moreover, the tumor can be masked in some cases by its neighboring tissue, as in the case of the brain and the heart, where the cells have high metabolic demand and therefore require large amounts of glucose.

2.3.2 FLT

FLT tracer, a Thymidine (or deoxyribosylthymine) analogue, is increasingly being used clinically to target proliferation, which is the key biological process upregulated in cancer. When injected, FLT nucleoside is taken up by the cells and phosphorylated by thymidine kinase 1 with one, two, or three phosphoric acid groups, creating thymidine mono-, di-, or tri-phosphate (TMP, TDP, or TTP) nucleotide, respectively. It cannot be used further in the synthysis of DNA because its ribose sugar is lacking a hydroxyl group needed for bonding

with phosphate group in another nucleotide molecule to form the phosphate-deoxyribose backbone of DNA. FLT is trapped after phosphorylation, and the retention of FLT within the cell provides a measure of thymidine kinase 1 activity. Due to the increased proliferation in cancer, thymidine kinase 1 activity can increase about 10-fold during DNA synthesis [69, 70]. The DNA synthesis described above is the *salvage* pathway, since the cells to use thymidine nucleosides produced elsewhere. Thymidine nucleotides can also be produced endogenously in the cell, i.e. *de novo*, from deoxyuridine monophosphate [71, 72], Figure 2.4.

Compared to FDG, the uptake of FLT after an inflammatory response is less, which makes false positives less likely. Moreover, most of the chemotherapeutics drugs directly impact the proliferation. Therefore, FLT might be a better monitoring tracer in these cases.

One issue with FLT is its reliance on the thymidine *salvage* pathway, while ignoring the *de novo* pathway. Different cancer types can utilize either pathways to a varying degree. This make the FLT data difficult to interpret sometimes. For example, FLT cannot discriminate between moderately proliferating thymidine *salvage*-driven tumors and high proliferating tumors that rely on the *de novo* thymidine synthesis [73]. Moreover, some types of chemotherapies that inhibit the *de novo* path can cause increase in the synthesis from the *salvage* path and thus FLT, despite the overall reduction of proliferation [74, 75].

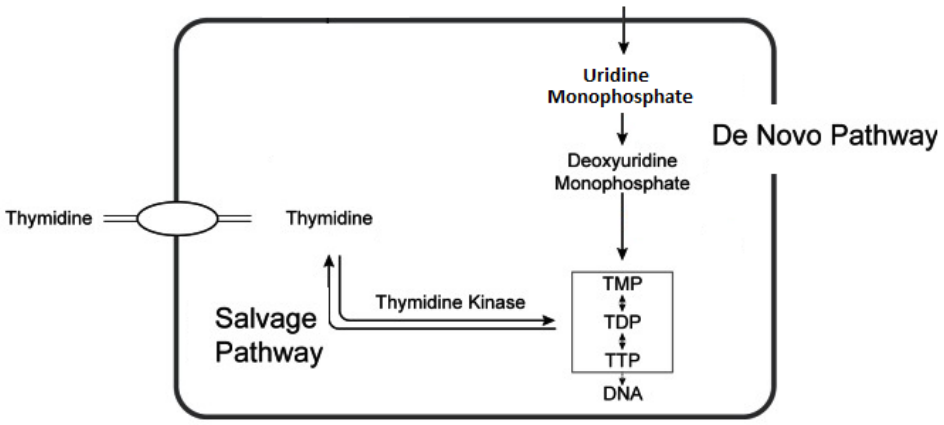

Figure 2.4: DNA synthesis from *de novo* and *salvage pathways*.

3

Imaging Cancer with Hyperpolarized ^{13}C MRS

3.1 NMR

Magnetic resonance imaging is based on nuclei with spin quantum number $I \geq 1/2$. These nuclei, also called spins, possess angular momentum, $\vec{L}$, and can be thought of as spinning around a spin axis. Due to this angular momentum, spins also have magnetic dipole moment, $\vec{\mu}$,

$$\vec{\mu} = \gamma \vec{L} \tag{3.1}$$

where γ, called the gyromagnetic ratio, is the ratio between the magnetic dipole moment and the angular momentum and it is a property of the nucleus. The resultant of the magnetic dipole moments from spins in an ensemble, also termed the magnetization $\vec{M}$, is what gives rise to the signal in MR. In the absence of an external magnetic field, the spins are randomly oriented and the resultant magnetization , $\vec{M}$, is zero (see Figure 3.1). When a static field $\vec{B_0}$ is applied, they start precessing around this field and the previously randomly oriented spins tend to slightly point more toward $\vec{B_0}$ and less away from it, Figure 3.2, therefore making the resultant magnetization non zero.

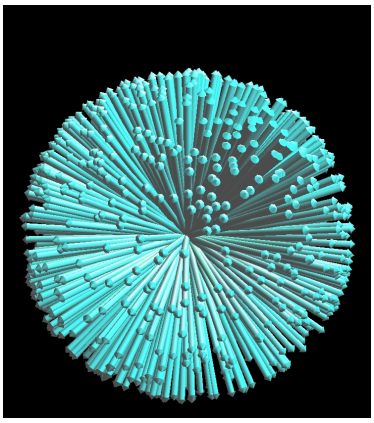

Figure 3.1: Randomly oriented spins in the absence of an external magnetic field. The resultant magnetization from superposition of the magnetic dipole moments of the spins in the ensemble is zero. The figure was reproduced with permission from [78].

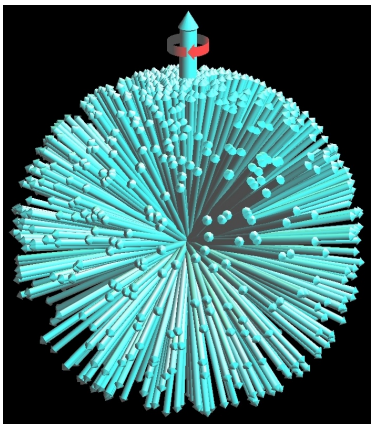

Figure 3.2: Spins orientation with the application of a magnetic field $\vec{B_0}$. The resultant magnetization from the spins' magnetic dipole moments points in the direction of the magnetic field. The figure was reproduced with permission from [78].

From quantum mechanics point of view[1], there are two eigenstates for spins with quantum number $I = 1/2$. The energy difference, δE, between the two is a function of the applied magnetic field $\vec{B_0}$,

[1]See [79] for more complete interpretation on this non trivial split in the eigenstates.

$$\delta E = \gamma \hbar B_0 \tag{3.2}$$

where γ is the gyromagnetic ratio of a given isotope and $\hbar$ is Planck's constant. The distribution of population between the two levels is described by Boltzmann equation,

$$\frac{N_\downarrow}{N_\uparrow} = e^{\gamma \hbar B_0 / kT} \tag{3.3}$$

where k is Boltzmann's constant and T is the absolute temperature. The two energy levels are almost equally populated in ambient temperature. This makes the net magnetization of an ensemble very small. The degree of spin alignment is termed the polarization, P, and it can be derived from 3.3,

$$P = \frac{N_\downarrow - N_\uparrow}{N_\downarrow + N_\uparrow} = tanh(\frac{\gamma \hbar B_0}{KT}) \tag{3.4}$$

Therefore, the magnetization, M, can be expressed in terms of the polarization, P, as follows

$$\vec{M} = NP\vec{\mu} \tag{3.5}$$

where N is the total number of spins in the volume.

What makes the MR sensitivity inherently low is this low alignment of spins in the ensemble for most of the biologically relevant nuclei. For nuclei such as ^{1}H and ^{13}C the polarization value at ambient temperature is in the range of $(10^{-6} - 10^{-5})$.

3.2 DNP

It has been known since the middle of the last century that polarization can be increased artificially by orders of magnitude above thermal equilibrium [80]. A number of techniques have been used to achieve this. These techniques work

by transferring the polarization to the nuclei of interest from spins that can be highly polarized under certain conditions. The source of polarization can be the electron spins in a paramagnetic agent as in dynamic nuclear polarization (DNP) [14,81–83], or in alkali metal vapor as in spin-exchange optical pumping [84–86]. Another source that has been used for polarization is parahydrogen as in parahydrogen induced polarization based methods [87–93].

DNP, the hyperpolarization method used here, makes use of the fact that the polarization of electron spins is significantly large than ^{1}H or ^{13}C nuclear spins at the same temperature, Figure 3.3, due to the high gyromagnetic ratio of the electron. For example, in a 14 T magnetic field at 10 K the electron's spins has almost achieved 100% polarization, while at the same temperature the polarization of ^{1}H spins is around 0.2%.

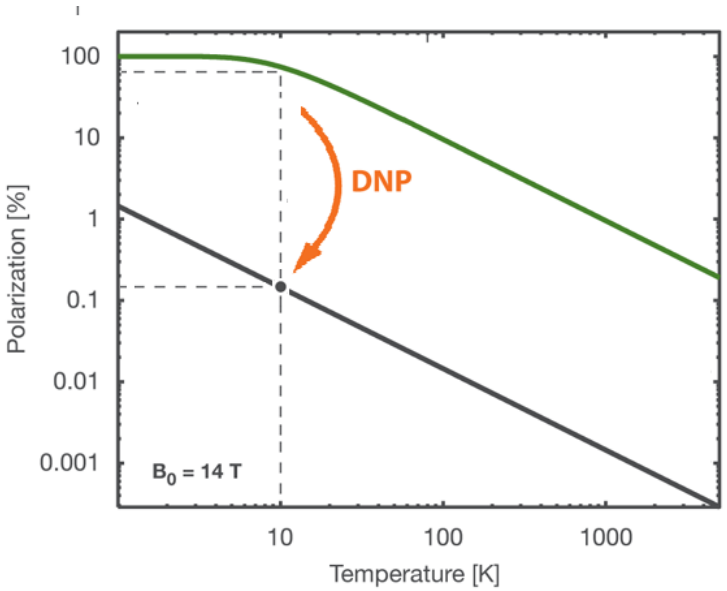

Figure 3.3: Polarization values of proton and electron spins at 14 T magnet. In the high temperature approximation, the polarization of electron spins is 658 times greater than proton spins. At low temperature, $<$ 10 K, electron spins has already achieved full polarization.

In the dDNP technique, a biological compound of interest is mixed with a hydrophilic and chemically stable substance, such as trityl or nitroxide radicals, that has abundance of unpaired electron spins. The mixture is then cooled

to a very low temperature, around 1 K, in a magnetic field to achieve unity polarization for the electron spins. The sample is then subjected to microwave irradiation close to the resonance frequency of the electron spin, which leads to the transfer of polarization to the nuclear spins of interest (e.g. ^{13}C, ^{1}H or ^{15}N) through various mechanisms [95]. Once the sample is polarized, it is rapidly dissolved (hence, dissolution DNP, dDNP) in a heated buffer that also ensures the right physiological pH and osmolarity/tonicity for *in vivo* use. The hyperpolarzied compound is then injected, typically intravenously, in a subject and its cellular uptake and enzymatic pathways is monitored using magnetic resonance spectroscopy.

3.3 Characterization of Cancer with Hyperpolarized ^{13}C Substrates

Numerous compounds have been polarized with dDNP and used in cancer studies. [U-^{2}H, U-^{13}C]Glucose has been used to image the glycolytic fluxes in cancer *in vitro* [97] and *in vivo* to study the variation in these fluxes following treatment [98, 99]. Another molecule that has been used to investigate the glycolysis in tumor cells is [2-^{13}C]fructose [100]. Since cancer cells tend to deplete much of the intermediates in the TCA cycle while using them as precursors for bio-synthetic and proliferation pathways (cataplerosis), most cancer types exhibit an increased anaplerosis, the biochemical reactions used to refuel the TCA cycle with intermediates. This has been studied using hyperpolarized glutamine [101,102], [1-^{13}C]glutamine and [5-^{13}C]glutamine, and its oxidation (glutaminolysis) into glutamate, which is a precursor for α-ketoglutarate, a TCA cycle intermediate. Hyperpolarized [1-^{13}C] ketoisocaproate [103] and its increased transamination into leucine, which is associated with the increased conversion of glutamate into α-ketoglutarate has also been used to characterize cancer. Moreover, hyperpolarized [1-^{13}C]dehydroascorbic acid was proposed as a noninvasive biomarker of redox status *in vivo*, and it was shown that tumor has increased conversion rate of dehydroascorbic acid to ascorbic acid due to its high reducing environment [104–106]. [^{13}C]bicarbonate is another important substrate that can be used to probe the tissue pH homeostasis *in vivo*, and it has been used to demonstrate the alterations in the extracellular pH in cancer [107, 108].

3.3.1 Monitoring Cancer Metabolism with Hyperpolarized Pyruvate

The most commonly used substrate in dDNP studies is [1-^{13}C]pyruvate. Pyruvate, which is the final product of the glycolysis, is the main fuel for the TCA cycle that takes place inside the mitochondria to generate energy in the form of ATP. When pyruvate crosses the membranes of the mitochondria, it is decarboxylated by the pyruvate dehydrogenase enzyme complex into acetyl-CoA. Pyruvate can also be converted into lactate via the lactate dehydrogenase enzyme and into alanine via the alanine transaminase enzyme in the cytoplasmic matrix.

It has been shown that tumors have increased [1-^{13}C]lactate production [16, 18, 109], and in some type of cancer also increased [1-^{13}C]alanine production [16, 110], after *in vivo* injection of hyperpolarized [1-^{13}C]pyruvate. There is also evidence that the relative amount of lactate produced with respect to pyruvate can reflect the tumor grade in some cancer types [16]. Moreover, it have been shown in numerous studies [15, 20, 24, 111–118] that the conversion rate of hyperpolarized [1-^{13}C]pyruvate into lactate can provide an early prediction for the response of cancer to treatment, and thus offering a valuable modality to assess cancer therapy. Hyperpolarized [1-^{13}C]pyruvate has already been used in the clinic to study prostate cancer [17].

3.3.2 [1,4-$^{13}C_2$]Fumarate as a Marker for Necrosis

Necrosis was once thought of as non-programmed cell death. Evidence now suggests that there is some degree of programming involved in necrosis, and that it serves important biological processes, like the induction of inflammatory responses [119]. In necrosis, the cellular membranes are broken, which results in the cells spilling their contents into their neighborhood. Due to the cessation of active processes in the cell, digestive enzymes are released and the cell is destroyed. This process can potentially cause inflammatory response, which can be damaging. In apoptosis, a programmed death mechanisms, the cell condenses and collapses on itself forming number of apoptotic bodies that are phagocytosed and digested neatly without damaging its neighbors.

Necrosis has been shown to play a role in many pathological processes like neurodegenerative disorders [120, 121], ischemia/reperfusion injuries [122], and viral and microbial infections [123, 124]. Necrosis may also play an important role in many physiological processes like ovulation [125] and embryogenesis [126]. In addition, many chemotheributical agents used for cancer treatment are known to induce death in cancer cells through necrosis [127–129]. A common method to study necrosis *in vivo* is by diffusion weighted imaging, which can image the loss of cellularity [130–133]. However, it may take some time, after necrosis, before any sign can be seen in these images [134]. Hyperpolarized [1,4-$^{13}C_2$]fumarate has been shown to allow early detection of necrosis and has been used *in vivo* to monitor the necrosis in cancer induced by chemotherapy [21, 22, 114]. Hyperpolarized [1,4-$^{13}C_2$]fumarate has also been used *in vivo* in early detection of renal acute tubular necrosis [23]. The conversion of fumarate into malate, catalyzed by fumarase, is one of the steps in the mitochondrial TCA cycle. The amount of [1,4-$^{13}C_2$]malate produced in normal intact cells following the injection of [1,4-$^{13}C_2$]fumarate is very low due to the limited amount of fumarate that crosses the cellular and mitochondrial membranes. As fumarase is exposed by cells that undergo necrosis, an increased [1,4-$^{13}C_2$]malate production can be observed from necrotic tissue.

3.4 Magnetic Resonance Spectroscopic Imaging

When the magnetization from an isochromat[2] of spins in a magnetic field, $\vec{B_0}$, is excited, it precesses around this field with a frequency, f_σ, dictated by the gyromagnetic ratio, γ, of the spins and the strength of the magnetic field, B_σ, that the spins experience.

$$f_\sigma = \gamma B_\sigma \tag{3.6}$$

The magnetic field strength B_σ that the spins experience can be slightly different from the strength of the applied static magnetic field, B_0, due to the fact that the electron clouds around the spins reorient themselves to slightly oppose and thus weaken the field B_0.

[2]Isochromat in this context refers to spins that have the same chemical shift and experience the same magnetic field.

$$B_\sigma = B_0 + (\Delta B)_\sigma \tag{3.7}$$

Here $(\Delta B)_\sigma$ is the field due to the electron cloud. If the magnetization, after excitation, is observed from a reference frame rotating with frequency equal to γB_0, which is the case with MR imaging due to signal demodulation, then the magnetization will appear to be precessing with a frequency given by

$$f_\sigma = \gamma(\Delta B)_\sigma \tag{3.8}$$

Then, neglecting the relaxation, the magnetization vector in the transverse plane, xy, at any time t will be

$$M_{xy}(t) = M_0(f_\sigma)e^{-i2\pi f_\sigma t} \tag{3.9}$$

where $M_0(f_\sigma)$ is the amplitude of the equilibrium magnetization from the spins with chemical shift f_σ and it is proportional to the number of spins in this population as in equation 3.5. We can write the signal received in time as[3],

$$s(t) = M_0(f_\sigma)e^{-i2\pi f_\sigma t} \tag{3.10}$$

If more than one isochromat of spins with different chemical shifts are present in the ensemble, then the signal collected will be a superposition of the magnetizations precessing at the different frequencies as

$$s(t) = \int_{f_\sigma} M_0(f_\sigma)e^{-i2\pi f_\sigma t} df_\sigma \tag{3.11}$$

Equation 3.11 shows the Fourier nature by which the signal collected in the time domain and the magnitude of the magnetizations from the different spin isochromats in the frequency domain are related. Direct Fourier transform can be applied on the signal collected to obtain the magnetization of each spin isochromat and thus their relative populations.

[3]The signal received is proportional to the magnetization,$s(t) \propto M_{xy}(t)$, but for simplicity we can write $s(t) = M_{xy}(t)$

Up till now we considered the case of single point spectroscopy, where the signal is assumed to be originating from a single point source. In MR imaging, spatial localization is achieved by applying gradient magnetic fields. In the case of two dimensional MR imaging gradients, for instance G_x and G_y, are employed along two directions, x and y. The effect of these gradient is that, the magnetic field experienced by the spins will be a function of the position in addition to the chemical shift. Again assuming the rotating frame of reference,

$$B = (\Delta B)_\sigma + G_z x + G_y y \tag{3.12}$$

After excitation the precession frequency of the magnetization at any position (x,y) for a metabolite with chemical shift frequency f_σ is

$$f = f_\sigma + \gamma G_x x + \gamma G_y y \tag{3.13}$$

and the magnetization vector will be

$$M_{xy}(x, y, f_\sigma, t) = M_0(x, y, f_\sigma) e^{-i(2\pi f_\sigma t + \gamma \int_0^t G_x dt\, x + \gamma \int_0^t G_y dt\, y)} \tag{3.14}$$

where $t = 0$ is time the receiver was turned on. We can define k-space coordinates, k_x and k_y, at which the signal is collected in time as function of the applied gradients, G_x and G_y, as follows

$$k_x = \frac{\gamma}{2\pi} \int_0^t G_x(t) dt \tag{3.15}$$

and

$$k_y = \frac{\gamma}{2\pi} \int_0^t G_y(t) dt \tag{3.16}$$

The signal received is derived from the contributions of the transverse magnetizations precessing at all metabolic frequencies in the excited space.

$$s(k_x, k_y, t) = \int_{f_\sigma} \int_y \int_x M_0(x, y, f_\sigma) e^{-i2\pi(f_\sigma t + k_x x + k_y y)} dx dy df_\sigma \tag{3.17}$$

The last equation shows that the signal can be collected in the temporal and k-space domains, $k_x - k_y - t$, and then transformed into the spatial and frequency domain, $x - y - f_\sigma$, to obtain spectroscopic images of the spins in the ensemble.

Due to Fourier relationship, it can be shown that the spatial and frequency resolutions, Δx, Δy and Δf are dictated by the extend of the k-space and the total acquisition duration T,

$$\Delta x = \frac{1}{k_{x,max} - k_{x,min}} \tag{3.18}$$

$$\Delta y = \frac{1}{k_{y,max} - k_{y,min}} \tag{3.19}$$

$$\Delta f = \frac{1}{T} \tag{3.20}$$

Similarly the spectral bandwidth, BW (the extend in the frequency domain), and the fields of view, FOV_x and FOV_y (the extend in spatial domain), are related to the resolution in k-space, Δk_x and Δk_y, and the dwell time, t_s (the time elapsed between the successive acquisitions of the same point in k-space), as follows

$$FOV_x = \frac{1}{\Delta k_x} \tag{3.21}$$

$$FOV_y = \frac{1}{\Delta k_y} \tag{3.22}$$

$$BW = \frac{1}{t_s} \tag{3.23}$$

3.4.1 k-t Sampling Schemes for Hyperpolarized ^{13}C

The different spectroscopic imaging methods adopt various techniques to fill the data in $k_x - k_y - t$ space. The classical 2D phase-encoded chemical shift imaging (CSI) [136, 137] sequence works by traversing the k-space via two phase encoding gradients. One point in k-space is sampled for each excitation, see Figure 3.4a. With a high sampling rate along the temporal dimension, the spectral bandwidth with phase encoded CSI is very large. However, obtaining high spatial resolution with CSI requires additional phase encoding steps. sampling only one point in the k-space at each excitation makes the total imaging duration of CSI relatively long.

In the case of ^{1}H magnetic resonance spectroscopic imaging (MRSI), where long acquisition durations can be tolerable, the robust CSI sequence can be used with no severe penalty. However, since the enhanced magnetization obtained from hyperpolarization methods is short lived, and the magnetization spent on excitations is non-recoverable. This dictates the use of faster MRSI sequences that can efficiently utilize the decaying signal.

In fast MRSI methods, the gradients are employed to collect the data from more than one k-space point at each excitation. For instance, in echo planar spectroscopic imaging (EPSI) [138–142], the gradients are oscillated to traverse back and forth along one line in the k-space while the data are collected, Figure 3.4b. This is also the case with multi-echo b-SSFP [143–145]. This sampling scheme requires less excitations to cover all the k-space and therefore the total acquisition duration with EPSI is relatively short compared with CSI. The points along the time dimension are typically sampled with a dwell time dictated by the echo spacing, which can be in the order of hundreds of microseconds to milliseconds. Thus, EPSI typically has a narrow bandwidth compared to CSI.

Spiral spectroscopic imaging [146–149] and IDEAL spiral [150] pushes the demand on gradients further by acquiring few full k-space frames in each excitation using a spiral trajectory, Figure 3.4c. Since the sampling rate along the time axis is very low with spiral spectroscopic imaging, additional interleaved acquisitions are made in which the data collected in k-t space are shifted along the time axis to increase the spectral bandwidth.

The short imaging time and fewer excitations of such fast sequences make them more attractive for imaging of hyperpolarized nuclear spins, since they facilitate observing the conversion of the hyperpolarized substrates to their metabolic products with reasonable temporal resolution. These sequences, however, are characterized by a limited spectral bandwidth due to gradient slew rate constraints, which requires spectral prior knowledge to be taken into consideration for spatial-spectral reconstruction. This reduced spectral bandwidth is not usually a limitation for hyperpolarized MRI, since the spectrum of the hyperpolarized ^{13}C substrate and its metabolic products is sparse and spectral aliasing can be controlled to avoid peak overlap. However, compared to conventional CSI, these fast acquisition sequences are more demanding on gradient strength and slew rate, and require extensive ramp sampling on clinical MR scanners as opposed to preclinical systems, which reduces the SNR per unit square root time. The limitations on gradient performance make it challenging to translate the use of these sequences from animal to human studies.

3.4.2 Echo Planar Spectroscopic Imaging

EPSI is one of the most established sequence to achieve dynamic imaging of the metabolism clinical studies with hyperpolarized [1-^{13}C]pyruvate [17]. The sequence was first introduced to ^{13}C hyperpolarized imaging by Cunningham et al [138]. It has been combined with various excitation modules like double spin echo [139], variable flip angle [141] and multiband excitation [140]. Compared with other fast acquisition techniques, EPSI can be easily incorporated with acceleration schemes like parallel imaging [151] and compressed sensing [152] to achive fast dynamic 3D MR spectroscopic imaging. In a study by Durst et al [153], EPSI, spiral and IDEAL spiral spectroscopic imaging were compared with respect to SNR, encoding efficiency, demand on gradients, and artifact behavior. They reported that these sequences were are not very different in terms of SNR. Moreover, EPSI was the most robust choice compared to spiral and IDEAL spiral imaging, which were most prone to artifacts.

EPSI with symmetric readout gradients typically suffer from ghosting artifacts [154, 155] due to gradient imperfection, which require reference scans to estimate and correct the discrepancies between the odd and even echoes [156].

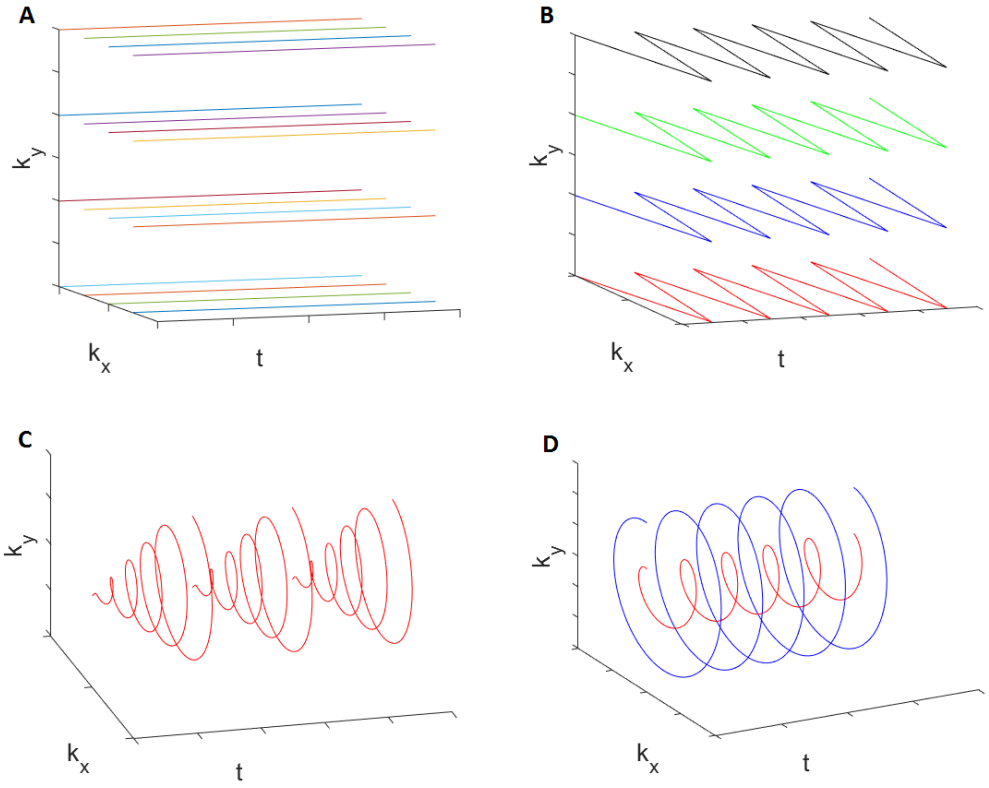

Figure 3.4: Different k-t space acquisition schemes. CSI (a) has the highest spectral bandwidth, but require more excitations. EPSI (b) achieves a good compromise between the encoding efficiency and robustness by filling the data in on line in k-space at each excitation. Spiral spectroscopic imaging (c) can fill the k-t space in one excitation, but the resultant spectral bandwidth is very narrow, which dictates the use of interleave acquisitions. In centric ring acquisition (d), circles in the k-space are covered at the successive excitations using sinusoidal oscillating gradients.

Flyback EPSI is sometimes preferred over symmetric EPSI to avoid the need to correct these differences [153, 157]. However, flyback EPSI suffers from lower SNR because the receiver is idle for longer duration [138, 158]. Symmetric EPSI with separate reconstruction of the odd and even echo data is sufficient and simple, if the resultant smaller spectral bandwidth is acceptable. The simplest way to reconstruct the even and odd data is via FFT assuming that the data are collected on a Cartesian grid. However, the data in the k-t space are acquired on a zig-zag trajectory, so the phase evolution during the acquisition of individual k-space lines must be corrected before carrying out FFT to avoid spatial blurring due to chemical shift artefacts in opposite directions for odd and even gradient echoes [159, 160]. Chapter 6 details the implementaion and the design consideration of a symmetric EPSI in a clinical MR system with k-t re-gridding to correct for the chemical shift artefacts.

4

Treatment Response in Non-Small-Cell Lung Cancer with Hyperpolarized [1-^{13}C]Pyruvate, FLT- and FDG-PET

4.1 Objective

This chapter investigates the effectiveness of hyperpolarized [1-^{13}C]pyruvate in detecting the treatment response in two NSCLC tumors, HCC-827 and NCI-H1975, xenografted in a mice. In addition, hyperpolarized [1-^{13}C]pyruvate was compared with FDG and FLT-PET. HCC827 have previously been shown to elicit a high response to inhibition of the EGFR by tyrosine kinase inhibitors, such as erlotinib, whereas H-1975 shows little response to similar treatment, due to a secondary mutation, see section 2.1. Additional *ex vivo* signatures, LDH activity level (a marker for aerobic glycolysis) and Ki-67 staining (a marker for proliferation), are compared between the treated and untreated groups of HCC-827 tumors and correlated with the *in vivo* imaging signatures.

4.2 Animal Population

58 Nude NMRI mice (Taconic, Denmark) weighing about 20-25 g were inoculated subcutaneously in the two flank regions with either HCC-827 or H-1975 cells. When the tumors reached a size of about 300 mm^3 (about 5 weeks after inoculation) the mice were randomized in two groups, one group for PET

imaging and the other for hyperpolarized ^{13}C MRS. Each group was again randomly divided into two subgroups. One subgroup received Erlotinib treatment (50 mg/kg) in a phosphate buffered saline (PBS, 0.5% Tween 20), 24 hours before imaging. The other was a control group, which received a sham treatment (PBS, 0.5% Tween 20) of the same volume. The animals were fasted overnight before scanning.

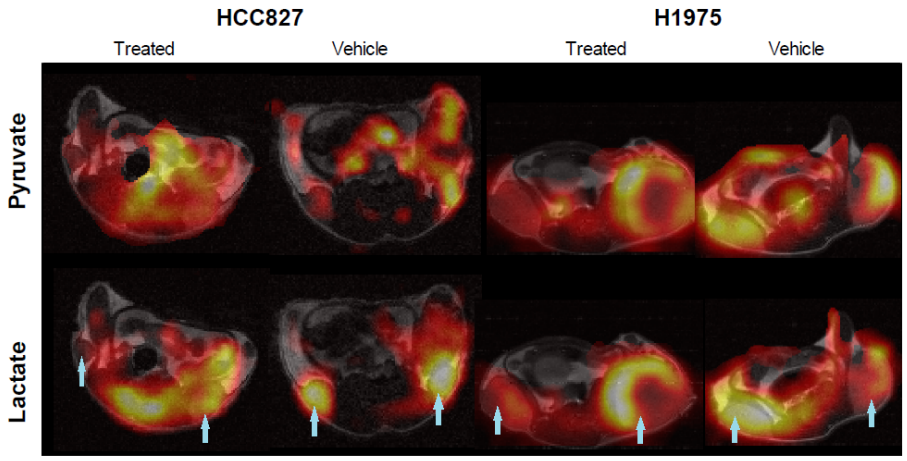

Figure 4.1: Representative ^{13}C metabolic maps of pyruvate and lactate for both treated and untreated HCC-827 and H-1975 xenografted tumors. The metabolic maps are overlaid on proton images acquired at the same position as the CSI, with white arrows indicating the tumor position.

4.3 Hyperpolarization and MR Experiment

The pyruvate sample, consisting of 14 M [1-^{13}C]pyruvic acid (Sigma Aldrich, Denmark), 15 mM trityl radical OX063 (Oxford Instruments, UK), and 1.5 mM Dotarem (Guerbet, France), was polarized in a HyperSense polarizer (Oxford Instruments, UK). The MR imaging was conducted in a 4.7 T small animal scanner (Agilent Technologies, US). During the MR experiment, proton images were acquired to locate the two tumors. After dissolution, each animal received 200 μL injection of hyperpolarized [1-^{13}C]pyruvate, 80 mM. Then, CSI acquisition was made 8 s after the end of the injection. The duration of each injection was about 6-8 s. The CSI acquisitions were made with matrix size 16x16, repetition time (TR) 70 ms, echo time (TE) 0.65 ms, field of view (FOV) 35x35 mm^2 and

slice thickness 5-6 mm. In addition, T_1-weighted dynamic proton images, 12 s per frame, were acquired after the injection of 200 μL of 0.1 mM gadolinium (Dotarem, Guerbet, France) to assess tumor perfusion.

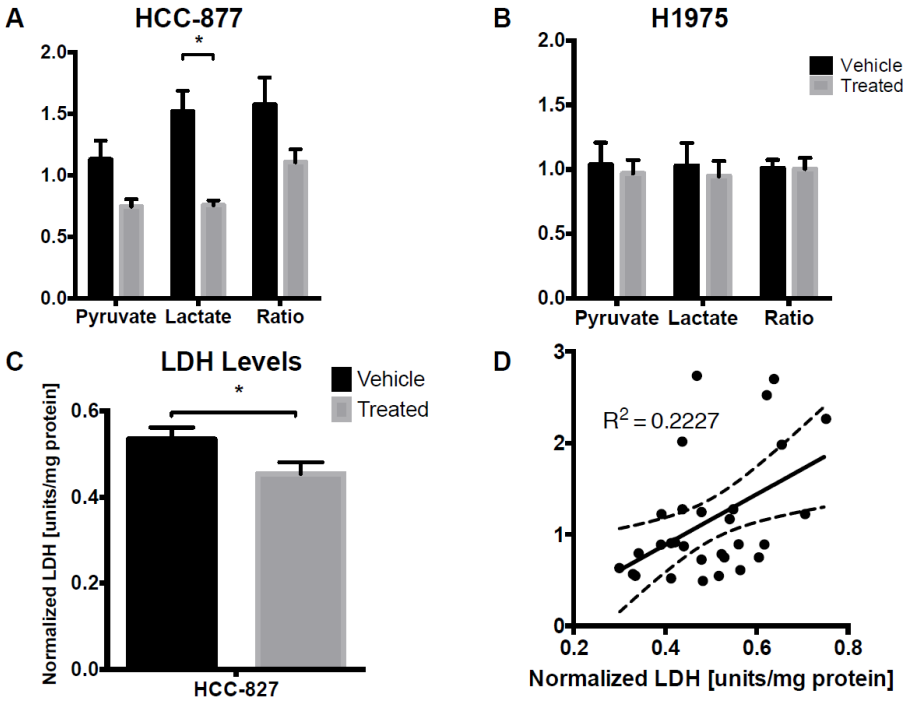

Figure 4.2: Quantitative evaluation of pyruvate, lactate and their ratio in HCC-827 (A) and H-1975 (B) tumors. A significant reduction in lactate level ($p < 0.005$) was observed for treated HCC-827 tumors compared to untreated. No significant change in metabolite levels was seen for H-1975 tumors. (C) Levels of LDH enzyme normalized to total protein content in HCC-827 tumor samples. A significant reduction was found in the treated tumors compared to untreated tumors ($p < 0.05$). (D) Correlation between levels of LDH enzyme normalized to the total protein content and lactate level evaluated by ^{13}C MRSI ($p < 0.01$).

A clear lactate signal was observed in the tumors of both models, see Figure 4.1. When quantified, the average level of lactate detected in the untreated HCC-827 tumors was 1.52 ± 0.17 (n=18), see Figure 4.2A. This is significantly higher than the levels found in treated HCC-827 tumors, which was 0.76 ± 0.04 (n=14, $p < 0.005$). This is contrasted by the pattern seen in the H-1975 model (Figure 4.2B), where the lactate levels were found to be similar with treatment, 1.03 ± 0.18 and 0.95 ± 0.12 respectively (n=8 both groups, $p = 0.718$).

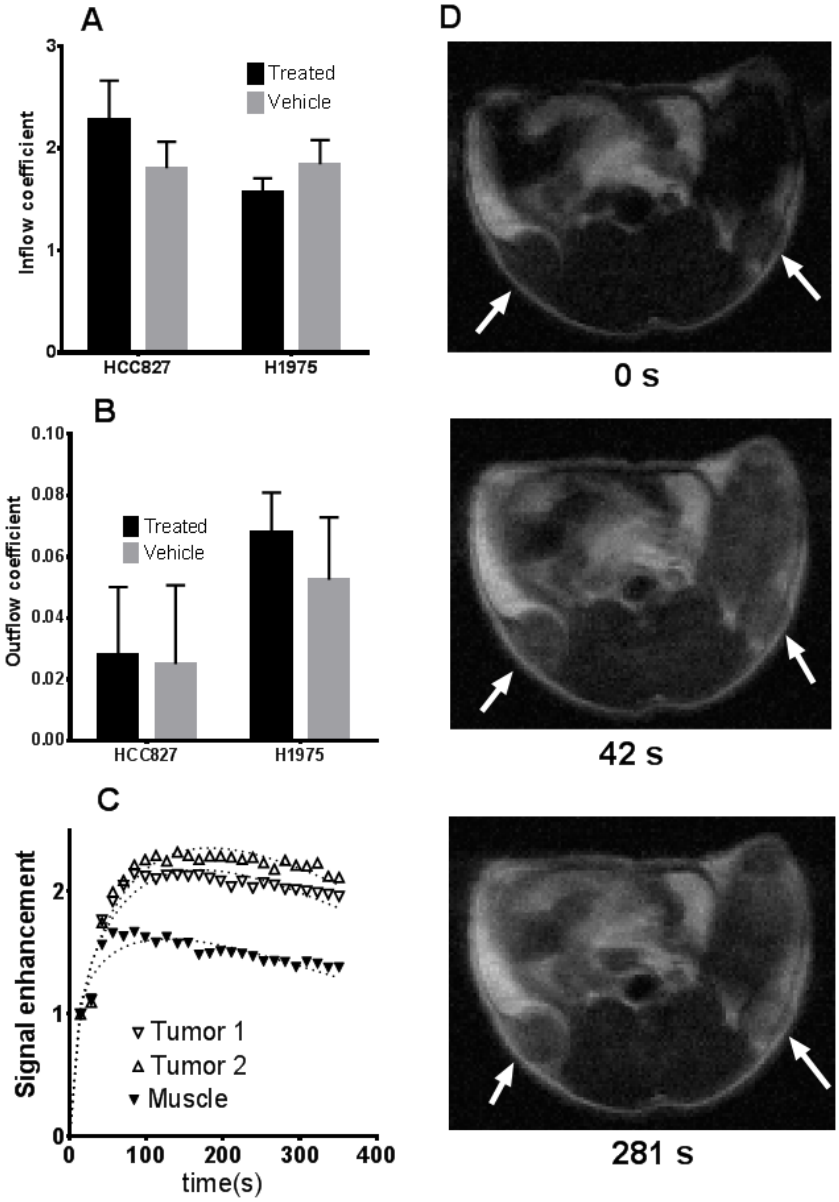

Figure 4.3: Quantification of perfusion imaging, showing inflow (A) and outflow (B) coefficients for treated and untreated HCC-827 and H-1975 tumors. No significant difference in coefficients was found between cell lines and treatment. (C) shows a representative temporal development in signal enhancement, as well as the fitted, gamma-variate curves. Corresponding representative images are shown for three time points in (D), with arrows indicating the tumors.

The ratio of lactate to pyruvate was also calculated. However, in HCC-827 tumors the difference between the groups in the lactate/pyruvate ratio was less significant than the lactate difference, probably due to the observed increase in the pyruvate level in the untreated HCC-827 tumors compared to the treated. The ratio was 1.57 ± 0.22 in the untreated group, versus 1.06 ± 0.07 in the treated tumors (Figure 4.2). For the H-1975 tumors, the ratios were found to be 1.01 ± 0.06 and 1.00 ± 0.08 for the vehicle and treated group, respectively. For the analysis of the LDH activity level and its correlation with the lactate levels from ^{13}C MRS, see section 4.5.

The analysis of T_1-weighted dynamic contrast enhancement (DCE) imaging showed that both groups of tumors (treated and untreated) exhibit typical DCE curves with fast wash-in and slow wash-out, indicating well-perfused tumors (Figure 4.3). Furthermore, the analysis of the perfusion curves did not show a significant difference between the two groups of tumors.

4.4 FLT- and FDG-PET Experiment

The mice in the PET group were intravenously injected with 10-15 MBq of ^{18}F-FDG or ^{18}F-FLT, one hour before PET imaging. A 5-7 min PET scan was then acquired using a PET/CT scanner (Inveon MM , Siemens Medical Solutions, Germany), followed by a CT scan for anatomical reference and attenuation correction.

The FDG level was found to be significantly lower with treatment, 1.37 ± 0.13 %ID/g and 0.85 ± 0.05 %ID/g, for the vehicle and treated group, respectively ($p < 0.002$, n=10 in each group). For H-1975, the FDG levels were similar, 1.94 ± 0.09 %ID/g in the vehicle group and 1.91 ± 0.06 %ID/g in the treated group ($p = 0.766$, n=8 in each group).

Similar results were obtained for FLT. The FLT uptake levels for HCC-827 was found to be 2.45 ± 0.22 %ID/g and 1.12 ± 0.28 %ID/g for the vehicle and treated group, respectively ($p < 0.002$, n=8 in each group). For H-1975, the levels were 2.39 ± 0.13 %ID/g in the vehicle group and 2.39 ± 0.11 %ID/g in the treated group ($p = 0.965$, $n = 8$ in each group).

4.5 LDH and Ki-67 Signatures

The mice with HCC-827 tumor that underwent hyperpolarized ^{13}C MRS were euthanized after experiment and the tumors were extracted and frozen. Later, LDH activity in each sample was estimated using a NADH-colorimetric assay (Sigma-Aldrich, Copenhagen, Denmark) according to the instructions of the manufacturer. Similar procedures were followed with the mice that underwent FLT-PET to estimated the cellular proliferation in HCC-827 tumors using Ki-67 assay.

The Ki-67 levels for HCC-827 tumors that underwent FLT-PET imaging were found to be 9.6 ± 0.6 (n=5) and 6.6 ± 0.7 (n=6) for the untreated and treated groups, respectively ($p < 0.02$), Figure 4.4C. Whereas, The levels of LDH normalized to the total protein content in the HCC-827 tumors that underwent ^{13}C MRS were found to be 0.54 ± 0.03 (n = 18) and 0.45 ± 0.03 (n=14) for the untreated and treated group, respectively ($p < 0.05$) (Figure 4.2C). The normalized LDH values were correlated to the levels of lactate from ^{13}C MRS, yielding a positive correlation ($R^2 = 0.20$, $p < 0.05$), Figure 4.2D.

4.6 Discussion

In many studies, the reduction in pyruvate to lactate conversion has been observed in response to chemo- or radiation therapies [15, 20, 24, 111–118]. The main objective in this study was to validate these findings and investigate the effectiveness of hyperpolarized [1-^{13}C]pyruvate in monitoring the response of non-small-cell lung cancer to erlotininb treatment, in comparison with FDG- and FLT-PET. All the investigated imaging modalities were able to identify the response to treatment after 24 hours, which agrees with literature [162]. As expected from other reports [163, 164], the most prominent response to treatment was observed from PET imaging using the thymidine analog FLT. The response seen using FDG-PET, which reflect the glucose uptake, was less pronounced but still significant. We confirmed that the response to treatment could also be detected using [1-^{13}C]pyruvate MRS. We observed that [1-^{13}C]pyruvate and FDG-PET showed comparable response to treatment. We found that the level of lactate obtained by ^{13}C MRS correlated with the normalized LDH activity obtained *ex vivo*, as reported in other studies [117, 118, 165]. This confirms

the role of LDH as one of the primary mechanisms behind [1-^{13}C]pyruvate MRS contrast.

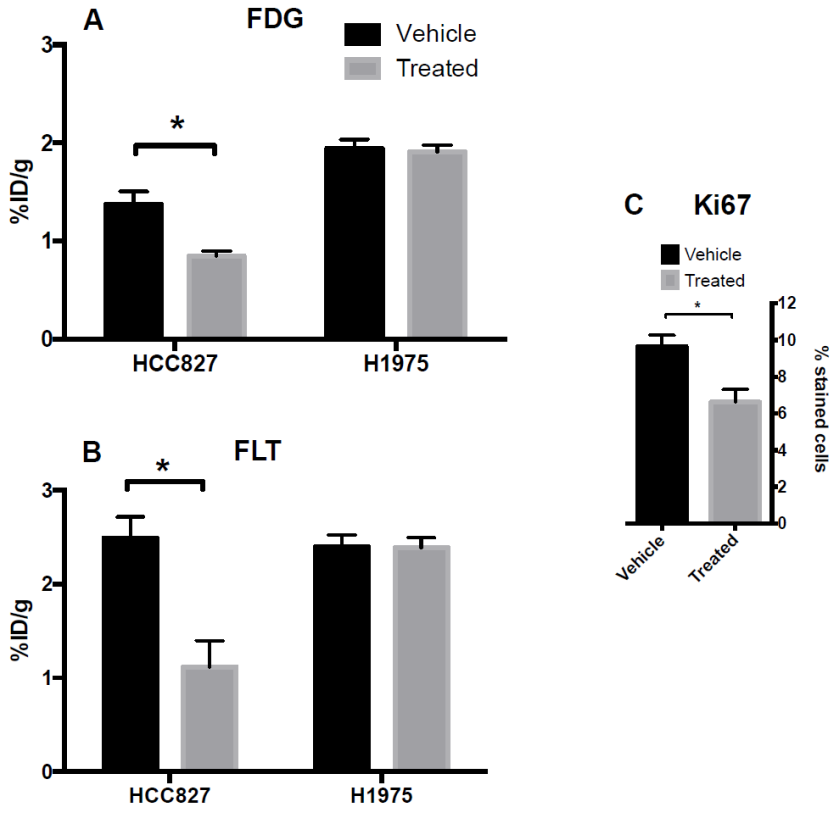

Figure 4.4: (A) and (B) quantitative comparison between FDG and FLT uptake for treated and untreated HCC-827 and H-1975 tumors in units of % ID / g. Significant reduction in uptake was seen for both FDG and FLT (both $p < 0.002$) in treated HCC-827 tumors compared to untreated. No significant change in uptake was observed for H-1975 tumors. (C) Quantitative evaluation of Ki-67 staining showed a significantly reduced number of stained cells in treated HCC-827 tumors compared to the untreated ones ($p < 0.05$).

The ratios between lactate and pyruvate were shown to be less significantly different between treated and untreated groups with $p = 0.058$, compared to $p = 0.001$ for lactate difference between the two groups. This can be due to the significantly lower pyruvate uptake in the treatment group. This may indicate that the transport of pyruvate into the cells, as facilitated by the mono-carboxylate transporters, might also be affected by treatment with erlotinib.

Further studies are needed to clarify if this is indeed the case, and explain the mechanisms behind.

Contrast-enhanced perfusion imaging showed similar perfusion in both the treated and untreated groups. As further expected, we also observed a significantly slower washout of the gadolinium in tumors compared to muscle tissue. This could be attributed to the enhanced permeability and retention of the tumor.

Both FDG-PET and ^{13}C MRS of hyperpolarized [1-^{13}C]pyruvate are valuable in monitoring the glycolysis. FDG-PET can assess the beginning of glycolysis, i.e., the delivery and uptake of glucose and its phosphorylation by hexokinase, which is the first step in this process. ^{13}C MRS of hyperpolarized [1-^{13}C]pyruvate can monitor the end of glycolysis, i.e., the exchange between pyruvate and lactate catalyzed by LDH. Therefore, the two might be used together for better assessment of the entire glycolytic pathway and a combined PET/MR setup is well suited to achieve such task. However, since an increased metabolic activity is seen in many physiological states, such as inflammation and muscle activity, the lactate levels are more specific cancer marker due to specific imaging of the Warburg effect.

In this study, we were not able to evaluate the markers from ^{13}C MRS and PET in the same animal. This was impractical, since the imaging with the two modalities took place at different sites. Therefore, the study population had to be divided into two separate groups for MR and PET examinations. In the subsequent studies, that involved both PET and MR acquisition, these modalities were acquired simultaneously in a combined PET/MR setup.

4.7 Conclusion

In this study, we showed the reduction in lactate level following the injection of hyperpolarized [1-^{13}C]pyruvate can be used as marker to monitor the response to erlotinib in two different tumor models of NSCLC. We also found that the reduction in lactate levels was comparable to the reduction in the glucose uptake as monitored by FDG-PET. The difference in FLT-PET between the treated and untreated group was the most significant, whereas the reduction in the lactate-to-pyruvate ratio with treatment was found to be insignificant.

5

Necrosis Monitoring with hyperpolarized [1,4-$^{13}C_2$]fumarate

5.1 Objectives

The objective of the studies introduced in this chapter is to investigate the effectiveness of [1,4-$^{13}C_2$]fumarate as a marker for monitoring necrosis. These studies were performed in models in which the necrotic process is well understood by our group.

The chapter first presents a polarization scheme for [1,4-$^{13}C_2$]fumarate in the SPINlab polarizer, since there is no previous work published on this. Moreover, the sparsity that is often seen in hyperpolarized ^{13}C spectra will be exploited by adopting a co-polarization scheme for [1,4-$^{13}C_2$]fumarate and [1-^{13}C]pyruvate to simultaneously assess their enzymatic pathways in a combined PET/MR setup. Phantom experiments are conducted to ensure that there is no significant difference in the polarization values between the dual and single substrate polarization. *In vivo* assessment is performed in necrotic rat muscles.

This chapter also investigates the use of hyperpolarized [1,4-$^{13}C_2$]fumarate in quantifying necrosis associated with acute kidney injury (AKI). Here, AKI was induced in rats via ischemia/reperfusion (IR), which is one of the main causes of cellular necrosis in renal tubular cells due to severe ATP depletion. Hyperpolarized [1,4-$^{13}C_2$]fumarate is compared in this study with widely used blood biomarkers for AKI such as plasma creatinine, creatinine clearance (CrCl), and blood urea nitrogen (BUN). Moreover, biomarkers from renal biopsies such as

kidney injury molecule 1 (KIM-1), and neutrophil gelatinase-associated lipocalin (NGAL) expression levels in the RNA were also investigated to see if there is correlation with the ^{13}C MRS signature.

5.2 Formulation of [1,4-$^{13}C_2$]Fumarate and [1-^{13}C]Pyruvate

Fumarate was prepared by dissolving [1,4-$^{13}C_2$]fumaric acid (FA) (Cambridge Isotope Laboratories, MA, USA) in dimethyl sulfoxide (Sigma Aldrich, Denmark). Sonication and vortex mixing were used until all the FA crystals had dissolved. AH111051 trityl radical (GE Healthcare, US) was then added and dissolved in the solution. Three different batches were prepared with FA/radical concentrations of 3.6 M/8 mM, 3.6 M/12 mM and 2.8 M/15 mM to see if there is difference in the polarization performance. For pyruvate preparation, AH111501 was added to a sample of 14 M [1-^{13}C]pyruvic acid (PA) (Sigma Aldrich, Denmark) to a final concentration of 15 mM.

5.3 Single [1,4-$^{13}C_2$]Fumarate Polarization

The polarization was made in a SPINlab polarizer (GE Healthcare, US). Figure 5.1A shows the fluid path assembly designed for use with the SPINlab. The fluid path consists of a vial (1) containing the sample and connected to the dissolution syringe (2) via two concentric tubes (3). The tubes can be pushed into the polarizer through the dynamic seal (4) without compromising the vacuum. The syringe has an port that connects to an exit tube (5) for the transfer of the hyperpolarized solution.

The regular sample preparation procedure for the SPINlab fluid path requires that the vial, after adding the ^{13}C substrate, is frozen in liquid nitrogen (LN_2). This freezing is necessary to perform pressure check and helium purging. Helium purging is needed to have a helium exchange gas inside the fluid path when the vial is cooled to less than 1 K. Then the loading of the sample into the SPINlab involves lowering the sample vial into the sample pot (see Figure 5.1C), were the

hyperpolarization takes place, through multiple steps (gradual insertion over 15 min) to avoid excessive increase in the helium temperature. This multi-step lowering process was found to result in FA crystallization. To avoid this, the sample preparation and loading was modified as follows.

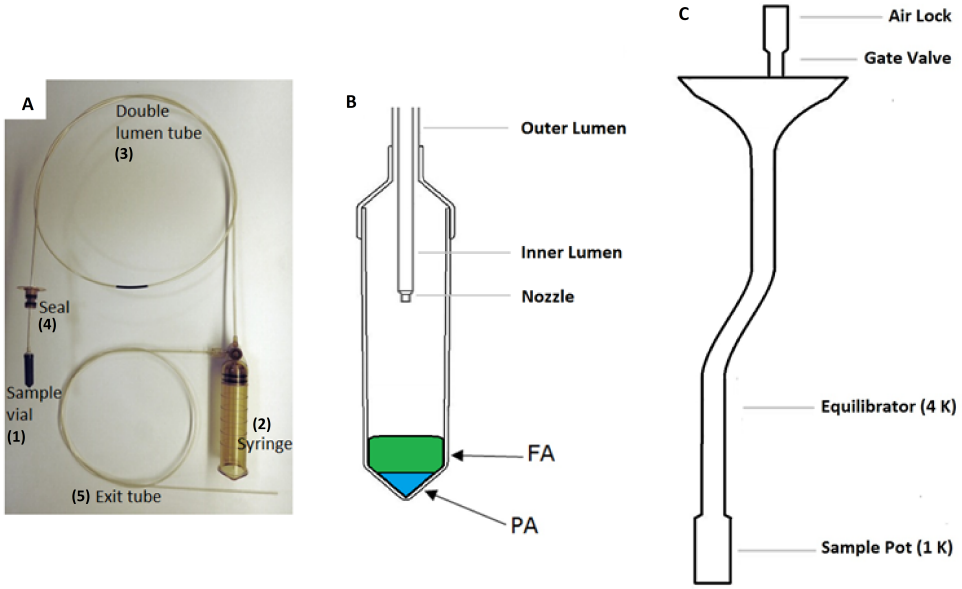

Figure 5.1: (A) The fluid path that goes into the SPINlab. The path consists of a syringe that contains the dissolution media and sample vial that contains the ^{13}C substrate to be polarized. The two are connected by two concentric tubes. During the dissolution, the dissolution medium is transferred through the inner tube to the sample vial where it dissolves the hyperpolarized substrate. The dissolved material flows back through the outer tube lumen toward the syringe and out of the SPINlab via the exit tube. (B) shows schematic draw of the sample vial. The vial is prepared, in the dual polarization scheme, by first adding the PA and then freezing it in LN_2 and then adding the FA. The vial is then kept in LN_2 during the rest of preparation of the fluid path to attain two separate layers in the vial. (C) shows the path of the vial once it is inserted in the SPINlab. The vial is initially placed in the airlock for 20 min to allow the sample to melt. Then, it is lowered in multiple steps, back and forth, along the path until it settles at the He sample pot to avoid excessive increase in temperature at the He pot.

The fluid path was prepared by placing 100 μL (about 350 μmol) of the FA solution in the sample cup and then freezing it in liquid nitrogen. The vial is

then glued to the tube set with the tip immersed in LN_2 and the neck above the liquid surface. The rest of the fluid path preparations (pressure check and He purging) were done according to the manufactures instructions. After the preparation, the fluid path was placed in the SPINlab and the vial containing the compound was initially placed at the airlock for 20 to 30 min, thus allowing the substrate to thaw before lowering the sample vial into the helium pot. Then the sample vial was directly lowered into the helium bath in either one (A: directly to the 1 K pot) or two steps (B: directly to the 1 K pot and then retracted to the 4 K thermal link for 10 min), instead of the normal scheme of going through multi-steps lowering process, to avoid the crystallization of the FA in the sample.

The dissolution syringe was filled with approximately 15 g of a dissolution media, sterile water with 0.1 g/L ethylenediaminetetraacetic acid disodium salt dehydrate (EDTA) (Sigma Aldrich, Denmark). After dissolution, the sample was mixed with 0.54 g of neutralizing buffer, sterile water with 0.72 M NaOH, 0.4 M 2-Amino-2-(hydroxymethyl)-1,3-propanediol (Tris) (Sigma Aldrich, Denmark), and 0.1 g/L EDTA.

The solid-state polarization of samples containing 600 mg of FA from the three different batches (with fumarate/AH111051 concentrations of 2.8M/15mM, 3.6M/8mM and 3.6M/12mM) resulted in build-up time constants and final solid-state polarization values detailed in Table 5.1, for one and two insertion steps. No dissolution is done here. There was some difference between the one (A) and two (B) lowering steps in the characteristics of the build-up curves. However, the solid state NMR signals vary significantly between measurements due to the uncontrolled position of the sample within the NMR coil that is dimensioned to hold up to four samples. Therefore, the comparison is based on the liquid state polarization obtained post dissolution of the 100 μL samples.

Table 5.1 shows these liquid state polarization measurements obtained for the three formulations of fumarate via dynamic acquisition of ^{13}C spectra in the PET/MR scanner 30 s after dissolution, see the setup in section 5.5. There was no difference in the measured polarization between the batches. Since they gave similar polarization results, the subsequent experiments were conducted with the 3.6M/12mM fumarate/AH111051 batch and with two insertion steps. This batch gives higher concentration of fumarate. In addition, this batch had

relatively faster polarization build-up.

batch	**2.8 M/15 mM**		**3.6 M/8 mM**		**3.6 M/12 mM**	
insertion steps	one	two	one	two	one	two
pol time constant (s)	9448	5913	6718	6765	2725	3659
S($t = \infty$) (a.u.)	1311	1054	740	1140	969	993
liquid-state pol (%)	39		38		37	

Table 5.1: Solid state DNP build-up data for three different samples with two different loading profiles.

5.4 Dual [1,4-$^{13}C_2$]Fumarate and [1-^{13}C]Pyruvate Polarization

In the dual co-plarization scheme, the fluid path was prepared by first placing 25 μL (around 350 μmol) of PA in the sample vial and then freezing it in LN_2. 100 μL (about 350 μmol) of FA was then added on top of the PA, see Figure 5.1B, and the vial was placed in LN_2 again. Pressure check and He purging were then performed. When the fluid path was placed in the SPINlab, the substrates were allowed to thaw by placing the vial in the airlock for 20-30 minutes. The sample vial was then lowered in a fast two-step scheme to avoid the crystallization of the FA in the sample. The sample was polarized for approximately 4 hours by microwave irradiation at 139.64 GHz and 40 mW (the two samples have the same optimal microwave frequency). The dissolution syringe was filled with about 15 g of a dissolution medium. The dissolved sample was mixed with 0.95 g of neutralizing medium.

5.5 Phantom MR Experiments for polarization and T_1 measurements

A phantom experiment was performed to measure the polarization and T_1 values of fumarate, and to ensure that here are no differences in polarization between

single and dual substrate polarization schemes. The imaging was performed in a clinical 3T PET/MR scanner (Siemens mMR Biograph, Siemens, Erlangen, Germany). A dual-tuned transmit/receive flex surface coil (RAPID Biomedical) was used for both ^{1}H and ^{13}C acquisitions. Phantoms were placed in the center of the 11 cm loop coil.

About 5 mL of the polarized material, either fumarate or dually polarized fumarate and pyruvate, was injected into a previously shimmed phantom tube, approximately 30 s after the dissolution. A ^{13}C-urea phantom (4 M) was placed next to the tube with the hyperpolarized solution and was used to calibrate the 90^o flip angle and as a reference to measure the polarization. Dynamic ^{13}C spectra were acquired without spatial encoding using an excitation pulse with 5^o flip angle and TR of 5 s. The sampling spectral window was set to 6000 Hz with 512 spectral points. To quantify the polarization, the initial signal of the hyperpolarized sample was compared to the urea signal and corrected for the concentration difference.

n=5	**fumarate**		**pyruvate**
scheme	dual	single	dual
T_1 (s)	57 ± 2	58 ± 2	70 ± 3
Polarization (%)	35 ± 5	37 ± 6	37 ± 6

Table 5.2: Liquid state polarization and T_1 measurements for the sample with FA (3.6 M) with 8 mM of AH111501 radical.

The results of the experiment to determine whether there is a difference in the polarization and T_1 values between the dual and single substrate polarization is summarized in Table 5.2. No significant difference was found in the measured values of polarization of FA for single and dual FA/PA polarization schemes. The polarization level of pyruvate, 37%, obtained with the dual polarization scheme agrees with the SPINlab polarization values of PA found in the literature [166].

5.6 Necrosis Imaging in Rat Muscles

5.6.1 Animal Model

The first *in vivo* [1,4-$^{13}C_2$]fumarate study to quantify necrosis was conducted in two rats weighing 400 g. One rat was only injected with hyperpolarized FA. The second rat received two injections separated by 10 min. The first injection was only hyperpolarized FA, and the second injection was dual polarized FA and PA. Necrosis was induced by intramuscular injection of 200 μL of sterile turpentine oil in one of the hind legs. This was followed by subcutaneous injection of 400 μL of buprenorphine hydrochloride (TEMGESIC, 0.03 mg/ml) to control the acute pain from the turpentine injection. Two hours later, the animal was transferred to the PET/MR scanner to acquire ^{13}C MRS and PET images.

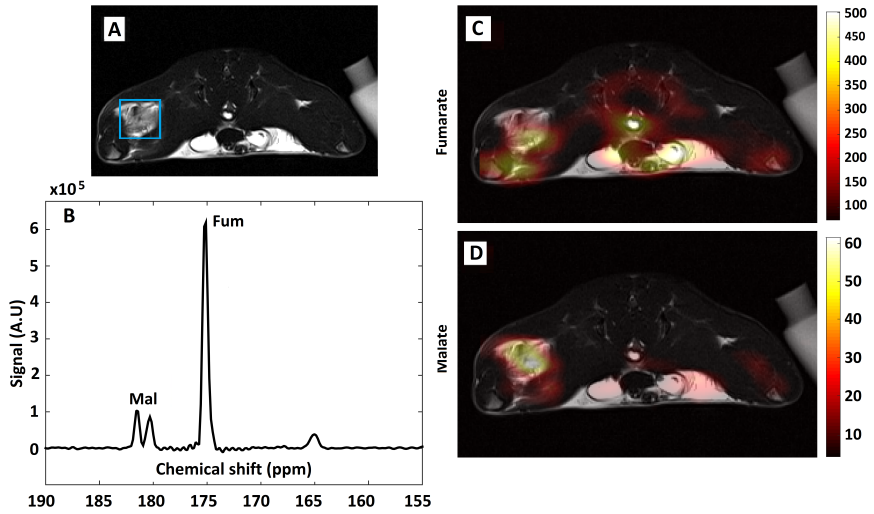

Figure 5.2: The anatomical axial image of the first rat (A) acquired at the location of the necrotic tissue. The image was acquired with turbo spin echo (TR= 5.7 s, TE= 84 ms, echo train length of 18, number of phase encoding steps 234, Number of averages of 5, final matrix size of 256x256 covering a FOV of 100 mm x 100 mm with slice thickness of 2 mm). (B) shows the spectrum at the necrotic tissue with the fumarate peak the malate doublet. Clear malate signal can be observed in the spectrum. The small peak at the right of the spectrum at 164 ppm is due to fold over of the ^{13}C-urea phantom. (C) and (D) show the metabolic maps of fumarate and malate, respectively. Notice that the malate production is confined to the necrotic region.

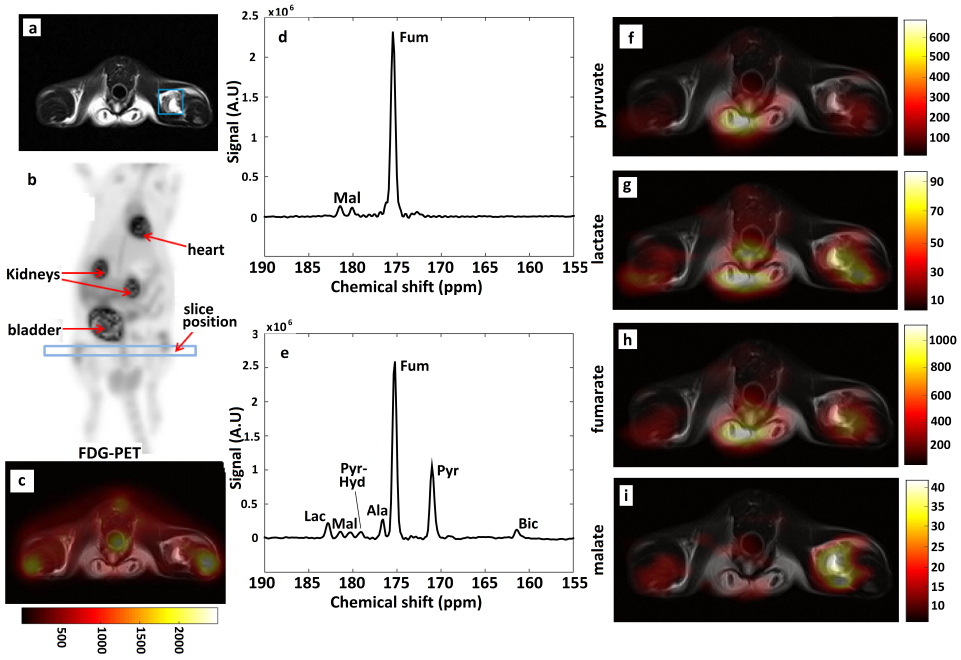

Figure 5.3: The anatomical axial image of the second rat (A) acquired at the location of the necrotic tissue. The proton image was acquired similar to Figure 5.2A. A coronal maximum intensity projection image, which shows the FDG uptake by the different organs is illustrated in (B). (C) shows an axial slice (thickness of 12 mm, sum of 6 frames) with the FDG uptake in a plane containing the necrotic tissue. (D) and (E) show the phased real part spectra at the necrotic tissue, the blue box in (A), acquired for single injection of FA and dual injection of FA and PA, respectively. The malate signal can be seen in both spectra. In the dual FA and PA experiment, additional peaks are observed for lactate, alanine, pyruvate-hydrate and bicarbonate. The metabolic map of pyruvate, lactate, fumarate and malate, obtained from the dually polarization of FA and PA, are shown in (F, G , H and I). High lactate and malate signals are observed at the necrotic tissue.

5.6.2 Combined PET/MR Experiments

The imaging was performed in a clinical 3T PET/MR scanner (Siemens mMR Biograph, Siemens, Erlangen, Germany) using a dual-tuned ^{1}H and ^{13}C transmit/receive flex surface coil (RAPID Biomedical). During the MR scanning, the animals were anaesthetized with 3 % Sevoflurane mixed in O_2. A catheter was inserted in the tail vein for the administration of the hyperpolarized mix-

ture of pyruvate and fumarate or fumarate alone. 2 mL (0.14 mmol/kg) of the co-polarized substrates was injected in the rat. This injection was done approximately 20 s after dissolution. During this period the co-polarized material was transferred to the MRI room from the SPINlab in a syringe that was then connected to the tail vein catheter. The hyperpolarized substrate was injected manually over a period of 10 s.

Anatomical long axis proton MR images are acquired prior to the ^{13}C MRS scans for spatial localization of the necrotic tissue within muscle. CSI with FA 10°, TR 80 ms, TE 1.4 ms, FOV 50 mm x 80 mm, matrix size 16x16, and slice thickness 25 mm was acquired 20 s after the end of administration of the hyperpolarised material. One hour before the PET/MR imaging session, the rats were intravenously injected with 80 MBq of ^{18}F-FDG. An 8 min PET scan (2.0 mm resolution) was acquired during the acquisition of the MR images.

Figure 5.2 shows the anatomical image and the ^{13}C spectrum at the necrotic tissue for the rat that was injected with only hyperpolarized FA. The maps of fumarate and malate distributions within a slice covering the necrotic region are also shown in Figure 5.2. Figure 5.3, shows the anatomical image and the ^{13}C spectrum at the necrotic tissue for the rat that received both FA and the dually hyperpolarized FA and PA. The figure also shows the metabolic maps of pyruvate, lactate, fumarate and malate. Clear malate signal was visible at the necrotic site with both the single fumarate and dual pyruvate/fumarate injections and no malate signal was observed elsewhere. Moreover, an increased production of lactate is observed at the necrotic site. Figure 5.3 also shows the PET images acquired for the same animal during the same MR imaging session. The FDG uptake by the different organs is represented using maximum intensity projection. There is no clear effect from the necrosis on the FDG-PET.

5.7 Ischemia/Reperfusion Induced Necrosis in Rat Kidneys

5.7.1 Animal Model

IR kidney injuries were induced surgically on male Wistar rats (weighing 200–250 g). Prior to surgery, the rats were kept in a metabolic cage. After 24 h in the metabolic cage, urine was collected and the rats were anesthetized for blood sample collection and surgery. During surgery, the animals were anesthetized with sevoflurane (induction 6%, sustained 2.5%) mixed with air (2 L/min). A surgical incision was made in the abdomen and the left renal artery was carefully dissected. A non-traumatic clamp was placed on the left artery for 40 min to induce ischemia, after which the clamp was released. Reperfusion was visually confirmed. The incision was sutured separately through both the muscle tissue and skin. The contralateral (CL) kidney was left intact, and was used as control kidney. At the beginning of surgery buprenorphine hydrochloride was provided subcutaneously (0.05 mg/kg) to control the pain. After surgery, the rats were again put in metabolic cages, and buprenorphine hydrochloride was supplied in the drinking water (0.3 mg/mL) until euthanization. At the time of euthanization (24 h after surgery), arterial blood and urine was collected again.

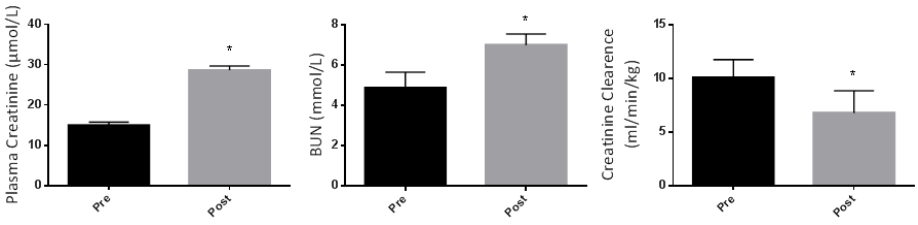

Figure 5.4: Comparison between plasma creatinine, CrCl and BUN biomarkers before and after surgery.

5.7.2 AKI Biomarkers

A total of seven animals were used for the imaging experiments. From six of these animals, the urine and blood samples collected before and after surgery

were used to measure fumarase activity. The blood samples were also used to measure creatinine, CrCl, and BUN.

A 2 mm kidney section was dissected from both the CL kidney and post-ischemic kidney. The dissected sections were used to evaluate the necrosis using eosin and hematoxylin staining. Morever the RNA was isolated from the renal cortex and the expression levels of KIM-1 and NGAL were quantified.

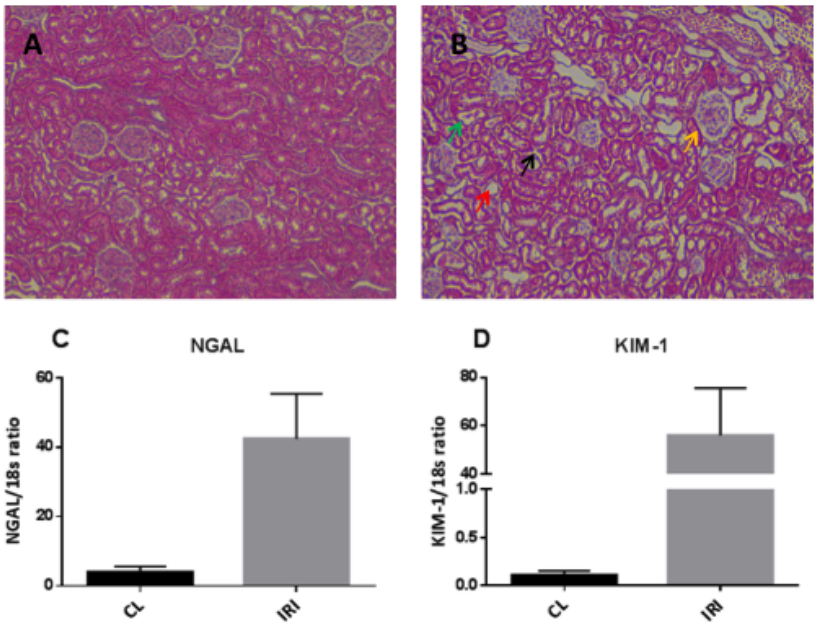

Figure 5.5: Representative histological sections are shown in (A) for a CL kidney showing normal intact tubular cells and glomeruli, and (B) for a post-ischemic kidney showing a cellular cast in the tubular lumina (green arrow), complete sloughing of tubular epithelium (red arrow), interstitial edema (black arrow), and glomerular edema (yellow arrow). The relative expression of injury markers, in (C) and (D), indicated significant upregulation of NGAL ($p = 0.0145$, $n = 6$) and KIM-1 ($p = 0.0256$, $n = 6$) respectively A paired two-sided Student's t-test was used to compare the CL and IR injured kidneys.

Functional kidney parameters showed consistent signs of renal injury with an elevated plasma creatinine level of 91% ($p = 0.0002$) and a reduced CrCl and BUN level of 44% ($p = 0.04$) and 30% ($p = 0.003$), respectively, when comparing pre-surgical with post-surgical values, see Figure 5.4.

Figure 5.5 shows representative histological sections with hematoxylin and eosin stain from a CL kidney and a post-ischemic kidney. The CL kidney showed normal intact tubular epithelial cells compared to the post-ischemic kidney, with tubular lumina filled with cellular debris, complete sloughing of tubular epithelium, interstitial edema, and glomerular edema, Figure 1A and B. The classical cortical kidney injury markers NGAL and KIM-1 were significantly elevated ($p = 0.01$ and $p = 0.03$) compared to those in the CL kidney, Figure 5.5C and D.

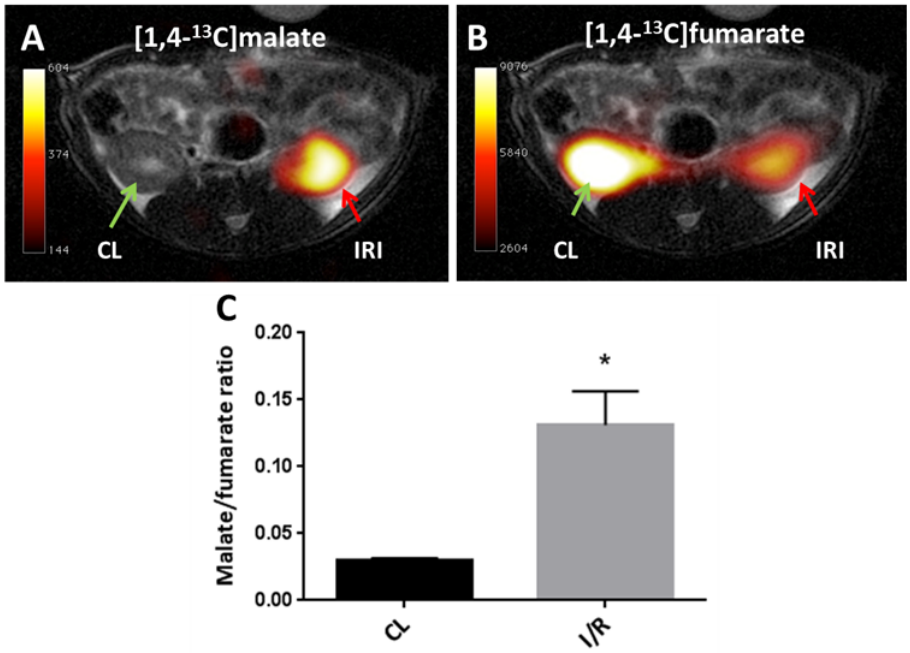

Figure 5.6: Anatomical ^{1}H kidney sections overlaid with (A) ^{13}C-labelled fumarate images and (B) ^{13}C-labelled malate images. Red arrow indicates the post-ischemic kidney and green arrow indicate contralateral kidney. (C) A malate/fumarate ratio is calculated from each kidney, giving rise to an elevated ratio in the post-ischemic kidney.

5.7.3 MR Experiment

At the MRI scanning session, 24 h after the surgery, tail vein catheterization was performed for hyperpolarized [1,4-$^{13}C_2$]fumarate administration. Each animal

was injected with 1.5 mL of hyperpolarized [1,4-$^{13}C_2$]fumarate. MRI scans were performed using a 3T clinical MRI system (GE Healthcare, USA) equipped with a dual tuned $^{13}C/^{1}H$ volume rat coil (GE Healthcare, USA). A slice-selective ^{13}C IDEAL spiral sequence was used to detect hyperpolarized [1,4-$^{13}C_2$]fumarate, and images were acquired every 5 s, initiated 20 s after the start of injection. The spiral acquisition was performed using a flip angle of 10°, 11 IDEAL echoes, and one initial spectrum per IDEAL encoding. The following parameters were also used: TR/TE/ΔTE 100 ms/0.9 ms/1.45 ms, field of view 80 x 80 mm^2, 5 x 5 mm^2 resolution, and an axial slice thickness of 15 mm covering both kidneys.

An elevated malate/fumarate ratio of 339% (p = 0.002) (Figure 5.6C) in the ischemic kidneys relative to the CL kidney was found. In order to examine the relationship between renal cortical injury and malate/fumarate ratio, the correlation between NGAL and KIM-1 levels with the malate/fumarate ratio was investigated. A linear correlation was found in both cases (R^2 = 0.78, p = 0.008 and R^2 = 0.80, p = 0.006, respectively), Figure 5.7A and B.

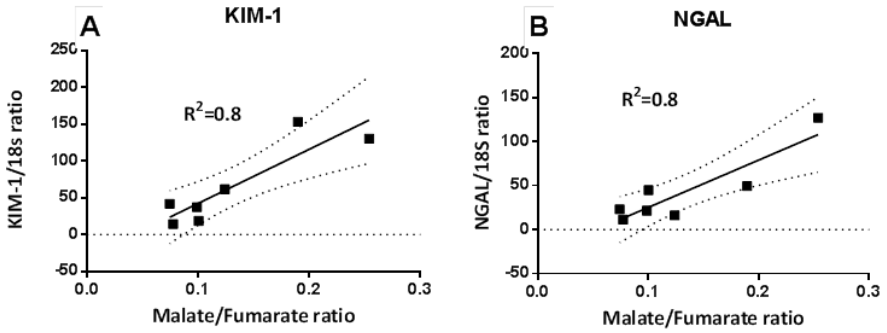

Figure 5.7: Correlation between renal injury and malate/fumarate ratio. A significant correlation was found between (A) NGAL and malate/fumarate ratios, (B) KIM-1 and malate/fumarate ratio.

Fumarase activity measured in urine samples collected immediately after sacrifice was correlated with malate/fumarate ratios (R2 = 0.77, p = 0.02) (Figure 5.8A), as was plasma fumarase activity (R2 = 0.72, p = 0.03) (Figure 5.8B).

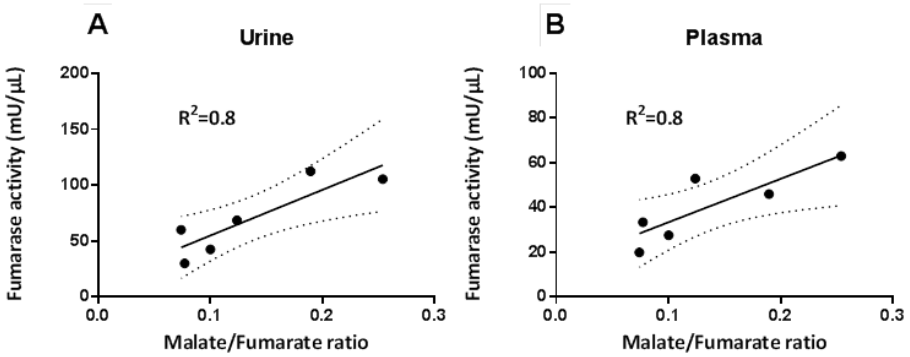

Figure 5.8: Correlation between urine and plasma fumarase activity. A significant correlation was found between (A) Urine fumarase activity and (B) Plasma fumarase activity.

5.8 Discussion

This study investigated the use of [1,4-$^{13}C_2$] fumarate to monitor necrosis in rat muscles and kidneys. To be able to image necrosis with fumarate, we needed to device a new scheme to polarize [1,4-$^{13}C_2$]fumarate in the SPINlab polarizer. Our initial trials to polarize the [1,4-$^{13}C_2$]fumarate was not successful because the freezing speed of the sample with the insertion procedure from the manufacturer was not sufficient to avoid the crystallization of the fumarate sample. The new faster lowering scheme with fewer steps was sufficient for mitigating this problem and for achieving high polarization values for [1,4-$^{13}C_2$]fumarate, 36±4%.

Moreover, simultaneous assessment of necrosis and metabolism has been demonstrated using dually polarized [1,4-$^{13}C_2$]fumarate and [1,4-^{13}C]pyruvate in rat models. We found no significant difference in the polarization values between the dual and single substrate polarization. We also demonstrated the feasibility of small animal research on a typical clinical scanner.

High [1,4-$^{13}C_2$]malate signal was observed from the necrotic tissue in both muscle and kidney models. In the rat muscles, we noticed a reduction in the amount of malate produced as time passes. We attribute this to the escape

of fumarase from the extracellular space of the necrotic tissue into the plasma. High lactate signal, and also high signal from other pyruvate products like alanine and bicarbonate, was observed at the necrotic muscle tissue in the *in vivo* experiment with dual FA and PA polarization. The increased signal from pyruvate products is not unexpected, since all intracellular enzymes like LDH also escape to the extracellular space when the cellular membranes are broken [167]. This is important to bear in mind, since many types of therapies induce necrosis in cancer tissue, which may result in elevated lactate production after injection of hyperpolarized pyruvate. Moreover, there is also evidence that cancer cells that survive the treatment, that induces necrosis, can benefit from the inflammatory response that follows, since it promote proliferation by providing the tumor environment with growth factors, survival factors and proangiogenic factors [168, 169]. Therefore, simultaneous assessment of metabolism and necrosis with the setup proposed here can give more complete picture and allow distinguishing whether the high lactate signal is because the necrosis process from therapy is taking effect or because the tumor is thriving.

The necrosis was induced in the rat muscles with turpentine injection. Turpentine is a mixture of alkylated aromatic hydrocarbons designed to dissolve fat, and thus they can effectively cause lipid dissolution. Therefore, Turpentine injection into living tissue provides a robust and easy to control method that causes necrosis and inflammatory response, and can be useful in studying cellular death via necrosis.

In the AKI model, all rats showed evidence of injury 24 h after surgery according to the functional kidney parameters plasma creatinine, CrCl, and BUN. The elevated malate signal observed in the AKI model showed high correlation with the well-known renal cortical injury markers; KIM- and NGAL. Additionally, the histological hematoxylin and eosin-stained sections showed typical signs of tubular necrosis. Plasma and urine fumarase activity levels were highly increased after the onset of IR injury, and were correlated with the hyperpolarized malate/fumarate ratios.

Although functional kidney parameters like plasma creatinine, CrCl, and BUN provide measurement tool to characterize IR injuries, they are unable to specify which kidney (or both) is suffering from necrotic injury. Therefore, the

addition of hyperpolarized [1,4-$^{13}C_2$]fumarate for local necrosis examinations further improves the characterization of IR injuries.

5.9 Conclusion

We demonstrated the feasibility of using [1,4-$^{13}C_2$]fumarate to characterize the necrosis in rat muscles and kidneys. High polarization was obtained for [1,4-$^{13}C_2$]fumarate in SPINlab polarizer with the new modified lowering scheme, 36±4%. Simultaneous polarization of [1,4-$^{13}C_2$]fumarate and [1,4-^{13}C]pyruvate was feasible with no significant deference in polarization values. High [1,4-$^{13}C_2$]malate signal was observed from the necrotic tissue in both muscle and kidney models. For the kidney model, the malate production correlated well with the urine and blood parameters and other well-known renal cortical injury markers like KIM- and NGAL. In the rat muscles, we observed high malate production within an hour of inducing the necrosis by turpentine injection. We also noticed an increase in the signal from pyruvate products due to the necrosis, when we simultaneously polarized [1,4-$^{13}C_2$]fumarate and [1,4-^{13}C]pyruvate.

6

Implementation of ^{13}C Echo Planar Spectroscopic Imaging Sequence in a Clinical System

6.1 Objective

This chapter details the development of a symmetric ^{13}C EPSI sequence in a clinical PET/MR platform with separate reconstruction of the odd and even echo data, which provides acceptable spectral bandwidth with reduced artifacts from gradient imbalances. Moreover, a correction is introduced for the phase evolution during the acquisition of the zig-zag trajectory in k-t space [159, 160], to avoid spatial blurring due to chemical shift artifacts in opposite directions for odd and even gradient echoes. Firstly, the design and optimization of the various sequence components, i.e. encoding gradients, RF pulses and sampling events are detailed. Secondly, a validation of the sequence on phantoms is presented, in which the EPSI was compared with the conventional phase encoded CSI. The sequence was also validated *in vivo* in a canine cancer patient after the injection of hyperpolarized [1-^{13}C]pyruvate.

6.2 Design of ^{13}C EPSI

The sequence was designed for a 3 T PET/MR scanner (mMR Biograph, Siemens Healthcare, Erlangen, Germany), with maximum gradient strength of 43 mT/m,

maximum slew rate of 180 mT/m/ms, gradient raster time of 10 μs, analog-to-digital converter (ADC) raster time of 100 ηs, and minimum delay between ADC readout events of 100 μs. The raster time is the smallest temporal unit that can be used to specify the timing of the ADC event. The acoustic resonances of the gradient coil were in the frequency bands of 530-630 Hz and 1010-1230, which should be avoided in the EPI readout spectrum.

6.2.1 Echo Planar Readout Gradient

The design of the echo planar readout gradient is dictated by the target spectral bandwidth and the spatial resolution required. For a certain spectral bandwidth (SW),

$$SW = \frac{1}{2T_{ES}} \tag{6.1}$$

where T_{ES}, which is the echo spacing, is the upper limit for readout time, T_{RO}. Thus, the target spectral bandwidth also sets the limit for the highest spatial resolution achievable in the readout direction, Δx, since Δx for a gradient waveform, G_{RO}, is given by

$$\Delta x = \frac{1}{\gamma \int_{t=0}^{t=T_{RO}} G_{RO}(t)dt} \tag{6.2}$$

where γ is the gyromagnetic ratio, and $t = 0$ is the time of the start of recording of the signal.

A SW of about 500 Hz in a 3 T magnet is acceptable for the case of hyperpolarized [1-^{13}C]pyruvate. The pyruvate and its products alanine, pyruvate-hydrate and lactate are located at 171.1, 176.3, 177.6, and 183.2 ppm respectively (i.e. a range of 372 Hz in a 3 T scanner).

The iterative optimization of the gradient waveform under the given hardware constraints, yielded a spectral bandwidth of 495 Hz corresponding to gradient lobe duration of 1010 μs, see Figure 6.1. Using trapezoidal gradients with ramp up and ramp down durations of 170 μs, the maximum gradient strength achievable during ramping at the maximum slew rate was 30 mT/m. The ADC

was switched on 57 μs after the start of the gradient and switched off 57 μs before the end of the gradient lobe to ensure more than 100 μs between successive ADC periods. The effective gradient moment accumulated during the readout was 26.6 mTs/m, which provided a maximum achievable spatial resolution of 3.75 mm with 495 Hz spectral bandwidth on the mMR Biograph. The corresponding ADC period was 896 μs.

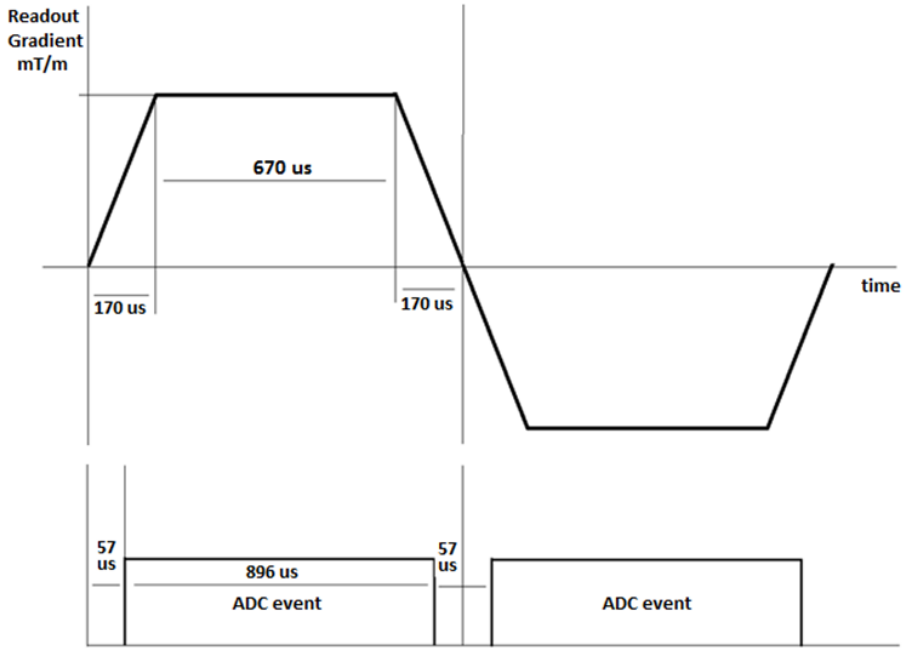

Figure 6.1: Design of even and odd lobes of the readout gradient with the ADC readout events.

6.2.2 Phase Encoding Gradient

The total duration of the phase encoding gradient was set to 1700 μs (ramp time of 200 μs and flat plateau duration of 1300 μs). The smallest resolution that can be attained in the phase encoding direction is 1.9 mm. An EPSI version with centric phase encoding was designed and used in the hyperpolarization experiments in phantom and *in vivo*.

6.2.3 RF Pulses

An excitation RF pulse (Hanning-filtered sinc pulse with time bandwidth product of 4) with total duration of 1280 μs and central lobe duration of 640 μs was used. The smallest slice thickness achievable with this pulse was 6 mm.

The excitation pulse had an approximate bandwidth (BW) of 3000 Hz. The chemical shift displacement $\delta_{p,l}$ between pyruvate and lactate in the slice direction is

$$\delta_{p,l} = \frac{\Delta f_{p,l}}{\gamma G_z} \tag{6.3}$$

where $\Delta f_{p,l}$ is the chemical shift between pyruvate and lactate (372 Hz at 3 T).

We can rewrite the chemical shift displacement between pyruvate and lactate in terms of the slice thickness Δz for the above pulses as,

$$\delta_{p,l} = \frac{\Delta f_{p,l}}{BW}\Delta z = 0.12\Delta z \tag{6.4}$$

Figure 6.2 shows the pulse sequence diagram of the EPSI FID with an echo train length (ETL) of 128.

Figure 6.2: Pulse sequence diagram of the EPSI-FID with ETL = 128.

6.3 SNR Efficiency

The theoretical SNR analysis of EPSI was done based on the work by Pohmann et al. [170] and Pipe and Duerk [171]. Pohmann et al. compared different chemical shift imaging methods and analyzed their sensitivity with respect to the conventional phase encoded CSI. For an EPSI sequence, the sensitivity, Ψ_{EPSI}, with respect to the CSI sensitivity, Ψ_{CSI}, can be written as

$$\Psi_{EPSI} = \frac{\Psi_{EPSI}}{\Psi_{CSI}} = \sqrt{1 - \frac{\tau_s}{T_{ES}}} \tag{6.5}$$

where τ_s is the time needed for gradient switching and T_{ES} is the echo spacing.

Pipe and Duerk showed that the variance in the reconstructed image depends on the shape of the gradient waveform used to record the signal. The smallest variance for even sampling occurs in the case of constant gradient, in which case the variance in the reconstructed image is equal to the variance of the thermal noise, σ^2. They also showed that the variance in the reconstructed image, σ_i^2, can be expressed in terms of the first and second moments of the gradients waveform, $G(t)$, and thermal noise variance σ^2 as,

$$\frac{\sigma_i^2}{T} = \frac{\sigma^2 \int_0^T G^2(t)dt}{(\int_0^T G(t)dt)^2} \tag{6.6}$$

6.4 Reconstruction and Postprocessing

Initially, 1D regridding was applied to compensate uneven k-space sampling over the ramp. After regridding, the odd and even echoes were separated into two matrices. Time reversal was performed on the odd echo data. Temporal Fourier transformation was applied to the two data sets to obtain two $k_x - k_y - f$ arrays. Before applying the spatial Fourier transform, a linear phase correction was introduced along the readout direction k_x [159, 160] to account for the time evolution, which would otherwise results in a chemical shift displacement in the spatial domain, differing between even and odd numbered echoes. If b is the acquisition bandwidth per pixel, given by $b = 1/T_{RO}$, then for a metabolite at

frequency f the spatial chemical shift is f/b. This chemical shift corresponds to a linear phase roll $\exp(-ikf/b)$ in the k-space. Therefore, the Corrected signal arrays $\bar{S}_{even}$ and $\bar{S}_{odd}$ can be constructed from the even and odd echo signal arrays, S_{even} and S_{odd} according to,

$$\bar{S}_{odd}(k_x, k_y, f) = e^{ik_x f/b} S_{odd}(k_x, k_y, f) \tag{6.7}$$

$$\bar{S}_{even}(k_x, k_y, f) = e^{-ik_x f/b} S_{even}(k_x, k_y, f) \tag{6.8}$$

Subsequently, 2D spatial Fourier transform was applied to obtain odd and even $x - y - f$ arrays. The data corresponding to odd and even echoes, I_{odd} and I_{even}, were then summed, after matching the phase, to obtain a ^{13}C spectroscopic image, I.

$$I(x, y, f) = I_{even}(x, y, f) + e^{i2\pi f T_{ES}} I_{odd}(x, y, f) \tag{6.9}$$

Figure 6.3 shows the reconstruction pipeline used. The chemical shift correction described above assumes there is no aliasing of metabolites in the spectrum, which may occur in practice since the spectral bandwidth is relatively small. Therefore, any aliased peaks should be unfolded to its true frequency position before applying the corrections. This can be done if peaks do not overlap in the aliased spectra by simply applying phase ramps corresponding to spatial shifts of non-aliased peak frequencies.

6.5 SNR Phantom Experiment

6.5.1 MR Acquisition Method

A phantom experiment was conducted to compare EPSI with CSI in terms of SNR and localization robustness. The ^{13}C images were acquired using a 270 mm diameter ^{13}C birdcage head coil (RAPID Biomedical, Germany). The phantom

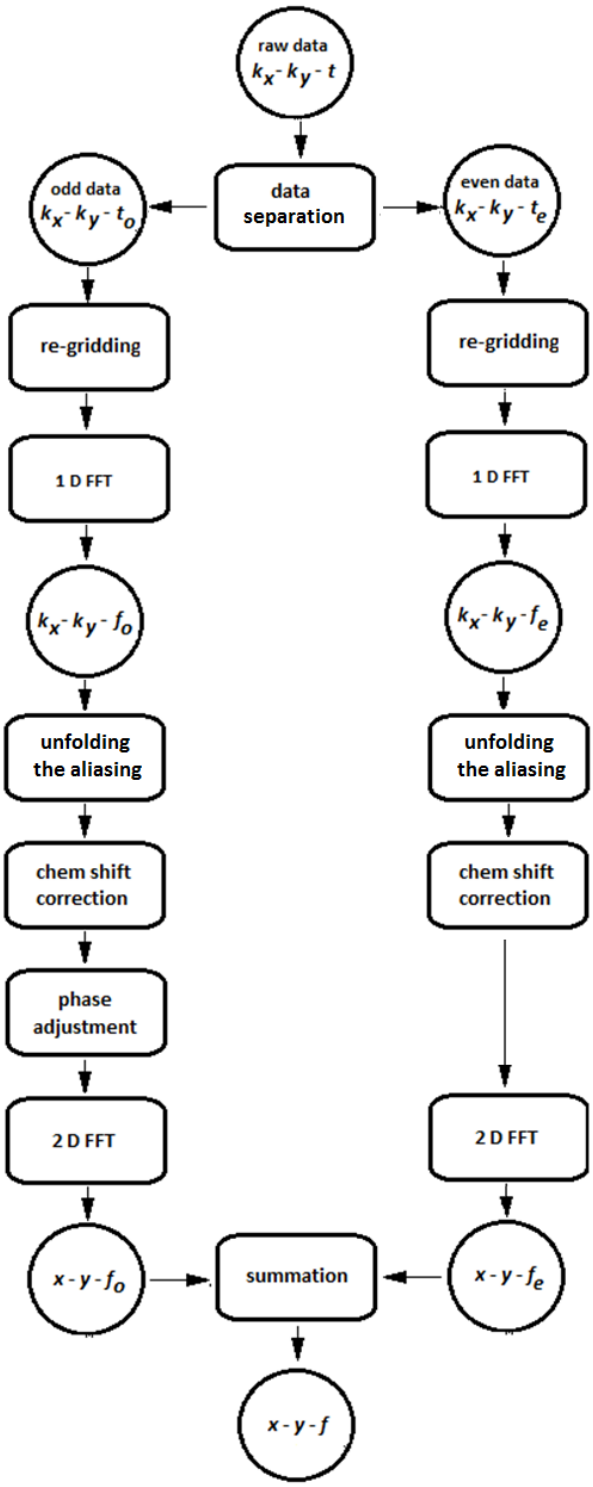

Figure 6.3: The pipeline used for the reconstruction of the raw data and the correction of the broadening due to chemical shifts in opposite directions in the odd and even data.

used was a cylinder with diameter of 250 mm and length of 200 mm. It has four cylindrical compartments with inner diameters of 19 mm each. The outer volume of the phantom was filled with ethylene glycol with natural abundance of ^{13}C, and three of the inner compartments were filled with ^{13}C-bicarbonate, [1-^{13}C]acetate and ^{13}C-urea. The concentration of each substrate is 1.0 M. The fourth compartment was left empty.

The product CSI sequence served as the SNR reference. The CSI data were acquired with TR of 1000 ms, FOV 100x100 mm^2, spatial matrix 16x16, flip angle 90°, slice thickness 100 mm, spectral bandwidth 5000 Hz, number of spectral points 512, sampling time of 102.4 ms, and no averaging, resulting in a CSI scan time of 4 min and 16 s. The time between excitation and sampling was 2.3 ms. EPSI data were acquired with TR of 1000 ms, FOV 100x100 mm^2, spatial matrix 16x16, flip angle 90°, slice thickness 100 mm, ETL 128, T_{ES} 1010 μs, and 16 averages, resulting in a scan time of 4 min and 16 s, echo train duration of 129.3 ms and a spectral bandwidth of 495 Hz. The time between excitation and the start of the first readout gradient lobe was 2.4 ms. For noise estimation, both CSI and EPSI sequences were run after nulling the transmitted signal.

6.5.2 Results of SNR Comparison

Figure 6.4 shows the comparison between EPSI reconstruction algorithms. Direct FFT reconstruction, Figure 6.4A, results in spatial blurring of the substrates in the ^{13}C image due to chemical shifts in opposite directions. On the other hand, spectral-spatial regridding using the apparent frequency positions, Figure 6.4B, results in narrower and more accurate spatial representation of ^{13}C urea and ^{13}C bicarbonate. [1-^{13}C]Acetate, however, was outside of the critically sampled bandwidth and aliased, which resulted in increased spatial broadening. When accounting for aliasing by using the actual frequency offset of the non-aliased peak, the chemical shift displacement of [1-^{13}C]acetate was compensated as well, Figure 6.4C.

To calculate the theoretical relative SNR between the CSI and the EPSI, (Eq-6.5) was used. The EPSI acquisition time was 896 μs with 114 μs delay between acquisitions reducing the SNR by 5% compared to CSI. To account for sampling

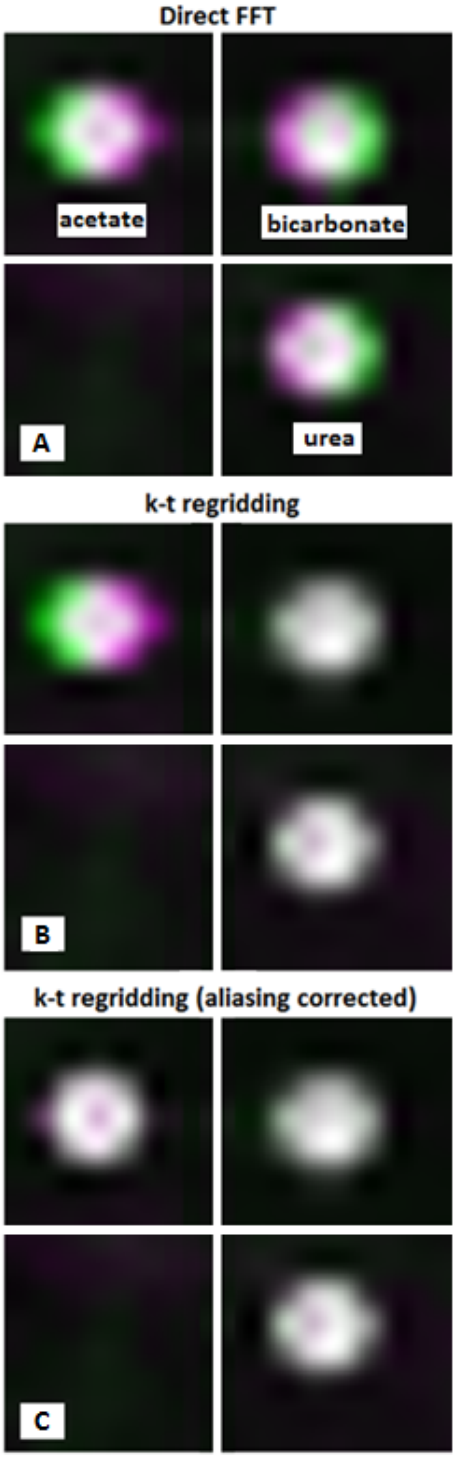

Figure 6.4: A comparison of chemical shift displacement with (A) direct FFT reconstruction and (B and C) with reconstruction after spectral-spatial regridding. The images from odd (green) and even (magenta) echoes are overlaid. The locations of overlap appear in white and the non-overlap locations appear colored. In (B) spectral-spatial regridding removes the chemical shift displacement of bicarbonate and urea, which are within the spectral bandwidth, but increases the chemical shift displacement of acetate that is aliased. In (C) the chemical shift displacement of the acetate peak is additionally corrected using its non-aliased frequency location in the reconstruction.

over the ramps, (Eq-6.6) was used to calculate the SNR efficiency relative to a square readout gradient waveform, which amounts to 94%. Therefore, the relative theoretical SNR of EPSI with respect to CSI is 89%.

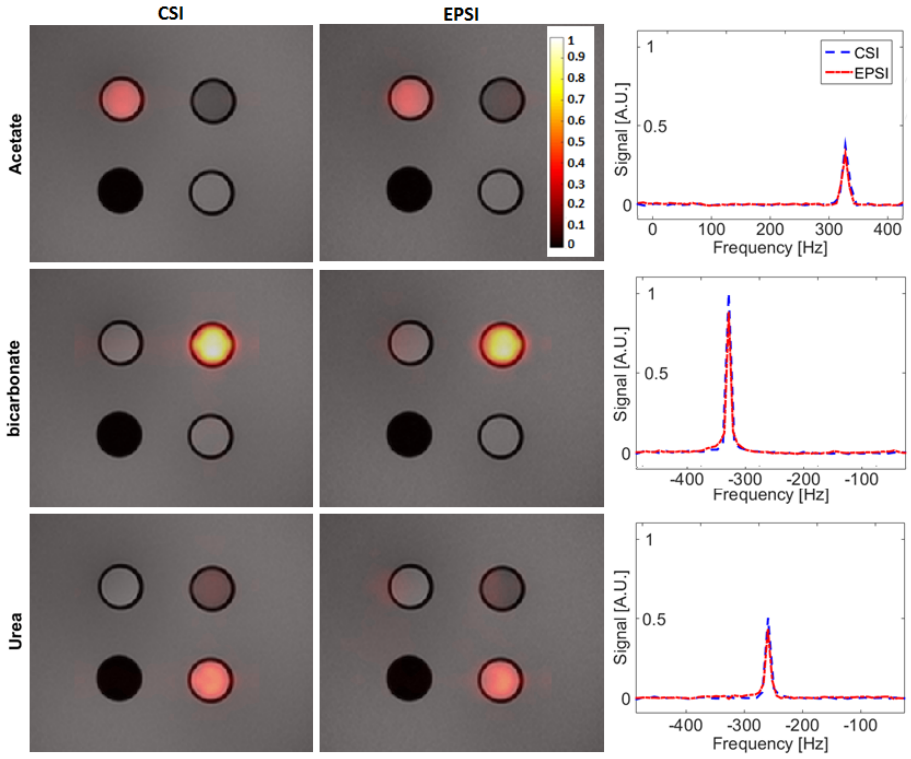

Figure 6.5: The [1- ^{13}C]acetate, ^{13}C-bicarbonate and ^{13}C-urea maps acquired by CSI and EPSI. Only the central part of the phantom is shown. The signal level in the maps is normalized with respect to the bicarbonate signal acquired with CSI. The spectrum from a single voxel at the center of each substrate is also shown for both CSI and EPSI. The line width (full width at half height) obtained with CSI was 12.2 Hz, 9.2 Hz and 10.6 Hz for [1-^{13}C]acetate, ^{13}C-bicarbonate and ^{13}C-urea respectively, whereas the line width obtained with EPSI was 11.7 Hz, 8.7 Hz and 9.8 Hz.

Figure 6.5 shows the signal for the three substrates ^{13}C-urea, ^{13}C-bicarbonate and [1-^{13}C]acetate in the multi-compartments phantom obtained with CSI and EPSI using the birdcage coil, superimposed on the proton image. The strength of the signal varied between the substrates due to differences in T_1 relaxation time constants and line width. To quantify the SNR of each substrate, the signal was estimated at each voxel from the peak amplitude (real phased spectrum).

Then the signal was averaged in a 4x4 pixel region of interest encompassing the substrate, and normalized by the noise standard deviation in the spectra in the same region. For the CSI, the SNR values were 290, 153 and 113 for ^{13}C-bicarbonate, ^{13}C-urea and [1-^{13}C]acetate, respectively. For EPSI the SNR values were 257, 135 and 99 for the three phantoms respectively. This corresponds to relative SNR values of 0.89, 0.87, and 0.88 respectively, which are close to the theoretical values.

6.5.3 Localization Assessment

To assess the localization of the spectroscopic sequences, the proton image was taken as a reference. For each substrate, the location of the center of the cylinder in the ^{13}C image and proton image were compared. The shift in millimeters between the two locations was reported. Since each substrate is in a cylinder, a circle was fitted to the contour spatial distribution and the center of the circle was taken as the location in the proton image. The ^{13}C images were obtained using general linear model (GLM) fitting. Then spline fitting was applied to the ^{13}C spatial distribution of each substrate to achieve sub-voxel precision at the same resolution as the proton image. The position of the peak intensity in the metabolite distribution after spline fitting was used as the substrate location in the ^{13}C image.

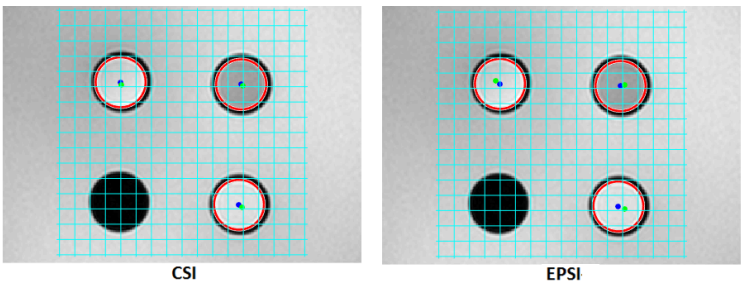

Figure 6.6: The center of each substrate as obtained from the proton image (blue dot) and the position of the substrate obtained from the CSI and EPSI acquisitions (green dot).

Figure 6.6 shows the locations of the three substrates obtained with the CSI and EPSI sequences with respect to the true position obtained from the proton image. The CSI sequence has the smallest offsets with 0.8 mm for [1-^{13}C]-

acetate, 0.9 mm for ^{13}C-bicarbonate and 1.5 mm for ^{13}C-urea. The offsets are higher for the EPSI sequence; 1.9 mm, 1.7 mm and 3.1 mm, respectively.

6.6 Phantom Experiment with Hyperpolarized [1-^{13}C]Pyruvate

6.6.1 Hyperpolarized Phantom Preparation

A phantom experiment was conducted with hyperpolarized [1-^{13}C]pyruvate and dual tuned ^{1}H/^{13}C surface coil (RAPID Biomedical, Germany). A hyperpolarized phantom made from a rectangular bottle (200x185x125 mm^3) was initially filled with 4.5 L of saline solution. A hyperpolarized sample containing 14 mmol of [1-^{13}C]pyruvate was added to the phantom after dissolution. Then the phantom was briefly shaken, placed on top of the surface ^{1}H/^{13}C coil and the dynamic imaging was acquired. To prepare the hyperpolarized sample, 1 mL of [1-^{13}C]pyruvic acid with 15 mM of electron paramagnetic agent, AH111501 (Syncom BV, Netherlands), was polarized in a SPINlab polarizer (GE Healthcare, USA) for 4 hours. The sample was then dissolved in 49.8 mL of dissolution media containing 0.1 g/L of EDTA in water. The sample was neutralized with 14.6 mL of neutralizing media containing 0.72 M NaOH, 0.4 M Tris and 0.1 g/L EDTA disodium salt in water.

Two different dynamic measurements were acquired, one with EPSI and the second with CSI. The EPSI acquisition was made using a FOV 200x200 mm^2, 32x32 matrix with central phase encoding, ETL 64, flip angle 6°, TR 80 ms, and TE 2.4 ms. The acquisition time per frame was 2.5 s and an image was acquired every 5 s. The CSI was acquired using FOV 200x200 mm^2, truncated 16x16 matrix, flip angle 3°, TR 80 ms, and TE 2.3 ms. The acquisition time per frame was 12 s and 3 images were acquired sequentially without delay.

The dynamic frames acquired with EPSI and CSI for hyperpolarized [1-^{13}C]pyruvate in the 4.5 L rectangular phantom are shown in Figure 6.7. The signal decay (sum of the signal over the phantom) with both CSI and EPSI is shown in Figure 6.8B. For the dynamic measurements obtained with CSI, the time resolution was very coarse, 12 s, despite the smaller matrix size used, and

thus coarser spatial resolution. The coil profile derived from the EPSI image of the phantom is shown in Figure 6.8A.

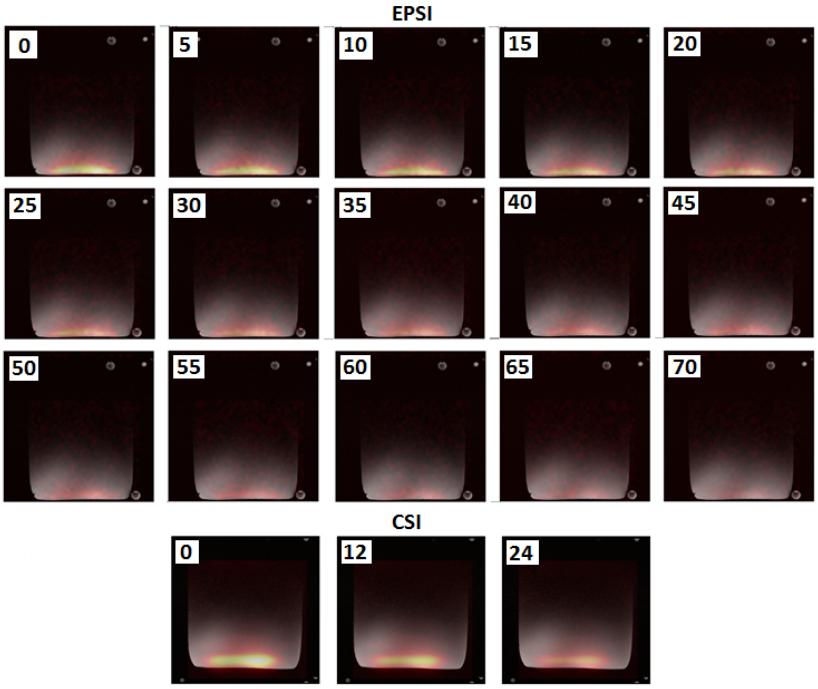

Figure 6.7: Dynamic images acquired for hyperpolarized [1-^{13}C]pyruvate in a 4.5 L phantom with EPSI and CSI.

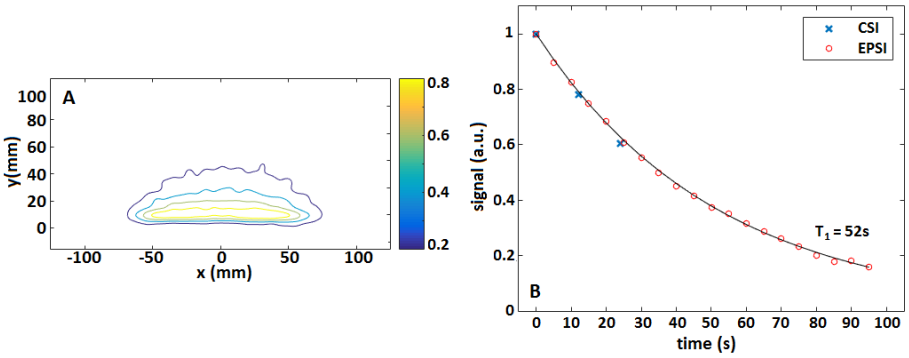

Figure 6.8: (A) The the coil profile first dynamic image acquired for hyperpolarized [1-^{13}C]pyruvate as obtained with EPSI (A). (B) shows the decay of the signal from hyperpolarized pyruvate obtained by both EPSI and CSI. An exponential function was fitted to EPSI signal giving a time constant of 52 s.

6.7 Animal experiment

6.7.1 Animal Model

An animal experiment was conducted to test the EPSI sequence on a 27 kg dog with acanthotic ameloblastoma. The dog underwent PET/MRI as part of the diagnostic and staging work-up and hyperpolarized ^{13}C-MRSI was included in a combined PET/MR examination. The owner gave informed consent and the study was approved by the relevant ethics and administrative committee.

6.7.2 Hyperpolarzed Media Preparation

Three 500 μL samples of [1-^{13}C]pyruvic acid with 15 mM of AH111501 were hyperpolarized in the SPINlab polarizer for 4 hours. The samples were dissolved in 29.1 mL dissolution media and neutralized with 7.3 mL of neutralizing media. After dissolution, 18 mL (0.68 mL/kg) of 250 mM [1-^{13}C]pyruvate was injected intravenously over 7–8 s.

6.7.3 PET/MR Acquisition

The ^{1}H/^{1313}C dual tuned flex coil was used again for imaging. Coronal, transversal and sagittal anatomic ^{1}H MR images were acquired for planning using a T_2 weighted turbo spin-echo sequence (TR 4,000 ms; TE 89 ms; voxel size 0.5 x 0.5 mm^2; 19 slices of 3 mm thickness).

The dog received three injections of hyperpolarized [1-^{13}C]pyruvate with 10 min intervals. A dynamic FID sequence with no in-plane spatial encoding was started at the beginning of the sample injection with the following parameters: slice thickness 4 cm, TR 1 s, flip angle 5°, acquisition delay 2.3 ms, spectral bandwidth of 6000 Hz and 512 points. The purpose of the dynamic FID was to find the time point with maximum lactate signal, which was used to determine the start time of the subsequent CSI acquisition. Acquisition of a CSI data set was initiated 30 s after the start of the injection of the second pyruvate sample with TR 80 ms, FOV 150x180 mm^2, matrix size 16x16, slice thickness 15 mm, flip angle 10°, acquisition delay 2.3 ms, spectral bandwidth 10000 Hz,

and number of spectral points 512. A dynamic EPSI acquisition was started at the end of the injection of the third hyperpolarized sample using a FOV of 150x180 mm^2, 16x32 matrix with central phase encoding, slice thickness 15 mm, ETL 64, flip angle 6°, TR 80 ms, and acquisition delay 2.4 ms. The acquisition time per frame was 1.3 s and a frame was acquired every 3 s (with idle time of 1.7 s between frames).

PET images were acquired as a single-bed with 5 min acquisition duration, after intravenous injection of 216 MBq (8 MBq/kg) of ^{18}F-FDG, 1 hour prior to imaging. The resolution of PET images was 2.1x2.1 mm^2 and the slice thickness was 2.0 mm.

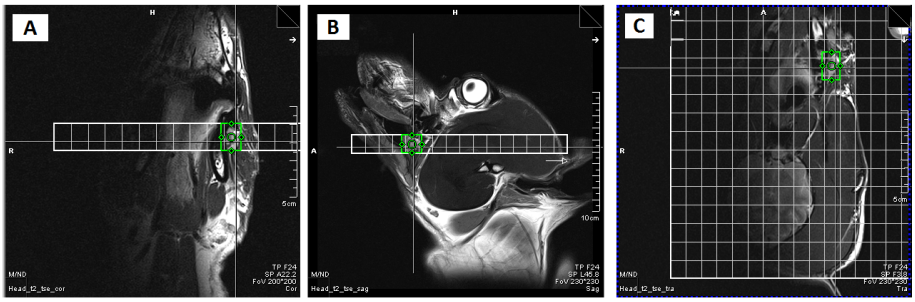

Figure 6.9: The anatomical images (transversal, coronal and sagittal) acquired with TSE and used to position the spectroscopic grids for both CSI and EPSI (A, B and C). The green box is at the location of the tumor.

6.7.4 Results from Canine Cancer Patient

Figure 6.9 shows the anatomical images used to plan the positioning of the spectroscopic grids for both CSI and EPSI. The 16x12 mm tumor is located at the buccal side of the left mandible, as shown in Figure 6.10A. The dynamic FID (Figure 6.12A) shows that pyruvate starts accumulating in the slab containing the tumor about 10 s after the start of the injection, and reaches a peak value 9 s later. Lactate starts building up 22 s after the start of the injection and reaches a maximum value after 32 s. The CSI acquisition was timed to start 30 s after injection to obtain the highest possible lactate signal from the slice. Figure 6.10 (B and E) shows the pyruvate and lactate signals at the slice containing the tumor. Relatively high pyruvate uptake and an increased lactate production can be observed at the tumor site. Additionally, lactate signal can be seen at

the masticator muscle in the lower right region. The PET-FDG image (Figure 6.10D) also shows high metabolism at the tumor site in addition to the typical high FDG uptake in the brain.

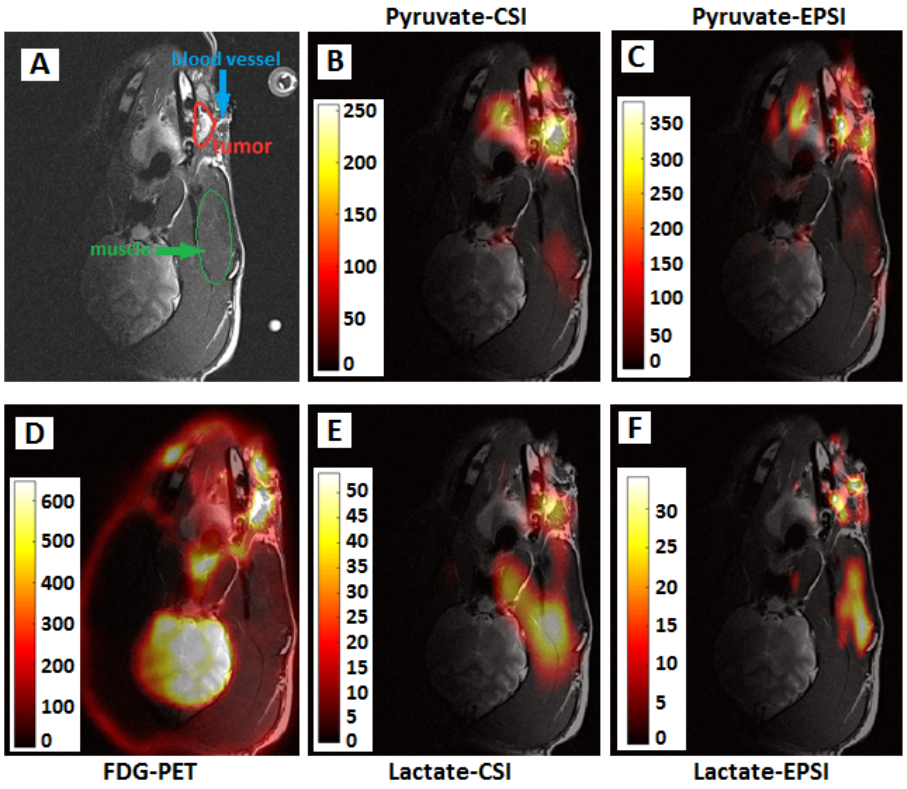

Figure 6.10: The acanthomatous ameloblastoma in the left mandible of the canine cancer patient (A). The PET-FDG image (slice thickness 2 mm) with high uptake in the tumor and brain regions is shown in (D). (B and E) show the pyruvate and lactate signals, obtained from the CSI acquisition using GLM, at the slice containing the tumor. Increased lactate production can be observed at the tumor and muscle sites. (C and F) show pyruvate and lactate images calculated from the dynamic EPSI by integrating over the frames in Figure 6.11.

In Figures 6.11, the series of metabolic maps obtained with EPSI are given. These maps show the buildup and decay of pyruvate and lactate across the slice. To allow for comparison with the dynamic FID, the pyruvate and lactate signals in each frame were summed over the entire frame, to obtain the time plots shown in Figure 6.12B. The pyruvate and lactate signals were also integrated at the tumor to obtain the dynamic build-up and decay at this site, Figure 6.12C.

Moreover, the pyruvate and lactate series were integrated into one pyruvate and one lactate image, Figure 6.10 (C and F), for comparison with the corresponding CSI maps in Figure 6.10 (B and E). The signal level in all the metabolic maps in Figures 6.10 and 6.11 were normalized with respect to the standard deviation of the noise.

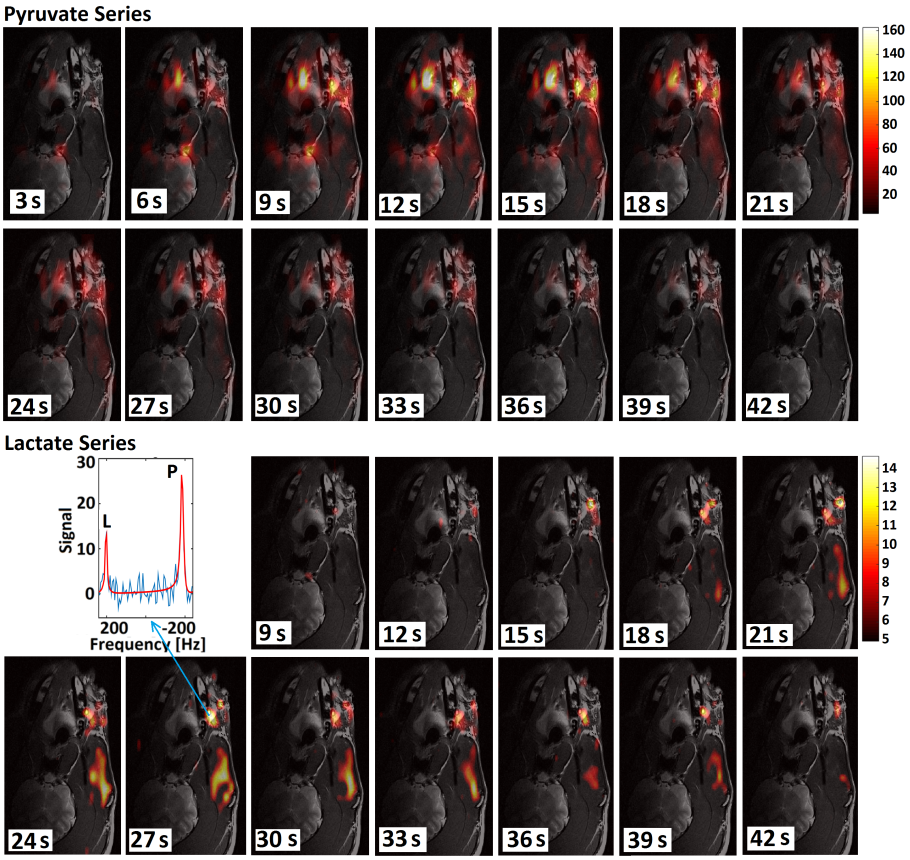

Figure 6.11: Pyruvate and lactate build-up and decay across the slice containing the tumor. The figure also shows the spectrum with GLM fitting at the tumor site in the EPSI frame acquired 27 s after the end of injection.

6.8 Discussion

An implementation was presented of a symmetric EPSI sequence for hyperpolarized ^{13}C in a hybrid clinical PET/MR system, and was evaluated in phantoms

and *in vivo*. To our knowledge this is the first ^{13}C EPSI sequence implemented in a clinical Siemens platform. The SNR obtained with this sequence was around 88% compared to CSI, and this agrees with the theoretical estimation.

The reconstruction employed in this work provides better accuracy compared to direct FFT. However, the bandwidth in EPSI is relatively small and aliasing may occur. Aliased metabolites cause an error in the spatial-spectral regridding. However, the ^{13}C spectrum in hyperpolarization experiments is often sparse and the metabolite frequencies known a priori, and thus aliasing can be corrected before applying the reconstruction algorithm.

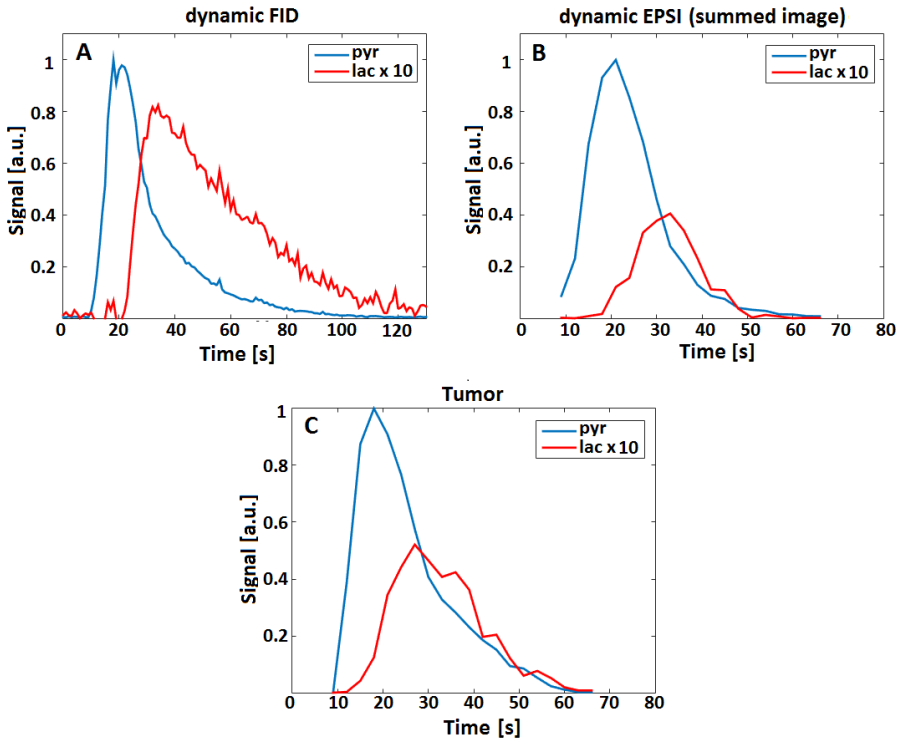

Figure 6.12: (A) The build-up of pyruvate and its conversion to lactate obtained with dynamic FID acquisition over a 4 cm axial slab that includes the tumor region. (B and C) show the time curves for lactate and pyruvate obtained from the EPSI series (Figure 6.11) by integrating the pyruvate and lactate signals in each frame at the whole image and at the tumor region, respectively.

In the phantom experiment with hyperpolarized [1-^{13}C]pyruvate and *in vivo* canine experiment, EPSI allowed dynamic imaging with reasonable temporal

resolution. Moreover, higher spatial resolution was achieved for the metabolic maps obtained with EPSI compared to CSI in the these experiments. Despite employing dynamic acquisition with EPSI in the *in vivo* hyperpolarization experiment, using a larger matrix size was feasible, compared to the matrix size of CSI. Moreover, CSI is prone to blurring from T_1 decay due to the relatively long acquisition duration per frame. Therefore, the pyruvate and lactate signals were sharper and better localized in the EPSI metabolic maps, whereas the maps obtained from the CSI acquisition were blurry.

Both the EPSI and the CSI sequences showed similar metabolite distributions in the *in vivo* experiment. The slight differences could be because the imaging windows for the two sequences were different: CSI was acquired over 12 s from 30 s after injection, whereas EPSI was acquired over 60 s from the end of the injection. Also, the spatial resolution of CSI was lower than that of EPSI, 10x9 mm^2 and 5x9 mm^2 for the two sequences respectively.

6.9 Conclusion

A symmetric ^{13}C EPSI sequence was presented. The sequence mitigates the artifacts from the imbalanced gradients by separate reconstruction of odd and even echo data. The reconstruction algorithm employed with the sequence provides better accuracy compared to direct FFT even for aliased peaks. The SNR of the EPSI sequence was comparable to the CSI SNR in the phantom experiment at thermal equilibrium. In the *in vivo* experiment with hyperpolarized [1-^{13}C]pyruvate, EPSI allowed imaging with higher spatial and temporal resolutions compared to CSI, 5x9 mm^2 1.3 s per frame for EPSI and 10x9 mm^2 and 12 s per frame for CSI.

7

Perspectives and Future Work

We have evaluated [1-^{13}C]pyruvate as marker to monitor the response of cancer to treatment. We also presented a comparison between the [1-^{13}C]pyruvate and the more clinically established FDG- and FLT-PET tracers. We found that all three markers were able to detect the response to treatment. Each of PET and ^{13}C MRS has it is own merit, and combination of both to assess the tumor progression or remission can be of great value. Particularly, the possibility of assessing tumor metabolism using [1-^{13}C]pyruvate in a joint PET/MR scanner, thus leaving the PET modality available for measuring other biological characteristics, can be of great interest.

At this stage we have used fumarate with models in which the necrotic process is very well studied and understood by our group and collaborators. The findings from these studies will be used as a starting point for future researches on monitoring therapy-induced necrosis in cancer with hyperpolarized [1,4-$^{13}C_2$]fumarate. We also believe that hyperpolarized [1,4-$^{13}C_2$]fumarate holds great promise as an *in vivo* diagnostic tool for pathologies in which the necrotic process plays a major role, like the case with acute kidney injuries.

The presented EPSI sequence allowed fast imaging with good SNR and no artifacts from the imbalanced gradients. The sequence also facilitates kinetic modeling in cancer, and this is now being investigated in rats with xenografted tumors. Currently, the reconstruction algorithm is implemented offline, and an online implementation of the reconstruction algorithm is planned. We are also investigating new excitation modules that utilize the non-recoverable magnetization more efficiently, e.g., dynamically changing flip angles and spatial-spectral selective excitations.

Bibliography

[1] P. Therasse, S. G. Arbuck, E. A. Eisenhauer, J. Wanders, R. S. Kaplan, L. Rubinstein, J. Verweij, M. V. Glabbeke, A. T. van Oosterom, M. C. Christian, and S. G. Gwyther, "New Guidelines to Evaluate the Response to Treatment in Solid Tumors," *Journal of the National Cancer Institute*, vol. 92, pp. 205–216, dec 2000.

[2] S. S. Gambhir, "Molecular imaging of cancer with positron emission tomography," *Nature Reviews Cancer*, vol. 2, no. 9, pp. 683–693, 2002.

[3] R. K. Doot, E. S. McDonald, and D. A. Mankoff, "Role of PET quantitation in the monitoring of cancer response to treatment: Review of approaches and human clinical trials," 2014.

[4] A. Langer, "A systematic review of PET and PET/CT in oncology: a way to personalize cancer treatment in a cost-effective manner?," *BMC health services research*, vol. 10, p. 283, 2010.

[5] A. Zhu, D. Lee, and H. Shim, "Metabolic positron emission tomography imaging in cancer detection and therapy response," *Seminars in Oncology*, vol. 38, pp. 55–69, feb 2011.

[6] R. J. Gillies and D. L. Morse, "In vivo magnetic resonance spectroscopy in cancer.," *Annual review of biomedical engineering*, vol. 7, pp. 287–326, 2005.

[7] D. Bertholdo, A. Watcharakorn, and M. Castillo, "Brain Proton Magnetic Resonance Spectroscopy: Introduction and Overview," aug 2013.

[8] P. R. Carroll, F. V. Coakley, and J. Kurhanewicz, "Magnetic resonance imaging and spectroscopy of prostate cancer.," *Reviews in urology*, vol. 8 Suppl 1, no. Suppl 1, pp. S4–S10, 2006.

[9] P. L. Jager, J. A. Gietema, and W. T. van der Graaf, "Imatinib mesylate for the treatment of gastrointestinal stromal tumours: best monitored with FDG PET," *Nucl Med Commun*, vol. 25, pp. 433–438, may 2004.

[10] f. t. G. C. P. E. T. S. G. O. Annick D. Van den Abbeele, "F18-FDG-PET Provides Early Evidence of Biological Response to STI571 in Patients with Malignant Gastrointestinal Stromal Tumors (GIST).," in *ASCO*, p. Abstract No: 1444, 2001.

[11] F. A. Howe, S. J. Barton, S. A. Cudlip, M. Stubbs, D. E. Saunders, M. Murphy, P. Wilkins, K. S. Opstad, V. L. Doyle, M. A. McLean, B. A. Bell, and J. R. Griffiths, "Metabolic profiles of human brain tumors using quantitative in vivo 1H magnetic resonance spectroscopy.," *Magnetic resonance in medicine*, vol. 49, pp. 223–32, feb 2003.

[12] J. Kurhanewicz and D. B. Vigneron, "Advances in MR Spectroscopy of the Prostate," nov 2008.

[13] U. G. Mueller-Lisse and M. K. Scherr, "Proton MR spectroscopy of the prostate," *European Journal of Radiology*, vol. 63, pp. 351–360, sep 2007.

[14] J. H. Ardenkjær-Larsen, B. Fridlund, A. Gram, G. Hansson, L. Hansson, M. H. Lerche, R. Servin, M. Thaning, and K. Golman, "Increase in signal-to-noise ratio of¿ 10,000 times in liquid-state nmr," *Proceedings of the National Academy of Sciences*, vol. 100, no. 18, pp. 10158–10163, 2003.

[15] S. E. Day, M. I. Kettunen, F. A. Gallagher, D.-E. Hu, M. Lerche, J. Wolber, K. Golman, J. H. Ardenkjaer-Larsen, and K. M. Brindle, "Detecting tumor response to treatment using hyperpolarized 13c magnetic resonance imaging and spectroscopy," *Nature medicine*, vol. 13, no. 11, pp. 1382–1387, 2007.

[16] M. J. Albers, R. Bok, A. P. Chen, C. H. Cunningham, M. L. Zierhut, V. Y. Zhang, S. J. Kohler, J. Tropp, R. E. Hurd, Y.-F. Yen, *et al.*, "Hyperpolarized 13c lactate, pyruvate, and alanine: noninvasive biomarkers for prostate cancer detection and grading," *Cancer research*, vol. 68, no. 20, pp. 8607–8615, 2008.

[17] S. J. Nelson, J. Kurhanewicz, D. B. Vigneron, P. E. Larson, A. L. Harzstark, M. Ferrone, M. van Criekinge, J. W. Chang, R. Bok, I. Park, *et al.*, "Metabolic imaging of patients with prostate cancer using hyperpolarized [1-13c] pyruvate," *Science translational medicine*, vol. 5, no. 198, pp. 198ra108–198ra108, 2013.

[18] K. Golman, M. Lerche, R. Pehrson, J. H. Ardenkjaer-Larsen, *et al.*, "Metabolic imaging by hyperpolarized 13c magnetic resonance imaging for in vivo tumor diagnosis," *Cancer research*, vol. 66, no. 22, pp. 10855–10860, 2006.

[19] M. L. Zierhut, Y. F. Yen, A. P. Chen, R. Bok, M. J. Albers, V. Zhang, J. Tropp, I. Park, D. B. Vigneron, J. Kurhanewicz, R. E. Hurd, and S. J. Nelson, "Kinetic modeling of hyperpolarized 13C1-pyruvate metabolism in normal rats and TRAMP mice," *Journal of Magnetic Resonance*, vol. 202, no. 1, pp. 85–92, 2010.

[20] A. P. Chen, W. Chu, Y.-P. Gu, and C. H. Cunnhingham, "Probing early tumor response to radiation therapy using hyperpolarized [1-13 c] pyruvate in mda-mb-231 xenografts," *PLoS One*, vol. 8, no. 2, p. e56551, 2013.

[21] F. A. Gallagher, M. I. Kettunen, D.-E. Hu, P. R. Jensen, M. Karlsson, A. Gisselsson, S. K. Nelson, T. H. Witney, S. E. Bohndiek, G. Hansson, *et al.*, "Production of hyperpolarized [1, 4-13c2] malate from [1, 4-13c2] fumarate is a marker of cell necrosis and treatment response in tumors," *Proceedings of the National Academy of Sciences*, vol. 106, no. 47, pp. 19801–19806, 2009.

[22] L. Mignion, P. Dutta, G. V. Martinez, P. Foroutan, R. J. Gillies, and B. F. Jordan, "Monitoring chemotherapeutic response by hyperpolarized 13c-fumarate mrs and diffusion mri," *Cancer research*, vol. 74, no. 3, pp. 686–694, 2014.

[23] M. R. Clatworthy, M. I. Kettunen, D.-E. Hu, R. J. Mathews, T. H. Witney, B. W. Kennedy, S. E. Bohndiek, F. A. Gallagher, L. B. Jarvis, K. G. Smith, *et al.*, "Magnetic resonance imaging with hyperpolarized [1, 4-13c2] fumarate allows detection of early renal acute tubular necrosis," *Proceedings of the National Academy of Sciences*, vol. 109, no. 33, pp. 13374–13379, 2012.

[24] T. Witney, M. Kettunen, D. Hu, F. Gallagher, S. Bohndiek, R. Napolitano, and K. Brindle, "Detecting treatment response in a model of human breast adenocarcinoma using hyperpolarised [1-13c] pyruvate and [1, 4-13c2] fumarate," *British journal of cancer*, vol. 103, no. 9, pp. 1400–1406, 2010.

[25] D. Hanahan and R. A. Weinberg, "The hallmarks of cancer," *Cell*, vol. 100, pp. 57–70, 2000.

[26] D. Hanahan and R. A. Weinberg, "Hallmarks of cancer: The next generation," mar 2011.

[27] A. B. Pardee, "G1 events and regulation of cell proliferation," *Science*, vol. 246, no. 4930, p. 603, 1989.

[28] C. Basilico and D. Moscatelli, "The fgf family of growth factors and oncogenes," *Advances in cancer research*, vol. 59, pp. 115–165, 1992.

[29] A. M. De Vos, M. Ultsch, and A. A. Kossiakoff, "Human growth hormone and extracellular domain of its receptor: crystal structure of the complex," *Science*, vol. 255, no. 5042, p. 306, 1992.

[30] Y. Yarden and A. Ullrich, "Growth factor receptor tyrosine kinases," *Annual review of biochemistry*, vol. 57, no. 1, pp. 443–478, 1988.

[31] S. A. Aaronson, "Growth factors and cancer," *Science*, vol. 254, no. 5035, p. 1146, 1991.

[32] A. Ashkenazi and V. M. Dixit, "Apoptosis control by death and decoy receptors," *Current opinion in cell biology*, vol. 11, no. 2, pp. 255–260, 1999.

[33] S. Nagata, "Apoptosis by death factor," *cell*, vol. 88, no. 3, pp. 355–365, 1997.

[34] S. Nagata and P. Golstein, "The fas death factor," *Science*, vol. 267, no. 5203, p. 1449, 1995.

[35] H. Symonds, L. Krall, L. Remington, M. Saenz-Robles, S. Lowe, T. Jacks, and T. Van Dyke, "p53-dependent apoptosis suppresses tumor growth and progression in vivo," *Cell*, vol. 78, no. 4, pp. 703–711, 1994.

[36] H. L. Moses, E. Y. Yang, and J. A. Pietenpol, "Tgf-β stimulation and inhibition of cell proliferation: new mechanistic insights," *Cell*, vol. 63, no. 2, pp. 245–247, 1990.

[37] J. L. Wrana, L. Attisano, R. Wieser, F. Ventura, and J. Massague, "Mechanism of activation of the tgf-b receptor," *Nature*, vol. 370, no. 6488, pp. 341–346, 1994.

[38] A. H. Wyllie, J. R. Kerr, and A. Currie, "Cell death: the significance of apoptosis," *International review of cytology*, vol. 68, pp. 251–306, 1980.

[39] C. B. Thompson, "Apoptosis in the pathogenesis and treatment of disease," *Science*, vol. 267, no. 5203, p. 1456, 1995.

[40] A. A. Samani, S. Yakar, D. LeRoith, and P. Brodt, "The role of the igf system in cancer growth and metastasis: overview and recent insights," *Endocrine reviews*, vol. 28, no. 1, pp. 20–47, 2007.

[41] J. F. Kerr, C. M. Winterford, and B. V. Harmon, "Apoptosis. its significance in cancer and cancer therapy," *Cancer*, vol. 73, no. 8, pp. 2013–2026, 1994.

[42] T. J. Lynch, D. W. Bell, R. Sordella, S. Gurubhagavatula, R. A. Okimoto, B. W. Brannigan, P. L. Harris, S. M. Haserlat, J. G. Supko, F. G. Haluska, *et al.*, "Activating mutations in the epidermal growth factor receptor underlying responsiveness of non–small-cell lung cancer to gefitinib," *New England Journal of Medicine*, vol. 350, no. 21, pp. 2129–2139, 2004.

[43] W. Pao, V. Miller, M. Zakowski, J. Doherty, K. Politi, I. Sarkaria, B. Singh, R. Heelan, V. Rusch, L. Fulton, *et al.*, "Egf receptor gene mutations are common in lung cancers from "never smokers" and are associated with sensitivity of tumors to gefitinib and erlotinib," *Proceedings of the National Academy of Sciences of the United States of America*, vol. 101, no. 36, pp. 13306–13311, 2004.

[44] S. V. Sharma, D. W. Bell, J. Settleman, and D. A. Haber, "Epidermal growth factor receptor mutations in lung cancer," *Nature Reviews Cancer*, vol. 7, no. 3, pp. 169–181, 2007.

[45] T. S. Mok, Y.-L. Wu, S. Thongprasert, C.-H. Yang, D.-T. Chu, N. Saijo, P. Sunpaweravong, B. Han, B. Margono, Y. Ichinose, *et al.*, "Gefitinib or carboplatin–paclitaxel in pulmonary adenocarcinoma," *New England Journal of Medicine*, vol. 361, no. 10, pp. 947–957, 2009.

[46] R. Rosell, E. Carcereny, R. Gervais, A. Vergnenegre, B. Massuti, E. Felip, R. Palmero, R. Garcia-Gomez, C. Pallares, J. M. Sanchez, *et al.*, "Erlotinib versus standard chemotherapy as first-line treatment for european patients with advanced egfr mutation-positive non-small-cell lung cancer

(eurtac): a multicentre, open-label, randomised phase 3 trial," *The lancet oncology*, vol. 13, no. 3, pp. 239–246, 2012.

[47] W. Pao, V. A. Miller, K. A. Politi, G. J. Riely, R. Somwar, M. F. Zakowski, M. G. Kris, and H. Varmus, "Acquired resistance of lung adenocarcinomas to gefitinib or erlotinib is associated with a second mutation in the egfr kinase domain," *PLoS medicine*, vol. 2, no. 3, p. e73, 2005.

[48] C.-H. Yun, K. E. Mengwasser, A. V. Toms, M. S. Woo, H. Greulich, K.-K. Wong, M. Meyerson, and M. J. Eck, "The t790m mutation in egfr kinase causes drug resistance by increasing the affinity for atp," *Proceedings of the National Academy of Sciences*, vol. 105, no. 6, pp. 2070–2075, 2008.

[49] L. V. Sequist, B. A. Waltman, D. Dias-Santagata, S. Digumarthy, A. B. Turke, P. Fidias, K. Bergethon, A. T. Shaw, S. Gettinger, A. K. Cosper, *et al.*, "Genotypic and histological evolution of lung cancers acquiring resistance to egfr inhibitors," *Science translational medicine*, vol. 3, no. 75, pp. 75ra26–75ra26, 2011.

[50] A. Y. Helena, M. E. Arcila, N. Rekhtman, C. S. Sima, M. F. Zakowski, W. Pao, M. G. Kris, V. A. Miller, M. Ladanyi, and G. J. Riely, "Analysis of tumor specimens at the time of acquired resistance to egfr-tki therapy in 155 patients with egfr-mutant lung cancers," *Clinical cancer research*, vol. 19, no. 8, pp. 2240–2247, 2013.

[51] Z. Chen, C. M. Fillmore, P. S. Hammerman, C. F. Kim, and K.-K. Wong, "Non-small-cell lung cancers: a heterogeneous set of diseases," *Nature Reviews Cancer*, vol. 14, no. 8, pp. 535–546, 2014.

[52] O. Warburg *et al.*, "On the origin of cancer cells," *Science*, vol. 123, no. 3191, pp. 309–314, 1956.

[53] R. Moreno-Sánchez, S. Rodríguez-Enríquez, A. Marín-Hernández, and E. Saavedra, "Energy metabolism in tumor cells," *Febs Journal*, vol. 274, no. 6, pp. 1393–1418, 2007.

[54] M. G. Vander Heiden, L. C. Cantley, and C. B. Thompson, "Understanding the warburg effect: the metabolic requirements of cell proliferation," *science*, vol. 324, no. 5930, pp. 1029–1033, 2009.

[55] R. J. DeBerardinis, J. J. Lum, G. Hatzivassiliou, and C. B. Thompson, "The biology of cancer: metabolic reprogramming fuels cell growth and proliferation," *Cell metabolism*, vol. 7, no. 1, pp. 11–20, 2008.

[56] A. A. Shestov, X. Liu, Z. Ser, A. A. Cluntun, Y. P. Hung, L. Huang, D. Kim, A. Le, G. Yellen, J. G. Albeck, *et al.*, "Quantitative determinants of aerobic glycolysis identify flux through the enzyme gapdh as a limiting step," *Elife*, vol. 3, p. e03342, 2014.

[57] T. Epstein, L. Xu, R. J. Gillies, and R. A. Gatenby, "Separation of metabolic supply and demand: aerobic glycolysis as a normal physiological response to fluctuating energetic demands in the membrane," *Cancer & metabolism*, vol. 2, no. 1, p. 7, 2014.

[58] R. A. Cairns, I. S. Harris, and T. W. Mak, "Regulation of cancer cell metabolism," *Nature Reviews Cancer*, vol. 11, no. 2, pp. 85–95, 2011.

[59] V. R. Fantin, J. St-Pierre, and P. Leder, "Attenuation of ldh-a expression uncovers a link between glycolysis, mitochondrial physiology, and tumor maintenance," *Cancer cell*, vol. 9, no. 6, pp. 425–434, 2006.

[60] M. V. Liberti and J. W. Locasale, "The warburg effect: how does it benefit cancer cells?," *Trends in biochemical sciences*, vol. 41, no. 3, pp. 211–218, 2016.

[61] T. Vander Borght, D. Labar, S. Pauwels, and L. Lambotte, "Production of [2-11c] thymidine for quantification of cellular proliferation with pet," *International Journal of Radiation Applications and Instrumentation. Part A. Applied Radiation and Isotopes*, vol. 42, no. 1, pp. 103–104, 1991.

[62] K. A. Krohn, D. A. Mankoff, and J. F. Eary, "Imaging cellular proliferation as a measure of response to therapy," *The Journal of Clinical Pharmacology*, vol. 41, no. S7, 2001.

[63] A. F. Shields, J. R. Grierson, B. M. Dohmen, H.-J. Machulla, J. C. Stayanoff, J. M. Lawhorn-Crews, J. E. Obradovich, O. Muzik, and T. J. Mangner, "Imaging proliferation in vivo with [f-18] flt and positron emission tomography," *Nature medicine*, vol. 4, no. 11, pp. 1334–1336, 1998.

[64] H. H. Coenen, P. Kling, and G. Stöcklin, "Cerebral metabolism of l-[2-18f] fluorotyrosine, a new pet tracer of protein synthesis.," *Journal of nuclear*

medicine: official publication, Society of Nuclear Medicine, vol. 30, no. 8, pp. 1367–1372, 1989.

[65] P. L. Jager, W. Vaalburg, J. Pruim, E. G. De Vries, K.-J. Langen, and D. A. Piers, "Radiolabeled amino acids: basic aspects and clinical applications in oncology," *Journal of nuclear medicine*, vol. 42, no. 3, pp. 432–445, 2001.

[66] T. Hara, N. Kosaka, and H. Kishi, "Pet imaging of prostate cancer using carbon-11-choline," *The Journal of Nuclear Medicine*, vol. 39, no. 6, p. 990, 1998.

[67] J. Kotzerke, J. Prang, B. Neumaier, B. Volkmer, A. Guhlmann, K. Kleinschmidt, R. Hautmann, and S. N. Reske, "Experience with carbon-11 choline positron emission tomography in prostate carcinoma," *European Journal of Nuclear Medicine and Molecular Imaging*, vol. 27, no. 9, pp. 1415–1419, 2000.

[68] D. T. Price, R. E. Coleman, R. P. Liao, C. N. Robertson, T. J. Polascik, and T. R. Degrado, "Comparison of [18 f] fluorocholine and [18 f] fluorodeoxyglucose for positron emission tomography of androgen dependent and androgen independent prostate cancer," *The Journal of urology*, vol. 168, no. 1, pp. 273–280, 2002.

[69] J. E. Cleaver, "Thymidine metabolism and cell kinetics," 1967.

[70] I. Tannock, "Cell proliferation," *The basic science of oncology*, pp. 154–177, 1992.

[71] C. N. Baumunk and D. L. Friedman, "Absence of an effect of amethopterin and 5-fluorodeoxyuridine upon levels of thymidine triphosphate in hela cells," *Cancer research*, vol. 31, no. 12, pp. 1930–1935, 1971.

[72] D. Kuebbing and R. Werner, "A model for compartmentation of de novo and salvage thymidine nucleotide pools in mammalian cells," *Proceedings of the National Academy of Sciences*, vol. 72, no. 9, pp. 3333–3336, 1975.

[73] E. T. McKinley, G. D. Ayers, R. A. Smith, S. A. Saleh, P. Zhao, M. K. Washington, R. J. Coffey, and H. C. Manning, "Limits of [18 f]-flt pet as a biomarker of proliferation in oncology," *PLoS One*, vol. 8, no. 3, p. e58938, 2013.

[74] V. Frings, A. A. van der Veldt, R. Boellaard, G. J. Herder, E. Giovannetti, R. Honeywell, G. J. Peters, E. Thunnissen, O. S. Hoekstra, and E. F. Smit, "Pemetrexed induced thymidylate synthase inhibition in non-small cell lung cancer patients: a pilot study with 3-deoxy-3-[18 f] fluorothymidine positron emission tomography," *PloS one*, vol. 8, no. 5, p. e63705, 2013.

[75] M. Murakami, S. Zhao, Y. Zhao, W. Yu, C. N. Fatema, K.-I. Nishijima, M. Yamasaki, M. Takiguchi, N. Tamaki, and Y. Kuge, "Increased intratumoral fluorothymidine uptake levels following multikinase inhibitor sorafenib treatment in a human renal cell carcinoma xenograft model," *Oncology letters*, vol. 6, no. 3, pp. 667–672, 2013.

[76] M. P. Schulman, "Purines and pyrimidines," *Metabolic pathways*, vol. 2, pp. 389–457, 1961.

[77] S. C. Hartman, "Purines and pyrimidines," *Metabolic pathways*, vol. 4, pp. 1–68, 1970.

[78] L. G. Hanson, "Is quantum mechanics necessary for understanding magnetic resonance?," *Concepts in Magnetic Resonance Part A*, vol. 32, no. 5, pp. 329–340, 2008.

[79] L. G. Hanson, "The ups and downs of classical and quantum formulations of magnetic resonance," in *Anthropic Awareness*, Elsevier Science, 2015.

[80] A. W. Overhauser, "Polarization of nuclei in metals," *Physical Review*, vol. 92, no. 2, p. 411, 1953.

[81] T. Carver and C. Slichter, "Polarization of nuclear spins in metals," *Physical Review*, vol. 92, no. 1, p. 212, 1953.

[82] A. Bornet, R. Melzi, A. J. Perez Linde, P. Hautle, B. van den Brandt, S. Jannin, and G. Bodenhausen, "Boosting dissolution dynamic nuclear polarization by cross polarization," *The journal of physical chemistry letters*, vol. 4, no. 1, pp. 111–114, 2012.

[83] B. Vuichoud, J. Milani, A. Bornet, R. Melzi, S. Jannin, and G. Bodenhausen, "Hyperpolarization of deuterated metabolites via remote cross-polarization and dissolution dynamic nuclear polarization," *The Journal of Physical Chemistry B*, vol. 118, no. 5, pp. 1411–1415, 2014.

[84] W. Happer, E. Miron, S. Schaefer, D. Schreiber, W. Van Wijngaarden, and X. Zeng, "Polarization of the nuclear spins of noble-gas atoms by spin exchange with optically pumped alkali-metal atoms," *Physical Review A*, vol. 29, no. 6, p. 3092, 1984.

[85] T. G. Walker and W. Happer, "Spin-exchange optical pumping of noble-gas nuclei," *Reviews of Modern Physics*, vol. 69, no. 2, p. 629, 1997.

[86] S. Appelt, A. B.-A. Baranga, C. Erickson, M. Romalis, A. Young, and W. Happer, "Theory of spin-exchange optical pumping of 3 he and 129 xe," *Physical Review A*, vol. 58, no. 2, p. 1412, 1998.

[87] C. R. Bowers and D. P. Weitekamp, "Transformation of symmetrization order to nuclear-spin magnetization by chemical reaction and nuclear magnetic resonance," *Physical Review Letters*, vol. 57, no. 21, p. 2645, 1986.

[88] C. R. Bowers and D. P. Weitekamp, "Parahydrogen and synthesis allow dramatically enhanced nuclear alignment," *Journal of the American Chemical Society*, vol. 109, no. 18, pp. 5541–5542, 1987.

[89] M. G. Pravica and D. P. Weitekamp, "Net nmr alignment by adiabatic transport of parahydrogen addition products to high magnetic field," *Chemical physics letters*, vol. 145, no. 4, pp. 255–258, 1988.

[90] M. Haake, J. Natterer, and J. Bargon, "Efficient nmr pulse sequences to transfer the parahydrogen-induced polarization to hetero nuclei," *Journal of the American Chemical Society*, vol. 118, no. 36, pp. 8688–8691, 1996.

[91] K. Golman, O. Axelsson, H. Jóhannesson, S. Månsson, C. Olofsson, and J. Petersson, "Parahydrogen-induced polarization in imaging: Subsecond 13c angiography," *Magnetic resonance in medicine*, vol. 46, no. 1, pp. 1–5, 2001.

[92] M. Goldman, H. Jóhannesson, O. Axelsson, and M. Karlsson, "Hyperpolarization of 13 c through order transfer from parahydrogen: a new contrast agent for mri," *Magnetic resonance imaging*, vol. 23, no. 2, pp. 153–157, 2005.

[93] R. W. Adams, J. A. Aguilar, K. D. Atkinson, M. J. Cowley, P. I. Elliott, S. B. Duckett, G. G. Green, I. G. Khazal, J. López-Serrano, and D. C. Williamson, "Reversible interactions with para-hydrogen enhance nmr

sensitivity by polarization transfer," *Science*, vol. 323, no. 5922, pp. 1708–1711, 2009.

[94] J. Natterer and J. Bargon, "Parahydrogen induced polarization," *Progress in Nuclear Magnetic Resonance Spectroscopy*, vol. 31, no. 4, pp. 293–315, 1997.

[95] T. Can, Q. Ni, and R. Griffin, "Mechanisms of dynamic nuclear polarization in insulating solids," *Journal of Magnetic Resonance*, vol. 253, pp. 23–35, 2015.

[96] B. Corzilius, "Theory of solid effect and cross effect dynamic nuclear polarization with half-integer high-spin metal polarizing agents in rotating solids," *Physical Chemistry Chemical Physics*, vol. 18, no. 39, pp. 27190–27204, 2016.

[97] T. Harris, H. Degani, and L. Frydman, "Hyperpolarized 13c nmr studies of glucose metabolism in living breast cancer cell cultures," *NMR in Biomedicine*, vol. 26, no. 12, pp. 1831–1843, 2013.

[98] H. Allouche-Arnon, T. Wade, L. F. Waldner, V. N. Miller, J. M. Gomori, R. Katz-Brull, and C. A. McKenzie, "In vivo magnetic resonance imaging of glucose–initial experience," *Contrast media & molecular imaging*, vol. 8, no. 1, pp. 72–82, 2013.

[99] T. B. Rodrigues, E. M. Serrao, B. W. Kennedy, D.-E. Hu, M. I. Kettunen, and K. M. Brindle, "Magnetic resonance imaging of tumor glycolysis using hyperpolarized 13c-labeled glucose," *Nature medicine*, vol. 20, no. 1, pp. 93–97, 2014.

[100] K. R. Keshari, D. M. Wilson, A. P. Chen, R. Bok, P. E. Larson, S. Hu, M. V. Criekinge, J. M. Macdonald, D. B. Vigneron, and J. Kurhanewicz, "Hyperpolarized [2-13c]-fructose: a hemiketal dnp substrate for in vivo metabolic imaging," *Journal of the American Chemical Society*, vol. 131, no. 48, pp. 17591–17596, 2009.

[101] F. A. Gallagher, M. I. Kettunen, S. E. Day, M. Lerche, and K. M. Brindle, "13c mr spectroscopy measurements of glutaminase activity in human hepatocellular carcinoma cells using hyperpolarized 13c-labeled glutamine," *Magnetic resonance in medicine*, vol. 60, no. 2, pp. 253–257, 2008.

[102] C. Cabella, M. Karlsson, C. Canape, G. Catanzaro, S. C. Serra, L. Miragoli, L. Poggi, F. Uggeri, L. Venturi, P. Jensen, *et al.*, "In vivo and in vitro liver cancer metabolism observed with hyperpolarized [5-13 c] glutamine," *Journal of Magnetic Resonance*, vol. 232, pp. 45–52, 2013.

[103] M. Karlsson, P. R. Jensen, A. Gisselsson, G. Hansson, J. Ø. Duus, S. Meier, M. H. Lerche, *et al.*, "Imaging of branched chain amino acid metabolism in tumors with hyperpolarized 13c ketoisocaproate," *International journal of cancer*, vol. 127, no. 3, pp. 729–736, 2010.

[104] S. E. Bohndiek, M. I. Kettunen, D.-e. Hu, B. W. Kennedy, J. Boren, F. A. Gallagher, and K. M. Brindle, "Hyperpolarized [1-13c]-ascorbic and dehydroascorbic acid: vitamin c as a probe for imaging redox status in vivo," *Journal of the American Chemical Society*, vol. 133, no. 30, pp. 11795–11801, 2011.

[105] K. R. Keshari, J. Kurhanewicz, R. Bok, P. E. Larson, D. B. Vigneron, and D. M. Wilson, "Hyperpolarized 13c dehydroascorbate as an endogenous redox sensor for in vivo metabolic imaging," *Proceedings of the National Academy of Sciences*, vol. 108, no. 46, pp. 18606–18611, 2011.

[106] K. R. Keshari, V. Sai, Z. J. Wang, H. F. VanBrocklin, J. Kurhanewicz, and D. M. Wilson, "Hyperpolarized [1-13c] dehydroascorbate mr spectroscopy in a murine model of prostate cancer: comparison with 18f-fdg pet," *Journal of Nuclear Medicine*, vol. 54, no. 6, pp. 922–928, 2013.

[107] F. A. Gallagher, M. I. Kettunen, S. E. Day, D.-E. Hu, J. H. Ardenkjær-Larsen, P. R. Jensen, M. Karlsson, K. Golman, M. H. Lerche, K. M. Brindle, *et al.*, "Magnetic resonance imaging of ph in vivo using hyperpolarized 13c-labelled bicarbonate," *Nature*, vol. 453, no. 7197, pp. 940–943, 2008.

[108] D. J. Scholz, M. A. Janich, U. Köllisch, R. F. Schulte, J. H. Ardenkjaer-Larsen, A. Frank, A. Haase, M. Schwaiger, and M. I. Menzel, "Quantified ph imaging with hyperpolarized 13c-bicarbonate," *Magnetic resonance in medicine*, vol. 73, no. 6, pp. 2274–2282, 2015.

[109] I. Park, P. E. Larson, M. L. Zierhut, S. Hu, R. Bok, T. Ozawa, J. Kurhanewicz, D. B. Vigneron, S. R. VandenBerg, C. D. James, *et al.*, "Hyperpolarized 13c magnetic resonance metabolic imaging: application to brain tumors," *Neuro-oncology*, vol. 12, no. 2, pp. 133–144, 2010.

[110] Y.-F. Yen, P. Le Roux, D. Mayer, R. King, D. Spielman, J. Tropp, K. Butts Pauly, A. Pfefferbaum, S. Vasanawala, and R. Hurd, "T2 relaxation times of 13c metabolites in a rat hepatocellular carcinoma model measured in vivo using 13c-mrs of hyperpolarized [1-13c] pyruvate," *NMR in Biomedicine*, vol. 23, no. 4, pp. 414–423, 2010.

[111] C. S. Ward, H. S. Venkatesh, M. M. Chaumeil, A. H. Brandes, M. VanCriekinge, H. Dafni, S. Sukumar, S. J. Nelson, D. B. Vigneron, J. Kurhanewicz, *et al.*, "Noninvasive detection of target modulation following phosphatidylinositol 3-kinase inhibition using hyperpolarized 13c magnetic resonance spectroscopy," *Cancer research*, vol. 70, no. 4, pp. 1296–1305, 2010.

[112] H. Dafni, P. E. Larson, S. Hu, H. A. Yoshihara, C. S. Ward, H. S. Venkatesh, C. Wang, X. Zhang, D. B. Vigneron, and S. M. Ronen, "Hyperpolarized 13c spectroscopic imaging informs on hypoxia-inducible factor-1 and myc activity downstream of platelet-derived growth factor receptor," *Cancer research*, vol. 70, no. 19, pp. 7400–7410, 2010.

[113] S. E. Day, M. I. Kettunen, M. K. Cherukuri, J. B. Mitchell, M. J. Lizak, H. D. Morris, S. Matsumoto, A. P. Koretsky, and K. M. Brindle, "Detecting response of rat c6 glioma tumors to radiotherapy using hyperpolarized [1-13c] pyruvate and 13c magnetic resonance spectroscopic imaging," *Magnetic resonance in medicine*, vol. 65, no. 2, pp. 557–563, 2011.

[114] S. E. Bohndiek, M. I. Kettunen, D.-e. Hu, T. H. Witney, B. W. Kennedy, F. A. Gallagher, and K. M. Brindle, "Detection of tumor response to a vascular disrupting agent by hyperpolarized 13c magnetic resonance spectroscopy," *Molecular cancer therapeutics*, vol. 9, no. 12, pp. 3278–3288, 2010.

[115] G. Lin, G. Andrejeva, A.-C. W. Te Fong, D. K. Hill, M. R. Orton, H. G. Parkes, D.-M. Koh, S. P. Robinson, M. O. Leach, T. R. Eykyn, *et al.*, "Reduced warburg effect in cancer cells undergoing autophagy: steady-state 1 h-mrs and real-time hyperpolarized 13 c-mrs studies," *PloS one*, vol. 9, no. 3, p. e92645, 2014.

[116] I. Park, J. Mukherjee, M. Ito, M. M. Chaumeil, L. E. Jalbert, K. Gaensler, S. M. Ronen, S. J. Nelson, and R. O. Pieper, "Changes in pyruvate metabolism detected by magnetic resonance imaging are linked to dna

damage and serve as a sensor of temozolomide response in glioblastoma cells," *Cancer research*, vol. 74, no. 23, pp. 7115–7124, 2014.

[117] A. Lodi, S. M. Woods, and S. M. Ronen, "Treatment with the mek inhibitor u0126 induces decreased hyperpolarized pyruvate to lactate conversion in breast, but not prostate, cancer cells," *NMR in biomedicine*, vol. 26, no. 3, pp. 299–306, 2013.

[118] K. Saito, S. Matsumoto, Y. Takakusagi, M. Matsuo, H. D. Morris, M. J. Lizak, J. P. Munasinghe, N. Devasahayam, S. Subramanian, J. B. Mitchell, *et al.*, "13c-mr spectroscopic imaging with hyperpolarized [1-13c] pyruvate detects early response to radiotherapy in scc tumors and ht-29 tumors," *Clinical Cancer Research*, vol. 21, no. 22, pp. 5073–5081, 2015.

[119] A. L. Edinger, C. B. Thompson, "Death by design: apoptosis, necrosis and autophagy," *Current opinion in cell biology*, vol. 16, no. 6, pp. 663–669, 2004.

[120] H. Akiyama, S. Barger, S. Barnum, B. Bradt, J. Bauer, G. Cole, N. Cooper, P. Eikelenboom, M. Emmerling, B. Fiebich, *et al.*, "Webster. s.; wegrzyniak, b.; wenk, g.; wyss-coray, t," *Inflammation and Alzheimer's disease. Neurobiol. Aging*, vol. 21, no. 3, pp. 383–421, 2000.

[121] C. Cosi, H. Suzuki, D. Milani, L. Facci, M. Menegazzi, G. Vantini, Y. Kanai, and S. Skaper, "Poly (adp-ribose) polymerase: Early involvement in glutamate-induced neurotoxicity in cultured cerebellar granule cells," *Journal of neuroscience research*, vol. 39, no. 1, pp. 38–46, 1994.

[122] L. Colletti, D. Remick, G. Burtch, S. Kunkel, R. Strieter, and D. Campbell Jr, "Role of tumor necrosis factor-alpha in the pathophysiologic alterations after hepatic ischemia/reperfusion injury in the rat.," *Journal of Clinical Investigation*, vol. 85, no. 6, p. 1936, 1990.

[123] M. A. Brennan and B. T. Cookson, "Salmonella induces macrophage death by caspase-1-dependent necrosis," *Molecular microbiology*, vol. 38, no. 1, pp. 31–40, 2000.

[124] M. J. Lenardo, S. B. Angleman, V. Bounkeua, J. Dimas, M. G. Duvall, M. B. Graubard, F. Hornung, M. C. Selkirk, C. K. Speirs, C. Trageser, *et al.*, "Cytopathic killing of peripheral blood cd4+ t lymphocytes by human immunodeficiency virus type 1 appears necrotic rather than apoptotic

and does not require env," *Journal of virology*, vol. 76, no. 10, pp. 5082–5093, 2002.

[125] W. Murdoch, C. Wilken, and D. Young, "Sequence of apoptosis and inflammatory necrosis within the formative ovulatory site of sheep follicles," *Journal of reproduction and fertility*, vol. 117, no. 2, pp. 325–329, 1999.

[126] M. Chautan, G. Chazal, F. Cecconi, P. Gruss, and P. Golstein, "Interdigital cell death can occur through a necrotic and caspase-independent pathway," *Current biology*, vol. 9, no. 17, pp. 967–S1, 1999.

[127] G. Di Chiro, E. Oldfield, D. C. Wright, D. De Michele, D. A. Katz, N. J. Patronas, J. Doppman, S. Larson, M. Ito, and C. Kufta, "Cerebral necrosis after radiotherapy and/or intraarterial chemotherapy for brain tumors: Pet and neuropathologic studies," *American Journal of Roentgenology*, vol. 150, no. 1, pp. 189–197, 1988.

[128] P. Picci, T. Böhling, G. Bacci, S. Ferrari, L. Sangiorgi, M. Mercuri, P. Ruggieri, M. Manfrini, A. Ferraro, R. Casadei, *et al.*, "Chemotherapy-induced tumor necrosis as a prognostic factor in localized ewing's sarcoma of the extremities.," *Journal of Clinical Oncology*, vol. 15, no. 4, pp. 1553–1559, 1997.

[129] A. J. Kumar, N. E. Leeds, G. N. Fuller, P. Van Tassel, M. H. Maor, R. E. Sawaya, and V. A. Levin, "Malignant gliomas: mr imaging spectrum of radiation therapy-and chemotherapy-induced necrosis of the brain after treatment 1," *Radiology*, vol. 217, no. 2, pp. 377–384, 2000.

[130] Y.-l. Chan, D. K. Yeung, S.-f. Leung, and P.-n. Chan, "Diffusion-weighted magnetic resonance imaging in radiation-induced cerebral necrosis: apparent diffusion coefficient in lesion components," *Journal of computer assisted tomography*, vol. 27, no. 5, pp. 674–680, 2003.

[131] I. R. Kamel, D. A. Bluemke, D. Ramsey, M. Abusedera, M. Torbenson, J. Eng, G. Szarf, and J.-F. Geschwind, "Role of diffusion-weighted imaging in estimating tumor necrosis after chemoembolization of hepatocellular carcinoma," *American Journal of Roentgenology*, vol. 181, no. 3, pp. 708–710, 2003.

[132] H. Lyng, O. Haraldseth, and E. K. Rofstad, "Measurement of cell density and necrotic fraction in human melanoma xenografts by diffusion weighted

magnetic resonance imaging," *Magnetic resonance in medicine*, vol. 43, no. 6, pp. 828–836, 2000.

[133] D. A. Hamstra, A. Rehemtulla, and B. D. Ross, "Diffusion magnetic resonance imaging: a biomarker for treatment response in oncology," *Journal of clinical oncology*, vol. 25, no. 26, pp. 4104–4109, 2007.

[134] H. C. Thoeny and B. D. Ross, "Predicting and monitoring cancer treatment response with diffusion-weighted mri," *Journal of Magnetic Resonance Imaging*, vol. 32, no. 1, pp. 2–16, 2010.

[135] K. M. Brindle, S. E. Bohndiek, F. A. Gallagher, and M. I. Kettunen, "Tumor imaging using hyperpolarized 13c magnetic resonance spectroscopy," *Magnetic resonance in medicine*, vol. 66, no. 2, pp. 505–519, 2011.

[136] T. R. Brown, B. Kincaid, and K. Ugurbil, "Nmr chemical shift imaging in three dimensions," *Proceedings of the National Academy of Sciences*, vol. 79, no. 11, pp. 3523–3526, 1982.

[137] A. Maudsley, S. Hilal, W. Perman, and H. Simon, "Spatially resolved high resolution spectroscopy by "four-dimensional" nmr," *Journal of Magnetic Resonance (1969)*, vol. 51, no. 1, pp. 147–152, 1983.

[138] C. H. Cunningham, D. B. Vigneron, A. P. Chen, D. Xu, S. J. Nelson, R. E. Hurd, D. A. Kelley, and J. M. Pauly, "Design of flyback echo-planar readout gradients for magnetic resonance spectroscopic imaging," *Magnetic resonance in medicine*, vol. 54, no. 5, pp. 1286–1289, 2005.

[139] C. H. Cunningham, A. P. Chen, M. J. Albers, J. Kurhanewicz, R. E. Hurd, Y.-F. Yen, J. M. Pauly, S. J. Nelson, and D. B. Vigneron, "Double spin-echo sequence for rapid spectroscopic imaging of hyperpolarized 13 c," *Journal of Magnetic Resonance*, vol. 187, no. 2, pp. 357–362, 2007.

[140] P. E. Larson, A. B. Kerr, A. P. Chen, M. S. Lustig, M. L. Zierhut, S. Hu, C. H. Cunningham, J. M. Pauly, J. Kurhanewicz, and D. B. Vigneron, "Multiband excitation pulses for hyperpolarized 13 c dynamic chemical-shift imaging," *Journal of magnetic resonance*, vol. 194, no. 1, pp. 121–127, 2008.

[141] Y.-F. Yen, S. Kohler, A. Chen, J. Tropp, R. Bok, J. Wolber, M. Albers, K. Gram, M. Zierhut, I. Park, *et al.*, "Imaging considerations for in vivo

13c metabolic mapping using hyperpolarized 13c-pyruvate," *Magnetic resonance in medicine*, vol. 62, no. 1, pp. 1–10, 2009.

[142] P. E. Larson, R. Bok, A. B. Kerr, M. Lustig, S. Hu, A. P. Chen, S. J. Nelson, J. M. Pauly, J. Kurhanewicz, and D. B. Vigneron, "Investigation of tumor hyperpolarized [1-13c]-pyruvate dynamics using time-resolved multiband rf excitation echo-planar mrsi," *Magnetic resonance in medicine*, vol. 63, no. 3, pp. 582–591, 2010.

[143] J. Leupold, O. Wieben, S. Månsson, O. Speck, K. Scheffler, J. S. Petersson, and J. Hennig, "Fast chemical shift mapping with multiecho balanced ssfp," *Magnetic Resonance Materials in Physics, Biology and Medicine*, vol. 19, no. 5, pp. 267–273, 2006.

[144] J. Leupold, S. Månsson, J. S. Petersson, J. Hennig, and O. Wieben, "Fast multiecho balanced ssfp metabolite mapping of 1h and hyperpolarized 13c compounds," *Magnetic Resonance Materials in Physics, Biology and Medicine*, vol. 22, no. 4, pp. 251–256, 2009.

[145] W. H. Perman, P. Bhattacharya, J. Leupold, A. P. Lin, K. C. Harris, V. A. Norton, J.-B. Hövener, and B. D. Ross, "Fast volumetric spatial-spectral mr imaging of hyperpolarized 13 c-labeled compounds using multiple echo 3d bssfp," *Magnetic resonance imaging*, vol. 28, no. 4, pp. 459–465, 2010.

[146] D. Mayer, Y.-F. Yen, Y. S. Levin, J. Tropp, A. Pfefferbaum, R. E. Hurd, and D. M. Spielman, "In vivo application of sub-second spiral chemical shift imaging (csi) to hyperpolarized 13 c metabolic imaging: comparison with phase-encoded csi," *Journal of Magnetic Resonance*, vol. 204, no. 2, pp. 340–345, 2010.

[147] S. Josan, Y.-F. Yen, R. Hurd, A. Pfefferbaum, D. Spielman, and D. Mayer, "Application of double spin echo spiral chemical shift imaging to rapid metabolic mapping of hyperpolarized [1- 13 c]-pyruvate," *Journal of Magnetic Resonance*, vol. 209, no. 2, pp. 332–336, 2011.

[148] S. Josan, R. Hurd, J. M. Park, Y.-F. Yen, R. Watkins, A. Pfefferbaum, D. Spielman, and D. Mayer, "Dynamic metabolic imaging of hyperpolarized [2-13c] pyruvate using spiral chemical shift imaging with alternating spectral band excitation," *Magnetic resonance in medicine*, vol. 71, no. 6, pp. 2051–2058, 2014.

[149] J. M. Park, S. Josan, T. Jang, M. Merchant, R. Watkins, R. E. Hurd, L. D. Recht, D. Mayer, and D. M. Spielman, "Volumetric spiral chemical shift imaging of hyperpolarized [2-13c] pyruvate in a rat c6 glioma model," *Magnetic resonance in medicine*, vol. 75, no. 3, pp. 973–984, 2016.

[150] F. Wiesinger, E. Weidl, M. I. Menzel, M. A. Janich, O. Khegai, S. J. Glaser, A. Haase, M. Schwaiger, and R. F. Schulte, "Ideal spiral csi for dynamic metabolic mr imaging of hyperpolarized [1-13c] pyruvate," *Magnetic resonance in medicine*, vol. 68, no. 1, pp. 8–16, 2012.

[151] J. Tropp, J. M. Lupo, A. Chen, P. Calderon, D. McCune, T. Grafendorfer, E. Ozturk-Isik, P. E. Larson, S. Hu, Y.-F. Yen, *et al.*, "Multi-channel metabolic imaging, with sense reconstruction, of hyperpolarized [1-13 c] pyruvate in a live rat at 3.0 tesla on a clinical mr scanner," *Journal of magnetic resonance*, vol. 208, no. 1, pp. 171–177, 2011.

[152] P. E. Larson, S. Hu, M. Lustig, A. B. Kerr, S. J. Nelson, J. Kurhanewicz, J. M. Pauly, and D. B. Vigneron, "Fast dynamic 3d mr spectroscopic imaging with compressed sensing and multiband excitation pulses for hyperpolarized 13c studies," *Magnetic resonance in medicine*, vol. 65, no. 3, pp. 610–619, 2011.

[153] M. Durst, U. Koellisch, A. Frank, G. Rancan, C. V. Gringeri, V. Karas, F. Wiesinger, M. I. Menzel, M. Schwaiger, A. Haase, *et al.*, "Comparison of acquisition schemes for hyperpolarised 13c imaging," *NMR in Biomedicine*, vol. 28, no. 6, pp. 715–725, 2015.

[154] H. Bruder, H. Fischer, H.-E. Reinfelder, and F. Schmitt, "Image reconstruction for echo planar imaging with nonequidistant k-space sampling," *Magnetic resonance in medicine*, vol. 23, no. 2, pp. 311–323, 1992.

[155] Y. P. Du, X. Joe Zhou, and M. A. Bernstein, "Correction of concomitant magnetic field-induced image artifacts in nonaxial echo-planar imaging," *Magnetic resonance in medicine*, vol. 48, no. 3, pp. 509–515, 2002.

[156] J. W. Gordon, D. B. Vigneron, and P. E. Larson, "Development of a symmetric echo planar imaging framework for clinical translation of rapid dynamic hyperpolarized 13c imaging," *Magnetic resonance in medicine*, 2016.

[157] J. M. Lupo, A. P. Chen, M. L. Zierhut, R. A. Bok, C. H. Cunningham, J. Kurhanewicz, D. B. Vigneron, and S. J. Nelson, "Analysis of hyperpolarized dynamic 13 c lactate imaging in a transgenic mouse model of prostate cancer," *Magnetic resonance imaging*, vol. 28, no. 2, pp. 153–162, 2010.

[158] W. Jiang, M. Lustig, and P. E. Larson, "Concentric rings k-space trajectory for hyperpolarized 13c mr spectroscopic imaging," *Magnetic resonance in medicine*, vol. 75, no. 1, pp. 19–31, 2016.

[159] L. G. Hanson, K. Schaumburg, and O. B. Paulson, "Reconstruction strategy for echo planar spectroscopy and its application to partially undersampled imaging," *Magnetic resonance in medicine*, vol. 44, no. 3, pp. 412–417, 2000.

[160] G. Metzger and X. Hu, "Application of interlaced fourier transform to echo-planar spectroscopic imaging," *Journal of Magnetic Resonance*, vol. 125, no. 1, pp. 166–170, 1997.

[161] H. Jadvar and P. M. Colletti, "Competitive advantage of pet/mri," *European journal of radiology*, vol. 83, no. 1, pp. 84–94, 2014.

[162] T. H. Witney, M. I. Kettunen, S. E. Day, D.-e. Hu, A. A. Neves, F. A. Gallagher, S. M. Fulton, and K. M. Brindle, "A comparison between radiolabeled fluorodeoxyglucose uptake and hyperpolarized 13c-labeled pyruvate utilization as methods for detecting tumor response to treatment," *Neoplasia*, vol. 11, no. 6, pp. 574IN11–582, 2009.

[163] A. Zannetti, F. Iommelli, A. Speranza, M. Salvatore, and S. Del Vecchio, "3-deoxy-3-18f-fluorothymidine pet/ct to guide therapy with epidermal growth factor receptor antagonists and bcl-xl inhibitors in non–small cell lung cancer," *Journal of Nuclear Medicine*, vol. 53, no. 3, pp. 443–450, 2012.

[164] R. T. Ullrich, T. Zander, B. Neumaier, M. Koker, T. Shimamura, Y. Waerzeggers, C. L. Borgman, S. Tawadros, H. Li, M. L. Sos, *et al.*, "Early detection of erlotinib treatment response in nsclc by 3-deoxy-3-[18 f]-fluoro-l-thymidine ([18 f] flt) positron emission tomography (pet)," *PloS one*, vol. 3, no. 12, p. e3908, 2008.

[165] S. Hu, A. Balakrishnan, R. A. Bok, B. Anderton, P. E. Larson, S. J. Nelson, J. Kurhanewicz, D. B. Vigneron, and A. Goga, "13 c-pyruvate imaging reveals alterations in glycolysis that precede c-myc-induced tumor formation and regression," *Cell metabolism*, vol. 14, no. 1, pp. 131–142, 2011.

[166] I. Park, P. E. Larson, J. L. Tropp, L. Carvajal, G. Reed, R. Bok, F. Robb, J. Bringas, A. Kells, P. Pivirotto, *et al.*, "Dynamic hyperpolarized carbon-13 mr metabolic imaging of nonhuman primate brain," *Magnetic resonance in medicine*, vol. 71, no. 1, pp. 19–25, 2014.

[167] F. K.-M. Chan, K. Moriwaki, and M. J. De Rosa, "Detection of necrosis by release of lactate dehydrogenase activity," *Immune Homeostasis: Methods and Protocols*, pp. 65–70, 2013.

[168] S. I. Grivennikov, F. R. Greten, and M. Karin, "Immunity, inflammation, and cancer," *Cell*, vol. 140, no. 6, pp. 883–899, 2010.

[169] K. E. De Visser, A. Eichten, and L. M. Coussens, "Paradoxical roles of the immune system during cancer development," *Nature reviews cancer*, vol. 6, no. 1, pp. 24–37, 2006.

[170] R. Pohmann, M. von Kienlin, and a. Haase, "Theoretical evaluation and comparison of fast chemical shift imaging methods.," *Journal of magnetic resonance (San Diego, Calif. : 1997)*, vol. 129, no. 2, pp. 145–160, 1997.

[171] J. Pipe and J. L. Duerk, "Analytical resolution and noise characteristics of linearly reconstructed magnetic resonance data with arbitraryk???space sampling," *Magnetic Resonance in Medicine*, vol. 34, no. 2, pp. 170–178, 1995.

Appendices

A

Treatment response in non-small-cell lung cancer estimated with hyperpolarized ^{13}C pyruvate, FLT- and FDG-PET

The following paper is currently in preparation for submission to *Cancer Research*.

Treatment response in non-small-cell lung cancer estimated with hyperpolarized ^{13}C pyruvate, FLT- and FDG-PET.

Running title (57/60): Treatment response in xenografts using 13C-MRS, FLT- and FDG-PET.

Andreas E Clemmensen[1,3,¥], Carsten H Nielsen[1,¥], Abubakr Eldirdiri[2,3,¥], Lotte K Kristensen[1], Kasper W Lipsø[2,3], Mette H Lauritzen[3], Lise V Søgaard[3,†], Jan Henrik Ardenkjær-Larsen[2,3,4], Andreas Kjær[1,*]

¥ These authors contributed equally to this work.

1. Department of Clinical Physiology, Nuclear Medicine and PET, Rigshospitalet, Cluster for Molecular Imaging, Department of Biomedical Medical Sciences, University of Copenhagen, Denmark
2. Department of Electrical Engineering, Technical University of Denmark, Kgs Lyngby, Denmark
3. Danish Research Center for Magnetic Resonance, Copenhagen University Hospital Hvidovre, Denmark
4. GE Healthcare, Copenhagen, Denmark

* Corresponding author: Professor Andreas Kjær, akjaer@sund.ku.dk

The authors disclose no potential conflicts of interest.

Keywords (5): Hyperpolarized 13C, FDG-PET, FLT-PET, treatment response, cancer.

Word count: 4227/5000

Abstract (203/250 words)

Treatment of non-small-cell lung cancer (NSCLC) using tyrosine-kinase inhibitors (TKI) like Erlotinib, targeting the epidermal growth factor receptor (EGFR) is being established as a routine clinical treatment. Here, we demonstrate that the treatment response can be identified using hyperpolarized [1-^{13}C]pyruvate-MRS, FLT-PET and FDG-PET in xenograft NSCLC tumors, probing different glycolytic steps as well as proliferation.

We show here a significant reduction in tumor lactate levels obtained by MRS, as well as lower FLT- and FDG-PET uptake in HCC-827 tumors treated with Erlotinib, compared to untreated tumors. Similarly, reduction in signal/ uptake was also observed for [1-^{13}C]pyruvate and was most pronounced in FLT-PET. H-1975 tumors, which harbor a second EGFR mutation, yielding them insensitive to Erlotinib, showed no difference in either tumor lactate levels, FLT- or FDG-PET uptake with treatment. These findings were validated ex-vivo, demonstrating significantly lower LDH activity levels and Ki-67 IHC staining in treated HCC-827 tumors compared to untreated. Furthermore, the LDH activity levels found ex-vivo correlated to the lactate levels found using [1-^{13}C]pyruvate-MRS, an important validation of the technique. Finally, we performed two injections for several mice, in order to evaluate the robustness of [1-^{13}C]pyruvate-MRS, which showed a strong correlation. Our findings indicate the [1-^{13}C]pyruvate-MRS could replace FDG-PET in a combined PET/MRI examination.

Introduction

The scientific understanding of the complex individualism of cancer has grown immensely in the last years, thereby marking the coming of the personalized medicine paradigm. Traditionally, treatment response in cancer has been evaluated using anatomical imaging following the RESIST criteria (1), which is neither a very specific nor an early measure (2). Functional imaging has the potential to overcome these issues, and Positron Emission Tomography (PET) is a pivotal imaging modality in this setting. The continuous development of new PET tracers enables better diagnostics, staging and monitoring of treatment response.

The workhorse of modern clinical PET imaging is 2'-deoxy-2'-[^{18}F]fluoro-D-glucose (FDG), which is used as a marker of glucose uptake. More specifically, it reflects the up-regulation of glucose transporters and hexokinase activity due to the ineffective, anaerobic metabolism observed in many cancer cells (3). The nature of the FDG tracer yields some limitations, however; high natural- or inflammation-induced background uptake can cloud the contrast and ultimately lead to false positive findings. 3'-deoxy-3'-[^{18}F]fluorothymidine (FLT) is a thymidine analog, which is intracellularly trapped after phosphorylation by thymidine kinase 1 (TK-1). TK-1 is responsible of the thymidine salvage pathway of DNA synthesis, making FLT a marker of TK-1 activity, and thereby to some extent cell proliferation (4). This newer tracer has previously been shown to be able to predict treatment response within 24 hours in a xenograft model similar to the one used in the present work (5-10). More recent, FLT has been incorporated into the clinical routine for evaluation of treatment response (11-13).

Magnetic Resonance Imaging (MRI) is similarly superior with respect to anatomical imaging. Its functional cousin, Magnetic Resonance Spectroscopy (MRS) is a powerful

modality, but with limited clinical acceptance, primarily due to relatively low sensitivity (14). MRS of ^{13}C-enhanced molecules has shown the ability to non-invasively probe the metabolic profile (15,16). This is facilitated by the use of Dynamic Nuclear Polarization (DNP) techniques that increase the MR sensitivity by more than 10,000-fold compared to thermal equilibrium, and allows for the hyperpolarized agents to be injected and imaged *in-vivo* (17). The use of ^{13}C-enhanced pyruvate, which lies at a crossroad of major metabolic pathways, has been of particular interest (18-20) and most studies have shown elevated levels of lactate in some cancers compared to non-malignant tissue (21). This can be explained by the Warburg effect, in which neoplastic cells use inefficient anaerobic glycolysis for energy instead of mitochondrial metabolism, despite sufficient supplies of oxygen.

Lately, combination of MRS of hyperpolarized ^{13}C-labelled substrates and PET has emerged as a promising tool in the understanding of cancer biology [Gutte H]. This work aims to evaluate these two modalities and present a comparison between hyperpolarized ^{13}C-MRS and FDG- and FLT-PET in monitoring the treatment response of two non-small-cell lung carcinoma (NSCLC) xenograft tumor mouse models (HCC-827 and NCI-H1975). HCC827 have previously been shown to elicit a high response to inhibition of the epidermal growth factor receptor (EGFR) by tyrosine kinase 1 (TK1) inhibitors, such as gefitinib or erlotinib, whereas H-1975 shows little response to similar treatment, due to a secondary mutation (24).

Materials and Methods

Cell culturing and animal preparation

Human HCC-827 and H-1975 non-small cell lung carcinoma cells were obtained from ATCC and cultured in RPMI-1640 media with GlutaMAX (Life Technologies) supplemented with 10% fetal calf serum (Biological Industries) and 1% penicillin-streptomycin (Gibco, Life Technologies) in 5% CO2 at 37 °C.

All animal care and experimental procedures were performed under the approval of the Animal Experiments Inspectorate in Denmark. Nude NMRI mice (n = 58) (Taconic, Denmark) weighing about 20-25 g were inoculated with 2 x $5 \cdot 10^6$ cells in 100 µl media and matrigel (1:1) subcutaneously in the flank region. Tumor growth was monitored twice a week by caliper measurement.

When the tumors reached a size of about 300 mm^3 (8-10 mm diameter, about 5 weeks after inoculation), the mice were randomized in two groups, one for PET imaging and one for DNP-MRS. Each group was again randomly divided into two subgroups, one to receive treatment, the other to receive vehicle. 24 hours before scanning, the mice received an oral gavage of either the tyrosine kinase 1 inhibitor Erlotinib (50 mg/kg, 100 µL (PBS, 0.5% Tween 20)) or vehicle (PBS, 0.5% Tween 20) dose (same volume). The animals were fasted overnight before scanning in order to reduce background uptake.

Hyperpolarization and MRI/MRS acquisition

The pyruvate sample was prepared by mixing ^{13}C pyruvic acid (Sigma Aldrich, denmark) with trityl radical OX063 (Oxford Instruments, UK) and Dotarem (Guerbet,France) to achieve concentrations of 14 M, 15 mM, and 1.5 mM for the three substances respectively. 20 uL (~26 mg) of the sample was polarized in a HyperSense polarizer

(Oxford Instruments, UK) and then dissolved in neutralizing buffer to yield a final concentration of 80 mM for the [^{13}C] pyruvic acid.

The MR imaging was conducted in a 4.7 T small animal scanner (Agilent Technologies, US). A ^{13}C/^{1}H transmit-receive coil and a ^{13}C four-channel array coil (RAPID Biomedical, Germany) were used to acquire proton MR images and ^{13}C phase-encoded chemical shift images (CSI). The animals were anaesthetized during scanning with 3% Isoflorane (Baxter) mixed with 35% O_2 in N_2.

Proton images were acquired first to locate the two tumors. These images were a series of 15-20 axial slices acquired to cover a field of view of 50 mm x 50 mm x 15-20 mm around the tumor region. The images were acquired using Turbo Spin Echo (TSE) sequence with repetition time (TR) of 2 s, effective echo time (TE) of 22 ms, echo spacing of 7.5 ms, Echo Train Length (ETL) of 8 and a resolution of 0.25 mm x 0.25 mm x 1 mm in the readout, phase encoding and slice directions respectively.

The CSI images were positioned to include the two tumors in one slice (figure 1). Two CSI images were acquired for each mouse, 8 and 14 s after the end of the injection of the 200 μl hyperpolarized media, respectively. The imaging was done using a spiral phase encoding trajectory with a matrix size of 16 x 16, TR = 70 ms, TE = 0.65 ms, FOV = 35 mm x 35 mm, slice thickness = 5-6 mm, and with spectral bandwidth of 4000 Hz and 256 spectral points.

Tumor perfusion was assessed using a Dynamic TSE that was acquired during administration of 200 μl of 0.1 mM Dotarem (Guerbet). The TSE slice was positioned at the same site as the CSI image. The acquisition was done using TR = 200 ms, TE = 7.2 ms, and a resolution of 0.25 mm x 0.25 mm and covered a field of view of 50 mm x 50

mm. The number of signal averaging was set to 5, yielding a scan time of about 12 s per dynamic frame.

PET imaging

One hour before each scan, mice were intravenously injected with 10-15 MBq of ^{18}F-FDG or ^{18}F-FLT from the clinical production at Rigshospitalet (Copenhagen, Denmark). The animals were anaesthetized with 3% Sevofluran (Abbott Scandinavia) mixed with 35% O_2 in N_2 and fixed on a custom-made, double subject bed. A 5-7 min PET scan was acquired using a Siemens Inveon MM combined PET/CT (Siemens Medical Solutions), followed by a CT scan for anatomical reference and attenuation correction. The parameters for CT acquisition was 70 kVp voltage, 500 µA current, binning factor 4 and 350 ms exposure, yielding a final CT image with 210 µm isotropic resolution after down-sampled reconstruction. PET data was arranged into static sinograms and reconstructed using the ordered subset expectation maximization (OSEM), maximum a posteriori (MAP) reconstruction algorithm using attenuation correction. The voxel size was 0.388 x 0.388 x 0.796 mm, with a center field of view resolution of 1.4 mm full-width-at-half-maximum.

LDH activity assay

LDH activity was estimated using a NADH-colorimetric assay (Sigma-Aldrich, Copenhagen, Denmark) in extracted tumors from mice that underwent HP-13C MRS. After each scan session, the mice were euthanized by cervical dislocation and tumors were quickly dissected, snap-frozen in liquid nitrogen, and transferred for storage at -80 °C. Extracted tumor tissue was mixed with assay buffer (1 ml mg^{-1}), homogenized and centrifuged for 15 minutes at 10000 rpm at 5 °C. The supernatant was removed and diluted 1:500. After mixing with reactant substance, the well plate was shaken and incubated for 150 seconds at 37°C. The plate was then read every 5 minutes using a

FLUOstar Omega microplate reader (BMG Labtech, Ortenberg, Germany), and calculations done as described by the assay manufacturer. The total protein content of the samples was estimated using a BCA protein assay kit (Thermo Scientific, Slangerup, Denmark) according to the manufactures protocol.

Immunohistochemical staining

Cell proliferation was estimated in tumor tissue from mice that underwent FLT-PET. The extracted tissue samples were fixed in 4% neutral buffered formalin, transferred to 70% EtOH after 24 hours and subsequently embedded in paraffin. A central cryostat section, 8 µm thick, was cut from each tumor, and manual staining procedures were performed as follows: After air-drying, antigen was retrieved with microwave heating in citrate buffer, followed by rinsing in phosphate buffered saline (PBS) with 0.1% Tween. Endogenous enzyme activity was blocked through 8 minutes' soak with Dako REALTM peroxidase-blocking solution (Dako, Glostrup, Denmark) and 10 minutes' soak with 2 % bovine serum albumin (BSA). Incubation with monoclonal mouse anti-human antibody for Ki-67 antigen clone MIB-1 (Dako, Glostrup, Denmark) was then performed for 1 hour at room temperature at a concentration of 1:200. The secondary antibody, an anti-mouse peroxidase labeled polymer (Envision+ System-HRP, Dako, Glostrup, Denmark) was linked to the primary antibody during 40 min of incubation and peroxidase activity was visualized through addition of DAB+ Subtrate Chromogen (Dako, Glostrup, Denmark) as detection system. Counterstaining was performed with Mayer's haematoxylin (Clinical Pharmaceutical Service, Copenhagen University Hospital Pharmacy, Denmark) before dehydration and mounting of cover glass. Each of the described steps until and including DAB+ was followed by rinses with PBS, except between the BSA and primary antibody. A negative control, where the primary antibody was replaced with nonsense anti-body (FLEX Negative Control Mouse, Dako, Glostrup,

Denmark) was also included. Ki67 index was quantified using the ImmunoRatio plugin (25) for ImageJ (26).

Image analysis and statistics

PET and CT images were fused and analyzed using Inveon Research Workplace (version 4.2, Siemens Medical Solutions, Knoxville, USA). Tumor Regions of Interest (ROIs) were delineated on the CT scan, and the percentage-injected dose per gram (%ID/g) was quantified from the PET scan. Similar quantification was done for the MRS CSI images using the anatomical reference image in MATLAB (The Mathworks Inc., Natick, USA).

The acquired Free Induction Decay (FID) signal at each voxel of the CSI data was first zero-filled to increase the spectral resolution and the signal was then apodized using an exponential function, $e^{f.t}$ with $f = 20\ \mathrm{Hz}$, to reduce the noise. General Linear Model (GLM) was used to decompose the frequency spectrum and to resolve the signal of each metabolite. The quantified lactate and pyruvate signals were used to generate metabolic maps that were resampled and registered onto the anatomical proton image. To compare the signal of the tumors in the different mice, the lactate signal from the tumor was normalized with respect to the lactate signal in the surrounding muscle tissues.

To analyze the perfusion, the wash-in and washout coefficients were estimated in the tumor regions using the relative signal enchantment over time that was calculated from the MR perfusion images. A gamma-variate function was fitted to the dynamic contrast enhancement curves obtained from the perfusion images.

Statistical analysis

Student's t-test with Holm-Sidak correction was used to assess the difference between the two (treated and untreated) mice groups across all modalities using Prism 6.0 software (GraphPad, La Jolla, US). Values are reported as mean ± SEM (standard error of the mean) unless otherwise indicated and $p < 0.05$ was considered statistically significant.

Results

Lactate levels determined by [1-^{13}C]pyruvate-MRS predicts treatment response to Erlotinib after 24 hours

A primary objective of this study was to determine if [1-^{13}C]pyruvate-MRS can be used to predict a known treatment response in a xenograft tumor model. A clear lactate signal was observed in the tumors of both models (Figure 1), but when quantified, the average level of lactate detected in untreated HCC-827 tumors was 1.52 ± 0.17 (n=18) for the images acquired 8 s after injection (Figure 4a), which is significantly higher than the levels found in treated HCC-827 tumors, which was 0.76 ± 0.04 (n=14, $p < 0.005$). This is contrasted by the pattern seen in the H-1975 model (Figure 4b), where the lactate levels were found to be similar in the treatment and vehicle group (1.03 ± 0.18 and 0.95 ± 0.12, respectively, n=8 both groups, $p = 0.718$).

The ratio of lactate to pyruvate conversion was also determined. In HCC-827 tumors, the difference between groups was not significant due to the observed increase in the pyruvate level in the untreated HCC-827 tumors compared to the treated, which was 1.13 ± 0.15 and 1.35 ± 0.18 for the two injections respectively, versus 0.75 ± 0.06 and

0.97 ± 0.07 in the treated tumors (Figure 4). For the H-1975 tumors, the ratios were found to be 1.01 ± 0.06 and 1.00 ± 0.08 for the vehicle and treated group, respectively.

Magnitude of treatment response is similar in FDG-PET uptake and MRS lactate level

In theory, FDG-PET and [1-^{13}C]pyruvate-MRS probe the same metabolic pathway at different stages, hence it is natural to compare the two modalities. We imaged the same tumor models at identical time points, with representative images of FDG uptake shown (Figure 1, top row), with the uptake quantified as percentage injected dose per gram (% ID/g). For HCC-827, the level was found to be 1.37 ± 0.13 and 0.85 ± 0.05 for the vehicle and treated group, respectively ($p < 0.002$, n=10 in each group). For H-1975, levels were 1.94 ± 0.09 in the vehicle group and 1.91 ± 0.06 in the treated group ($p = 0.766$, n=8 in each group).

FLT-PET shows most prominent response after 24 hours, which is supported by reduction in Ki-67 staining ex-vivo

Similarly, we evaluated the treatment response using FLT-PET imaging in the same tumor models, with representative images of FLT uptake shown (Figure 1, bottom row). Uptake levels was for HCC-827 found to be 2.45 ± 0.22 and 1.12 ± 0.28 for the vehicle and treated group, respectively ($p < 0.002$, n=8 in each group). For H-1975, the levels were 2.39 ± 0.13 in the vehicle group and 2.39 ± 0.11 in the treated group ($p = 0.965$, n = 8 in each group).

Slices of extracted HCC-827 tumors were immuno-histochemically stained for Ki-67 to evaluated cell proliferation, as done with FLT-PET imaging. Levels of Ki-67 were quantified as percentage of positively stained nuclei, and found to be 9.6 ± 0.6 (n=5) and 6.6 ± 0.7 (n=6) for the untreated and treated groups, respectively (Figure 3, $p < 0.02$).

Levels of LDH enzyme ex-vivo correlates to levels of lactate found in-vivo by [1-^{13}C]pyruvate-MRS

To validate the [1-^{13}C]pyruvate-MRS findings, we determined the levels of lactate dehydrogenase (LDH) normalized to total protein content in extracted HCC-827 tumors. Levels were quantified in units/mg protein, and found to be 0.54 ± 0.03 (n = 18) and 0.45 ± 0.03 (n=14) for the untreated and treated group, respectively ($p < 0.05$) (Figure 4c).

In order to further substantiate the findings by [1-^{13}C]pyruvate-MRS, the normalized LDH values were correlated to the levels of lactate found by [1-^{13}C]pyruvate-MRS, yielding a positive correlation to lactate levels both when imaging 8 (Figure 4d, and 14 seconds following injection (Supplementary figure 1b, $R^2 = 0.20$, $p < 0.05$).

[1-^{13}C]pyruvate-MRS is a highly robust method for assessing tumor metabolism

During [1-^{13}C]pyruvate-MRS of the HCC827 tumor model, two injections were performed for each animal with slightly different timing, in order to evaluate the robustness of the method. Strong correlations were found (Figure 6) between the levels from each injection on both pyruvate and lactate levels ($R^2 = 0.8253$ and $R^2 = 0.6164$, respectively.)

To preclude differences in perfusion between the groups as an explanation of uptake differences, T_1-weighted dynamic contrast enhancement (DCE) imaging was performed. The analysis showed that both groups of tumors (treated and untreated) exhibit typical DCE curves with fast wash in and slow wash out, indicating well-perfused tumors (Figure 5). Furthermore, the analysis of the perfusion curves did not show significant difference between the two groups of tumors.

Discussion

Overall, all the investigated imaging modalities were able to identify the response to treatment after 24 hours. Since 13C MRS and PET were acquired at two different sites it was impractical to evaluate the response to treatment in the same mouse using both imaging modalities. Therefore the study population was divided into two separate groups. This limitation could be overcome by the use of combined PET/MRI scanners (27,28).

As expected from previous reports (7,29), the most prominent response to treatment was observed from PET imaging using the thymidine analog FLT, and a less pronounced, but still significant response seen using FDG-PET, reflecting glucose uptake. We demonstrated that the response to treatment could also be identified using [1-^{13}C]pyruvate-MRS metabolic imaging, and confirmed our hypothesis that the identified response in lactate levels are similar to those found by FDG-PET. We found that levels of lactate attained by ^{13}C-MRS correlated with *ex-vivo* determined, normalized LDH activity, as reported elsewhere (30). This confirms the role of LDH as one of the primary mechanisms behind [1-^{13}C]pyruvate-MRS contrast, as has also been reported elsewhere (31-33).

The ratios between lactate and pyruvate did not prove significantly different between groups. However, this can be due to the significantly lower pyruvate uptake in the treatment group. This finding indicates that the transport of pyruvate into the cells, as facilitated by the mono-carboxylate transporters, might also be affected by treatment with erlotinib. Further studies are needed to clarify if this is indeed the case, and discover the mechanisms behind.

Due to the rapid relaxation of the hyperpolarized signal, perfusion of the investigated tissue remains a vital parameter in hyperpolarized ^{13}C-MRS. Hence, we performed contrast-enhanced perfusion imaging, which showed similar perfusion in both the treated and untreated groups. This is an important verification in order to validate the effect of increased lactate levels. As further expected, we also observed a significantly slower washout of the gadolinium in tumors compared to muscle tissue. This could be attributed to the enhanced permeability and retention (EPR) effect.

In the present study, ^{13}C-pyruvate and FDG-PET identified a similar response to treatment, which is expected, as they are both cancer metabolism markers. Although the two modalities image different phases of glycolysis, the resulting information seems to be the same in this specific setting. However, increased metabolic activity is seen in many physiological states, such as inflammation and muscle activity, making lactate levels a more specific cancer marker due to specific imaging of the Warburg effect (34).

In this preclinical trial, the in-plane resolution of both techniques was comparable; about 2.2 mm for the ^{13}C spectroscopic maps and about 1.4 mm the PET images. PET images have an isotropic image resolution, whereas the CSI images have around 5 mm thicknesses, which give the PET modality an advantage with the current imaging techniques in the preclinical setting. However, when moving into the clinical domain, the game becomes more even, as both modalities can obtain a spatial resolution of 3-4 mm at present.

Dividing the population into two separate groups, one undergoing MRSI and another for PET imaging, makes it hard to compare individual tumors and biological references. The introduction of combined PET/MRI scanners allows for direct comparison of these modalities, which is something we are pursuing (28). In the present study, we observed

lower levels of PET uptake than has previously been reported, which is ascribed to the animal handling between the injection of tracer and scanning. Finally, a technical issue with 13C MRS is the variation in signal level due to tumor positioning with respect to the coil, shimming conditions and coil degradation. All this can make the results, from different experiments, difficult to compare.

In summary, we have evaluated the ^{13}C-pyruvate as strong marker to monitor the response to treatment with erlotinib in NSCLC using MRSI. We also presented a comparison between the [1-^{13}C]pyruvate and the more clinically established FDG- and FLT-PET tracers. We found that all three markers were able to identify the response to treatment, most pronounced was FLT-PET. Each method has it is own merit and combination of both assess the tumor progression or retreat can be of great value. Especially the possibility of assessing tumor metabolism using [1-^{13}C]pyruvate MRS in a joint PET/MR scanner, leaving the PET imaging available for other biological targets.

Acknowledgements

This work was supported by the Danish National Research Foundation (Grant Number DNRF124) and the Danish Research Council (Grant Numbers 12-127232 and 1331-00259A).

We gratefully acknowledge laboratory technicians Sascha Gude and Michelle Kaijer for their assistance with experimental procedures and immunohistochemical analysis.

References (34/50)

1. Eisenhauer EA, Therasse P, Bogaerts J, Schwartz LH, Sargent D, Ford R, et al. New response evaluation criteria in solid tumours: Revised RECIST guideline (version 1.1). European Journal of Cancer. 2009;45:228–47.

2. van Persijn van Meerten EL, Gelderblom H, Bloem JL. RECIST revised: implications for the radiologist. A review article on the modified RECIST guideline. Eur Radiol. 2009;20:1456–67.

3. Vander Heiden MG, Cantley LC, Thompson CB. Understanding the Warburg Effect: The Metabolic Requirements of Cell Proliferation. Science. 2009;324:1029–33.

4. McKinley ET, Ayers GD, Smith RA, Saleh SA, Zhao P, Washington MK, et al. Limits of [18F]-FLT PET as a Biomarker of Proliferation in Oncology. Srivastava RK, editor. PLoS ONE. 2013;8:e58938.

5. Vesselle H, Grierson J, Muzi M, Pugsley JM, Schmidt RA, Rabinowitz P, et al. In Vivo Validation of 3′deoxy-3′-[18F]fluorothymidine ([18F]FLT) as a Proliferation Imaging Tracer in Humans. Clinical Cancer Research. American Association for Cancer Research; 2002;8:3315–23.

6. Munk Jensen M, Erichsen KD, Björkling F, Madsen J, Jensen PB, Højgaard L, et al. Early Detection of Response to Experimental Chemotherapeutic Top216 with [18F]FLT and [18F]FDG PET in Human Ovary Cancer Xenografts in Mice. Boswell A, editor. PLoS ONE. 2010;5:e12965.

7. Ullrich RT, Zander T, Neumaier B, Koker M, Shimamura T, Waerzeggers Y, et al. Early Detection of Erlotinib Treatment Response in NSCLC by 3′-Deoxy-3′-[18F]-Fluoro-L-Thymidine ([18F]FLT) Positron Emission Tomography (PET). You M, editor. PLoS ONE. 2008;3:e3908.

8. Bardram Johnbeck C, Munk Jensen M, Haagen Nielsen C, Fisker Hag AM, Knigge U, Kjaer A. 18F-FDG and 18F-FLT-PET Imaging for Monitoring Everolimus Effect on Tumor-Growth in Neuroendocrine Tumors: Studies in Human Tumor Xenografts in Mice. Chen X, editor. PLoS ONE. Public Library of Science; 2014;9:e91387–8.

9. Munk Jensen M, Erichsen KD, Johnbeck CB, Björkling F, Madsen J, Bzorek M, et al. [18F]FLT and [18F]FDG PET for Non-invasive Treatment Monitoring of the Nicotinamide Phosphoribosyltransferase Inhibitor APO866 in Human Xenografts. Chen C-T, editor. PLoS ONE. 2013;8:e53410.

10. Jensen MM, Kjaer A. Monitoring of anti-cancer treatment with (18)F-FDG

and (18)F-FLT PET: a comprehensive review of pre-clinical studies. Am J Nucl Med Mol Imaging. 2015;5:431–56.

11. Ribas A, Benz MR, Allen-Auerbach MS, Radu C, Chmielowski B, Seja E, et al. Imaging of CTLA4 Blockade-Induced Cell Replication with 18F-FLT PET in Patients with Advanced Melanoma Treated with Tremelimumab. Journal of Nuclear Medicine. 2010;51:340–6.

12. Benz MR, Czernin J, Allen-Auerbach MS, Dry SM, Sutthiruangwong P, Spick C, et al. 3′-deoxy-3′-[18F]fluorothymidine positron emission tomography for response assessment in soft tissue sarcoma. Cancer. 2011;118:3135–44.

13. Zander T, Scheffler M, Nogova L, Kobe C, Engel-Riedel W, Hellmich M, et al. Early Prediction of Nonprogression in Advanced Non-Small-Cell Lung Cancer Treated With Erlotinib By Using [18F]Fluorodeoxyglucose and [18F]Fluorothymidine Positron Emission Tomography. Journal of Clinical Oncology. 2011;29:1701–8.

14. Kwock L, Smith JK, Castillo M, Ewend MG, Collichio F, Morris DE, et al. Clinical role of proton magnetic resonance spectroscopy in oncology: brain, breast, and prostate cancer. The Lancet Oncology. 2006;7:859–68.

15. Day SE, Kettunen MI, Gallagher FA, Hu D-E, Lerche M, Wolber J, et al. Detecting tumor response to treatment using hyperpolarized 13C magnetic resonance imaging and spectroscopy. Nature Medicine. 2007;13:1382–7.

16. Nelson SJ, Kurhanewicz J, Vigneron DB, Larson PEZ, Harzstark AL, Ferrone M, et al. Metabolic Imaging of Patients with Prostate Cancer Using Hyperpolarized [1-13C]Pyruvate. Science Translational Medicine. 2013;5:198ra108–8.

17. Ardenkjaer-Larsen JH, Fridlund B, Gram A, Hansson G, Hansson L, Lerche MH, et al. Increase in signal-to-noise ratio of > 10,000 times in liquid-state NMR. Proc Natl Acad Sci USA. 2011;100:10158–63.

18. Chen AP, Chu W, Gu Y-P, Cunnhingham CH. Probing Early Tumor Response to Radiation Therapy Using Hyperpolarized [1-13C]pyruvate in MDA-MB-231 Xenografts. Monleon D, editor. PLoS ONE. 2013;8:e56551.

19. Lin G, Andrejeva G, Wong Te Fong A-C, Hill DK, Orton MR, Parkes HG, et al. Reduced Warburg Effect in Cancer Cells Undergoing Autophagy: Steady- State 1H-MRS and Real-Time Hyperpolarized 13C-MRS Studies. Filleur S, editor. PLoS ONE. 2014;9:e92645.

20. Park I, Mukherjee J, Ito M, Chaumeil MM, Jalbert LE, Gaensler K, et al. Changes in Pyruvate Metabolism Detected by Magnetic Resonance Imaging Are Linked to DNA Damage and Serve as a Sensor of

Temozolomide Response in Glioblastoma Cells. Cancer Research. 2014;74:7115–24.

21. Albers MJ, Bok R, Chen AP, Cunningham CH, Zierhut ML, Zhang VY, et al. Hyperpolarized 13C Lactate, Pyruvate, and Alanine: Noninvasive Biomarkers for Prostate Cancer Detection and Grading. Cancer Research. 2008;68:8607–15.

22. Ardenkjaer-Larsen JH, Leach AM, Clarke N, Urbahn J, Anderson D, Skloss TW. Dynamic nuclear polarization polarizer for sterile use intent. Rizi R, editor. NMR Biomed. 2011;24:927–32.

23. Kurhanewicz J, Vigneron DB, Brindle K, Chekmenev EY, Comment A, Cunningham CH, et al. Analysis of Cancer Metabolism by Imaging Hyperpolarized Nuclei: Prospects for Translation to Clinical Research. Neoplasia. 2011;13:81–97.

24. Sharma SV, Bell DW, Settleman J, Haber DA. Epidermal growth factor receptor mutations in lung cancer. Nat Rev Cancer. 2007;7:169–81.

25. Tuominen VJ, Ruotoistenmäki S, Viitanen A, Jumppanen M, Isola J. ImmunoRatio: a publicly available web application for quantitative image analysis of estrogen receptor (ER), progesterone receptor (PR), and Ki-67. Breast Cancer Res. 2010;12:R56.

26. Schneider CA, Rasband WS, Eliceiri KW. NIH Image to ImageJ: 25 years of image analysis. Nat Meth. 2012;9:671–5.

27. Jadvar H, Colletti PM. Competitive advantage of PET/MRI. European Journal of Radiology. 2014;83:84–94.

28. Kjaer A, Loft A, Law I, Berthelsen AK, Borgwardt L, Löfgren J, et al. PET/MRI in cancer patients: first experiences and vision from Copenhagen. Magnetic Resonance Materials in Physics, Biology and Medicine. 2012;26:37–47.

29. Zannetti A, Iommelli F, Speranza A, Salvatore M, Del Vecchio S. 3“-Deoxy-3-”18F-Fluorothymidine PET/CT to Guide Therapy with Epidermal Growth Factor Receptor Antagonists and Bcl-xL Inhibitors in Non-Small Cell Lung Cancer. Journal of Nuclear Medicine. 2012;53:443–50.

30. Hu S, Balakrishnan A, Bok RA, Anderton B, Larson PEZ, Nelson SJ, et al. 13C-Pyruvate Imaging Reveals Alterations in Glycolysis that Precede c-Myc-Induced Tumor Formation and Regression. Cell Metabolism. Elsevier Inc; 2011;14:131–42.

31. Saito K, Matsumoto S, Takakusagi Y, Matsuo M, Morris HD, Lizak MJ, et al. 13C-MR Spectroscopic Imaging with Hyperpolarized [1-13C]pyruvate

Detects Early Response to Radiotherapy in SCC Tumors and HT-29 Tumors. Clinical Cancer Research. 2015;21:5073–81.

32. Dafni H, Larson PEZ, Hu S, Yoshihara HAI, Ward CS, Venkatesh HS, et al. Hyperpolarized 13C Spectroscopic Imaging Informs on Hypoxia-Inducible Factor-1 and Myc Activity Downstream of Platelet-Derived Growth Factor Receptor. Cancer Research. 2010;70:7400–10.

33. Lodi A, Woods SM, Ronen SM. Treatment with the MEK inhibitor U0126 induces decreased hyperpolarized pyruvate to lactate conversion in breast, but not prostate, cancer cells. NMR Biomed. 2012;26:299–306.

34. Gutte H, Hansen AE, Henriksen ST. Simultaneous hyperpolarized 13C-pyruvate MRI and 18F-FDG-PET in cancer (hyperPET): feasibility of a new imaging concept using a clinical PET/MRI scanner. American journal of …. 2015.

Figure legends

Figure 1

Representative ^{13}C metabolic maps of pyruvate, lactate and their ratio for both treated and untreated HCC-827 and H-1975 xenograft tumors. The metabolic maps are overlaid on proton images acquired at the same position as the CSI, with white arrows indicating tumor position. Individual, representative voxel spectra from the tumor are shown in the bottom row. Each spectrum is normalized to maximum peak value for comparison.

Figure 2

Representative PET/CT images showing FDG- (top row) and FLT- (bottom row) uptake 60 minutes after injection in both treated and untreated HCC-827 (left) and H-1975 (right) xenograft tumors. White arrows indicate the location of the two tumors on each mouse. Some central necrosis was observed, particularly in the H-1975 tumors.

Figure 3

Top row: Quantitative comparison between FDG and FLT uptake for treated and untreated HCC-827 and H-1975 tumors by % ID / g. Significant reduction in uptake was seen for both FDG and FLT (both $p < 0.002$) in treated HCC-827 tumors compared to untreated. No significant change in uptake was observed for H-1975 tumors.

Bottom row: Representative sections stained histologically for GLUT1, HK2 and Ki-67 is shown for treated and untreated HCC-827 tumors. Quantitative evaluation of Ki-67 staining showed a significantly reduced number of stained cells in treated HCC-827 tumors compared to untreated ($p < 0.05$).

Figure 4

Quantitative evaluation of pyruvate, lactate and ratio levels in HCC-827 (A) and H-1975 (B) tumors. A significant reduction in lactate level ($p < 0.005$) was observed for treated HCC-827 tumors compared to untreated. No significant change in metabolite levels was seen for H-1975 tumors.

C. Levels of LDH enzyme normalized to total protein content in HCC-827 tumor samples. A significant reduction was found in the treated compared to untreated tumors ($p < 0.05$). D. Correlation between levels of LDH enzyme normalized to total protein content and lactate level evaluated by ^{13}C-MRSI ($p < 0.01$).

Figure 5

Quantification of perfusion imaging, showing inflow (A) and outflow (B) coefficients for treated and untreated HCC-827 and H-1975 tumors. No significant difference in coefficients was found between cell lines and treatment. C shows a representative temporal development in signal enhancement, as well as the fitted, gamma-variate

curves for computing slope coefficients. Corresponding representative images are shown for three time points (D), with arrows indicating tumors.

Figure 6

Correlation between lactate (A) and pyruvate (B) levels from the two injections, with corresponding Bland-Altman plots (C and D). Both correlations are highly significant ($p < 0.001$) and have slopes of 0.96 and 0.81 for lactate and pyruvate, respectively. Three data points were removed as outliers; see Supplementary figure 2 for full dataset.

Supplementary figure 1

A: Quantitative evaluation of pyruvate, lactate and ratio levels in treated and untreated HCC-827 xenograft tumors. Similar to figure 4 A, although these levels were obtained 14 seconds after injection of hyperpolarized [1-^{13}C]pyruvate. B: Correlation between LDH enzyme level normalized to total protein content and lactate level determined by 13C MRS.

Supplementary figure 2

Correlation between lactate (A) and pyruvate (B) levels from the two injections, with corresponding Bland-Altman plots (C and D). Both correlations are highly significant ($p < 0.001$) and have slopes of 0.87 and 0.81 for lactate and pyruvate, respectively. Three data points were deemed as outliers (marked in red) were removed from analysis in Figure 6.

B

Simultaneous imaging of hyperpolarized [1,4-$^{13}C_2$]fumarate, [1-^{13}C]pyruvate and 18F-FDG in rat model of necrosis in a clinical PET/MR

The following paper was submitted to *NMR in Biomedicine* in November 2016, and it is currently in review. Some of the results from this paper were presented in the *Dynamic Nuclear Polarization Symposium* in August 2015.

Simultaneous imaging of hyperpolarized [1,4-$^{13}C_2$]fumarate, [1-^{13}C]pyruvate and ^{18}F-FDG in rat model of necrosis in a clinical PET/MR

Abubakr Eldirdiri[1, 3,*], Andreas Clemmensen[3, 4, 5,*], Sean Bowen[1], Andreas Kjær[4, 5], Jan Henrik Ardenkjær-Larsen[1, 2, ¥]

1. Department of Electrical Engineering, Technical University of Denmark, Kgs. Lyngby, Denmark
2. GE Healthcare, Broendby, Denmark
3. Danish Research Center for Magnetic Resonance, Copenhagen University Hospital Hvidovre, Denmark
4. Department of Clinical Physiology, Nuclear Medicine and PET, Rigshospitalet, Copenhagen, Denmark
5. Cluster for Molecular Imaging, Department of Biomedical Medical Sciences, University of Copenhagen, Denmark

* These authors contributed equally to this work.

¥ Corresponding author: Jan H. Ardenkjaer-Larsen, Ph.D., Technical University of Denmark, Orsted Plads 375/148, 2800 Kgs Lyngby, Denmark, jhar@elektro.dtu.dk

Word count: 5411

Keywords: Hyperpolarization; [1-^{13}C]pyruvate; [1,4-$^{13}C_2$]fumarate, ^{18}F-FDG, PET/MR

Abbreviations: dDNP: dissolution Dynamic Nuclear Polarization, PA: [1-^{13}C]pyruvate, FA: [1,4-$^{13}C_2$]fumarate

Abstract

A co-polarization scheme for [1,4-$^{13}C_2$]fumarate and [1-^{13}C]pyruvate is presented to simultaneously assess necrosis and metabolism in rats with hyperpolarized ^{13}C MR. The co-polarization was performed in a SPINlab polarizer. In addition, the feasibility of simultaneous PET and MR of small animals with a clinical PET/MR is demonstrated. The hyperpolarized metabolic MR and PET is demonstrated in a rat model of necrosis.

The polarization and T_1 of the co-polarized [1,4-$^{13}C_2$]fumarate and [1-^{13}C]pyruvate substrates were measured *in vitro* and compared to those obtained when the substrates were polarized individually. Polarization of 36±4 % for fumarate and 37±6% for pyruvate was obtained. We found no significant difference in the polarization values between the dual and single substrate polarization.

Rats weighing about 400 g were injected i.m. in one of the hind legs with 200 µL of turpentine to induce necrosis. Two hours later, ^{13}C metabolic maps were obtained with a Chemical Shift Imaging sequence (16x16) with a resolution of 3.1x5.0x25.0 mm^3. The ^{13}C spectroscopic images were acquired in 12 s, followed by an 8 min ^{18}F-FDG PET acquisition of 3.5 mm resolution. [1,4-$^{13}C_2$]malate was observed from the tissue injected with turpentine indicating necrosis. Normal [1-^{13}C]pyruvate metabolism and ^{18}F-FDG uptake were observed from the same tissue.

The proposed co-polarization scheme provides a means to utilize multiple imaging agents simultaneously, and thus to probe various metabolic pathways in a single examination. Moreover, it demonstrates the feasibility of small animal research on a clinical PET/MR scanner for combined PET and hyperpolarized metabolic MR.

Introduction

Since the introduction of the dissolution Dynamic Nuclear Polarization (dDNP) technique[1] to enhance the ^{13}C signal in applications like magnetic resonance spectroscopic imaging (MRSI), the metabolic fluxes of hyperpolarized ^{13}C substrates have shown great potential to improve the detection and characterization of many pathologies, especially cancer. For instance, studies have indicated that the lactate signal [2-4], and in some cancer types the alanine signal [5], are higher in cancer than in normal tissue, after the administration of hyperpolarized [1-^{13}C]pyruvate. This observation is referred to as the Warburg effect and it is due to the fact that most cancer cells have elevated glycolysis even in the presence of sufficient oxygen. Moreover, MR imaging with hyperpolarized [1,4-$^{13}C_2$]fumarate was shown to allow early detection of necrosis [6-8]. The conversion of fumarate into malate is a normal step in the mitochondrial tricarboxylic acid (TCA) cycle and is catalyzed by fumarase. As the enzyme is not present in the extracellular space, but exposed by cells that undergo necrosis, it is hypothesized that the observation of an increased [1,4-$^{13}C_2$]malate production, after intravenous administration of hyperpolarized [1,4-$^{13}C_2$]fumarate, can be used as a marker of necrosis.

In order for the DNP process to be effective, it is important to comply with certain requirements during sample preparation and polarization. First of all, the ^{13}C labeled substrates must be in an amorphous (glassy) solid state with the appropriate electron paramagnetic agent uniformly distributed so that an efficient coupling between electron spin and nuclear spins is achieved in the solid state [1,9,10]. Fumaric acid (FA) dissolved in dimethyl sulfoxide, for instance, requires rapid freezing to achieve this amorphous solid

state and to prevent the FA crystallization, which can significantly reduce the nuclear spin polarization. Pyruvic acid (PA), on the other hand, is a liquid at room temperature that glasses well without additives. Moreover, the concentration of the desired agents, solvent/glassing agents and the concentration and type of free radical must all be optimized to achieve optimal polarization for the ^{13}C substrates. In addition, appropriate dissolution and neutralizing media must be prepared for each agent in order to ensure physiological pH and osmolarity/tonicity for *in vivo* use.

The spectrum obtained following the *in vivo* infusion of a hyperpolarized ^{13}C material is often sparse. In some cases, this sparsity can be exploited to combine more than one ^{13}C agent during the hyperpolarization and imaging. This way multiple enzymatic pathways can be probed simultaneously. Previous attempts of multi-agent polarization have been performed with the Hypersense (Oxford Instruments, UK) polarizer [11-14]. This manuscript presents a co-polarization scheme for [1,4-$^{13}C_2$]fumarate and [1-^{13}C]pyruvate to simultaneously assess necrosis and metabolism. The co-polarization presented in this work is done in a SPINlab polarizer (GE Healthcare) [15,16]. Although the SPINlab benefits from relatively higher magnetic field and lower temperature, which result in high polarization, the polarization build-up durations are considerably long (2~4 hours). The SPINlab overcomes this in part by having four samples in parallel; however, the adoption of multi-substrate polarization scheme makes the polarization in SPINlab more appealing. The polarization of the co-polarized [1,4-$^{13}C_2$]fumarate and [1-^{13}C]pyruvate were measured in phantoms and compared to those obtained when the substrates were polarized individually. *In vivo* experiments were conducted in rats with induced necrosis via the injection of 200 µL of turpentine at the deep muscle of the left

hind leg. ^{13}C metabolic maps were obtained to assess the cellular uptake and the conversion of [1-^{13}C]pyruvate into [1-^{13}C]lactate and to assess the conversion of [1,4-$^{13}C_2$]fumarate into [1,4-$^{13}C_2$]malate. In addition, ^{18}F-fluorodeoxyglucose (^{18}F-FDG) Positron Emission Tomography (PET) images were acquired simultaneously with the ^{13}C MRSI.

Experimental

Sample preparation

For pyruvate preparation, AH111501 trityl radical (GE Healthcare, Denmark) was added to a sample of [1-^{13}C]pyruvic acid (PA) (14 M) (Sigma Aldrich, Denmark) to a final concentration of 15 mM. The fumarate was prepared by dissolving [1,4-$^{13}C_2$]fumaric acid (FA) (Cambridge Isotope Laboratories, MA, USA) in dimethyl sulfoxide (DMSO) (Sigma Aldrich, Denmark). Sonication and vortex mixing were used until all the FA crystals had dissolved. AH111051 radical was then added and dissolved in the solution. To optimize the formulation of FA, three different batches were prepared with FA/radical concentrations of 3.6 M/8 mM, 3.6 M/12 mM and 2.8 M/15 mM, respectively.

The polarizer and fluid path assembly

The co-polarization was made in a SPINlab polarizer (GE Healthcare, Denmark). Figure 1-a shows the fluid path assembly designed for use with the SPINlab. The fluid path consists of a vial (1) containing the sample and connected to the dissolution syringe (2) via two concentric tubes (3). The tubes can be pushed into the polarizer through the

dynamic seal (4) without compromising the vacuum. The syringe has an exit port (5) that connects to a tube for transfer of the hyperpolarized solution.

The regular sample preparation procedure for the SPINlab fluid path requires that the vial, after adding the ^{13}C substrate, is frozen in liquid nitrogen (LN_2). This freezing is necessary to perform pressure check and helium purging. Helium purging is needed to have a helium exchange gas inside the fluid path when the vial is cooled to <1 K.

The regular procedure to load the sample into the SPINlab involves lowering the sample vial into the sample pot (see Figure 1-c), were the hyperpolarization take place, through multiple steps (gradual insertion over 15 min) to avoid excessive increase in the helium temperature. This multi-steps lowering process was found to result in FA crystallization. Therefore, to avoid the FA crystallization, the sample preparation and loading was modified as detailed in the next section.

Co-polarization of FA and PA

The fluid path was prepared by first placing 25 µL (around 350 µmol) of PA in the sample vial and then freezing it in liquid nitrogen (LN_2). 100 µL (about 350 µmol) of FA was then added on top of the PA and the vial was placed in LN_2 again (see Figure 1-b). The vial is then glued to the tube set with the tip immersed in LN2 and the neck above the liquid surface. The rest of the fluid path preparations (pressure check and He purging) were done according to the manufactures instructions. After the preparation, the fluid path was placed in the SPINlab and the vial containing the two compounds was initially placed at the airlock for 20 to 30 min, thus allowing the substrates to thaw before lowering the sample vial into the helium pot. During the melting period, it is assumed

that the difference in density prevents the mixing of the two substrates. The densities of PA and FA solutions are 1.3 and 1.2 g/mL respectively. Then the sample vial was directly lowered into the helium bath in either one (A: directly to the 1 K pot) or two steps (B: directly to the 1 K pot and then retracted to the 4 K thermal link for 10 min) instead of the normal scheme of going through multi-steps lowering process, to avoid the crystallization of the FA in the sample.

For both in-vivo and in-vitro studies, the sample was irradiated with microwaves at 139.64 GHz and 40 mW (the two samples have the same optimal microwave frequency) for at least 4 hours in the *in vitro* phantom studies to measure the liquid-state polarization. Before dissolving the samples, it was ensured that the polarization curve in SPINlab reached the flat plateau. For logistic reasons, some of the sample in the *in vivo* animal experiments were polarized for about 3 hours and dissolved before reaching the maximum achievable polarization. The polarization curve was fitted with a single exponential.

The dissolution syringe was filled with about 15 g of a dissolution medium (DM) (WFI with 0.1 g/L EDTA). The dissolved sample was mixed with 0.95 g of neutralizing medium (NM) (WFI with 0.72 M NaOH, 0.4 M Tris and 0.1 g/L EDTA).

Some of the dissolved samples were used after the *in vitro* study to measure the concentration. The concertation was measured by quantitative NMR using 9.4 T spectrometer (NMR AS400, Oxford Instruments) and 100 mM urea reference.

Single substrate polarization

In addition to the dual polarization of FA and PA, the FA was polarized separately. This was to investigate if there are differences in the polarization values between the single and dual substrate polarization. The single FA polarization and dissolution was made in the same manner as described in the previous section for the dual substrate. About 350 µmol (100 µL) of FA sample was loaded in the vial and dissolved with 15 g of DM and 0.65 g of NM.

Phantom MR experiments for polarization and T_1 measurements

All imaging was performed in a clinical 3T PET/MR scanner (Siemens mMR Biograph, Siemens, Erlangen, Germany). A dual-tuned transmit/receive flex surface coil (RAPID Biomedical) was used for both ^{1}H and ^{13}C acquisition. The coil consists of 110 mm loop for 13C and 180 mm x 244 mm butterfly for ^{1}H. The 90° flip angle was calibrated from a 13C-urea phantom at approximately the position of the rat. Phantoms and rats were placed in the center of the 11 cm loop coil.

About 5 mL of the polarized material was injected into a previously shimmed phantom tube, approximately 30 s after the dissolution. 180 ^{13}C spectra were acquired without spatial encoding using an excitation pulse with 5° flip angle (315 us pulse duration) and repetition time TR of 5 s. The sampling spectral window was set to 6000 Hz with 512 spectral points.

For each spectrum of the dynamic acquisition, the signal integrals were calculated after baseline correction. A mono-exponential decay function, equation 1, was fitted for each of the two substrate signals to obtain the relaxation time, $T_{1,}$ and the initial longitudinal magnetization, M_I.

$$S(n) \propto M_I \, sin(\alpha) \cos^n(\alpha) \, e^{-n\frac{TR}{T1}} \qquad (1),$$

where $S(n)$ is the signal recorded after the nth excitations, TR is the repetition time, and α is the flip angle.

A ^{13}C-urea phantom (4 M) was placed next to the tube with the hyperpolarized solution and was used to calibrate the 90^{o} flip angle and as a reference to measure the polarization. To quantify the polarization, the initial signal of the hyperpolarized sample was compared to the urea signal and corrected for the concentration difference.

In-vivo rat experiment

Animal handling and experimental procedures were performed according to the guidelines from Danish Animal Experiments Inspectorate (permit no. 2011/561−14). The *in vivo* study was conducted in two rats weighing (400 g). The first rat was only injected with hyperpolarized FA. The second rat received two injections separated by 10 min. The first injection was only hyperpolarized FA, and the second injection was dual polarized FA and PA. Necrosis was induced by intramuscular injection of 200 µL of sterile turpentine oil in one of the hind legs. This was followed by subcutaneous injection of 400 µL of Buprenorphine (TEMGESIC, 0.03 mg/mL) to control the acute paint from the turpentine injection. Two hours later, the animal was transferred to the PET/MR scanner to acquire ^{13}C MRS and PET images.

During the MR scanning, the animals were anaesthetized with 3 % Sevoflurane mixed in O_2. A catheter was inserted in the tail vein for the administration of the hyperpolarized mixture of pyruvate and fumarate or fumarate alone. 2 mL (0.14 mmol/kg) of the co-polarized substrates was injected in the rat. This injection was done approximately 20 s

after dissolution, during this period the co-polarized material was transferred to the MRI room from the SPINlab in a syringe that was then connected to the tail vein catheter. The hyperpolarized substrate was injected manually over a period of 10 s.

Anatomical long axis proton MR images are acquired prior to the ^{13}C MRS scans for spatial localization of the necrotic tissue within muscle. Chemical shift images (CSI) (with FA=10°, TR= 80 ms, TE = 1.4 ms, FOV = 50 x 80 mm^2, matrix=16x16, in-plane resolution 3.1 x 5 mm^2, slice thickness = 25 mm) were acquired 20 s after the end of administration of hyperpolarised [1-^{13}C]pyruvate and [1,4-$^{13}C_2$]fumarate mixture.

One hour before the PET/MR imaging session, the rats were intravenously injected with 80 MBq of ^{18}F-FDG. An 8 min PET scan (2 mm isotropic resolution) was acquired during the acquisition of the MR images. Dixon imaging was used to obtain fat and water maps that were used to correct for the attenuation in the PET images.

The acquired free induction decay signal at each voxel of the CSI data was first zero-filled to increase the spectral resolution and the signal was then apodized using an exponential function, $e^{f.t}$ with $f = 15\,\mathrm{Hz}$. Metabolic maps were generated for each metabolite from the peak amplitude in the real phased spectra after baseline correction. The metabolic maps were resampled to the same resolution of the anatomical proton images, 0.4x0.4 mm^2, and registered onto them. Thresholding was applied to reduce remove the noise level.

Results

Polarization of [1,4-$^{13}C_2$]fumarate and [1-^{13}C]pyruvate

Figure 2 shows representative polarization build-up and the temperature curves recorded at the equilibrator and sample pot for multi-step lowering process, used typically for pyruvate, and two-step lowering, used for samples containing fumarate. The efficiency of the multi-step lowering in minimizing the temperature variation at the sample pot is evident.

The polarization of samples containing 600 mg of FA from the three different batches (with fumarate/AH111051 concentrations of 2.8M/15mM, 3.6M/8mM and 3.6M/12mM) resulted in build-up time constants and final solid-state polarization values detailed in Table 1, for one and two insertion steps. The batches showed high discrepancy in build-up time constant and less discrepancy in the saturation level. The batch with 3.6M/12mM fumarate/AH111051 concentration had the lowest build-up time constant. This batch also showed no significant difference between the one (A) and two (B) lowering steps in the final saturation level but the build-up time constant was lower for (A) ; however, the one-step lowering can result in a higher increase in the sample pot temperature. The final solid state polarization values for these batches were comparable. The solid state NMR signals might vary significantly between measurements due to the uncontrolled position of the sample within the NMR coil that is dimensioned to hold up to four samples. However, the comparison is based on the liquid state polarization obtained post dissolution.

Table 1 also shows the liquid state polarization measurements obtained for the three formulations of fumarate via dynamic acquisition of ^{13}C spectra in the PET/MR scanner 30 s after dissolution. There was no difference between the batches in the measured polarization. Since all the batches gave similar polarization results, the subsequent experiments were conducted with the 3.6M/12mM fumarate/AH111051 batch. This batch gives higher concentration of fumarate, which results in higher MR signal. In addition, this batch had relatively faster polarization build-up.

The results of the experiment to determine whether there is a difference in the polarization and T_1 values between the dual and single substrate polarization is summarized in Table 2. No significant difference was found in the measured values of polarization of FA for single and dual FA/PA polarization. The polarization level of pyruvate, 37%, obtained with the dual polarization scheme agrees with the polarization values of PA in SPINlab found in the literature [17].

After the dissolution of the polarized materials in the (15 g) dissolution medium and (0.95 g) neutralizing buffer, the measured concentrations of fumarate and pyruvate were about 31±2 mM (n=2). The measured pH value was 7.7±0.3 (n=8). The volume of the sample received after dissolution was 6±1 mL (n=3). The remaining volume was retained in the fluid path during the dissolution as dead volume.

Animal experiment

Figure 3 shows the expected position of the metabolite peaks. The spectrum is sparse enough to allow clear quantification the injected substrates and their products. Figure 4 shows the anatomical image and the ^{13}C spectrum at the necrotic tissue for the rat that

was injected with only hyperpolarized FA. The maps of fumarate and malate distributions within a slice covering the necrotic region are also shown in Figure 4. Figure 5, shows the anatomical image and the ^{13}C spectrum at the necrotic tissue for the rat that received the dually hyperpolarized FA and PA. Clear malate signal was visible at the necrotic site with both the single fumarate and dual pyruvate/fumarate injections and no malate signal was observed elsewhere. Figure 5 also shows the PET images acquired for the same animal during the same MR imaging session. The FDG uptake by the different organs is represented using maximum intensity projection. Slight increase in lactate production is observed at the necrotic tissue. There is no clear effect from the necrosis on the FDG-PET signature.

Discussion

The main aim of this study was to investigate the technical feasibility of a method to simultaneously polarize a low dose of FA and PA in a SPINlab polarizer and to image their metabolism in small animals with a clinical MR scanner. This setup provides a mean to utilize multiple imaging agents at once, and thus to probe various physiological characteristics and obtain valuable biological data, in one single exam session. Secondly, it enables small animal research on a typical clinical scanner setup. Increased conversion of pyruvate into lactate, also known as the Warburg effect, is a main hallmark of neoplastic activity [18] and has the potential to effectively monitor the response to treatment [19]. The production of malate from fumarate has been proposed as sign for necrosis [6,8,20], and it is expected that the degree of necrosis induced by treatment, is proportional to the amount of malate produced. The amount of malate

observed in the ^{13}C spectrum depends also on the time of imaging following the intervention as seen in the difference in malate signal between the two injections in rat two. This is because the fumarase is washed out of the tissue within a few hours to the blood plasma and then to the urine [21].

Acquiring PET images at the same time as ^{13}C hyperpolarized MR imaging adds additional molecular imaging characterization, and allows comparing PET tracers with their analogous MR counterparts. For instance, although ^{18}F-FDG, unlike [1-^{13}C]pyruvate, does not show the actual metabolic reactions, the concentrations of ^{18}F-FDG in the PET images reflects regional uptakes of glucose. Thus, FDG-PET, to a degree, also reflects tissues with high metabolic activity, and the two markers, 18F-FDG and ^{13}C-pyruvate, can be complementary [22,23]. The lactate signal was clearly detectable at various tissues from the ^{13}C spectra of the CSI whereas the malate signal was confined to necrotic tissue. There was no change in the FDG uptake nor on the lactate production.

We were able to demonstrate the feasibility of using a state-of-the-art clinical PET/MR scanner for in vivo imaging of rats. Good image quality that allows the evaluation of metabolic activities in various tissues was achievable with both PET and ^{13}C-MRS imaging. In this study, the in-plane resolution used with CSI was 3.1 x 5 mm^2, but finer spatial resolution can be achieved. The minimal in-plane resolution for the CSI allowed on our system is 3.1 mm with nominal gradient strength, which is the maximum value that the manufacturer recommends for reliable performance. However, in theory, a resolution as fine as 1.5 mm can be achieved with the maximum gradient strength that can be realized by the scanner. This is because, the CSI sequence does not require

very strong gradients, unlike other faster spectroscopic sequences, such as Echo Planar Spectroscopic Imaging (EPSI), which can be very demanding on gradient strength and slew rate. The gradient strengths and slew rate on the Siemens mMR Biograph are 42 mT/m and 180 mT/m/ms respectively. These are significantly lower compared to 1,000 mT/m gradient strength and 5,000 mT/m/ms slew rates on some of the state-of-the-art animal scanners.

One of the major problems that faced previous attempts of multi substrate polarization was the limited sample volume that can be polarized stably and dissolved successfully in the Hypersense polarizer (Oxfords, Instruments, UK), which is used in these co-polarization attempts. This limited sample volume that can be used in the Hypersense subsequently results in relatively smaller concentrations of the co-polarized substrates in the final volume (13). SPINlab on the other hand is designed to efficiently polarize and dissolve larger substrate volumes (up to 2 g).

Relatively high polarization was achieved for both FA and PA (more than 30%) when they were polarized simultaneously in the SPINlab. In addition, there was no significant difference in the polarization measurement when two substrates were polarized separately. The final concentration of the two agents after dissolution was reasonable (30 mM). This concentration however can be increased by increasing the initial volume of PA and FA in the sample vial, but will be at the expense of a larger waste. The dissolution volume can also be lowered for higher final concentration of PA and FA. The minimal effective dissolution volume that can be reliably used on the SPINlab is approximately 5-7 mL.

Using multiple ^{13}C substrates, however, brings additional burden to resolve multiple peaks in the frequency spectrum with the possibility of overlapping between peaks; an issue which is less common in hyperpolarize ^{13}C MRS compared to ^{1}H MRS. Higher magnetic fields are more suitable for such tasks, since they give larger spacing between the peaks. Fortunately, the malate doublet was quantifiable in both single fumarate and dual fumarate/pyruvate scheme. There is also the problem of the difference in the ideal microwave irradiation frequencies for the different ^{13}C substrates, which can limit the solid state polarization for some of them. In our case, both FA and PA had the same frequency.

Necrosis has been shown to play an important many pathological processes like in many central nervous system and neurodegenerative disorders [24,25], ischemia/reperfusion injuries [21], viral and microbial infections [26,27]. Necrosis might also be playing an important rule in physiological processes like ovulation [28] and embryogenesis [29], In addition, Many chemotheributical agents used for cancer treatment are known to induce death in cancer cells through necrosis [6]. MRS of hyperpolarized [1,4-$^{13}C^{2}$]fumarate can play a big role in studying necrosis *in vivo* in these processes.

Turpentine is a mixture of alkylated aromatic hydrocarbons designed to dissolve fat, and thus they can effectively cause lipid dissolution. Turpentine injection into living tissue provides a robust and easy to control method that causes necrosis and inflammatory response, and therefore can be useful in studying cellular death via necrosis.

In conclusion, we have demonstrated the feasibility of probing the dual enzymatic pathways of [1-^{13}C]pyruvate and [1,4-$^{13}C_2$]fumarate in a clinical dual PET/MR system. The phantom measurements showed that the polarizations values achieved for two substrates when polarized together were comparable to those values obtained when each substrate is polarized individually. The experimental setup can be very useful to investigate the ability of various hyperpolarized ^{13}C substrates and PET tracers, like ^{18}F-FDG, malate/fumarate ratio and lactate/pyruvate ratio in monitoring the response of cancer tissues to treatment. The setup also can be used to investigate the correlation between the analogous PET and ^{13}C MRS markers. Moreover, clinical PET/MR scanners, that are becoming widely available, could contribute not only to human clinical routine examinations, but also to biomedical researches in small animals.

Acknowledgment

Adam E. Hansen is gratefully acknowledged for technical support. We would also like to acknowledge the financial support from Danish Research Council (Grant Number 1331-00259A) and the Danish National Research Foundation (Grant Number DNRF124).

Disclosure

Nothing to disclose.

References

1. Ardenkjær-Larsen JH, Fridlund B, Gram A, Hansson G, Hansson L, Lerche MH, Servin R, Thaning M, Golman K. Increase in signal-to-noise ratio of> 10,000 times in liquid-state NMR. *Proceedings of the National Academy of Sciences.* 2003;100(18):10158-10163.
2. Day SE, Kettunen MI, Gallagher FA, Hu DE, Lerche M, Wolber J, Golman K, Ardenkjaer-Larsen JH, Brindle KM. Detecting tumor response to treatment using hyperpolarized 13C magnetic resonance imaging and spectroscopy. *Nature medicine.* 2007;13(11):1382-1387.
3. Witney TH, Kettunen MI, Hu DE, Gallagher FA, Bohndiek SE, Napolitano R, Brindle KM. Detecting treatment response in a model of human breast adenocarcinoma using hyperpolarised [1-13C]pyruvate and [1,4-13C2]fumarate. *British journal of cancer.* 2010;103(9):1400-1406.
4. Kurhanewicz J, Vigneron DB, Brindle K, Chekmenev EY, Comment A, Cunningham CH, Deberardinis RJ, Green GG, Leach MO, Rajan SS, Rizi RR, Ross BD, Warren WS, Malloy CR. Analysis of cancer metabolism by imaging hyperpolarized nuclei: prospects for translation to clinical research. *Neoplasia.* 2011;13(2):81-97.
5. Albers MJ, Bok R, Chen AP, Cunningham CH, Zierhut ML, Zhang VY, Kohler SJ, Tropp J, Hurd RE, Yen YF, Nelson SJ, Vigneron DB, Kurhanewicz J. Hyperpolarized 13C lactate, pyruvate, and alanine: noninvasive biomarkers for prostate cancer detection and grading. *Cancer research.* 2008;68(20):8607-8615.
6. Gallagher FA, Kettunen MI, Hu DE, Jensen PR, Zandt RI, Karlsson M, Gisselsson A, Nelson SK, Witney TH, Bohndiek SE, Hansson G, Peitersen T, Lerche MH, Brindle KM. Production of hyperpolarized [1,4-13C2]malate from [1,4-13C2]fumarate is a marker of cell necrosis and treatment response in tumors. *Proceedings of the National Academy of Sciences of the United States of America.* 2009;106(47):19801-19806.
7. Clatworthy MR, Kettunen MI, Hu DE, Mathews RJ, Witney TH, Kennedy BW, Bohndiek SE, Gallagher FA, Jarvis LB, Smith KG, Brindle KM. Magnetic resonance imaging with hyperpolarized [1,4-(13)C2]fumarate allows detection of early renal acute tubular necrosis. *Proceedings of the National Academy of Sciences of the United States of America.* 2012;109(33):13374-13379.
8. Mignion L, Dutta P, Martinez GV, Foroutan P, Gillies RJ, Jordan BF. Monitoring Chemotherapeutic Response by Hyperpolarized 13C-Fumarate MRS and Diffusion MRI. *Cancer research.* 2014.
9. Hill DA, Hill JJ. An Investigation of Pol an" zed-Proton Target Materials by Differential Calorimetry-Preliminary Results. 1980.
10. Karlsson M, Jensen P, Duus J, Meier S, Lerche M. Development of Dissolution DNP-MR Substrates for Metabolic Research. *Appl Magn Reson.* 2012;43(1-2):223-236.
11. von Morze C, Bok RA, Reed GD, Ardenkjaer-Larsen JH, Kurhanewicz J, Vigneron DB. Simultaneous Multiagent Hyperpolarized (13)C Perfusion Imaging. *Magnetic resonance in medicine : official journal of the Society of Magnetic*

Resonance in Medicine / Society of Magnetic Resonance in Medicine. 2014;72(6):1599-1609.

12. von Morze C, Larson PE, Hu S, Yoshihara HA, Bok RA, Goga A, Ardenkjaer-Larsen JH, Vigneron DB. Investigating tumor perfusion and metabolism using multiple hyperpolarized 13 C compounds: HP001, pyruvate and urea. *Magnetic resonance imaging.* 2012;30(3):305-311.
13. Wilson DM, Keshari KR, Larson PEZ, Chen AP, Hu S, Van Criekinge M, Bok R, Nelson SJ, Macdonald JM, Vigneron DB, Kurhanewicz J. Multi-compound Polarization by DNP Allows Simultaneous Assessment of Multiple Enzymatic Activities In Vivo. *Journal of magnetic resonance (San Diego, Calif. : 1997).* 2010;205(1):141-147.
14. Witney TH, Kettunen MI, Hu De, Gallagher FA, Bohndiek SE, Napolitano R, Brindle KM. Detecting treatment response in a model of human breast adenocarcinoma using hyperpolarised [1-(13)C]pyruvate and [1,4-(13)C(2)]fumarate. *British Journal of Cancer.* 2010;103(9):1400-1406.
15. Ardenkjaer-Larsen JH, Leach AM, Clarke N, Urbahn J, Anderson D, Skloss TW. Dynamic nuclear polarization polarizer for sterile use intent. *NMR in biomedicine.* 2011;24(8):927-932.
16. Malinowski RM, Lipsø KW, Lerche MH, Ardenkjær-Larsen JH. Dissolution Dynamic Nuclear Polarization capability study with fluid path. *Journal of Magnetic Resonance.* 2016.
17. Park I, Larson PE, Tropp JL, Carvajal L, Reed G, Bok R, Robb F, Bringas J, Kells A, Pivirotto P. Dynamic hyperpolarized carbon-13 MR metabolic imaging of nonhuman primate brain. *Magnetic Resonance in Medicine.* 2014;71(1):19-25.
18. Hanahan D, Weinberg RA. Hallmarks of cancer: the next generation. *Cell.* 2011;144(5):646-674.
19. Brindle K. New approaches for imaging tumour responses to treatment. *Nature reviews. Cancer.* 2008;8(2):94-107.
20. Bohndiek SE, Kettunen MI, Hu DE, Witney TH, Kennedy BW, Gallagher FA, Brindle KM. Detection of tumor response to a vascular disrupting agent by hyperpolarized 13C magnetic resonance spectroscopy. *Mol Cancer Ther.* 2010;9(12):3278-3288.
21. Nielsen PM, Eldirdiri A, Bertelsen LB, Jørgensen HS, Ardenkjaer-Larsen JH, Laustsen C. Fumarase activity: an in vivo and in vitro biomarker for acute kidney injury. *Scientific Reports.* 2017;7:40812.
22. Gutte H, Hansen AE, Henriksen ST, Johannesen HH, Ardenkjaer-Larsen J, Vignaud A, Hansen AE, Børresen B, Klausen TL, Wittekind A-MN. Simultaneous hyperpolarized 13C-pyruvate MRI and 18F-FDG-PET in cancer (hyperPET): feasibility of a new imaging concept using a clinical PET/MRI scanner. *American journal of nuclear medicine and molecular imaging.* 2015;5(1):38.
23. Gutte H, Hansen AE, Larsen M, Rahbek S, Henriksen S, Johannesen H, Ardenkjær-Larsen J, Kristensen A, Højgaard L, Kjær A. Simultaneous hyperpolarized 13C-pyruvate MRI and 18F-FDG-PET (hyperPET) in 10 canine cancer patients. *Journal of Nuclear Medicine.* 2015:jnumed. 115.156364.

24. Akiyama H, Barger S, Barnum S, Bradt B, Bauer J, Cole GM, Cooper NR, Eikelenboom P, Emmerling M, Fiebich BL. Inflammation and Alzheimer's disease. *Neurobiology of aging.* 2000;21(3):383-421.
25. Cosi C, Suzuki H, Milani D, Facci L, Menegazzi M, Vantini G, Kanai Y, Skaper S. Poly (ADP-ribose) polymerase: Early involvement in glutamate-induced neurotoxicity in cultured cerebellar granule cells. *Journal of neuroscience research.* 1994;39(1):38-46.
26. Brennan MA, Cookson BT. Salmonella induces macrophage death by caspase-1-dependent necrosis. *Molecular microbiology.* 2000;38(1):31-40.
27. Lenardo MJ, Angleman SB, Bounkeua V, Dimas J, Duvall MG, Graubard MB, Hornung F, Selkirk MC, Speirs CK, Trageser C. Cytopathic killing of peripheral blood CD4+ T lymphocytes by human immunodeficiency virus type 1 appears necrotic rather than apoptotic and does not require env. *Journal of virology.* 2002;76(10):5082-5093.
28. Murdoch W, Wilken C, Young D. Sequence of apoptosis and inflammatory necrosis within the formative ovulatory site of sheep follicles. *Journal of reproduction and fertility.* 1999;117(2):325-329.
29. Chautan M, Chazal G, Cecconi F, Gruss P, Golstein P. Interdigital cell death can occur through a necrotic and caspase-independent pathway. *Current biology.* 1999;9(17):967-S961.

Figure legends

Figure 1

(a) The fluid path that goes into the SPINlab. The path consists of a syringe that contains the dissolution media and sample vial that contains the ^{13}C substrate to be polarized. The two are connected by two concentric tubes. During the dissolution the dissolution medium is transferred through the inner tube to the sample vial where it dissolves the hyperpolarized substrate. The dissolved material flows back through the outer tube lumen toward the syringe and out of the SPINlab via the exit tube. (b) shows schematic draw of the sample vial. The vial is prepared by first adding the PA and then freezing it in LN_2 and then adding the FA. The vial is then kept in LN_2 during the rest of preparation of the fluid path to attain two separate layers in the vial. (c) shows the path of the vial once it is inserted in the SPINlab. The vial is initially placed in the airlock for 20 min to allow the sample to melt. Then, it is lowered in multiple steps, back and forth, along the path until it settles at the He sample pot to avoid excessive increase in temperature at the He pot.

Figure 2

Typical polarization curve (shown with solid lines) starting from time = 0. The dashed and dash-dotted curves in the figure shows the temperature recorded at two positions in the SPINlab, which are the sample pot and the equilibrator, respectively. Before the start of the polarization build-up is the period during which the lowering process takes place. In (a) where multi-steps lowering is used, the variation in temperature at the equilibrator level is smaller compared with (b) where only two lowering steps were used.

At the helium pot, the temperature stays almost constant for multi-steps lowering, while for the two-step lowering there is a rise in temperature for some time (about 25 minutes) before the temperature settles at 0.8 K.

Figure 3

The expected positions of the peaks of interest following the administration of FA and PA. The figure illustrates that the ^{13}C spectrum is sparse allowing co-polarization and simultaneous imaging of [1,4-$^{13}C_2$]fumarate and [1-^{13}C]pyruvate.

Figure 4

The anatomical axial image of the first rat (a) acquired at the location of the necrotic tissue. The image was acquired with turbo spin echo (TR= 5.7 s, TE= 84 ms, echo train length of 18, number of phase encoding steps 234, Number of averages of 5, final matrix size of 256x256 covering a FOV of 100 mm x 100 mm with slice thickness of 2 mm). (b) shows the spectrum at the necrotic tissue with the fumarate peak and the malate doublet. Clear malate signal can be observed in the spectrum. The small peak at the right of the spectrum at 165 ppm is due to fold over of the ^{13}C-urea phantom. (c) and (d) shows the metabolic maps of fumarate and malate, respectively. Notice that the malate production is confined to the necrotic region.

Figure 5

The anatomical axial image of the second rat (a) acquired at the location of the necrotic tissue. The proton image was acquired similar to Figure 4-a. A coronal maximum intensity projection image which shows the FDG uptake by the different organs is illustrated in (b). (c) shows an axial slice with 12 mm thickness (sum of 6 adjacent

slices) with the FDG uptake in a plane containing the necrotic tissue. (d) and (e) show the phased real part spectra at the necrotic tissue, the blue box in (a), acquired for single injection of FA and dual injection of FA and PA, respectively. The malate signal can be seen in both spectra. In dual FA and PA experiment additional peaks are observed for lactate, alanine, pyruvate-hydrate and bicarbonate. (f to i) shows the metabolic maps of pyruvate, lactate, fumarate and malate respectively.

Tables

Table 1: Solid state DNP build-up data for three different samples with two different loading profiles

Concentrations (FA/AH111501)	2.8 M/15 mM		3.6 M/8 mM		3.6 M/12 mM	
No. insertion steps	ONE	TWO	ONE	TWO	ONE	TWO
Build-up time constant (s)	9448	5913	6718	6765	2725	3659
S(t=∞) (a.u.)	1311	1054	740	1140	969	993
Liquid-state polarization(%)	39		38		37	

Table 2: Liquid state polarization and T_1 measurements for the sample with FA (3.6 M) with 8 mM of AH111501 radical

n=5	Fumarate		Pyruvate
	Dual	Single	Dual
T_1 (s)	57±2	58±2	70±3
Polarization (%)	35±5	37±6	37±6

538 **Figure**

539 **Figure 1**

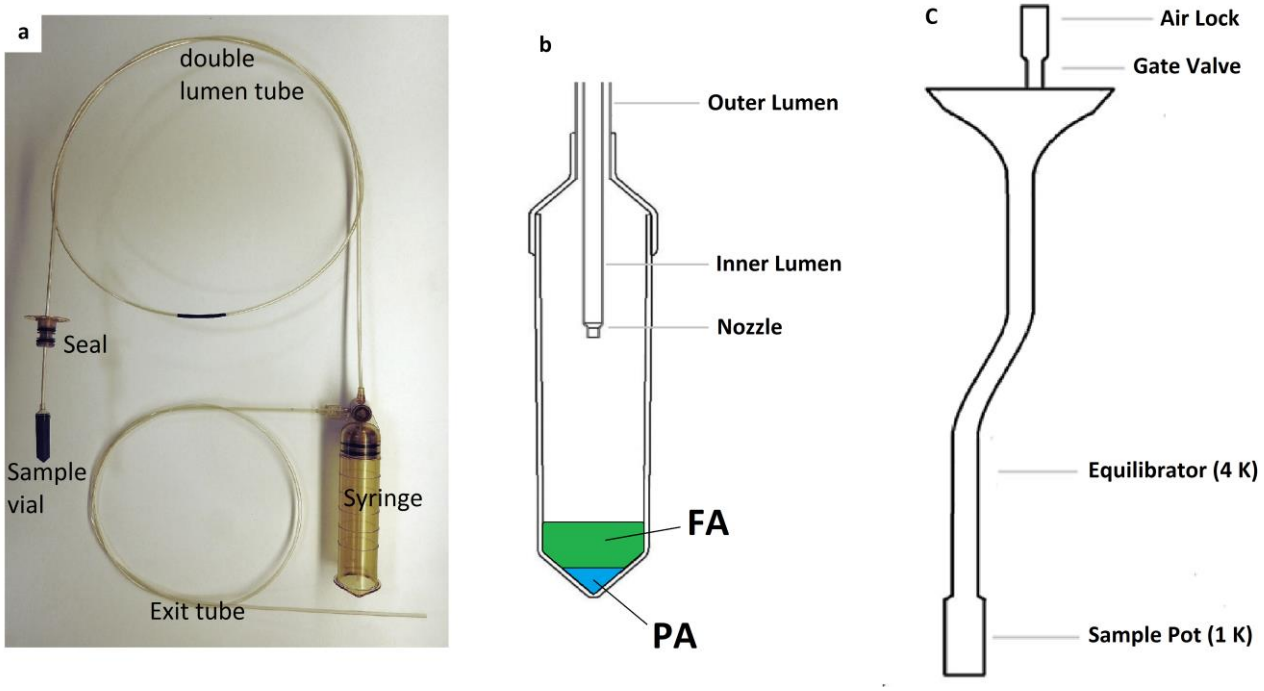

540

541

542 **Figure 2**

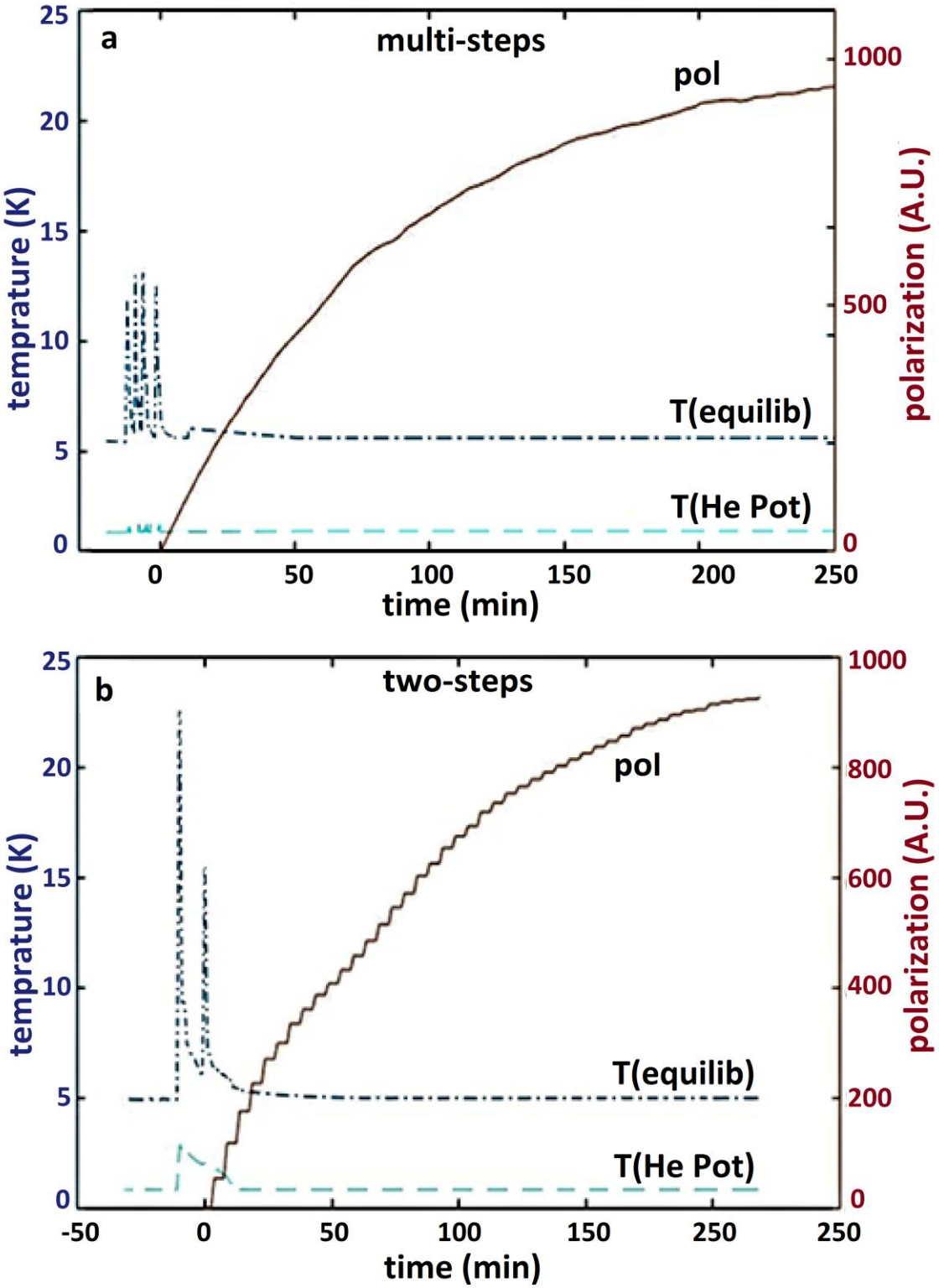

543

Figure 3

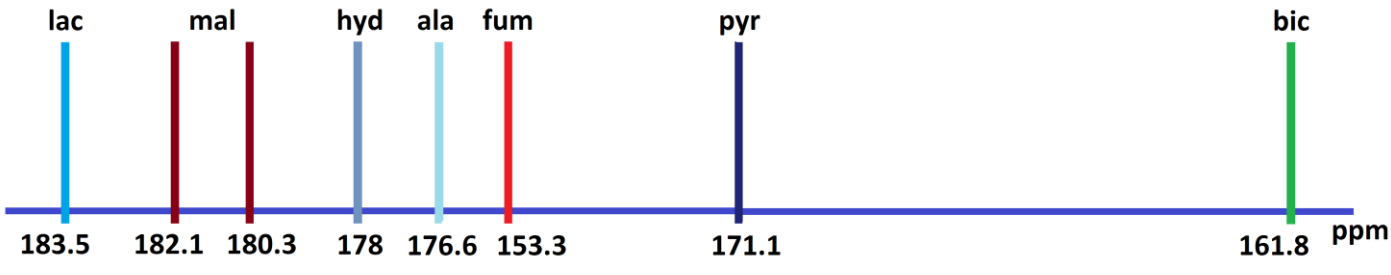
lac
mal
hyd
ala
fum
pyr
bic
183.5
182.1
180.3
178
176.6
153.3
171.1
161.8
ppm

Figure 4

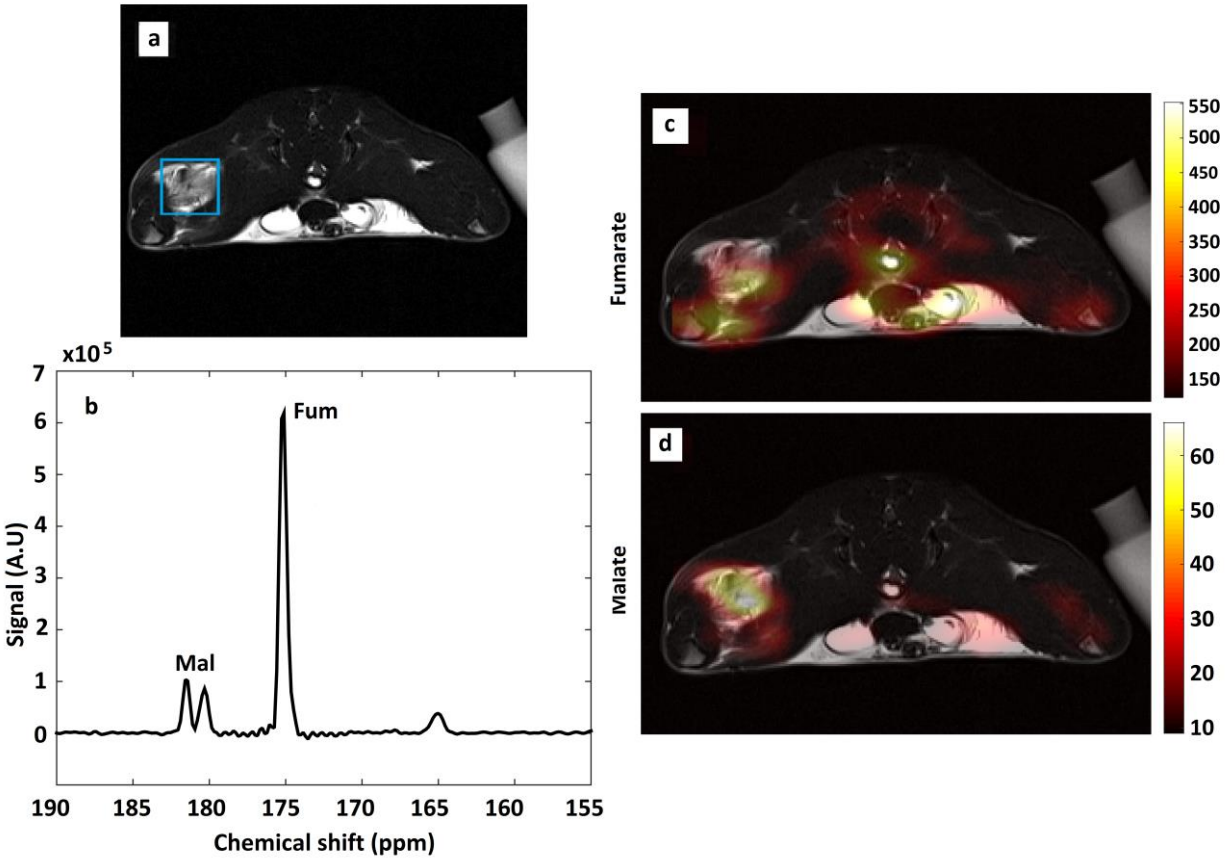
a
b
x10^5
Signal (A.U)
Fum
Mal
Chemical shift (ppm)
c
Fumarate
d
Malate

551 **Figure 5**

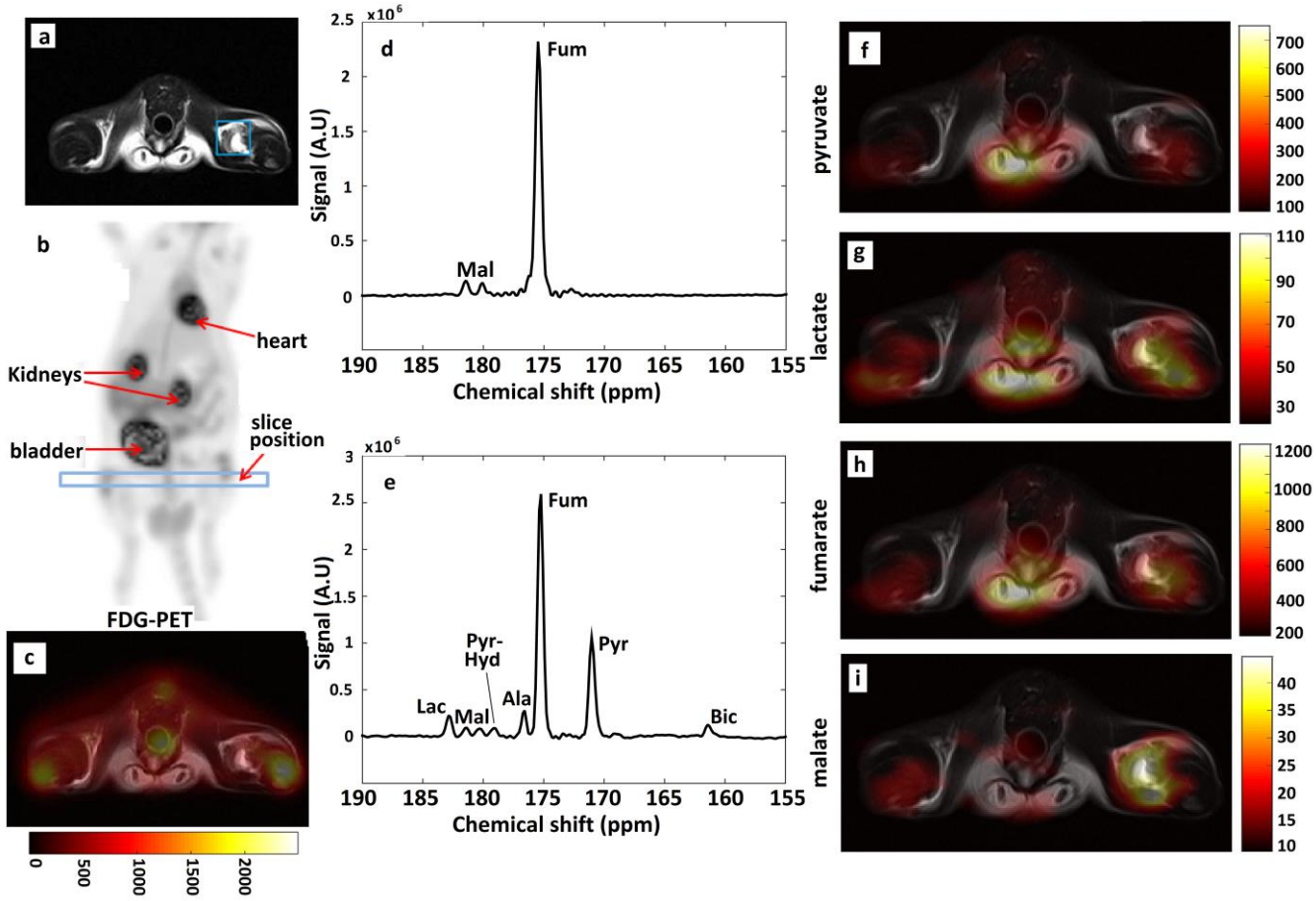

552

C

Fumarase activity: an in vivo and in vitro biomarker for acute kidney injury

This paper was published in *Scientific Reports* 2017 (published online prior to inclusion in an issue, DOI: 10.1038/srep40812). Some of the results from this paper were presented in the *Annual Meeting of International Society for Magnetic Resonance in Medicine* in May 2016.

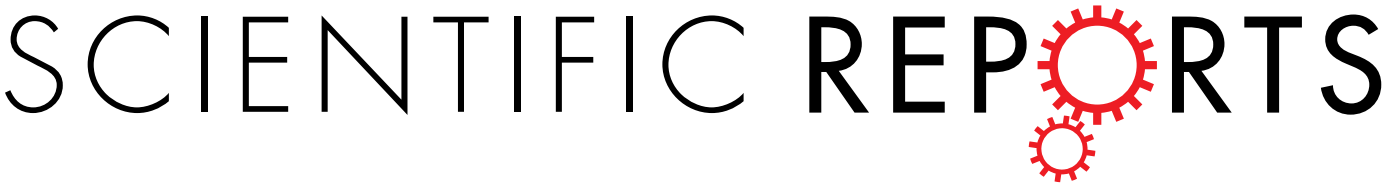

OPEN

Fumarase activity: an *in vivo* and *in vitro* biomarker for acute kidney injury

Received: 16 September 2016
Accepted: 12 December 2016
Published: 17 January 2017

Per Mose Nielsen[1], Abubakr Eldirdiri[2], Lotte Bonde Bertelsen[1], Hans Stødkilde Jørgensen[1], Jan Henrik Ardenkjaer-Larsen[2,3] & Christoffer Laustsen[1]

Renal ischemia/reperfusion injury (IRI) is a leading cause of acute kidney injury (AKI), and at present, there is a lack of reliable biomarkers that can diagnose AKI and measure early progression because the commonly used methods cannot evaluate single-kidney IRI. Hyperpolarized [1,4-$^{13}C_2$]fumarate conversion to [1,4-$^{13}C_2$]malate by fumarase has been proposed as a measure of necrosis in rat tumor models and in chemically induced AKI rats. Here we show that the degradation of cell membranes in connection with necrosis leads to elevated fumarase activity in plasma and urine and secondly that hyperpolarized [1,4-$^{13}C_2$]malate production 24 h after reperfusion correlates with renal necrosis in a 40-min unilateral ischemic rat model. Fumarase activity screening on bio-fluids can detect injury severity, in bilateral as well as unilateral AKI models, differentiating moderate and severe AKI as well as short- and long-term AKI. Furthermore after verification of renal injury by bio-fluid analysis the precise injury location can be monitored by *in vivo* measurements of the fumarase activity non-invasively by hyperpolarized [1,4-^{13}C]fumarate MR imaging. The combined *in vitro* and *in vivo* biomarker of AKI responds to the essential requirements for a new reliable biomarker of AKI.

Acute kidney injury (AKI)[1–3] occurs in 1.9% of all hospital in-patients[4]. The illness is especially common in critically ill patients, and the prevalence in this group is >40% at admission to the intensive-care unit if sepsis is present[4]. The underlying causes of AKI include sepsis, toxins, and urethral obstruction. However, the main contributor is renal ischemia/reperfusion injury (IRI), which accounts for up to 47% of all cases of AKI[2]. IRI can be caused by kidney transplants, hypovolemia, cardiogenic shock, and renal vascular diseases[2,5]. The effective treatment of AKI should begin at the earliest sign of renal dysfunction, but the current preferred biomarkers of AKI such as plasma creatinine, creatinine clearance (CrCl), glomerular filtration rate (GFR) determined using Inulin or Cr-EDTA[6,7] and blood urea nitrogen (BUN)[8,9] lack specificity and sensitivity as they only rise substantially above the normal levels once renal damage has already occurred.

The parameters listed above reflect the residual glomerular filtration rate rather than injury itself[10]. Alternatively, renal biopsies can identify single-kidney or local IRI by measuring the protein or mRNA expression levels of lactate dehydrogenase, kidney injury molecule 1 (KIM-1), and neutrophil gelatinase-associated lipocalin (NGAL)[11]. Renal biopsies provide high sensitivity, but are associated with the high risk of additional chronic injury and hemorrhage that should ideally be avoided in critically ill patients[12,13]. Thus, precise and non-invasive methods, preferably imaging methods or the sampling of urine and blood to continuously and directly evaluate the severity of single-kidney IRI in patients and animals, are urgently needed.

Hyperpolarization of ^{13}C-labeled molecules leads to a >10,000-fold increase in signal compared to conventional magnetic resonance imaging (MRI)[14]. This signal enhancement allows real-time imaging of metabolic pathways using ^{13}C-labeled endogenous substrates[15]. We have recently demonstrated metabolic alterations in post-ischemic unilateral IRI rats following hyperpolarized [1-^{13}C]pyruvate infusion[16]. Showing an upregulation of the anaerobic pathways, similarly to what has been demonstrated in diabetic kidney[17–19], albeit lower total turnover, most likely caused by necrosis. In principle any small molecular probe can be hyperpolarized as long as they contain a nuclear spin, typically ^{13}C[20,21]. Currently there is an large array of commercial available hyperpolarized of ^{13}C-labeled molecules which have been utilized in many different animal models of cancer[22,23], myocardial ischemia[24–26] and renal diseases[27–30], and more recently in patients and healthy volunteers[31,32] Additionally,

[1]MR Research Centre, Department of Clinical Medicine, Aarhus University, Aarhus, Denmark. [2]Department of Electrical Engineering, Technical University of Denmark, Kgs Lyngby, Denmark. [3]GE Healthcare, Broendby, Denmark. Correspondence and requests for materials should be addressed to C.L. (email: cl@clin.au.dk)

	Body weight (g)	Kidney weight (mg/g bodyweight)	Urine output (μL/min/kg)	Plasma creatinine (μmol/L)	CrCl (mL/min/kg)	BUN (μL/min/kg)
Pre Surgery (n = 6)	247 ± 6.3	—	30.7 ± 9.4	15 ± 1.7	10.1 ± 1.5	4.9 ± 0.7
Post Surgery (n = 6)	243 ± 9.5 (NS)	IRI 4.5 ± 0.1* CL 3.7 ± 0.04	41.6 ± 8.5 ns.	28.7 ± 2.4*	5.7 ± 3.2*	7.0 ± 0.5*

Table 1. Renal function parameters before and after surgery. CL = contralateral kidney; IRI = ischemia/reperfusion injury; CrCl = creatinine clearance; BUN = blood urea nitrogen; NS = not statistically significant. Values are given as mean ± s.e.m. *Indicate significant difference of P-value < 0.05.

[1,4-^{13}C]fumarate has been shown to be a reliable imaging biomarker for monitoring cellular necrosis[33] in a rat model of xenograft tumors and subsequently in a rat model with folic acid-induced AKI[34]. These previous results showed an increased ^{13}C-malate signal in kidneys with progressive tubular necrosis. In intact cells, the uptake and subsequent hydration of fumarate to malate occurs too slowly compared to the hyperpolarization signal decay, whereas in necrotic cells the cellular integrity is broken, allowing fumarate to enter the cell and fumarase to leak out. From this point, the enzymatic conversion via fumarase occurs rapidly and the malate product is detectable by MRI. This might also cause the release of fumarate in the urine and blood, yielding a biomarker detectable in the plasma and urine.

Based on the above, we question if hyperpolarized [1,4-^{13}C]fumarate can be used to asses renal necrosis in connection with IRI, and will be associated with fumarase activity in both urine and blood.

Results

A significantly elevated kidney weight ($p = 0.001$) following 40 min of unilateral ischemia and 24 h of reperfusion was observed. A tendency towards a reduction of body weight of 1.5% ± 4.5% ($p = 0.46$) and an increase in urine output of 52% ± 70% ($p = 0.11$) was observed, but did not reach statistical significance. Functional kidney parameters showed consistent signs of renal IRI with an elevated plasma creatinine level of 91% ($p = 0.0002$) and a reduced CrCl and BUN level of 44% ($p = 0.04$) and 30% ($p = 0.003$), respectively, when comparing pre-surgery with post-surgery values (Table 1). Figure 1 shows representative histological sections with hematoxylin and eosin stain from a CL kidney and a post-ischemic kidney. The CL kidney showed normal intact tubular epithelial cells compared to the post-ischemic kidney, with tubular lumina filled with cellular debris, complete sloughing of tubular epithelium, interstitial edema, and glomerular edema (Fig. 1A,B). The classical cortical kidney injury markers NGAL and KIM-1 were significantly elevated ($p = 0.01$ and $p = 0.03$) compared to those in the CL kidney (Fig. 1C,D). An elevated malate/fumarate ratio of 339% ($p = 0.002$) (Fig. 2C) in the ischemic kidneys compared that in the CL kidney was found. In order to examine the relationship between renal cortical injury and malate/fumarate ratio, the correlation between NGAL and KIM-1 levels with the malate/fumarate ratio was investigated. A linear correlation was found in both cases ($R^2 = 0.78$, $p = 0.008$ and $R^2 = 0.80$, $p = 0.006$, respectively) (Fig. 3A,B). To investigate the localization of fumarase in connection with renal IRI, molecular fumarase activity measurements were performed. Fumarase activity in the mitochondrial fraction and the whole tissue was significantly reduced by 48% ($p = 0.002$) and 54% ($p = 0.007$) when compared with the values of the CL (Fig. 4A,B). Fumarase activity measured in urine and plasma was significantly elevated ($p = 0.004$ and $p = 0.0001$), with practically no activity observed under control conditions (Fig. 4C,D). Fumarase activity measured in urine samples collected immediately after sacrifice was correlated with malate/fumarate ratios ($R^2 = 0.77$, $p = 0.02$) (Fig. 5A), as was plasma fumarase activity ($R^2 = 0.72$, $p = 0.03$) (Fig. 5B). A parallel investigation of fumarase activity in the urine of IRI and control rats showed a time and severity-dependent increase in urine fumarase activity. Elevated activity at as early as 30 min after reperfusion, followed by a reduction 24 h after and another increase in activity after 7 days was observed (Fig. 5C,D). Bilateral IRI was associated with a less pronounced increase in activity in the urine, while the plasma activity was greatly increased (Fig. 5C,D).

Discussion

The main finding of this study was the significantly elevated hyperpolarized malate/fumarate ratio in response to 40 min of unilateral ischemia and 24 h of reperfusion, and a time and severity-dependent increase in urine and plasma fumarase activity. This elevation correlated with the levels of the well-known renal cortical injury markers KIM-1 and NGAL. Furthermore, the findings verified the original report of Clatworthy *et al.*[33], who demonstrated that an elevated malate/fumarate ratio could be used as a direct marker of necrosis in renal disease.

All rats included in this study showed evidence of injury in the post-ischemic kidney 24 h after surgery according to the functional kidney parameters plasma creatinine, CrCl, and BUN. Additionally, the histological hematoxylin and eosin-stained sections showed typical signs of tubular necrosis. The molecular markers NGAL and KIM-1 were highly upregulated in the post-ischemic kidney. Although these markers are not specific to necrosis[35,36], they do indicate general injury in the cortical region of the post-ischemic kidney, which in this study was directly correlated with the malate/fumarate ratio. The reduced fumarase activity measured in the post-ischemic kidney compared to that in the CL kidney (whole-tissue and mitochondrial fraction) might seem counter-intuitive, as the malate/fumarate ratio is higher in the post-ischemic kidney. However, as the polarization-relaxation decay of [1,4-$^{13}C_2$]fumarate is fast compared to the uptake of fumarate through dicarboxylate transporters[37], malate production is blocked in the CL kidney despite the relatively higher fumarase activity. Meanwhile, in the post-ischemic kidney, the observed signal of hyperpolarized [1,4-$^{13}C_2$]malate is interpreted as the release of fumarase caused by cellular membrane disruption in connection with necrosis[38] to the interstitial space, plasma, and urine. Once released from the cells, fumarase, a highly potent enzyme, will produce malate in

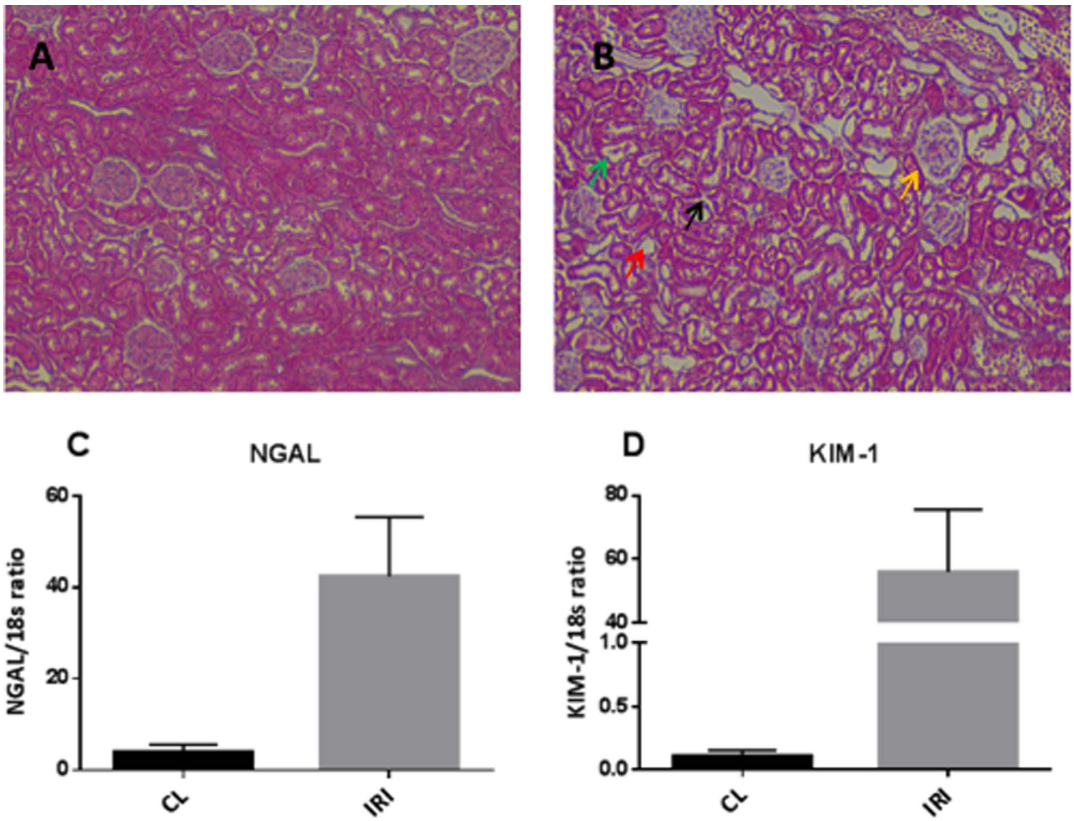

Figure 1. Verification of ischemia-reperfusion injury. Representative histological sections are shown in (**A**) a CL kidney showing normal intact tubular cells and glomeruli, and (**B**) a post-ischemic kidney showing a cellular cast in the tubular lumina (green arrow), complete sloughing of tubular epithelium (red arrow), interstitial edema (black arrow), and glomerular edema (yellow arrow). Magnification 20×, HE stain. The relative expression of injury markers indicated significant upregulation of (**A**) NGAL ($p = 0.0145$, $n = 6$) and (**B**) KIM-1 ($p = 0.0256$, $n = 6$). A paired two-sided Student's *t*-test was used to compare the CL and IRI kidneys. Blocks indicate means, while bars indicate the s.e.m. CL = contralateral kidney; HE = hematoxylin and eosin; NGAL = neutrophil gelatinase-associated lipocalin; KIM-1 = kidney injury molecule 1; IRI = ischemia/reperfusion injury.

the presence of fumarate. This is caused by an equilibrium constant favoring malate formation ($K_c = 4.3$, pH 7.5)[39], but also the fact that fumarase requires no co-substrates or co-enzymes to function, meaning that even though fumarase is exclusively intracellular, it functions just as well in the extracellular space under necrotic conditions.

Plasma and urine fumarase activity levels were highly increased after the onset of IRI, and were correlated with the hyperpolarized malate/fumarate ratios. Albeit giving rise to measurements characteristic of IRI, these values, like other blood/urine biomarkers of AKI, were unable to specify which kidney (or both) was suffering from necrotic injury. Several complementary MRI techniques have previously demonstrated promising results for AKI monitoring. Conventional perfusion imaging using either arterial spin labeling or contrast agents, have demonstrated reduced perfusion in the post-ischemic kidney[40,41], similarly recently found with hyperpolarized ^{13}C-urea[42]. Diffusion weighted imaging (DWI), a well-suited imaging marker of renal complications have shown diffusion restrictions already at onset of AKI and this restriction is associate with the severity of AKI, inflammatory cell infiltration and interstitial renal fibrosis[43]. Relaxation mechanisms has been shown to be related to edema, fibrosis and renal (oxygenation blood-oxygen-level-dependent contrast imaging (BOLD))[43–45]. The ability to non-invasively monitor both anatomical, hemodynamic, metabolic renal changes associated with AKI with sufficient sensitivity and specificity, support the use of MRI in both animal and patients studies. The addition of hyperpolarized [1,4-^{13}C]fumarate for local necrosis examinations to this powerful MR toolbox, further improves this toolbox. The combination of urine and plasma fumarase measurement with hyperpolarized MRI procedures shows great promise for future clinical translation. Figure 6 illustrates the proposed mechanisms for the new sensitive biomarker of renal necrosis in AKI. Furthermore, in some cases, the animal's fluid balance and fluid intake after IRI induction are associated with a high degree of variation, which will inevitably be reflected in the levels of plasma and urine fumarase activity. Interestingly, the bilateral IRI model showed comparable fumarase activity in the urine compared to that in the unilateral kidneys. While the plasma activity was significantly elevated, this is most likely due to a reduced urine output in the bilateral cases. The same situation was seen in the 60-min IRI model, wherein the post-ischemic animals had very little urine output, leading to very little secretion of fumarase. Therefore, enzymes released from necrotic tissue are mainly seen in the circulation (plasma fraction). In the

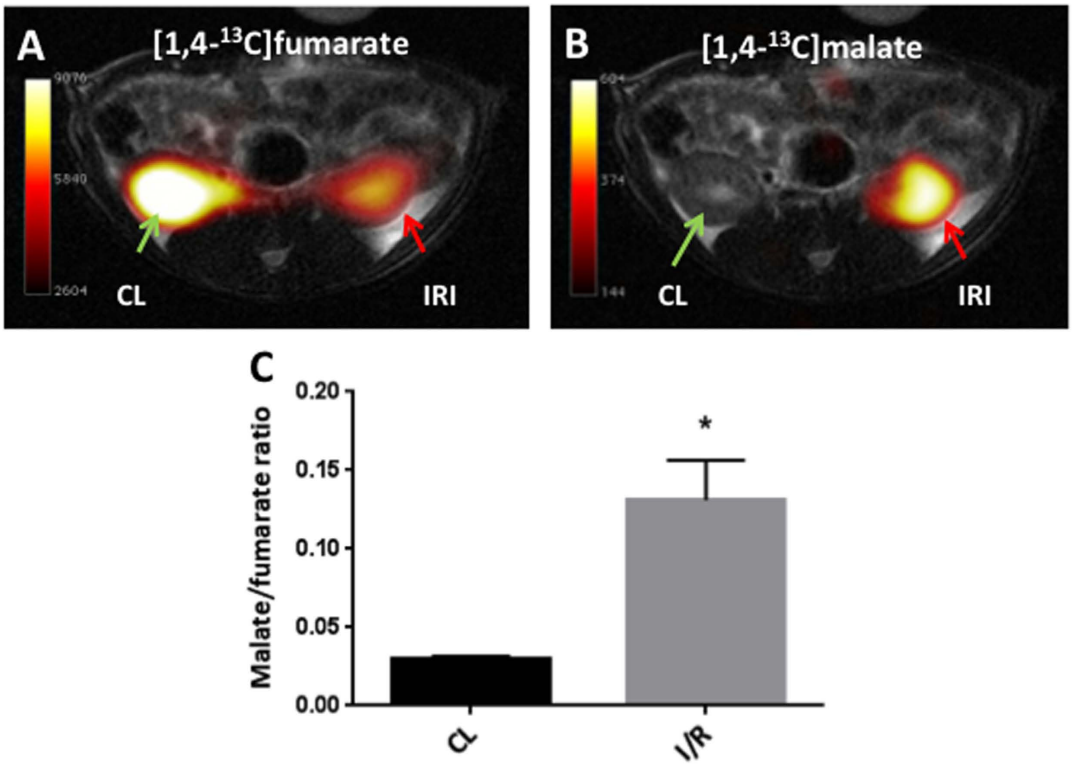

Figure 2. Magnetic resonance imaging maps and malate/fumarate ratios. Representative anatomical ^{1}H kidney sections from the post-ischemic animals overlaid with (**A**) ^{13}C-labeled fumarate images, and (**B**) ^{13}C-labeled malate images. (**C**) A malate/fumarate ratio calculated from each kidney (n = 6 CL, n = 6 IRI), giving rise to an elevated ratio in the post-ischemic kidney (p = 0.0065). The green arrow indicates the CL. The red arrow indicates the IRI kidney. A paired two-sided Student's *t*-test was used to compare the CL and IRI kidneys. Blocks indicate means, while bars indicate the s.e.m. All relevant abbreviations as in Fig. 1.

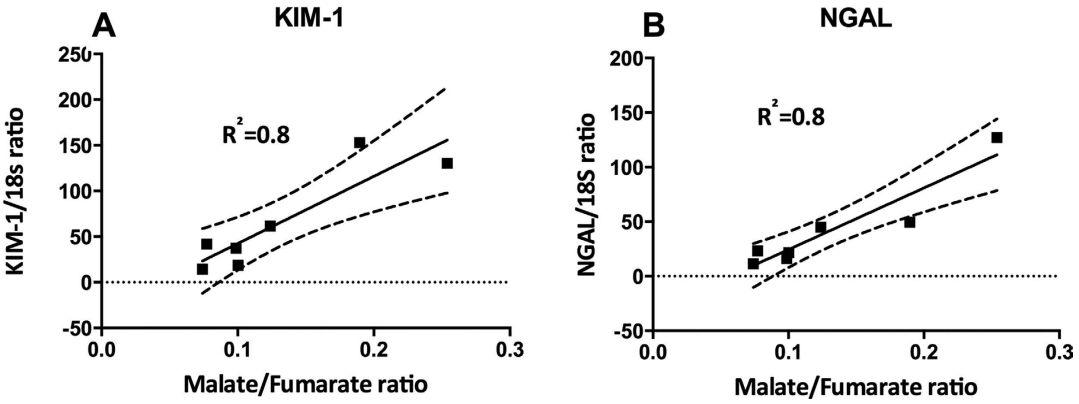

Figure 3. Correlation between renal injury and malate/fumarate ratio. A significant deviation from zero was found between (**A**) NGAL and malate/fumarate ratios (n = 7, p = 0.0017 and $R^2 = 0.88$), and (**B**) KIM-1 and malate/fumarate ratio (n = 7, p = 0.0064, $R^2 = 0.80$). The dashed line indicates the 95% confidence interval. The straight line indicates the regression line. All qPCR measurements were performed in duplicate. All relevant abbreviations as in Fig. 1. qPCR = quantitative PCR.

other IRI cases, there was elevated urine output, which is often seen in early/moderate IRI cases[46]. Therefore, we conclude that fumarase is mainly found in the urine.

In conclusion, these results highlight the potential for following disease progression using a simple urine and plasma test and the verification of the degree and location of the damage with more sensitive imaging tests such as MRI. We demonstrated a correlation between renal necrotic injury in connection with IRI with *in vivo* and *in vitro* fumarase activity, and described the underlying mechanisms of the proposed methods. We believe that the simple measurement of fumarase activity measurement in the blood and urine, in combination with

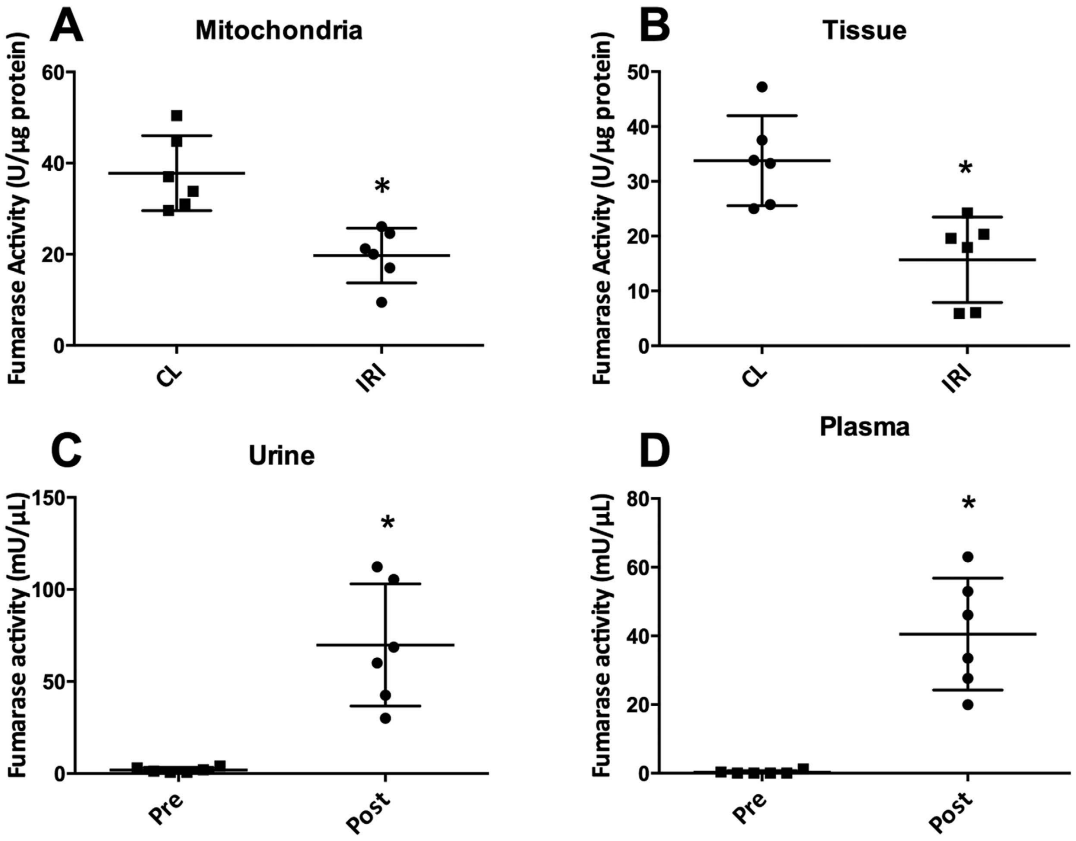

Figure 4. Biochemical analysis of fumarase activity. Fumarase activity was measured in (**A**) the mitochondrial fraction (n = 6, p = 0.0022), (**B**) whole-tissue biopsies (n = 6, p = 0.0067), (**C**) urine (n = 6, p = 0.004), and (**D**) plasma (n = 6, p = 0.0001) isolated from arterial blood samples. A paired two-sided Student's *t*-test was used to compare the CL and IRI kidneys and the pre and post-surgery urine or plasma samples. All activity measurements were performed in duplicate. Tissue and mitochondrial activity was normalized to protein content, while urine and plasma levels were normalized to the sample volume. Blocks indicate means, while bars indicate the s.e.m. All relevant abbreviations as in Fig. 1.

hyperpolarized MRI, holds great promise as a future diagnostic tool for AKI. These findings should serve as a starting point for future research in human subjects.

Methods

Animal models. The imaging experiments were performed on male Wistar rats (weighing 200–250 g). The animals were provided with ad libitum access to a standard rodent diet (Altromin, Germany) and tap water, and were kept under a 12/12-h light-dark cycle at a temperature of 21 ± 2 °C and a humidity of 55 ± 5%. The studies were carried out in accordance with the Danish National Guidelines for animal care, and were approved by the Danish Animal Experiments Inspectorate under the Danish Veterinary and Food Administration (License no. 2013/15-2934-00810).

During surgery (animal order randomized), the animals were placed on a heating pad (CMA 450 temperature controller, Harvard apparatus) to maintain a rectal temperature of approximately 36–37 °C, and respiration was visually monitored. A surgical incision was made in the abdomen, and the left renal artery was carefully dissected. A non-traumatic clamp was placed on the left artery for 40 min to induce ischemia, after which the clamp was released. Reperfusion was visually confirmed. The incision was sutured separately through both the muscle tissue and skin. The contralateral (CL) kidney was left intact, and was used as the control kidney. During surgery, the animals were anesthetized with sevoflurane (induction 6%, sustained 2.5%) mixed with air (2 L/min). At the beginning of surgery, Temgesic (buprenorphine hydrochloride) sublingual tablets were provided subcutaneously (0.05 mg/kg), after which buprenorphine hydrochloride was supplied in the drinking water (0.3 mg/mL) until euthanization. To maintain post-operative water balance, 2 mL of isotonic salt water was injected subcutaneously at the beginning of the operation. Prior to surgery, the rats were kept in metabolic cages. After 24 h in the metabolic cage, urine was collected and the rats were anesthetized for blood sample collection and surgery. After surgery, the rats were again put in metabolic cages. At the time of euthanization (24 h after surgery), arterial blood and urine was collected again to estimate fumarase activity.

A total of seven animals were used for the imaging experiments. From six of these animals, urine and blood samples were successfully extracted and used to measure fumarase activity (unsuccessful blood sampling lead to the loss of blood and urine measurements from one animal). The same seven animals were then used for

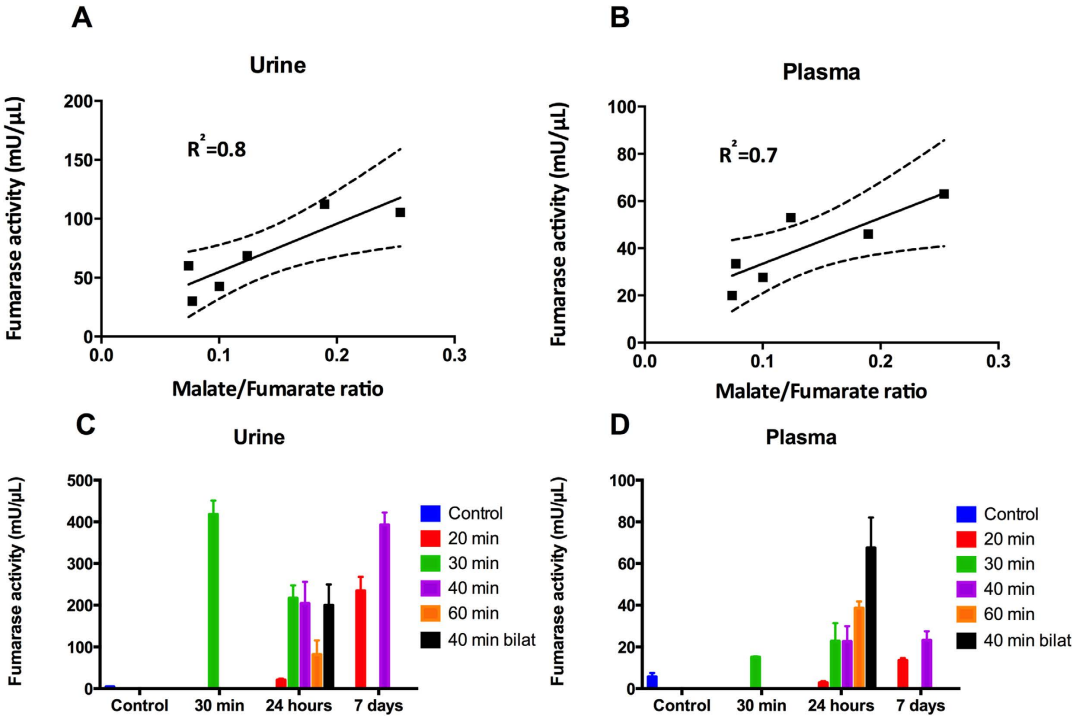

Figure 5. Correlation between urine and plasma fumarase activity and fumarase activity with varying degrees of ischemia/reperfusion injury. A deviation from zero was found between (**A**) Urine fumarase activity and fumarate/malate ratio ($n = 6$, $p = 0.021$, $R^2 = 0.77$.), and (**B**) Plasma fumarase activity and fumarate/malate ratio ($n = 6$, $p = 0$, $R^2 = 0.722$). The dashed line indicates the 95% confidence interval. The straight line indicates the regression line. Fumarase activity in 30-min/30-min IRI plasma ($p = NS$) and urine ($p \leq 0.001$), in 20-min/1-day IRI plasma ($p = NS$) and urine ($p = NS$), in 40-min/1-day IRI plasma ($p = NS$) and urine ($p = 0.0005$), in 20-min/1-week IRI plasma ($p = NS$) and urine ($p = 0.0001$), in 40-min/1-week IRI plasma ($p = NS$) and urine ($p \leq 0.0001$), in 40-min/1-day bilateral IRI plasma ($p \leq 0.0001$) and urine ($p = 0.0006$), in 30-min/1-day IRI plasma ($p = NS$) and urine ($p = 0.0003$) and in 60-min/1-day IRI plasma ($p = 0.0091$) and urine ($p = NS$). In all examples lists, the length of the period of ischemia is given first, followed by that of the period of reperfusion. One-way ANOVA with a Holm-Sidak's multiple comparisons test was used to compare values between the varying degrees of IRI. All relevant abbreviations as in Fig. 1. ANOVA = analysis of variance; NS = not statistically significant.

quantitative polymerase chain reaction (qPCR) measurements of tissue and mitochondrial fumarase activity following 40 min of unilateral ischemia and 24 h of reperfusion.

Urine and plasma sampling was performed on a total of 42 animals. The animals were placed in groups of six, and varying degrees of IRI were then induced. One group was exposed to 30 min of ischemia and 30 min of reperfusion. Two groups were exposed to 20 min and 40 min of ischemia, and urine and plasma samples were collected after 24 h and 1 week of reperfusion. Two groups were exposed to 30 min and 60 min of ischemia and 24 h of reperfusion. One group was exposed to 40 min of bilateral ischemia followed by 24 h of reperfusion. Finally, a sham-operated group was included to serve as a control.

Renal histology. A 2-mm kidney section was dissected from both the CL kidney and post-ischemic kidney from each rat at the time of euthanasia. The kidney sections were fixed in 4% paraformaldehyde for 2 h and washed 3 times (10 min) with 0.01 M phosphate-buffered saline. The fixed kidneys were then dehydrated, embedded in paraffin, and cut into 2-µm sections on a rotary microtome (Leica Microsystems A/S, Herlev, Denmark). The paraffin-embedded sections were stained with hematoxylin and eosin to evaluate the presence of tubular necrosis. Evaluation was performed blinded under high magnification (20x). Representative images are shown at 20x magnification.

Activity assays. Fumarase activity was measured in plasma, urine, whole renal cortex tissue, and mitochondrial fractions according to the manufacturer's instructions (Sigma Aldrich, Brøndby, Denmark). Fumarase activity in the mitochondria and tissue was normalized to the amount of protein in the sample. Plasma and urine fumarase activity was normalized to the amount of sample added to the assay. The mitochondrial fraction was isolated using Dounce homogenization of freshly dissected renal tissue followed by several centrifugal steps. Mitochondrial purity was verified by Western blotting. The tissue and mitochondrial fractions were then homogenized in the fumarase assay buffer. Analysis was performed in 96-well costar half plates using a PHERAstar FS micro plate reader (BMG Labtech, Birkerød, Denmark). Urine and/or plasma were distributed

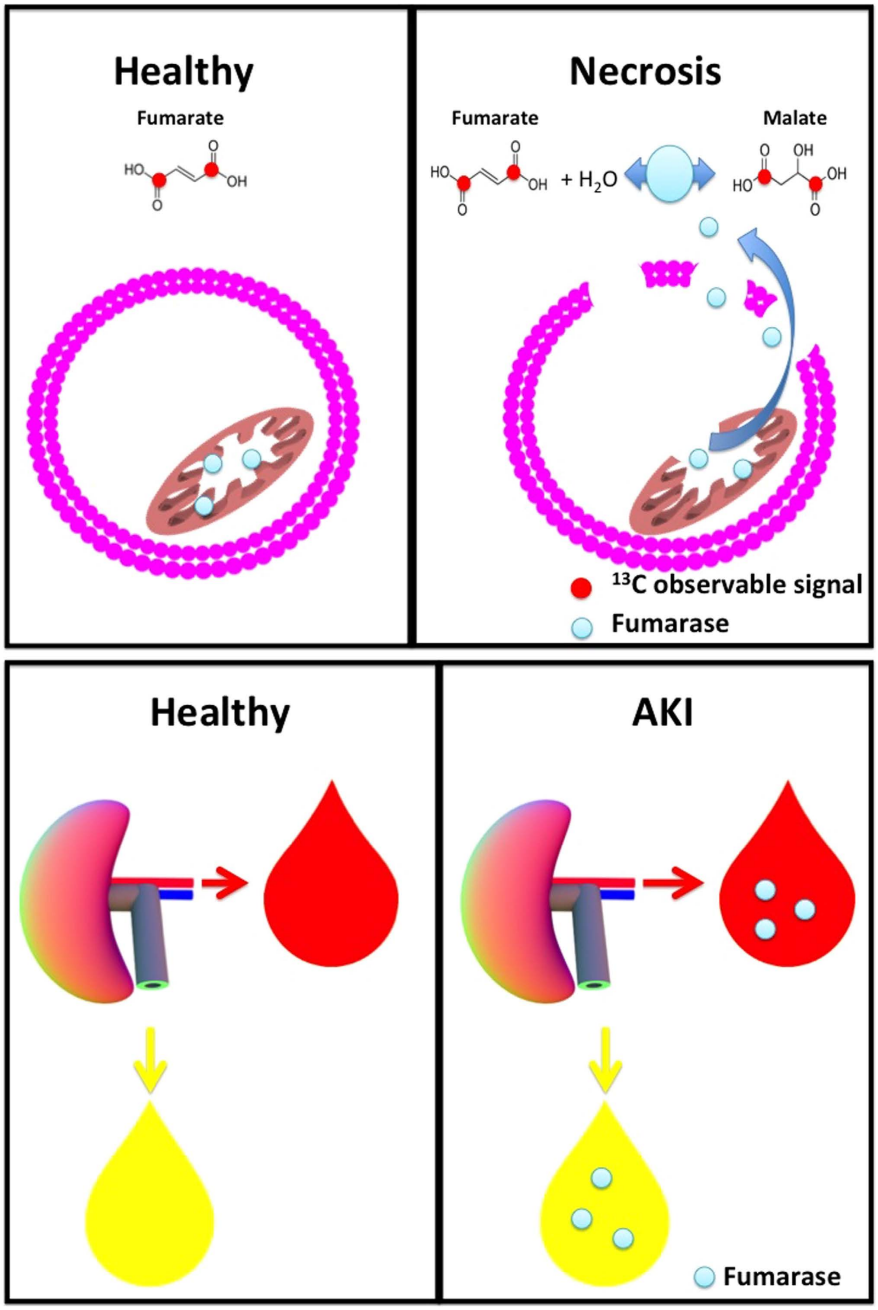

Figure 6. Proposed hypothesis for the sensitive biomarker of renal necrosis in AKI. In healthy cells the transport of hyperpolarized [1,4-^{13}C]fumarate across the cell membrane is slow compared to the decay of the hyperpolarized signal and thus no conversion to [1,4-^{13}C]malate via fumarase is seen. In necrotic cells the plasma membrane is compromised and thus fumarase is freely available for the substrates [1,4-^{13}C]fumarate and water to convert to [1,4-^{13}C]malate. Additionally in the healthy rat little or no fumarase are present in blood or urine, however following AKI both blood and urine show necrosis dependent fumarase activity.

without pre-treatment in 96-well costar half plates. Fumarase activity in urine was assessed at a wavelength of 670 nm instead of the usual 650 nm because of the presence of background interference.

RNA extraction and quantitative PCR. Total RNA was isolated from the renal cortex using a NucleoSpin RNA II mini kit according to the manufacturer's instructions (AH diagnostics, Aarhus, Denmark). RNA was quantified by spectrophotometry and stored at −80 °C. cDNA synthesis was performed with a RevertAid First strand cDNA synthesis kit (MBI Fermentas, Burlington, Canada). qPCR was performed using Maxima SYBR Green qPCR Master Mix according to the manufacturer's instructions (AH diagnostics, Aarhus, Denmark). Briefly, 100 ng of cDNA was used as a template for PCR amplification. The specificity of products was confirmed by melting curve analysis and gel electrophoresis. Primer sequences used included: 18 s forward 5′-CAT GGC CGT TCT TAG TTG-3′ and reverse 5′-CAT GCC AGA GTC TCG TTC-3′ designed from ascension no: M11188;

KIM-1 forward 5′-CCA CAA GGC CCA CAA CTA TT-3′, and reverse 5′-TGT CAC AGT GCC ATT CCA GT-3′ designed from ascension no: AF035963; and NGAL forward 5′-GAT CAG AAC ATT CGT TCC AA-3′ and reverse 5′-TTG CAC ATC GTA GCT CTG TA-3′ designed from ascension no: BC089053.

Hyperpolarized experiments. At the MRI scanning session 24 h after IRI surgery, tail vein catheterization was performed for hyperpolarized [1,4-$^{13}C_2$]fumarate administration. The animals were placed in a clinical 3 T MRI scanner (GE Healthcare, Waukesha, US) for imaging. Throughout the experiment, the animals were anesthetized with sevoflurane (2.5% sevoflurane and 2 L/min air). Rectal temperature, pO_2, and respiration were monitored throughout the MRI session. Each animal was injected with 1.5 mL of hyperpolarized 30 mM [1,4-$^{13}C_2$]fumarate. The pH was 7.4 and the solution was isotonic.

The [1,4-$^{13}C_2$]fumarate was polarized in a SPINlab based on Ardenkjaer-Larsen *et al.*'s original polarizer design[47]. (GE Healthcare, Brøndby, Denmark). The [1,4-$^{13}C_2$]fumarate sample was prepared by dissolving [1,4-$^{13}C_2$]fumaric acid (FA) (Cambridge Isotopes, Cambridge, UK) to a final concentration of 3.6 M in dimethyl sulfoxide containing the trityl radical (12 mM AH111501, GE Healthcare, Brøndby, Denmark). The fluid path was prepared by placing 100 μL (about 350 μmol) of the FA solution in the sample cup and then freezing it in liquid nitrogen. The remainder of the fluid path preparation was performed according to the manufacturer's instructions. The FA solution was allowed to melt for 10–30 min before lowering the fluid path into the helium bath. The sample vial was lowered in a fast two-step scheme to avoid the crystallization of the FA in the sample. The sample was polarized for approximately 3 h to a reproducible polarization of approximately 40%. The dissolution syringe was filled with approximately 15 g of a dissolution media (sterile water with 0.1 g/L EDTA). After dissolution, the sample was mixed with 0.54 g of neutralizing buffer (sterile water with 0.72 M NaOH, 0.4 M TRIS, and 0.1 g/L EDTA).

MRI scans were performed using a 3 T clinical MRI system (GE Healthcare, Brøndby, Denmark) equipped with a dual tuned $^{13}C/^{1}H$ volume rat coil (GE Healthcare, Brøndby, Denmark). A slice-selective ^{13}C IDEAL spiral sequence was used to detect hyperpolarized [1,4-$^{13}C_2$]fumarate, and images were acquired every 5 s, initiated 20 s after the start of injection. The spiral acquisition was performed using a flip angle of 10°, 11 IDEAL echoes, and one initial spectrum per IDEAL encoding[48]. The following parameters were also used: TR/TE/ΔTE = 100 ms/0.9 ms/1.45 ms; field of view = 80 × 80 mm^2; 5 × 5 mm resolution interpolated to a 0.3-mm resolution; and an axial slice thickness of 15 mm covering both kidneys. The $^{13}C/^{1}H$ images were converted to the DICOM format and analyzed using Osirix software[49]. Images of [1,4-$^{13}C_2$]fumarate and [1,4-$^{13}C_2$]malate were overlaid on anatomical ^{1}H images: representative images are provided in Fig. 3A,B. Analysis was performed according to the region of interest (ROI). The ROIs were placed around each kidney on the ^{1}H images and transferred to the ^{13}C images. The area under the time curve ratio between the hyperpolarized [1,4-$^{13}C_2$]malate signal and the hyperpolarized [1,4-$^{13}C_2$]fumarate signal from each individual kidney was calculated[50].

Statistics. All data are presented as means ± s.e.m. Normality was assessed with quantile plots. A P-value < 0.05 was considered statistically significant. A paired Student's *t*-test was used to compare values between the CL kidney and the post-ischemic kidney. The linear correlation was tested between the kidney injury markers Kim-1, NGAL, and the corresponding malate/fumarate ratio.

One-way analysis of variance with a Holm-Sidak's multiple comparisons test was used to evaluate fumarate activity in the urine and blood collected from animals with varying degrees of IRI. A linear regression test was performed on the qPCR measurements of KIM-1 and NGAL, which were tested against the corresponding malate/fumarate ratios. The goodness of fit was calculated to provide R^2 values, and the deviation from zero was also calculated. Statistical analyses were performed using GraphPad PRISM 6.

References

1. Susantitaphong, P. *et al.* World incidence of AKI: a meta-analysis. *Clin. J. Am. Soc. Nephrol.* **8,** 1482–1493 (2013).
2. Hoste, E. A. J. *et al.* Epidemiology of acute kidney injury in critically ill patients: the multinational AKI-EPI study. *Intensive Care Med.* **41,** 1411–1423 (2015).
3. Kaufman, J., Dhakal, M., Patel, B. & Hamburger, R. Community-acquired acute renal failure. *Am. J. Kidney Dis.* **17,** 191–198 (1991).
4. Bellomo, R., Kellum, J. A. & Ronco, C. Acute kidney injury. *Lancet* **380,** 756–766 (2012).
5. Bonventre, J. & Yang, L. Cellular pathophysiology of ischemic acute kidney injury. *J. Clin. Invest.* **121,** 4210–4221 (2011).
6. Fogo, A. B. *et al.* conscious mice using FITC-inulin clearance Serial determination of glomerular filtration rate in Serial determination of glomerular filtration rate in conscious mice using FITC-inulin clearance. *Am J Physiol Ren. Physiol Am. J. Physiol. -Renal Physiol.* **286,** 590–596 (2004).
7. Chaves, A. A. R., Buchpiguel, C. A., Praxedes, J. N., Bortolotto, L. A. & Sapienza, M. T. Glomerular filtration rate measured by (51) Cr-EDTA clearance: Evaluation of captopril-induced changes in hypertensive patients with and without renal artery stenosis. *Clin. (São Paulo, Brazil)* **65,** 607–612 (2010).
8. Edelstein, C. L. Biomarkers of acute kidney injury. *Adv. Chronic Kidney Dis.* **15,** 222–234 (2008).
9. Perazella, M. A. Acute Renal Failure in the Hospital : **D**, 51–58 (2006).
10. Zager, R. A., Johnson, A. C. M. & Becker, K. Renal Cortical Lactate Dehydrogenase: A Useful, Accurate, Quantitative Marker of *In Vivo* Tubular Injury and Acute Renal Failure. *PLoS One* **8,** e66776 (2013).
11. Coca, S. G. & Parikh, C. R. Urinary biomarkers for acute kidney injury: perspectives on translation. *Clin. J. Am. Soc. Nephrol.* **3,** 481–490 (2008).
12. Manno, C. *et al.* Predictors of bleeding complications in percutaneous ultrasound-guided renal biopsy. *Kidney Int.* **66,** 1570–1577 (2004).
13. Whittier, W. L. Timing of Complications in Percutaneous Renal Biopsy. *J. Am. Soc. Nephrol.* **15,** 142–147 (2004).
14. Ardenkjaer-Larsen, J. H. *et al.* Increase in signal-to-noise ratio of >10,000 times in liquid-state NMR. *Proc. Natl. Acad. Sci. USA* **100,** 10158–10163 (2003).
15. Golman, K., Axelsson, O., Jóhannesson, H., Månsson, S. & Olofsson, C. P. J. Parahydrogen-induced polarization in imaging: subsecond (13)C angiography. *Magn. Reson. Med.* **46,** 1–5 (2001).
16. Nielsen, P. M. *et al. In situ* lactate dehydrogenase activity - a novel renal cortical imaging biomarker of tubular injury? *Am. J. Physiol. Renal Physiol.* ajprenal.00561.2015 (2016).

17. Laustsen, C. *et al.* High altitude may alter oxygen availability and renal metabolism in diabetics as measured by hyperpolarized [1-(13)C]pyruvate magnetic resonance imaging. *Kidney Int.* **86,** 67–74 (2013).
18. Laustsen, C. *et al.* Insufficient insulin administration to diabetic rats increases substrate utilization and maintains lactate production in the kidney. *Physiol. Rep.* **2,** e12233 (2014).
19. Laustsen, C. *et al.* Antioxidant treatment attenuates lactate production in diabetic nephropathy. *Am. J. Physiol. - Ren. Physiol.* Ahead Of Print (2016).
20. Brindle, K. M. Imaging Metabolism with Hyperpolarized ^{13}C-Labeled Cell Substrates. *J. Am. Chem. Soc.* **137,** 6418–6427 (2015).
21. Ardenkjaer-Larsen, J. H. On the present and future of dissolution-DNP. *J. Magn. Reson.* **264,** 3–12 (2016).
22. Serrão, E. M. & Brindle, K. M. Potential Clinical Roles for Metabolic Imaging with Hyperpolarized [1-(13)C]Pyruvate. *Front. Oncol.* **6,** 59 (2016).
23. Kurhanewicz, J. *et al.* Analysis of cancer metabolism by imaging hyperpolarized nuclei: prospects for translation to clinical research. *Neoplasia* **13,** 81–97 (2011).
24. Tyler, D. J. Cardiovascular Applications of Hyperpolarized MRI. *Curr. Cardiovasc. Imaging Rep.* **4,** 108–115 (2011).
25. Golman, K. *et al.* Cardiac metabolism measured noninvasively by hyperpolarized 13C MRI. *Magn. Reson. Med.* **59,** 1005–1013 (2008).
26. Aquaro, G. D. *et al.* Cardiac Metabolism in a Pig Model of Ischemia–Reperfusion by Cardiac Magnetic Resonance with Hyperpolarized 13C-Pyruvate. *Ijcme* **6,** 17–23 (2015).
27. Koellisch, U. *et al.* Investigation of metabolic changes in STZ-induced diabetic rats with hyperpolarized [1-13C]acetate. *Physiol. Rep.* **3,** e12474 (2015).
28. Juul, T., Palm, F., Nielsen, P. M., Bertelsen, L. B. & Laustsen, C. *Ex vivo* hyperpolarized MR spectroscopy on isolated renal tubular cells: A novel technique for cell energy phenotyping. *Magn. Reson. Med.* Ahead Of Print (2016).
29. Laustsen, C. *et al.* Acute porcine renal metabolic effect of endogastric soft drink administration assessed with hyperpolarized [1-13c] pyruvate. *Magn. Reson. Med.* **74,** 558–563 (2015).
30. Laustsen, C. Hyperpolarized renal magnetic resonance imaging: Potential and pitfalls. *Front. Physiol.* **7,** 1–5 (2016).
31. Nelson, S. J. *et al.* Metabolic Imaging of Patients with Prostate Cancer Using Hyperpolarized [1- 13 C] Pyruvate. **108,** *198ra108* (2013).
32. Cunningham, C. H. *et al.* Hyperpolarized ^{13}C Metabolic MRI of the Human Heart: Initial Experience. *Circ. Res.* Ahead Of Print (2016).
33. Gallagher, F. a. *et al.* Production of hyperpolarized [1,4-13C2]malate from [1,4-13C2]fumarate is a marker of cell necrosis and treatment response in tumors. *Proc. Natl. Acad. Sci. USA* **106,** 19801–19806 (2009).
34. Clatworthy, M. R. *et al.* Magnetic resonance imaging with hyperpolarized [1,4-(13)C2]fumarate allows detection of early renal acute tubular necrosis. *Proc. Natl. Acad. Sci. USA* **109,** 13374–13379 (2012).
35. Han, W. K., Bailly, V., Abichandani, R., Thadhani, R. & Bonventre, J. V. Kidney Injury Molecule-1 (KIM-1): a novel biomarker for human renal proximal tubule injury. *Kidney Int.* **62,** 237–244 (2002).
36. Devarajan, P. Neutrophil gelatinase-associated lipocalin: a promising biomarker for human acute kidney injury. *Biomark Med.* **4,** 265–280 (2010).
37. Kippen, I., Hirayama, B., Klinenberg, J. R. & Wright, E. M. Transport of tricarboxylic acid cycle intermediates by membrane vesicles from renal brush border. *Proc. Natl. Acad. Sci. USA* **76,** 3397–3400 (1979).
38. Padanilam, B. J. Cell death induced by acute renal injury: a perspective on the contributions of apoptosis and necrosis. *Am. J. Physiol. Renal Physiol.* **284,** F608–F627 (2003).
39. Keruchenko, J. S., Keruchenko, I. D., Gladilin, K. L., Zaitsev, V. N. & Chirgadze, N. Y. Purification, characterization and preliminary X-ray study of fumarase from Saccharomyces cerevisiae. *Biochim. Biophys. Acta* **1122,** 85–92 (1992).
40. Zimmer, F. *et al.* Quantitative Renal Perfusion Measurements in a Rat Model of Acute Kidney Injury at 3T: Testing Inter- and Intramethodical Significance of ASL and DCE-MRI. *PLoS One* **8,** e53849 (2013).
41. Zöllner, F. G., Zimmer, F., Klotz, S., Hoeger, S. & Schad, L. R. Functional imaging of acute kidney injury at 3 Tesla: Investigating multiple parameters using DCE-MRI and a two-compartment filtration model. *Z. Med. Phys.* **25,** 58–65 (2015).
42. Nielsen, P. M. *et al.* Renal ischemia and reperfusion assessment with three-dimensional hyperpolarized (13) C,(15) N2-urea. *Magn. Reson. Med.* **5,** 1524–1530 (2016).
43. Hueper, K. *et al.* T2 relaxation time and apparent diffusion coefficient for noninvasive assessment of renal pathology after acute kidney injury in mice: comparison with histopathology. *Invest. Radiol.* **48,** 834–842 (2013).
44. Rosenberger, C., Rosen, S. & Heyman, S. N. Renal parenchymal oxygenation and hypoxia adaptation in acute kidney injury. *Clin. Exp. Pharmacol. Physiol.* **33,** 980–988 (2006).
45. Pedersen, M. *et al.* Validation of quantitative BOLD MRI measurements in kidney: Application to unilateral ureteral obstruction. *Kidney Int.* **67,** 2305–2312 (2005).
46. Fernández-Llama, P. *et al.* Decreased abundance of collecting duct aquaporins in post-ischemic renal failure in rats. *J. Am. Soc. Nephrol.* **10,** 1658–1668 (1999).
47. Ardenkjaer-Larsen, J. H. *et al.* Dynamic nuclear polarization polarizer for sterile use intent. *NMR Biomed.* **24,** 927–932 (2011).
48. Wiesinger, F. *et al.* IDEAL spiral CSI for dynamic metabolic MR imaging of hyperpolarized [1- 13C]pyruvate. *Magn. Reson. Med.* **68,** 8–16 (2012).
49. Rosset, A., Spadola, L. & Ratib, O. OsiriX: an open-source software for navigating in multidimensional DICOM images. *J. Digit. Imaging* **17,** 205–216 (2004).
50. Hill, D. K. *et al.* Model free approach to kinetic analysis of real-time hyperpolarized 13C magnetic resonance spectroscopy data. *PLoS One* **8,** e71996 (2013).

Acknowledgements

Laboratory tehnician Henrik Vestergaard Nielsen is acknowledged for his expertise and technical support. A.E. and J.A.L. acknowledge support from the Danish National Research Foundation (DNRF124). C.L. and A.E. is supported by the Danish Research Council for Independent Research. We would like to thank Editage (www.editage.com) for English language editing.

Author Contributions

P.M.N., C.L., and J.A.L. designed the study. P.M.N., A.E., L.B.B., J.A.L., and C.L. developed and performed the imaging experiments. P.M.N. developed and performed the laboratory protocols. P.M.N. and C.L. analyzed the data and wrote the initial manuscript. L.B.B., H.S., J.A.L. contributed greatly in finalizing the manuscript. C.L. directed the research.

Additional Information

Competing financial interests: The authors declare no competing financial interests.

How to cite this article: Nielsen, P. M. *et al.* Fumarase activity: an *in vivo* and *in vitro* biomarker for acute kidney injury. *Sci. Rep.* **7**, 40812; doi: 10.1038/srep40812 (2017).

Publisher's note: Springer Nature remains neutral with regard to jurisdictional claims in published maps and institutional affiliations.

D

Echo Planar Spectroscopic Imaging of Hyperpolarized ^{13}C in a Clinical PET/MRI scanner: Studies in Phantoms and Canine Cancer Patient

The following paper will be submitted to *Magnetic Resonance in Medicine* in April 2017. Some of the results from this paper will be presented in the *Annual Meeting of International Society for Magnetic Resonance in Medicine* in April 2017.

Echo Planar Spectroscopic Imaging of Hyperpolarized ^{13}C in a Clinical PET/MRI scanner: Studies in Phantoms and Canine Cancer Patient

Abubakr Eldirdiri[1,2], Stefan Posse[3,4,5], Lars G. Hanson[1,2], Rie B. Hansen[1], Pernille Holst[7], Christina Schøier[7], Annemarie T Kristensen[7], Helle Hjorth Johannesen[6], Andreas Kjaer[6], Adam E. Hansen[6], Jan Henrik Ardenkjaer-Larsen[1,¥]

1. Center for Hyperpolarization in Magnetic Resonance, Department of Electrical Engineering, Technical University of Denmark, Kgs. Lyngby, Denmark
2. Danish Research Centre for Magnetic Resonance, Centre for Functional and Diagnostic Imaging and Research, Copenhagen University Hospital Hvidovre, Denmark
3. Department of Neurology, University of New Mexico, Albuquerque, NM, USA
4. Department of Physics and Astronomy, University of New Mexico, Albuquerque, NM, USA
5. Department of Electrical and Computer Engineering, University of New Mexico, Albuquerque, NM, USA
6. Department of Clinical Physiology, Nuclear Medicine & PET and Cluster for Molecular Imaging, Rigshospitalet and University of Copenhagen, Copenhagen, Denmark
7. Department of Veterinary Clinical Sciences, Faculty of Health and Medical Sciences, University of Copenhagen, Frederiksberg C, Denmark

¥ Corresponding author: Jan Henrik Ardenkjær-Larsen, Department of Electrical Engineering, Technical University of Denmark, 2800 Kgs Lyngby, Denmark

Word count: (4997/5000)

Abstract (200/200):

Purpose: Symmetric echo planar spectroscopic imaging (EPSI) sequence for hyperpolarized ^{13}C imaging in clinical PET/MRI system is presented.

Methods: The sequence employs parallel reconstruction pipelines to separately reconstruct the data from odd and even echoes to reduce artifacts from gradient imbalances. The ramp sampled data in the spatio-temporal frequency space is regridded to compensate for the chemical shift displacements. The sequence was compared with conventional phase-encoded chemical-shift-imaging (CSI) in phantoms, and was evaluated in a canine cancer patient after injection of hyperpolarized [1-^{13}C]pyruvate.

Results: The relative SNR of EPSI with respect to CSI was 0.88, which is consistent with the decrease in sampling efficiency due to ramp sampling. Data regridding in spatio-temporal frequency space reduced spatial blurring compared to direct FFT. EPSI was able to capture both the spatial distributions of the metabolites and their dynamics *in vivo* with improved spatial resolution of 5 x 9 mm^2 in-plane and 3 s temporal resolution.

Conclusion: Higher spatial and temporal resolution was achieved for EPSI metabolic maps compared to CSI's maps, which were more prone to blurring. The sequence showed promising results with short acquisition time and sufficient spectral bandwidth of 500 Hz, and allowed adjusting the tradeoff between SNR and encoding-speed.

Key words: hyperpolarization; echo planar spectroscopic imaging; regridding; metabolic imaging; cancer; molecular Imaging; PET/MRI; hyperPET

Introduction

Since the introduction of the dissolution Dynamic Nuclear Polarization technique (dDNP) [1], Magnetic Resonance Spectroscopy (MRS) of hyperpolarized ^{13}C has emerged as an attractive modality that enables imaging of the metabolic activity *in vivo* [2–5]. Currently, hyperpolarized ^{13}C metabolic imaging is widely being examined in combination with the more established Positron Emission Tomography (PET) [6,7] to study its potential for clinical use. The hybrid PET/MRI systems are well suited for such tasks [8–10]. The enhanced magnetization obtained from hyperpolarization methods is short-lived, and the magnetization consumed on excitations is non-recoverable. This dictates the use of optimized imaging sequences that efficiently utilize the decaying magnetization. The conventional 2D phase-encoded chemical shift imaging (CSI) sequence encodes the k-space using two phase encoding gradients [11,12]. This results in a total imaging duration of CSI that is relatively long compared to the longitudinal relaxation time, and gives poor resolution for mapping the dynamics of metabolism. Accelerated spectroscopic imaging sequences, such as Echo Planar Spectroscopic Imaging (EPSI) [13–19], multiecho bSSFP (ME-bSSFP) [20–22], spiral MRSI [23–26], and IDEAL spiral [27], require fewer excitations because more than one k-space position is sampled for each excitation, e.g. one k-space line in the case of EPSI and ME-bSSFP and one image frame in the case of spiral acquisition. Therefore, the total imaging time for these sequences is reduced, typically by one order of magnitude. The short imaging time and reduced number of excitations make such sequences attractive for imaging of hyperpolarized nuclear spins, enabling observation of the conversion of the hyperpolarized substrates to their metabolic products with acceptable temporal resolution. These sequences, however, are characterized by a limited spectral bandwidth due to gradient slew rate constraints. The dwell time (time elapsed between consecutive acquisitions of the same point in k-space) is governed by the gradient echo spacing in the case of ME-bSSFP [20–22] and EPSI [13–19], and the echo time increment between spirals in the case of spiral MRSI and IDEAL spiral [23–27]. This reduced spectral bandwidth is usually not a limitation for hyperpolarized MRI, since the spectrum of the hyperpolarized ^{13}C substrate and its metabolic products is sparse, and spectral aliasing can be controlled to avoid peak overlap. However, compared to conventional

CSI, these fast acquisition sequences are more demanding in terms of gradient strength and slew rate, and require extensive ramp sampling on clinical MR scanners as opposed to preclinical systems, which reduces the signal-to-noise-ratio (SNR) per unit time. These limitations of gradient performance make it challenging to translate the use of these sequences from small animals to human studies.

EPSI is the most established sequence to achieve dynamic imaging of the metabolism in clinical studies [28] with hyperpolarized pyruvate. This sequence employs oscillating gradients in the readout direction during the data acquisition to efficiently sample one line at each TR interval at the expense of reduced spectral bandwidth. EPSI with symmetric readout gradients typically suffers from aliasing artifacts [29,30] due to gradient imperfection, which require reference scans to estimate and correct the discrepancies between the odd and even echoes [31]. Flyback EPSI is sometimes preferred over symmetric EPSI to avoid the need to correct these differences [32,33]. However, flyback EPSI suffers from lower SNR because the receiver is idle for longer duration [16,34]. We argue that symmetric EPSI with separate reconstruction of the odd and even echo data is sufficient and simple, if the resultant smaller spectral bandwidth is acceptable. The simplest way to reconstruct the even and odd data is via FFT assuming that the data are collected on a Cartesian grid. However, the data in the k-t space are acquired on a zig-zag trajectory, so the phase evolution during the acquisition of individual k-space lines must be corrected before carrying out FFT to avoid spatial blurring due to chemical shift artifacts in opposite directions for odd and even gradient echoes.

In this study, we present symmetric ^{13}C EPSI with separate reconstruction of the odd and even echo data and ramp sampling for application on a clinical PET/MRI system. The EPSI technique is based on our proton-echo-planar-spectroscopic-imaging (PEPSI) methodology [35–38], which provides high sampling efficiency without aliasing and acceptable spectral bandwidth. Moreover, we introduce a correction of the phase evolution during the acquisition of the zig-zag trajectory in k-t space [39,38], to avoid spatial blurring due to chemical shift artifacts in opposite directions for odd and even gradient echoes. This reconstruction algorithm is extended to give optimal reconstruction

for sufficiently band-limited signals, even for aliased non-overlapping peaks. Both free induction decay (FID) and spin echo excitation methods were evaluated. The sequence was validated and compared with CSI using a phantom with multiple compartments of ^{13}C labeled compounds. Moreover, a version of the sequence with centric phase encoding was evaluated *in vivo* with hyperpolarized [1-^{13}C]pyruvate in a canine cancer patient undergoing PET/MR, as part of the diagnostic work up for acanthomatous ameloblastoma.

Methods

Hardware

All experiments were performed on a 3 T PET/MR (mMR Biograph, Siemens Healthcare, Erlangen), with maximum gradient strength of 43 mT/m, maximum slew rate of 180 mT/m/ms, gradient raster time of 10 µs, analog-to-digital converter (ADC) raster time of 100 ns, and minimum delay between ADC readout events of 100 µs. The raster time is the smallest temporal unit that can be used to specify the timing of the ADC event. The acoustic resonances of the gradient coil were in the frequency bands of 530-630 Hz and 1010-1230.

Two coils were used in this work, a ^{13}C birdcage head coil (RAPID Biomedical, Germany) with 265 mm inner diameter and a ^{1}H/^{13}C transmit/receive flex coil (RAPID Biomedical, Germany) (110 mm loop for ^{13}C and 180 mm x 244 mm butterfly for ^{1}H). The head coil was used with a thermal phantom, and the flex coil was used with a hyperpolarized [1-^{13}C]pyruvate phantom and *in* vivo with the canine cancer patient. A 7 mL vial with 4.0 M ^{13}C-urea doped with Gadolinium (Dotarem, Guerbet, France) (0,23% v/v) was used for flip angle calibration in the hyperpolarized phantom experiments and for the canine cancer patient. Two phantoms were used. To compare the SNR between the sequences, a cylinder with diameter of 250 mm and length of 200 mm was used. It had four cylindrical compartments with inner diameters of 19 mm each. The outer volume of the phantom was filled with ethylene glycol with natural abundance of ^{13}C, and three of the inner compartments were filled with ^{13}C-bicarbonate, [1-^{13}C]acetate and ^{13}C-urea (all three compounds are from Sigma Aldrich, Denmark). The concentration of each substrate is 1.0 M. The three compounds were doped with Omniscan (GE Healthcare, USA) to T_1 values of 0.4 s, 0.7 s, and 0.7 s, respectively (measured at 9.4 T and 295 K). The fourth compartment was left empty.

A hyperpolarized phantom made from a rectangular bottle (200x185x125 mm^3) was initially filled with 4.5 L of saline solution. A hyperpolarized sample containing 14 mmol of [1-^{13}C]pyruvate was added to the phantom after dissolution. Then the phantom was briefly shaken, placed on top of the

surface $^{1}H/^{13}C$ coil and the dynamic imaging was acquired. To prepare the hyperpolarized sample, 1 mL of [1-^{13}C]pyruvic acid with 15 mM of electron paramagnetic agent, AH111501 (Syncom BV, Netherlands), was polarized in a SPINlab polarizer (GE Healthcare, USA) for 4 hours. The sample was then dissolved in 49.8 mL of dissolution media containing 0.1 g/L of EDTA (ethylenediaminetetraacetic acid disodium salt dehydrate) (Sigma Aldrich, Denmark) in water. The sample was neutralized with 14.6 mL of neutralizing media containing 0.72 M NaOH, 0.4 M 2-Amino-2-(hydroxymethyl)-1,3-propanediol (Tris) (Sigma Aldrich, Denmark) and 0.1 g/L EDTA disodium salt in water.

Design of ^{13}C EPSI

Echo Planar Readout Gradient

Both the desired spatial resolution and the target spectral bandwidth with separate processing of even and odd echo data [35,36,40] were taken into account when designing the trapezoidal echo planar readout gradient with ramp sampling. The echo spacing (ES) was chosen to avoid acoustic resonances, which must be outside of the ranges of 1.58-1.89 ms and 810-990 µs. A SW of about 500 Hz in a 3 T magnet, which avoids acoustic resonances, is acceptable for the case of hyperpolarized [1-^{13}C]pyruvate. The pyruvate and its products alanine, pyruvate-hydrate and lactate are located at 171.1, 176.3, 177.6, and 183.2 ppm respectively (i.e. a range of 372 Hz in a 3T scanner).

The iterative design process for the targeted spectral bandwidth, $SW = (2ES)^{-1}$, was initiated with a trapezoidal readout gradient waveform G_{RO} such that,

$$\Delta x = \frac{1}{\gamma \int_{t=0}^{t=T_{RO}} G_{RO}(t)\, dt} \qquad (1)$$

where Δx is the pixel dimension in the readout dimension, γ is the gyromagnetic ratio for the nucleus of interest, $t = 0$ is the start time of signal recording, and T_{RO} is the readout time, $T_{RO} < ES$. Further

increase in spatial resolution requires increasing the readout time T_{RO} and thus reducing the spectral bandwidth.

A SW of about 500 Hz in a 3 T magnet is acceptable for the case of hyperpolarized [1-^{13}C]pyruvate. The pyruvate and its products alanine, pyruvate-hydrate and lactate are located at 171.1, 176.3, 177.6, and 183.2 ppm respectively (i.e. a range of 372 Hz in a 3 T scanner).

The Iterative optimization of the gradient waveform under the given hardware constraints, yielded a spectral bandwidth of 495 Hz corresponding to gradient lobe duration of 1010 µs. Using trapezoidal gradients with ramp up and ramp down durations of 170 µs, the maximum gradient strength achievable during ramping at the maximum slew rate was 30 mT/m. The ADC was switched on 57 µs after the start of the gradient and switched off 57 µs before the end of the gradient lobe to ensure more than 100 µs between successive ADC periods. The effective gradient moment accumulated during the readout was 26.6 mTs/m, which provided a maximum achievable spatial resolution of 3.75 mm with 495 Hz spectral bandwidth on the mMR Biograph. The corresponding ADC period was 896 µs.

If the reference frequency is chosen to be exactly in the middle between pyruvate and lactate, then the resultant spectrum acquired with a bandwidth of 495 Hz will be as shown in Figure 1a (lactate at 186 Hz, pyruvate-hydrate at 24 Hz, alanine at -21 Hz and pyruvate at -186 Hz). The bicarbonate signal will be aliased to the center of the spectrum at 1 Hz, between alanine and pyruvate-hydrate. The peak positions of the three substrates in the multi-compartment phantom were acetate at 155 Hz, bicarbonate at 494 Hz (aliased to 71 Hz), and urea at 424 Hz (aliased to 1 Hz), Figure 1b.

Phase encoding gradient

The total duration of the phase encoding gradient was set to 1700 µs giving a maximum resolution of 1.9 mm in the phase encoding direction. An EPSI version with centric phase encoding was designed and used in the hyperpolarization experiments in phantom and *in vivo*.

Radiofrequency pulses

An excitation pulse (Hanning-filtered sinc with time bandwidth product of 4) with total duration of 1,280 μs and central lobe duration of 640 μs was used. The smallest slice thickness achievable with this pulse was 6 mm with a slice selection gradient of 43 mT/m. The excitation pulse used had an approximate bandwidth (BW) of 3000 Hz. The chemical shift displacement $\delta_{p,l}$ between pyruvate and lactate in the slice direction was therefore

$$\delta_{p,l} = \frac{\Delta f_{p,l}}{\gamma\, G_z} = \frac{\Delta f_{p,l}}{BW}\Delta z = 0.12\,\Delta z \qquad (2)$$

where $\Delta f_{p,l}$ is the chemical shift between pyruvate and lactate (372 Hz at 3 T) and Δz is the slice thickness.

In addition, a spin echo (SE) EPSI was implemented with Hanning-filtered sinc refocusing pulse with time bandwidth product of 8.The duration of the refocusing pulse was set during the pulse preparation, and the smallest allowed duration is assumed (2600 μs) without exceeding the B_1 limit. The maximum bandwidth of the pulse is therefore 2.2 kHz. The maximum allowed duration for the refocusing pulse was 7200 μs, giving a minimum bandwidth of 780 Hz. This sequence was used in the phantom SNR evaluation

SNR efficiency

We characterized the sensitivity of PEPSI as a function of field strength and computed the ramp sampling efficiency as in [40]. Pohmann et al [41] compared different chemical shift imaging methods and analyzed their sensitivity with respect to the conventional phase encoded CSI. For an EPSI sequence, the sensitivity, Ψ_{EPSI}, can be related to the CSI sensitivity, Ψ_{CSI}, as follows

$$\Omega_{EPSI} = \frac{\Psi_{EPSI}}{\Psi_{CSI}} = \sqrt{1 - \frac{\tau_s}{ES}} \qquad (4)$$

where τ_s is the time needed for gradient switching, and ES is the echo spacing.

Pipe and Duerk [42] showed that the variance in the reconstructed image depends on the shape of the gradient waveform used to record the signal. The smallest variance for even sampling occurs in the case of constant gradient, in which case the variance in the reconstructed image is equal to the variance of the thermal noise, σ^2. They also showed that the variance in the reconstructed image, ${\sigma_i}^2$, can be expressed in terms of the first and second moments of the gradients waveform $G(t)$, the thermal noise variance σ^2, and the measurement duration T:

$$\frac{{\sigma_i}^2}{T} = \frac{\sigma^2 \int_0^T G^2(t)\ dt}{\left(\int_0^T G(t)\ dt\right)^2} \qquad (5)$$

Reconstruction and post-processing

Initially, 1D regridding was applied to compensate uneven k-space sampling over the ramp. After regridding, the odd and even echoes were separated into two matrices. Time reversal was performed on the odd echo data. Temporal Fourier transformation was applied to the two data sets to obtain two k_x-k_y-f arrays. Before applying the spatial Fourier transform, a linear phase correction was introduced along the readout direction k_x [39,38] to account for the time evolution, which would otherwise results in a chemical shift displacement in the spatial domain, differing between even and odd numbered echoes. Subsequently, spatial Fourier transform was applied to obtain odd and even *x-y-f* matrices. The data corresponding to odd echoes were phase adjusted and then added to the even echo data to obtain a ^{13}C spectroscopic image. The reconstructed spectra were interpolated to 256 points using zero-filling in the time-domain. No apodization was used in the temporal dimension. Figure 2 shows the reconstruction pipeline. The chemical shift correction described above assumes there is no aliasing of metabolites in the spectrum, which may occur in practice since the spectral bandwidth is relatively small. Therefore, any aliased peaks should be unfolded to its true frequency position before applying the corrections. This can be done if peaks do not overlap in the aliased spectra by simply applying phase ramps corresponding to spatial shifts of non-aliased peak frequencies.

Phantom experiment

An experiment was conducted to evaluate the SNR and the localization of the EPSI sequence using the birdcage coil and the multi-compartment cylindrical phantom. A product CSI sequence served as the SNR reference. The CSI data were acquired with repetition time (TR) of 1,000 ms, field of view of (FOV) 100x100 mm^2, spatial matrix 16x16, flip angle 90^o, slice thickness 100 mm, spectral bandwidth 5,000 Hz, number of spectral points 512, sampling time of 102.4 ms, and no averaging, resulting in a CSI scan time of 4 min and 16 s. The time between excitation and sampling was 2.3 ms. EPSI data were acquired with TR of 1,000 ms, FOV 100x100 mm^2, spatial matrix 16x16, flip angle 90^o, slice thickness 100 mm, Echo Train Length (ETL) 128, ES 1,010 μs, 16 averages, resulting in a scan time of 4 min and 16 s, echo train duration of 129.3 ms and a spectral bandwidth of 495 Hz. The time between excitation and the start of the first readout gradient lobe was 2.4 ms. Additionally, a SE-EPSI was acquired with the same parameters as for the EPSI, except TE was 8.8 ms. For noise estimation, both CSI and EPSI sequences were run after nulling the transmitted signal. These sequences were also evaluated using the 7 mL vial of ^{13}C-urea and the surface coil.

To quantify the SNR of each substrate, the signal was estimated at each voxel from the peak amplitude (real phased spectrum). Then the signal was averaged in a 4x4 pixel region of interest (ROI) encompassing the substrate, and normalized by the noise standard deviation in the spectra in the same ROI.

To assess the localization of the spectroscopic sequences, the proton image was taken as a reference. For each substrate, the location of the center of the cylinder in the ^{13}C image and proton image were compared. The shift in millimeters between the two locations was reported. Since each substrate is in a cylinder, a circle was fitted to the contour spatial distribution and the center of the circle was taken as the location in the proton image. The ^{13}C images were obtained using general linear model (GLM) fitting. Then spline fitting was applied to the ^{13}C spatial distribution of each substrate to achieve sub-voxel precision at the same resolution as the proton image. The position of

the peak intensity in the metabolite distribution after spline fitting was used as the substrate location in the ^{13}C image.

A final phantom experiment was conducted with hyperpolarized [1-^{13}C]pyruvate and the surface coil. Two different dynamic measurements were acquired, one with EPSI and the second with CSI. The EPSI acquisition was made using a FOV 200x200 mm^2, 32x32 matrix with central phase encoding, ETL 64, flip angle 6^o, TR 80 ms, and TE 2.4 ms. The acquisition time per frame was 2.5 s and an image was acquired every 5 s. The CSI was acquired using FOV 200x200 mm^2, truncated 16x16 matrix, flip angle 3^o, TR 80 ms, and TE 2.3 ms. The acquisition time per frame was 12 s and 3 images were acquired sequentially without delay.

Clinical study in a canine cancer patient

A 9-year-old female intact Samojed weighing 27 kg, with a histopathologically confirmed ameloblastoma of the left mandible, underwent PET/MR examination as part of the diagnostic and staging workup prior to therapy. Hyperpolarized ^{13}C MRSI was included in this examination. The owner gave informed consent and the study was approved by the Ethical and Administrative Committee, Department of Veterinary Clinical Sciences, Faculty of Health and Medical Sciences, University of Copenhagen.

Three 500 µL samples of [1-^{13}C]pyruvic acid with 15 mM of AH111501 were hyperpolarized in the SPINlab polarizer for 4 hours. The samples were dissolved in 29.1 mL dissolution media and neutralized with 7.3 mL of neutralizing media. After dissolution, 18 mL (0.68 mL/kg) of 250 mM [1-^{13}C]pyruvate was injected intravenously over 7–8 s.

Coronal, transversal and sagittal anatomic ^1H MR images were acquired for planning using a T2 weighted turbo spin-echo (TSE) sequence (TR 4,000 ms; TE 89 ms; voxel size 0.5 x 0.5 mm^2; 19 slices of 3 mm thickness).

The dog received three injections of hyperpolarized [1-^{13}C]pyruvate with 10 min intervals. A dynamic FID sequence with no in-plane spatial encoding was started at the beginning of the sample injection with the following parameters: slice thickness 4 cm, TR 1 s, flip angle 5^{o}, acquisition delay 2.3 ms, spectral bandwidth of 6,000 Hz and 512 points. The purpose of the dynamic FID was to find the time point with maximum lactate signal, which was used to determine the start time of the subsequent CSI acquisition. Acquisition of a CSI data set was initiated 30 s after the start of the injection of the second pyruvate sample with TR 80 ms, FOV 150x180 mm^2, matrix size 16x16, slice thickness 15 mm, flip angle 10^{o}, acquisition delay 2.3 ms, spectral bandwidth 10,000 Hz, and number of spectral points 512. A dynamic EPSI acquisition was started at the end of the injection of the third hyperpolarized sample using a FOV of 150x180 mm^2, 16x32 matrix with central phase encoding, slice thickness 15 mm, ETL 64, flip angle 6^{o}, TR 80 ms, and acquisition delay 2.4 ms. The acquisition time per frame was 1.3 s and a frame was acquired every 3 s (with idle time of 1.7 s between frames).

PET images were acquired as a single-bed with 5 min acquisition duration, after intravenous injection of 216 MBq (8 MBq/kg) of ^{18}F-2-fluoro-2-deoxy-D-glucose (^{18}F-FDG) 1 hour prior to imaging. PET reconstruction used 3D OP-OSEM with 4 iterations, 21 subsets, matrix 344x344, 4 mm 3D Gaussian post-filter, pixel size 2.1x2.1 mm^2 and 2.0 mm slice thickness.

Results

Phantom Experiments

To calculate the theoretical relative SNR between the CSI and the EPSI, Eq. (4) was used. The EPSI acquisition time was 896 μs with 114 μs delay between acquisitions reducing the SNR by 5% compared to CSI. To account for ramp sampling, Eq. (5) was used to calculate the SNR efficiency relative to a square readout gradient waveform, which amounts to 94%. Therefore, the relative theoretical SNR of EPSI with respect to CSI was 89%.

Figure 3 shows the signal for the three substrates ^{13}C-urea, ^{13}C-bicarbonate and [1-^{13}C]acetate in the multi-compartments phantom obtained with CSI and EPSI using the birdcage coil, superimposed on the proton image. The strength of the signal varied between the substrates due to differences in T_1 relaxation time constants and line width. For the CSI, the SNR values were 290, 153 and 113 for ^{13}C-bicarbonate, ^{13}C-urea and [1-^{13}C]acetate, respectively. For EPSI the SNR values were 257, 135 and 99 for the three phantoms respectively. This corresponds to relative SNR values of 0.89, 0.87, and 0.88 respectively, which are close to the theoretical values. The SNR values for SE EPSI were 170 for ^{13}C-bicarbonate, 86 for ^{13}C-urea and 67 for [1-^{13}C]acetate, which correspond to relative SNR of 0.59, 0.56 and 0.59 relative to CSI. The CSI had the smallest spatial offsets with discrepancy of 0.8 mm for [1-^{13}C]acetate, 0.9 mm for ^{13}C-bicarbonate and 1.5 mm for ^{13}C-urea. The offsets were larger for the EPSI sequence; 1.9 mm, 1.7 mm and 3.1 mm, respectively.

The SNR values obtained with the ^{13}C-urea vial and the surface coil were 283 for CSI, 245 for EPSI and 263 for SE EPSI. This corresponds to relative SNR values of 0.87 and 0.93 for EPSI and SE EPSI with respect to CSI, respectively.

Figure 4 shows the comparison between EPSI reconstruction algorithms. Direct FFT reconstruction, Figure 4a, results in spatial blurring of the substrates in the ^{13}C image due to chemical shifts in opposite directions for even and odd echoes. On the other hand, spectral-spatial regridding using the apparent frequency positions, Figure 4b, results in narrower and more accurate

spatial representation of ^{13}C-urea and ^{13}C-bicarbonate. [1-^{13}C]acetate, however, was outside of the critically sampled bandwidth, and therefore aliased, which resulted in increased spatial broadening. When accounting for aliasing by using the actual frequency offset of the non-aliased peak when calculating phase ramps, the chemical shift displacement of [1-^{13}C]acetate was compensated as well, Figure 4c. The dynamic signal acquired for hyperpolarized [1-^{13}C]pyruvate in the 4.5 L rectangular phantom (sum of the signal over the phantom) with both CSI and EPSI is shown in Figure 5c. For the dynamic measurements obtained with CSI (see Figure 5), the time resolution was very coarse, 12 s, despite the smaller matrix size used, and thus coarser spatial resolution. The coil profile derived from the EPSI image of the phantom is shown in Figure 5a.

Canine Cancer Patient PET/Hyperpolarized MR Evaluation

Figure 6 shows the anatomical images used to plan the positioning of the spectroscopic grids for both CSI and EPSI. The 16x12 mm tumor is located at the buccal side of the left mandible, as shown in Figure 7a. The dynamic FID (Figure 9a) shows that pyruvate starts accumulating in the slab containing the tumor about 10 s after the start of the injection, and reaches a peak value 9 s later. Lactate starts building up 22 s after the start of the injection and reaches a maximum value after 32 s. The CSI acquisition was timed to start 30 s after injection to obtain the highest possible lactate signal from the slice. Figure 7b,e shows the pyruvate and lactate signals at the slice containing the tumor. Relatively high pyruvate uptake and an increased lactate production can be observed at the tumor site. Additionally, lactate signal can be seen at the masticator muscle in the lower right region. The PET-FDG image (Figure 7d) also shows high metabolism at the tumor site in addition to the typical high FDG uptake in the brain.

In Figures 8, the series of metabolic maps obtained with EPSI are given. These maps show the buildup and decay of pyruvate and lactate across the slice. To allow for comparison with the dynamic FID, the pyruvate and lactate signals in each frame were summed over the entire frame, to obtain the time plots shown in Figure 9b. The pyruvate and lactate signals were also integrated at the tumor and masticator muscle to obtain the dynamic build-up and decay at these two sites, Figure 9c,d.

Moreover, the pyruvate and lactate series were integrated into one pyruvate and one lactate image, Figure 7c,f, for comparison with the corresponding CSI maps in Figure 7b,e. The signal level in all the metabolic maps in figures 7 and 8 were normalized with respect to the standard deviation of the noise.

Discussion

This work presents an implementation of a symmetric EPSI sequence for hyperpolarized ^{13}C in a hyprid clinical PET/MR system and evaluates this sequence in phantoms and *in vivo*. The SNR obtained with this sequence was around 88% compared to CSI, and this agrees with the theoretical estimation and literature [33]. Although EPSI is susceptible to errors from gradient waveform imperfection, these errors were minor in this work. However, higher resolution can increase the demand on gradients, and this in turn could increase artifacts with this sequence. This may explain the error in localization where the substrates were slightly shifted outward. However, on average the localization error was less than one-third of the voxel dimension and the estimate may also be influenced by noise. Although all the substrates in the multi-compartment phantom had the same concentration, the SNR as measured from the CSI and EPSI acquisitions varied significantly due to the differences in T_1 relaxation times.

With the birdcage coil the SNR of the SE EPSI was about 58% of the CSI SNR, in contrast to 93% with the surface coil. This discrepancy in SNR values of SE EPSI is because of the difference in the refocusing pulse durations used with the two coils. Due to the relatively high power needed with the birdcage coil, the bandwidth of the refocusing pulse was limited to around 1000 Hz. This range is sufficient for the pyruvate-lactate range, but insufficient to uniformly cover the range from bicarbonate to acetate in the phantom experiments (peak separation of 650 Hz).

The reconstruction employed in this work provides better accuracy compared to direct FFT. For EPSI with flyback readout [33], direct FFT will cause less artifacts since the chemical shift displacement is in one direction and no broadening occurs. Aliased metabolites caused an error in the spatial-spectral regridding. This error was removed by adapting the algorithm to exploit that the ^{13}C spectrum in the hyperpolarization experiments is sparse and the metabolite frequencies known *a priori*. Other examples of hyperpolarized ^{13}C substrates that give sparse spectra, with two or three peaks, and for which this EPSI sequence can be used without major modifications include, but not

limited to, hyperpolarized ^{13}C-bicarbonate used measure pH values [34] and [1,4-^{13}C]fumarate used in imaging necrosis [44].

In the phantom experiment with hyperpolarized [1-^{13}C]pyruvate, EPSI allowed dynamic imaging with reasonable temporal resolution. However, faster imaging could have been achieved using fewer phase encoding steps, since the surface coil had a relatively superficial localized sensitivity and most of the signal came from a small part of the FOV. Similarly, for the *in vivo* evaluation of the canine cancer patient most of the observed signal came from the jaw close to the surface coil, where the tumor was located.

Higher spatial resolution was achieved for the metabolic maps obtained with EPSI compared to CSI in the hyperpolarization experiments. Despite employing dynamic acquisition with EPSI in the *in vivo* hyperpolarization experiment, using a larger matrix size was feasible, compared to the matrix size of CSI. Moreover, CSI is prone to blurring from T_1 decay due to the relatively long acquisition duration per frame. Therefore, the pyruvate and lactate signals were sharper and better localized in the EPSI metabolic maps, whereas the maps obtained from the CSI acquisition were blurry.

The dynamic measurements of pyruvate and lactate in Figure 9b obtained from EPSI agree with those obtained from the dynamic FID sequence (Figure 9a). Lactate reached the maximum about 27 s after the end of the injection (34 s after the start) in the EPSI series, whereas pyruvate was highest 13 s after the end of injection (20 s from the start of injection). The maximum lactate signal relative to maximum pyruvate was higher for the dynamic FID sequence compared to EPSI. This is probably due to higher number of excitations per unit time in the EPSI sequence that consumes more pyruvate magnetization before the conversion to lactate (5.3 excitations/s with 6° flip angle reduces the signal by 2.9%/s, compared to the 5° flip angle every second for the FID giving 0.4%/s signal reduction). Both the EPSI and the CSI sequences showed similar metabolite distributions. The slight differences could be because the imaging windows for the two sequences were different: CSI was acquired over

12 s from 30 s after injection, whereas EPSI was acquired over 60 s from the end of the injection. Also, the spatial resolution of CSI was lower than that of EPSI.

In conclusion, an implementation of a symmetric EPSI sequence in a clinical PET/MR system was presented with an adopted reconstruction that provides more accurate spatial mapping of the hyperpolarized signal compared to direct FFT, including for aliased non-overlapping peaks. EPSI provided an acceptable tradeoff between encoding speed and SNR in the phantom and in vivo experiments. Moreover, the *in vivo* experiment showed that the designed sequence provides high temporal and spatial resolution for mapping hyperpolarized metabolites and their dynamic behavior.

Acknowledgments

The Mind Research Network is acknowledged for providing their facilities to conduct the initial experiments. We would also like to acknowledge the financial support from Danish Research Council (Grant Number 1331-00259A), the Danish National Research Foundation (Grant Number DNRF124) and Innovation Fund Denmark.

Disclosure

Nothing to disclose.

References

1 Ardenkjaer-Larsen JH, Fridlund B, Gram A, Hansson G, Hansson L, Lerche MH, Servin R, Thaning M, Golman K. Increase in signal-to-noise ratio of > 10,000 times in liquid-state NMR. *Proc Natl Acad Sci USA* 2003; **100**: 10158–10163.

2 Golman K, Zandt RI, Lerche M, Pehrson R, Ardenkjaer-Larsen JH. Metabolic imaging by hyperpolarized 13C magnetic resonance imaging for in vivo tumor diagnosis. *Cancer Res* 2006; **66**: 10855–10860.

3 Day SE, Kettunen MI, Gallagher FA, Hu D-E, Lerche MH, Wolber J, Golman K, Ardenkjaer-Larsen JH, Brindle KM. Detecting tumor response to treatment using hyperpolarized 13C magnetic resonance imaging and spectroscopy. *Nat Med* 2007; **13**: 1382–1387.

4 Albers MJ, Bok R, Chen AP, Cunningham CH, Zierhut ML, Zhang VY, Kohler SJ, Tropp J, Hurd RE, Yen YF, Nelson SJ, Vigneron DB, Kurhanewicz J. Hyperpolarized 13C lactate, pyruvate, and alanine: Noninvasive biomarkers for prostate cancer detection and grading. *Cancer Res* 2008; **68**: 8607–8615.

5 Kurhanewicz J, Vigneron DB, Brindle K, Chekmenev EY, Comment A, Cunningham CH, Deberardinis RJ, Green GG, Leach MO, Rajan SS, Rizi RR, Ross BD, Warren WS, Malloy CR. Analysis of cancer metabolism by imaging hyperpolarized nuclei: prospects for translation to clinical research. *Neoplasia* 2011; **13**: 81–97.

6 Gallagher FA, Bohndiek SE, Kettunen MI, Lewis DY, Soloviev D, Brindle KM. Hyperpolarized 13C MRI and PET: in vivo tumor biochemistry. *J Nucl Med* 2011; **52**: 1333–1336.

7 Torigian DA, Kjær A, Zaidi H, Alavi A. PET/MR Imaging: Clinical Applications. *PET Clin* 2016; **11**: 10–12.

8 Gutte H, Hansen AE, Henriksen ST, Johannesen HH, Ardenkjaer-Larsen JH, Vignaud A, Hansen AE, Børresen B, Klausen TL, Wittekind A-MN, others. Simultaneous hyperpolarized 13C-pyruvate MRI and 18F-FDG-PET in cancer (hyperPET): feasibility of a new imaging concept using a clinical PET/MRI scanner. *Am J Nucl Med Mol Imaging* 2015; **5**: 38-45.

9 Gutte H, Hansen AE, Larsen MME, Rahbek S, Henriksen ST, Johannesen HH, Ardenkjaer-Larsen JH, Kristensen AT, Højgaard L, Kjær A. Simultaneous Hyperpolarized 13C-Pyruvate MRI and 18F-FDG PET (HyperPET) in 10 Dogs with Cancer. *J Nucl Med* 2015; **56**: 1786–1792.

10 Hansen AE, Andersen FL, Henriksen ST, Vignaud A, Ardenkjaer-Larsen JH, Højgaard L, Kjaer A, Klausen TL. Simultaneous PET/MRI with 13 C magnetic resonance spectroscopic imaging (hyperPET): phantom-based evaluation of PET quantification. *EJNMMI Phys* 2016; **3**: 7–20.

11 Brown TR, Kincaid BM, Ugurbil K. NMR chemical shift imaging in three dimensions. *Proc Natl Acad Sci* 1982; **79**: 3523–3526.

12 Maudsley AA, Hilal SK, Perman WH, Simon HE. Spatially resolved high resolution spectroscopy by "four-dimensional" NMR. *J Magn Reson* 1983; **51**: 147–152.

13 Cunningham CH, Vigneron DB, Chen AP, Xu D, Nelson SJ, Hurd RE, Kelley DA, Pauly JM. Design of flyback echo-planar readout gradients for magnetic resonance spectroscopic imaging. *Magn Reson Med* 2005; **54**: 1286–1289.

14 Cunningham CH, Chen AP, Albers MJ, Kurhanewicz J, Hurd RE, Yen YF, Pauly JM, Nelson SJ, Vigneron DB. Double spin-echo sequence for rapid spectroscopic imaging of hyperpolarized 13C. *J Magn Reson* 2007; **187**: 357–362.

15 Larson PEZ, Kerr AB, Chen AP, Lustig MS, Zierhut ML, Hu S, Cunningham CH, Pauly JM, Kurhanewicz J, Vigneron DB. Multiband excitation pulses for hyperpolarized 13C dynamic chemical-shift imaging. *J Magn Reson* 2008; **194**: 121–127.

16 Yen YF, Kohler SJ, Chen AP, Tropp J, Bok R, Wolber J, Albers MJ, Gram KA, Zierhut ML, Park I, Zhang V, Hu S, Nelson SJ, Vigneron DB, Kurhanewicz J, Dirven HAAM, Hurd RE. Imaging considerations for in vivo 13C metabolic mapping using hyperpolarized 13C-pyruvate. *Magn Reson Med* 2009; **62**: 1–10.

17 Larson PEZ, Bok R, Kerr AB, Lustig M, Hu S, Chen AP, Nelson SJ, Pauly JM, Kurhanewicz J, Vigneron DB. Investigation of tumor hyperpolarized [1-13C]-pyruvate dynamics using time-resolved multiband RF excitation echo-planar MRSI. *Magn Reson Med* 2010; **63**: 582–591.

18 Larson PEZ, Hu S, Lustig M, Kerr AB, Nelson SJ, Kurhanewicz J, Pauly JM, Vigneron DB. Fast dynamic 3D MR spectroscopic imaging with compressed sensing and multiband excitation pulses for hyperpolarized 13C studies. *Magn Reson Med* 2011; **65**: 610–619.

19 Tropp J, Lupo JM, Chen A, Calderon P, McCune D, Grafendorfer T, Ozturk-Isik E, Larson PEZ, Hu S, Yen YF, Robb F, Bok R, Schulte R, Xu D, Hurd R, Vigneron D, Nelson S. Multi-channel metabolic imaging, with SENSE reconstruction, of hyperpolarized [1-13C] pyruvate in a live rat at 3.0 tesla on a clinical MR scanner. *J Magn Reson* 2011; **208**: 171–177.

20 Leupold J, Wieben O, Månsson S, Speck O, Scheffler K, Petersson JS, Hennig J. Fast chemical shift mapping with multiecho balanced SSFP. *Magn Reson Mater Physics, Biol Med* 2006; **19**: 267–273.

21 Leupold J, Månsson S, Stefan Petersson J, Hennig J, Wieben O. Fast multiecho balanced SSFP metabolite mapping of 1H and hyperpolarized 13C compounds. *Magn Reson Mater Physics, Biol Med* 2009; **22**: 251–256.

22 Perman WH, Bhattacharya P, Leupold J, Lin AP, Harris KC, Norton VA, Hovener JB, Ross BD. Fast volumetric spatial-spectral MR imaging of hyperpolarized 13C-labeled compounds using multiple echo 3D bSSFP. *Magn Reson Imaging* 2010; **28**: 459–465.

23 Josan S, Yen YF, Hurd R, Pfefferbaum A, Spielman D, Mayer D. Application of double spin echo spiral chemical shift imaging to rapid metabolic mapping of hyperpolarized [1 - 13C]-pyruvate. *J Magn Reson* 2011; **209**: 332–336.

24 Josan S, Hurd R, Park JM, Yen YF, Watkins R, Pfefferbaum A, Spielman D, Mayer D. Dynamic metabolic imaging of hyperpolarized [2-13C]pyruvate using spiral chemical shift imaging with alternating spectral band excitation. *Magn Reson Med* 2014; **71**: 2051–2058.

25 Park JM, Josan S, Jang T, Merchant M, Watkins R, Hurd RE, Recht LD, Mayer D, Spielman DM. Volumetric spiral chemical shift imaging of hyperpolarized [2-13C]pyruvate in a rat c6 glioma model. *Magn Reson Med* 2015; **984**: 973–984.

26 Mayer D, Yen YF, Levin YS, Tropp J, Pfefferbaum A, Hurd RE, Spielman DM. In vivo application of sub-second spiral chemical shift imaging (CSI) to hyperpolarized 13C metabolic imaging: Comparison with phase-encoded CSI. *J Magn Reson* 2010; **204**: 340–345.

27 Wiesinger F, Weidl E, Menzel MI, Janich MA, Khegai O, Glaser SJ, Haase A, Schwaiger M, Schulte RF. IDEAL spiral CSI for dynamic metabolic MR imaging of hyperpolarized [1-13C]pyruvate. *Magn Reson Med* 2012; **68**: 8–16.

28 Nelson SJ, Kurhanewicz J, Vigneron DB, Larson PEZ, Harzstark AL, Ferrone M, van Criekinge M, Chang JW, Bok R, Park I, Reed G, Carvajal L, Small EJ, Munster P, Weinberg VK, Ardenkjaer-Larsen JH, Chen AP, Hurd RE, Odegardstuen L-I, Robb FJ, et al. Metabolic imaging of patients with prostate cancer using hyperpolarized [1-^{13}C]pyruvate. *Sci Transl Med* 2013; **5**: 198–108.

29 Bruder H, Fischer H, Reinfelder HE, Schmitt F. Image reconstruction for echo planar imaging with nonequidistant k-space sampling. *Magn Reson Med* 1992; **23**: 311–323.

30 Du YP, Zhou XJ, Bernstein MA. Correction of concomitant magnetic field-induced image artifacts in nonaxial echo-planar imaging. *Magn Reson Med* 2002; **48**: 509–515.

31 Gordon JW, Vigneron DB, Larson PEZ. Development of a symmetric echo planar imaging framework for clinical translation of rapid dynamic hyperpolarized 13C imaging. *Magn Reson Med* 2017; **77**: 826–832.

32 Lupo JM, Chen AP, Zierhut ML, Bok RA, Cunningham CH, Kurhanewicz J, Vigneron DB, Nelson SJ. Analysis of hyperpolarized dynamic 13C lactate imaging in a transgenic mouse model of prostate cancer. *Magn Reson Imaging* 2010; **28**: 153–162.

33 Durst M, Koellisch U, Frank A, Rancan G, Gringeri C V., Karas V, Wiesinger F, Menzel MI, Schwaiger M, Haase A, Schulte RF. Comparison of acquisition schemes for hyperpolarised 13C imaging. *NMR Biomed* 2015; **28**: 715–725.

34 Jiang W, Lustig M, Larson PEZ. Concentric rings K-space trajectory for hyperpolarized 13C MR spectroscopic imaging. *Magn Reson Med* 2016; **75**: 19–31.

35 Posse S, DeCarli C, Le Bihan D. Three-dimensional echo-planar MR spectroscopic imaging at short echo times in the human brain. *Radiology* 1994; **192**: 733–738.

36 Posse S, Tedeschi G, Risinger R, Ogg R, Le Bihan D. High speed 1H spectroscopic imaging in human brain by echo planar spatial-spectral encoding. *Magn Reson Med* 1995; **33**: 34–40.

37 Posse S, Otazo R, Caprihan A, Bustillo J, Chen H, Henry PG, Marjanska M, Gasparovic C, Zuo C, Magnotta V, Mueller B, Mullins P, Renshaw P, Ugurbil K, Lim KO, Alger JR. Proton echo-planar spectroscopic imaging of J-coupled resonances in human brain at 3 and 4 Tesla. *Magn Reson Med* 2007; **58**: 236–244.

38 Hanson LG, Schaumburg K, Paulson OB. Reconstruction strategy for echo planar spectroscopy and its application to partially undersampled imaging. *Magn Reson Med* 2000; **44**: 412–417.

39 Metzger G, Hu X. Application of interlaced Fourier transform to echo-planar spectroscopic imaging. *J Magn Reson* 1997; **125**: 166–170.

40 Otazo R, Mueller B, Ugurbil K, Wald L, Posse S. Signal-to-noise ratio and spectral linewidth improvements between 1.5 and 7 tesla in proton echo-planar spectroscopic imaging. *Magn Reson Med* 2006; **56**: 1200–1210.

41 Pohmann R, von Kienlin M, Haase A. Theoretical evaluation and comparison of fast chemical shift imaging methods. *J Magn Reson* 1997; **129**: 145–160.

42 Pipe J, Duerk JL. Analytical resolution and noise characteristics of linearly reconstructed magnetic resonance data with arbitrary k-space sampling. *Magn Reson Med* 1995; **34**: 170–178.

43 Gallagher FA, Kettunen MI, Day SE, Hu DE, Ardenkjær-Larsen JH, Jensen PR, Karlsson M, Golman K, Lerche MH, Brindle KM. Magnetic resonance imaging of pH in vivo using hyperpolarized 13C-labelled bicarbonate. *Nature* 2008; **453**: 940–943.

44 Gallagher FA, Kettunen MI, Hu DE, Jensen PR, Karlsson M, Gisselsson A, Nelson SK, Witney TH, Bohndiek SE, Hansson G, Peitersen T. Production of hyperpolarized [1, 4-13C2] malate from [1, 4-13C2] fumarate is a marker of cell necrosis and treatment response in tumors. *Proc Natl Acad Sci USA* 2009; **106**: 19801–19806.

Figure legends

Figure 1: A diagram showing the spectral positions of the metabolites with a spectral bandwidth of 495 Hz and a reference frequency chosen midway between lactate and pyruvate. (a) After injection of hyperpolarized [1-^{13}C]pyruvate lactate at 186 Hz, pyruvate-hydrate at 24 Hz, alanine at -21 Hz, pyruvate at -186 Hz and bicarbonate aliased to 1 Hz (true position at -494 Hz). The Figure also shows the peak positions of the substrates used in the phantom experiment (b); acetate at 155 Hz and the aliased urea and bicarbonate at 71 Hz (true position -424 Hz) and -1 Hz (true position 494 Hz), respectively. In the phantom experiment, however, the actual reference frequency was chosen at the middle between bicarbonate and acetate to ensure uniform excitation for the substrates. These frequency positions were calculated based on a synthesizer frequency of 30.995 MHz which corresponds to a magnetic field of 2.8954 T. The chemical shift values in ppm are obtained from: http://www.utsouthwestern.edu/education/medical-school/departments/airc/tools-references/chemical-shifts/chemical-shifts-sorted-by-compound-name.html

Figure 2: The pipeline used for the reconstruction of the raw data and the correction of the broadening due to chemical shifts in opposite directions for odd and even echoes.

Figure 3: The [1-^{13}C]acetate, ^{13}C-bicarbonate and ^{13}C-urea maps acquired by CSI and EPSI. Only the central part of the phantom is shown. The signal level in the maps is normalized with respect to the bicarbonate signal acquired with CSI. The spectrum from a single voxel at the center of each substrate is also shown for both CSI and EPSI. The line width (full width at half height) obtained with CSI was 12.2 Hz, 9.2 Hz and 10.6 Hz for [1-^{13}C]acetate, ^{13}C-bicarbonate and ^{13}C-urea respectively, whereas the line width obtained with EPSI was 11.7 Hz, 8.7 Hz and 9.8 Hz.

Figure 4: A comparison of chemical shift displacement with (a) direct FFT reconstruction and (b, c) with reconstruction after spectral-spatial regridding (b, c). The Image from odd (green) and even (magenta) echoes are overlaid. The locations of overlap appear in white and the non-overlap locations appear colored. In (b) spectral-spatial regridding removes the chemical shift displacement

of bicarbonate and urea, which are within the spectral bandwidth, but increases the chemical shift displacement of acetate that is aliased. In (c) the chemical shift displacement of the acetate peak is additionally corrected using its non-aliased frequency location in the reconstruction.

Figure 5: The first dynamic image acquired for hyperpolarized [1-^{13}C]pyruvate in a 4.5 L phantom with EPSI in (b) and the coil profile (a). (c) shows the decay of the signal from hyperpolarized pyruvate obtained by both EPSI and CSI dynamics. An exponential function was fitted to the EPSI signal giving a time constant of 52 s.

Figure 6: The anatomical images (transversal, coronal and sagittal) acquired with TSE and used to position the spectroscopic grids for both CSI and EPSI (a, b and c). The green box is at the location of the tumor.

Figure 7: The acanthomatous ameloblastoma in the left mandible of the canine cancer patient (a). The PET-FDG image (slice thickness 2 mm) with high uptake in the tumor and brain regions is shown in (d). (b and e) show the pyruvate and lactate signals, obtained from the CSI acquisition using GLM, at the slice containing the tumor. Increased lactate production can be observed at the tumor and muscle sites. (c and f) show pyruvate and lactate images calculated from the dynamic EPSI by integrating over the frames in Figure 8.

Figure 8: Pyruvate and lactate build-up and decay across the slice containing the tumor. The figure also shows the spectrum with GLM fitting at the tumor site in the EPSI frame acquired 27 s after the end of injection.

Figure 9: (a) The build-up of pyruvate and its conversion to lactate obtained with dynamic FID acquisition over a 4 cm axial slab that includes the tumor region. (b, c and d) show the time curves for lactate and pyruvate obtained from the EPSI series (Figure 8) by integrating the pyruvate and lactate signals in each frame at the whole image, at the tumor region, and at the masticator muscle, respectively.

Figures

FIG 1:

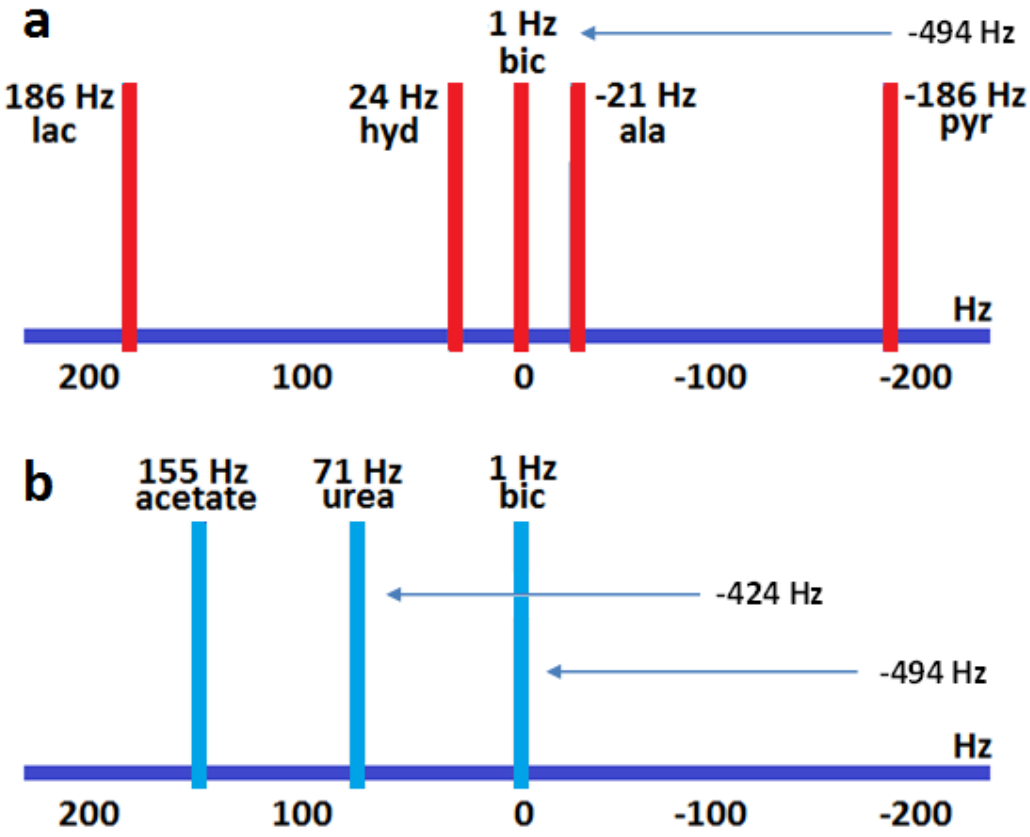
a
1 Hz
bic
-494 Hz
186 Hz
lac
24 Hz
hyd
-21 Hz
ala
-186 Hz
pyr
Hz
200
100
0
-100
-200
b
155 Hz
acetate
71 Hz
urea
1 Hz
bic
-424 Hz
-494 Hz
Hz
200
100
0
-100
-200

Fig 2:

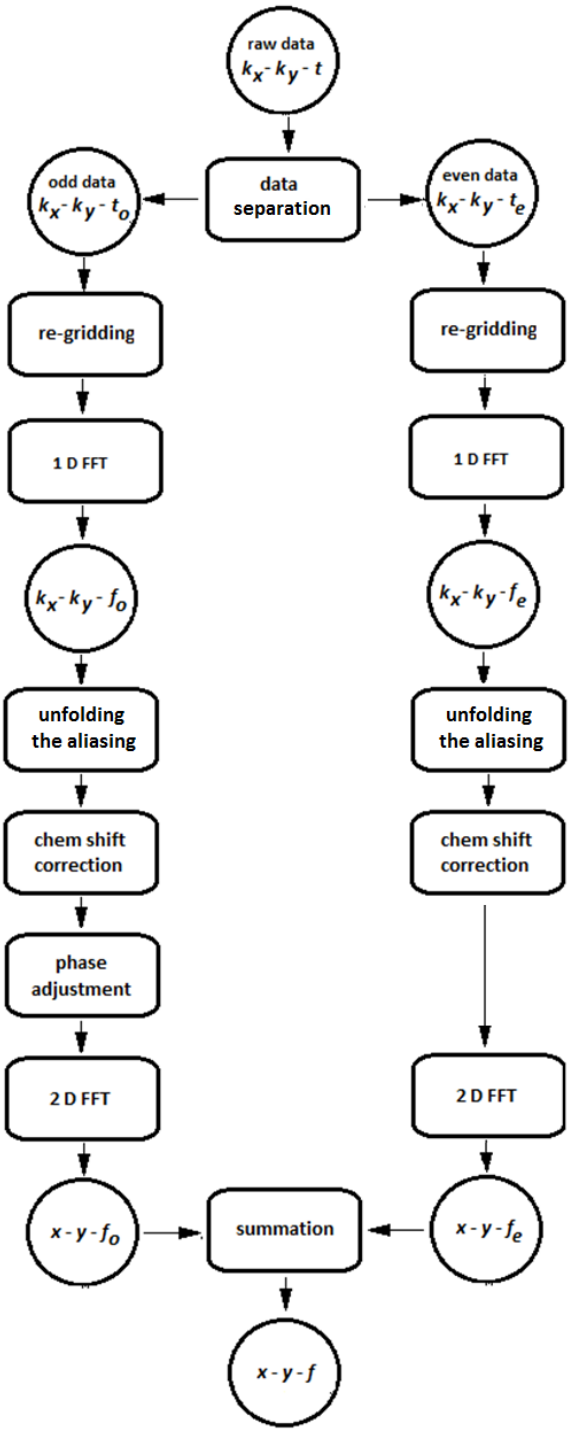
raw data
k_x- k_y- t
data separation
odd data
k_x- k_y- t_o
even data
k_x- k_y- t_e
re-gridding
re-gridding
1 D FFT
1 D FFT
k_x- k_y- f_o
k_x- k_y- f_e
unfolding the aliasing
unfolding the aliasing
chem shift correction
chem shift correction
phase adjustment
2 D FFT
2 D FFT
x - y - f_o
summation
x - y - f_e
x - y - f

FIG 3:

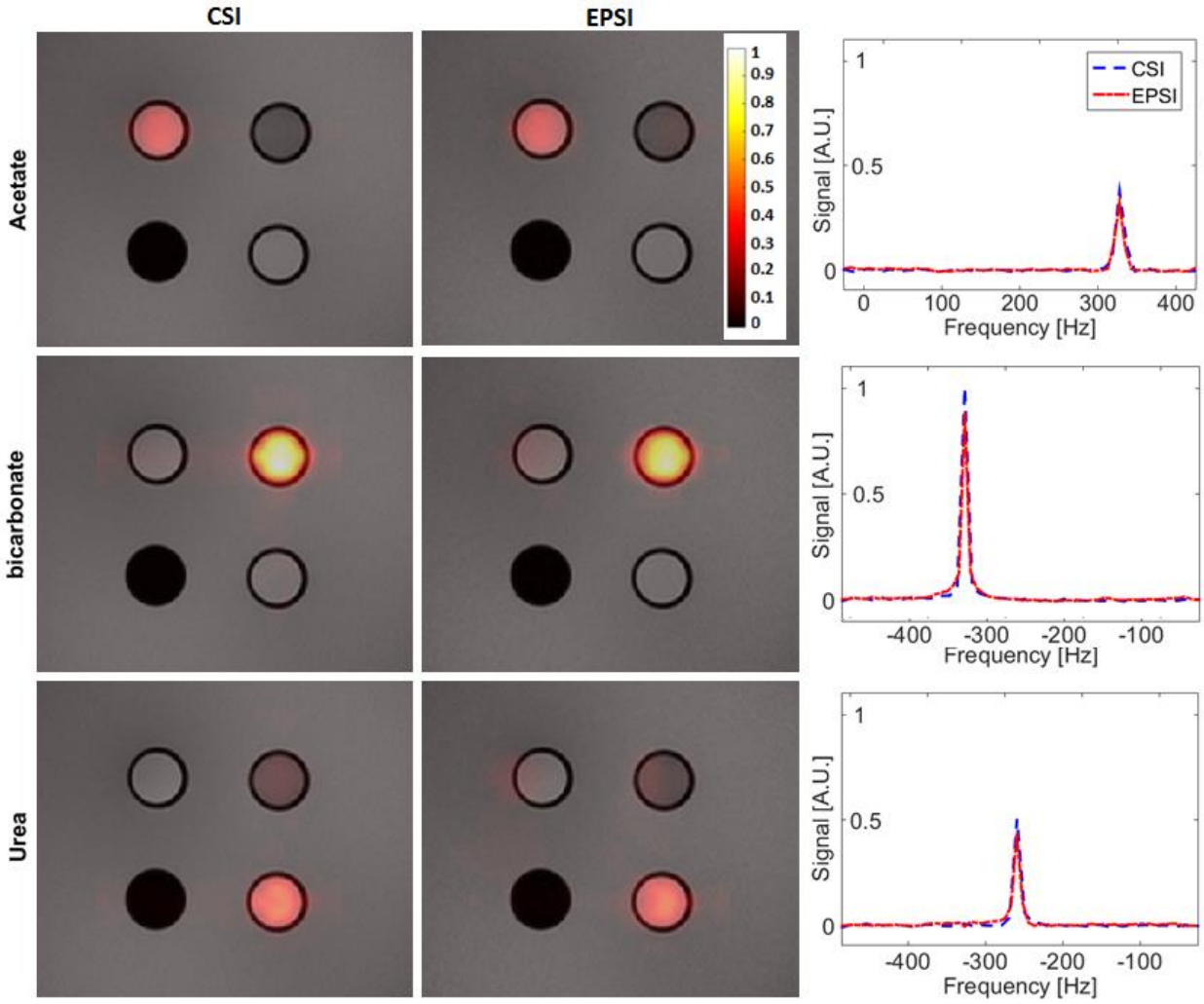
CSI
EPSI
Acetate
bicarbonate
Urea
1
0.9
0.8
0.7
0.6
0.5
0.4
0.3
0.2
0.1
0
CSI
EPSI
Signal [A.U.]
Frequency [Hz]
0
100
200
300
400
-400
-300
-200
-100
0.5
1

FIG 4:

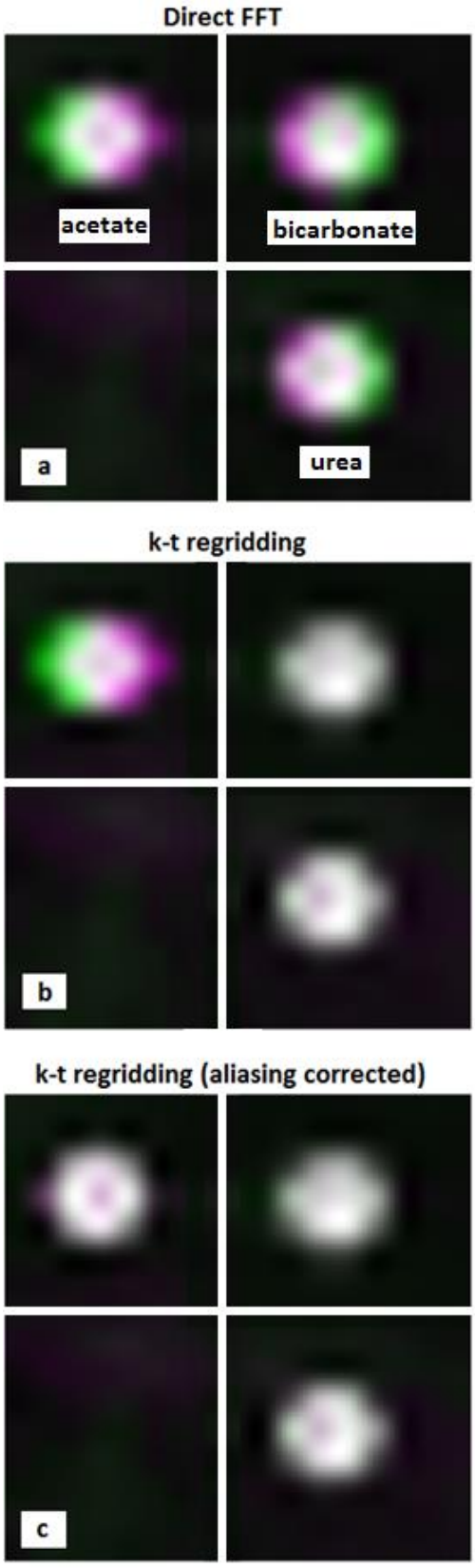
Direct FFT
acetate
bicarbonate
a
urea
k-t regridding
b
k-t regridding (aliasing corrected)
c

FIG 5:

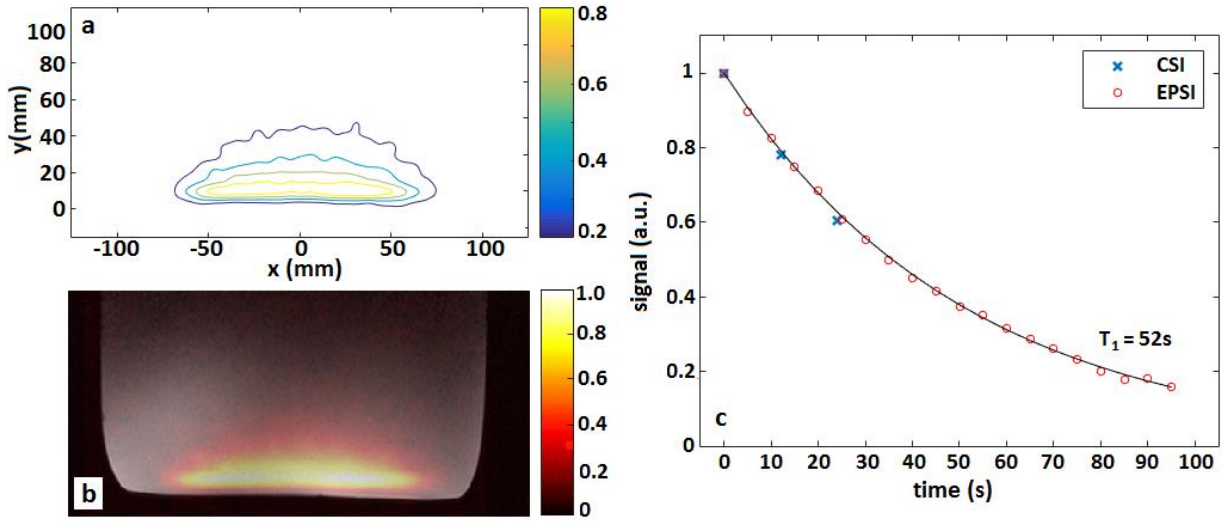

FIG 6:

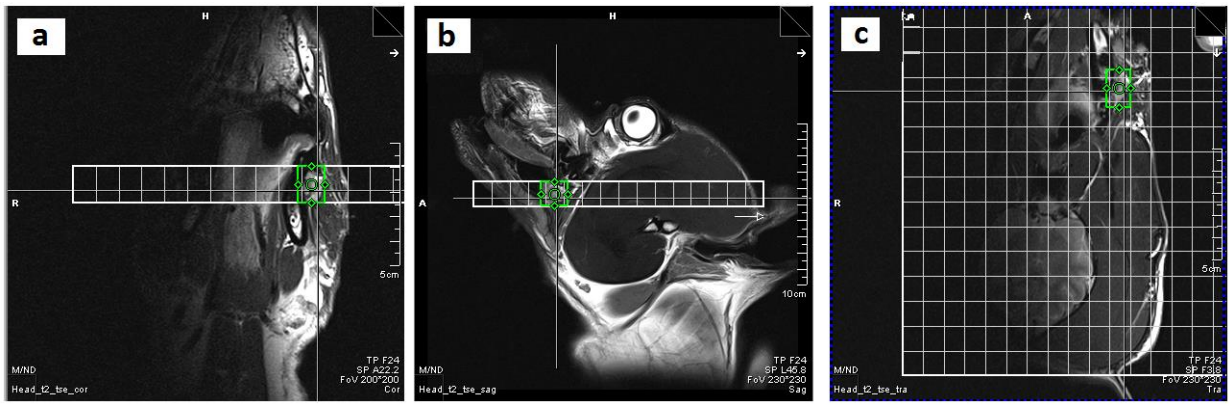
a
H
R
5cm
M/ND
Head_t2_tse_cor
b
H
A
10cm
M/ND
Head_t2_tse_sag
c
A
R
5cm
M/ND
Head_t2_tse_tra

FIG 7:

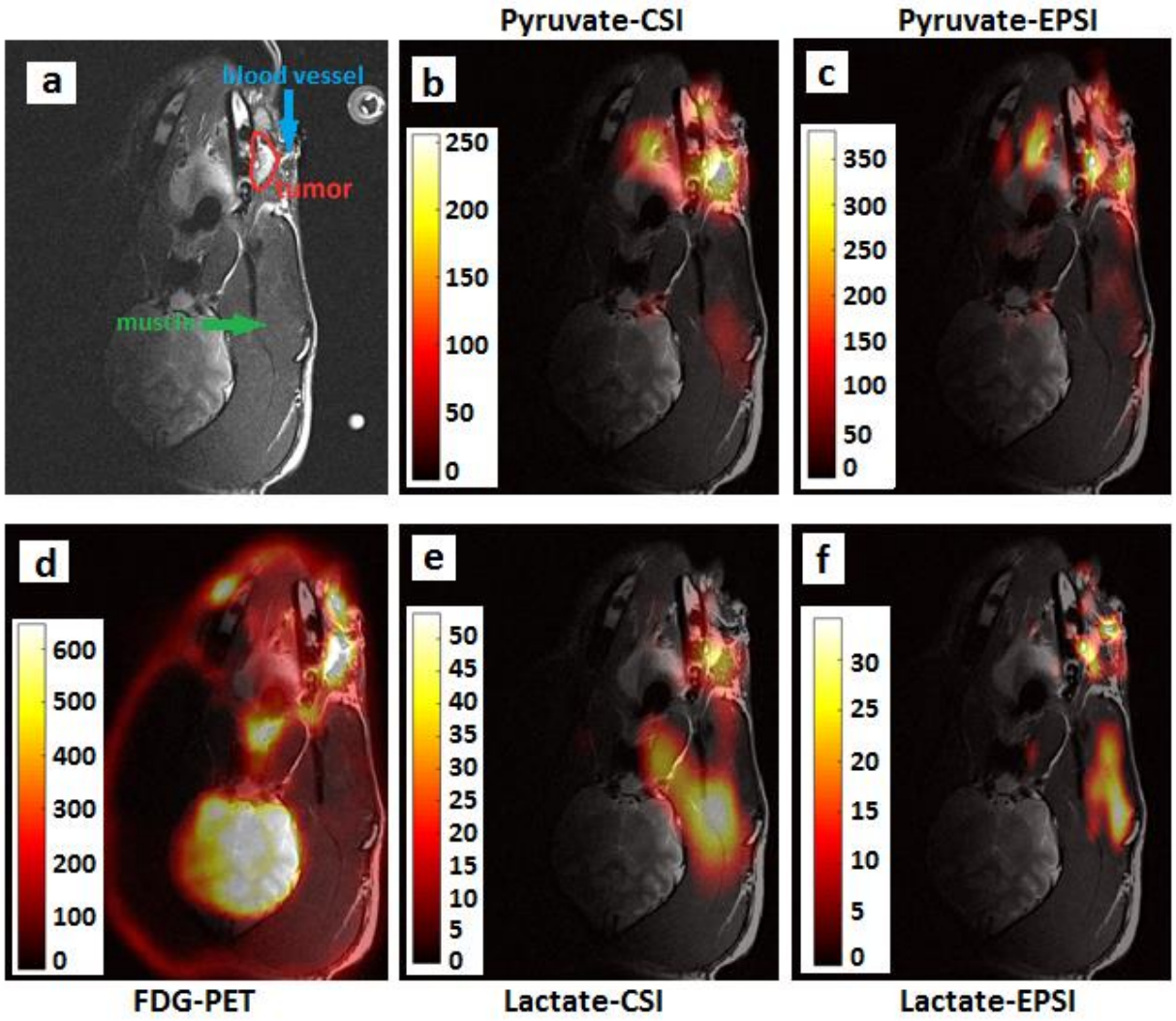
Pyruvate-CSI
Pyruvate-EPSI
a
blood vessel
tumor
muscle
b
250
200
150
100
50
0
c
350
300
250
200
150
100
50
0
d
600
500
400
300
200
100
0
e
50
45
40
35
30
25
20
15
10
5
0
f
30
25
20
15
10
5
0
FDG-PET
Lactate-CSI
Lactate-EPSI

FIG 8:

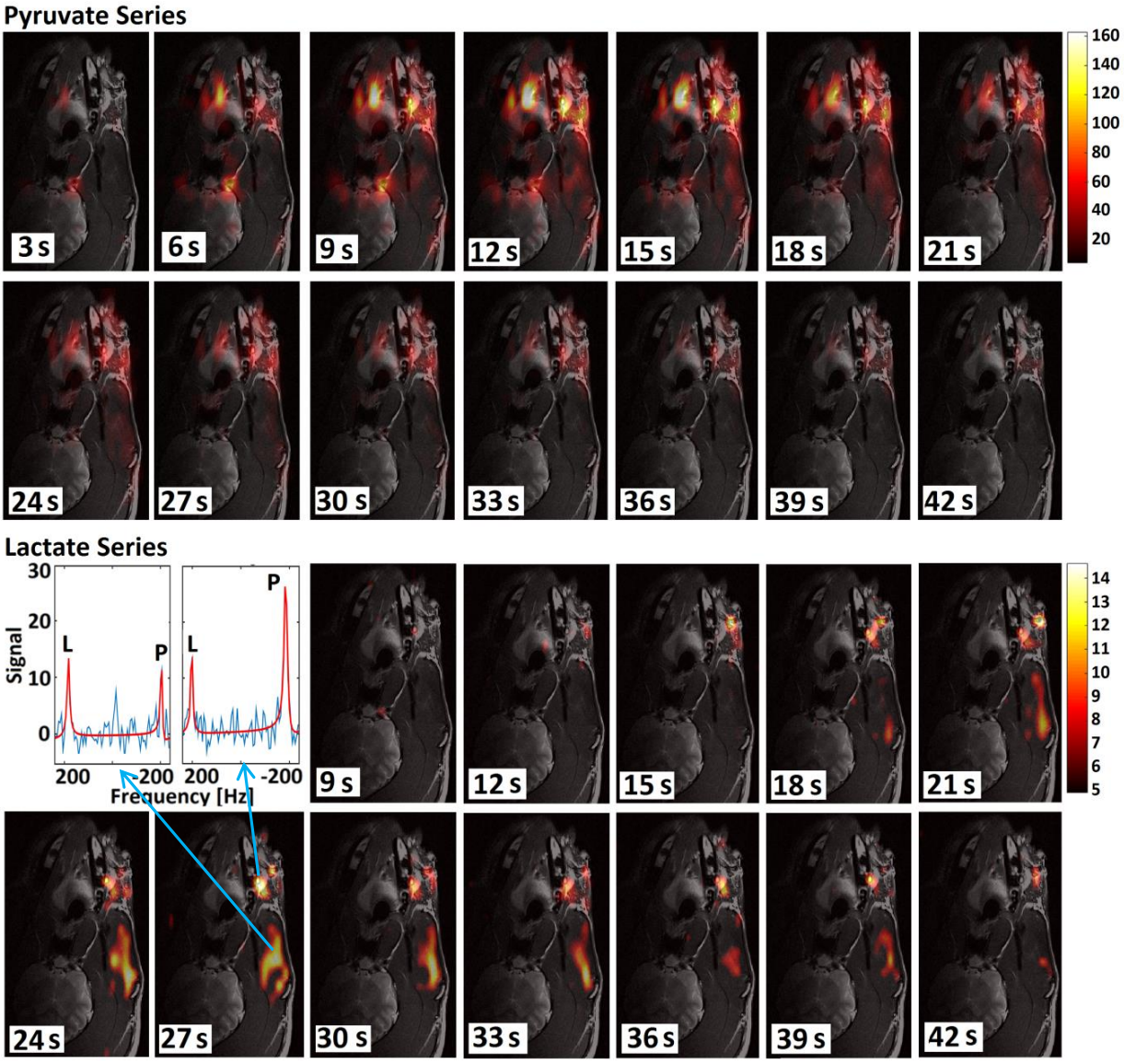
Pyruvate Series
3 s
6 s
9 s
12 s
15 s
18 s
21 s
24 s
27 s
30 s
33 s
36 s
39 s
42 s
160
140
120
100
80
60
40
20
Lactate Series
Signal
30
20
10
0
L
P
200
-200
Frequency [Hz]
14
13
12
11
10
9
8
7
6
5

FIG 9

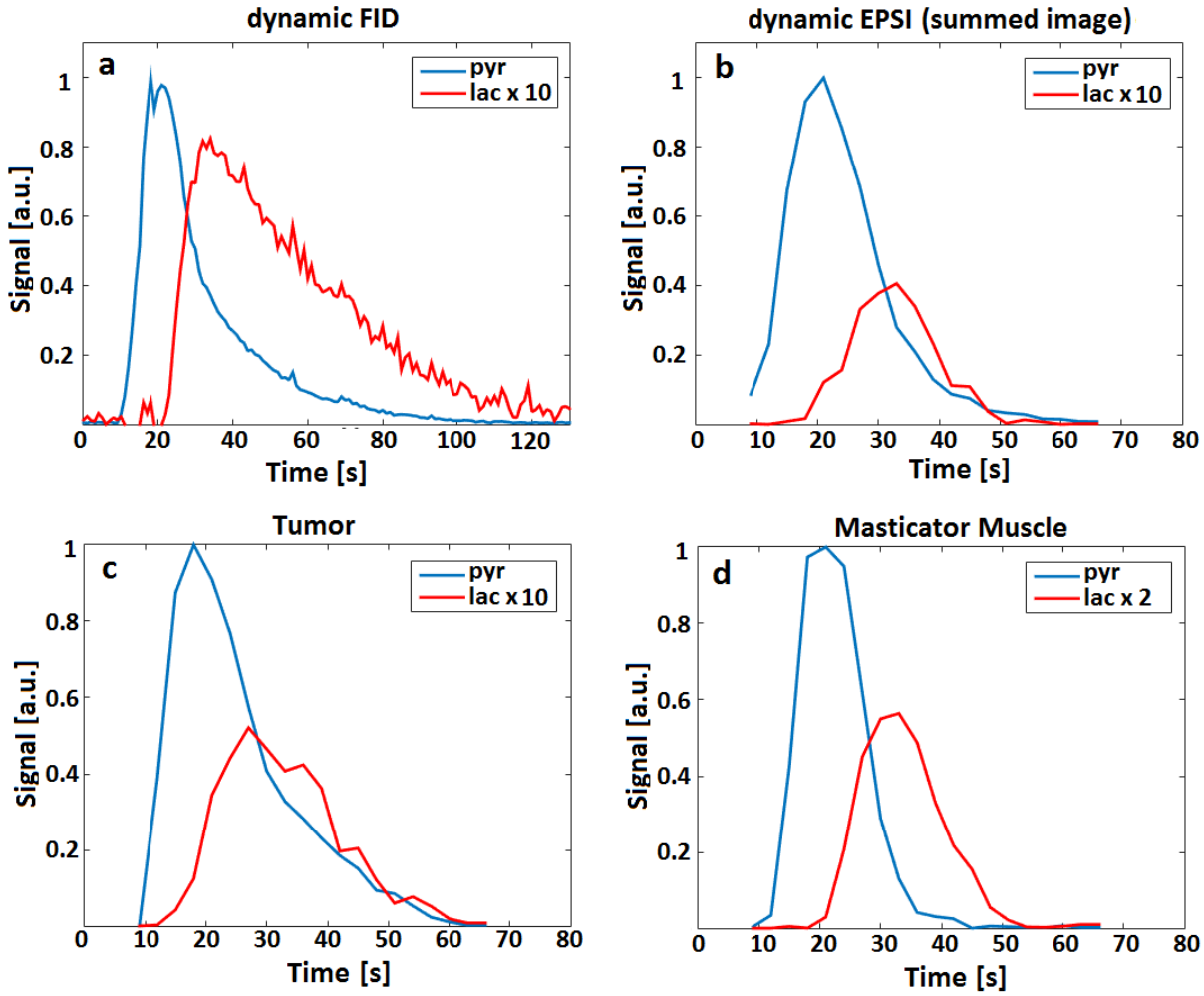
dynamic FID
a
pyr
lac x 10
Signal [a.u.]
Time [s]
dynamic EPSI (summed image)
b
pyr
lac x 10
Signal [a.u.]
Time [s]
Tumor
c
pyr
lac x 10
Signal [a.u.]
Time [s]
Masticator Muscle
d
pyr
lac x 2
Signal [a.u.]
Time [s]